QUEEN MARY UNIVERSITY OF LONDON

School of Physics and Astronomy
Particle Physics Research Centre

Submitted in partial fulfillment of the requirements of the
Degree of Doctor of Philosophy

MEASURING CHARGE ASYMMETRIES IN *B*-HADRON DECAYS USING TOP QUARK EVENTS WITH THE ATLAS EXPERIMENT

Supervisor:
Prof. LUCIO CERRITO

Student:
ADELINA D'ONOFRIO

April 4, 2019

Come sempre, alla mia famiglia: per quello che mi avete insegnato e per l'amore e la forza che mi date.

DECLARATION

I, Adelina D'Onofrio, confirm that the research included within this thesis is my own work or that where it has been carried out in collaboration with, or supported by others, that this is duly acknowledged below and my contribution indicated. Previously published material is also acknowledged below.

I attest that I have exercised reasonable care to ensure that the work is original, and does not to the best of my knowledge break any UK law, infringe any third party's copyright or other Intellectual Property Right, or contain any confidential material.

I accept that the College has the right to use plagiarism detection software to check the electronic version of the thesis.

I confirm that this thesis has not been previously submitted for the award of a degree by this or any other university.

The copyright of this thesis rests with the author and no quotation from it or information derived from it may be published without the prior written consent of the author.

Signature:

Date:

ABSTRACT

The large number of top-antitop pair events produced in pp collisions at the Large Hadron Collider (LHC) provides a unique source of b-quarks that can be used to probe the $\mathcal{CP}$ violation in heavy-flavour mixing and decay.
The measurement presented in this thesis focuses on semi-leptonic top-antitop events where one of the W-bosons decays hadronically and the other one decays leptonically. The charge of the lepton (electron or muon) from the W-boson tags the charge of the b-quark at production. In events where a muon is associated to the semi-leptonic decay of the b-quark (either directly or after a $b \to c$ hadronic transition), two charge asymmetries (CA) and several $\mathcal{CP}$ asymmetries, based on the charges of the lepton from the W-boson and this muon, can be measured.
My contribution to the first measurement of the CA and $\mathcal{CP}$ asymmetries in heavy flavour b- or c-decays from top-antitop lepton+jets events is presented, using the data collected with the ATLAS detector during Run 1 of the LHC ($20.3\,\text{fb}^{-1}$) at a centre of mass energy of $\sqrt{s} = 8\,\text{TeV}$.
However, most of the thesis focuses on my (larger) contribution to this same measurement, performed with data collected by the ATLAS experiment during Run 2, 2015-16 data taking periods, corresponding to an integrated luminosity of $36.1\,\text{fb}^{-1}$ at a centre of mass energy of $\sqrt{s} = 13\,\text{TeV}$.
Four $\mathcal{CP}$ asymmetries (one mixing and three direct) were measured, using Run 1 data, and they are found to be consistent with the Standard Model.
The Run 2 analysis results in the measurement of two charge asymmetries, both compatible with zero and consistent with the Standard Model expectations. The overall uncertainty on the Run 2 measurement is halved with respect to the Run 1 result.

ACKNOWLEDGEMENTS

Thanks a lot to my supervisor, Prof. Lucio Cerrito for his guidance and support over all these years, from the first months in London to the years at CERN. Long distance relations are not easy but I am grateful we made it work and I learnt a lot in these three years.
Thanks to Dr. Veronique Boisvert for all her useful suggestions and comments in our meetings!
Thanks to all the members of the analysis group I had the pleasure to work with during my PhD: John, Jacob, Lewis and all the NPTEV group.
Thanks to all the PPRC group of QMUL, you taught me a lot in these years!
Thanks to Andres, Rodrigo, Antony, Shivesh, Billy and all the PhD students for the beers and for sharing this adventure with me.
Grazie, immensamente grazie alla mia famiglia: a chi c'é ed a chi c'é stato ma continua ad essere nei nostri cuori. Grazie mamma, papá, Vitty, Tatti e Gnagna perché in qualunque parte del mondo io sia o saró voi sarete sempre il mio porto sicuro, la casa a cui tornare.
Grazie al mio Marcolino per il suo amore e sostegno infinito, nelle risate, nei pianti e nelle urla minacciose. Questa tesi é stata impegnativa per me, ma anche per te che mi sei stato sempre accanto: anche se momentaneamente dall'altra parte del mondo, non mi lasci mai sola.
Grazie a Stefi, Alberto, Marco, Federica, Laura e tutto il gruppo di Pisa per aver condiviso parte di questo lungo percorso con me, per l'affetto che mi avete dato in questi undici anni, per i viaggi, le cene e le risate.
In piú di due anni al CERN ho incontrato colleghi ma soprattutto amici ed ognuno di loro meriterebbe un ringraziamento speciale ma, come ben sa chi é qui al CERN in questi giorni, sono talmente esausta da crollare addormentata sul divano di Giulia nel bel mezzo di una cena quindi, per ora mi limiteró a ringraziarvi tutti assieme: Serena, Frankie, Lorenzo, Chicco, Fefe, Valentina, Giuliano, Giulia, Betto, Ale, Filippo, Cami, Grazia, Peter, Simona, Manfredi, Francesco G., Silvia, Federico, Fabio, Francesco D.B., Lorenzo, Maurizio e tutti tutti gli amici che, in questi anni, mi sono stati accanto con affetto e pazienza.
Grazie a Marco V. per il suo inesauribile ottimismo, per avermi sempre incoraggiata durante il dottorato con i suoi "Tranquilla che dopo va sempre peggio", per il suo sostegno e per tutte le volte che ha risposto ai miei "Ciao, Marco" seguiti da domande improbabili ad orari improbabili. Grazie, davvero!
Grazie ad Umberto per tutte le chiacchierate, i consigli, i caffé e per avermi presa per mano con questo unfolding ed avermi sostenuta fino alla fine. Grazie Umbe!
Grazie a Michele per il suo sostegno ed i suoi consigli e per i tanti strumenti che mi ha insegnato ad usare in questi anni. Grazie!

Dico grazie anche a me stessa perché la prima volta che si va via da casa ci vuole curiositá e coraggio, la seconda volta ci vuole determinazione e carattere, la terza ci vuole una grande forza di volontá, dalla quarta in poi ci vuole un po' di follia. Grazie alla mia ansia, amica fedele in questi mesi ma soprattutto grazie alla mia testa per non avermi (quasi) mai abbandonata.
Anche questa é fatta!

INTRODUCTION

The main subject of this thesis is my contribution to the measurement of charge asymmetries in b-hadron decays using top quark events collected by the ATLAS detector in proton-proton collisions at a centre of mass energy of $\sqrt{s} = 13\,\text{TeV}$, using the 2015 and 2016 datasets, corresponding to an integrated luminosity of $36.1\,\text{fb}^{-1}$ (from hereon this measurement will be referred to as Run 2 measurement).
This thesis also describes my contribution to the same measurement, performed at a centre of mass energy of $\sqrt{s} = 8\,\text{TeV}$, using the 2012 datasets, corresponding to an integrated luminosity of $20.3\,\text{fb}^{-1}$ (from hereon this measurement will be referred to as Run 1 measurement).
The underlying idea of this measurement is to exploit the large $t\bar{t}$ production at the Large Hadron Collider (LHC) as a source of b-quarks, to study $\mathcal{CP}$ violation in heavy flavour mixing and decays. The measurement focuses on $t\bar{t}$ events in the lepton+jets channel, where one of the W-bosons decays hadronically and the other one decays leptonically. The W-boson charge is related to the charge of the *soft* muon from a b-decay (this muon is labelled as *soft* because its p_{T} spectrum is softer with respect to the prompt lepton from the W-boson, a precise definition of soft muon will be given in Chapter 6).
Indeed, one of the peculiarities of the analysis presented in this thesis is the identification of a $soft$ muon from semi-leptonic b-hadron decays, performed with a Soft Muon Tagging (SMT) method.
My contributions to the charge asymmetries measurement are:

1. Calibration of the mistag rate of the SMT algorithm for the Run 1 measurement
2. Optimisation of the Kinematic Likelihood Fitter for the Run 2 measurement
3. Uncertainty evaluation for the Run 2 measurement
4. Unfolding procedure for the Run 2 measurement

Chapters 1-3 provide a general introduction to the theoretical and experimental framework for the analysis presented in this thesis. Chapter 1 contains a brief description of the $\mathcal{CP}$ violation and the Top quark, in the context of the Standard Model of Particle Physics and Chapter 2 highlights the physics motivations behind the analysis. Chapter 3 includes an overview of the ATLAS detector at the LHC, while Chapter 4 focuses on the ATLAS Level-1 Calorimeter based trigger, describing my contribution to the optimisation of the rates and efficiencies in view of high-luminosity runs of the LHC.
Chapter 5 describes the reconstruction of the physics objects of interest for the measurement presented in this thesis, using the ATLAS detector.

During the Run 1 measurement, I was in charge of the calibration of the mistag rate of the SMT algorithm, as described in Chapter 6. In Run 1, the soft muon tagger algorithm was based on the fractional difference in momentum between muon tracks, reconstructed in the inner detector and in the muon spectrometer (extrapolated back to the primary vertex) of the ATLAS detector. This technique, known as the momentum imbalance (MI) based SMT, was used to discriminate soft muons from heavy-flavour decays from fakes of other sources. My contribution consisted in the evaluation of the fake rate of the SMT, *i.e.* how many times the SMT mistakenly tags muons from light-flavour decays as muons from heavy-flavour decays.
Chapter 7 describes the event selection used for the charge asymmetry measurement in Run 2: it is based on the $t\bar{t}$ semi-leptonic event selection prescribed by the ATLAS Top Group and alterations to this selections are justified in this Chapter.
Chapter 8 describes the implementation of a Kinematic Likelihood Fitter used to reconstruct the $t\bar{t}$ events, based on topology information. I worked on the implementation and optimisation of this technique for the measurement in Run 2.
A description of the systematic uncertainties affecting the measurement of charge asymmetries is given in Chapter 9.
Chapter 10 includes the work I did to evaluate the systematic uncertainties and the unfolding procedure used to extract the charge asymmetry results.
Finally Chapter 11 outlines the conclusions and the future perspectives for the charge asymmetries measurement.

CONTENTS

Part I.

Theoretical and Experimental Framework

1

CP VIOLATION AND TOP QUARK IN THE STANDARD MODEL

A brief overview of the Standard Model of Particle Physics is outlined in this Chapter, in particular focussing on the theoretical aspects, like $\mathcal{CP}$ violation, which are relevant for the analysis presented in this thesis. Moreover, an introduction to Top quark Physics is given since it will be the core of the analysis.

1.1 THE STANDARD MODEL OF PARTICLE INTERACTIONS

The Standard Model (SM) of Particle Physics describes the basic building blocks of our (known) Universe and their interactions. Years of experimental results and theory predictions, since the early 30's, led to the formulation of a solid and nowadays well-tested model which describes our best understanding of the fundamental structure of matter. According to the SM, there are 12 elementary particles (plus their anti-particles) and four fundamental forces, carried by gauge bosons. The relative strength of these forces spread across wide range of orders of magnitude, as described in Table 1, and the SM theory describes three of the four forces observed in Nature: the electromagnetic, the weak and the strong forces.

Force	Strength	Propagator
Strong	1	Gluons (g)
Electromagnetic	10^{-3}	Photon (γ)
Weak	10^{-8}	$W^{\pm}$ and Z^0 bosons
Gravity	10^{-37}	Graviton

Table 1.: Relative strengths of the fundamental forces, considered for two particles at a distance of 10^{-15} m [2].

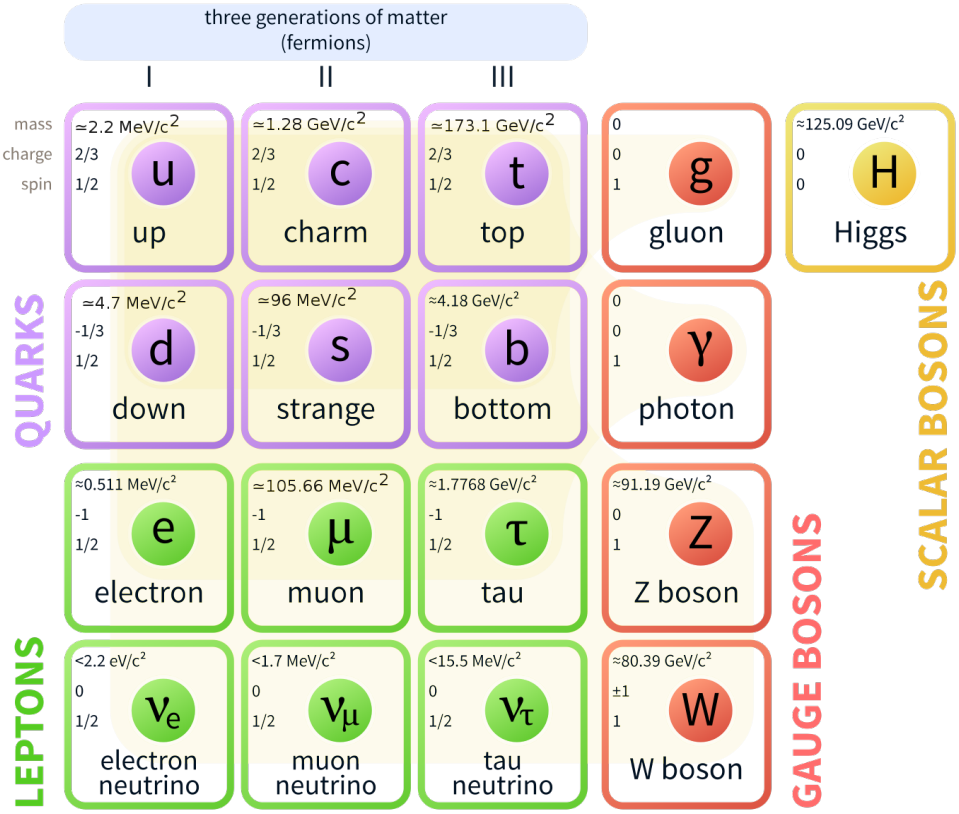

Figure 1.: Elementary particles in the SM. Each elementary particle is uniquely described by its quantum numbers: mass, charge and spin. Information from [1].

Gravity is currently not included in the SM and the reason why it is so weak is one of the open questions waiting for our answer.
The 12 point-like particles, summarised in Figure 1, have half-integer spin in units of $\hbar$ and they are classified as leptons (e, μ and τ with electric charge and ν_e, ν_μ and ν_τ without electric charge) and quarks (u,d,c,s,t,b).
The SM describes only 4% of our Universe; moreover it does not explain the predominance of matter with respect to antimatter. At present, the observed $\mathcal{CP}$ violation ($\mathcal{CPV}$) is not sufficient to explain the asymmetry of matter and anti-matter in the Universe, as detailed in Section 1.8. The analysis presented in this thesis shows a precise measurement of charge asymmetries which are related to fundamental $\mathcal{CPV}$ parameters to investigate deviations that might lead to the discovery of beyond SM (BSM) physics.

1.1.1 *The Standard Model: a theoretical introduction*

In the elementary particle physics scenario, the SM is a $SU(3)_C \bigotimes SU(2)_L \bigotimes U(1)_Y$ gauge field theory of strong and electroweak interactions [1]:

- $SU(3)_C$ is a representation of the Colour Symmetry and it provides massless gluons as gauge fields (G_μ) mediating the strong interactions which are responsible for binding the quarks in neutron and proton, and the neutrons and protons within nucleus.

- $SU(2)_L$ and $U(1)_Y$ are related to the electroweak interactions, and represent Weak Isospin Symmetry and Weak Hypercharge Symmetry. They imply the existence of massive bosons ($W^\pm$ and Z^0) as propagators of $\vec{W}_\mu$ and B_μ gauge fields, after the spontaneous symmetry breaking (detailed in Section 1.3). Electromagnetic interactions are responsible for most of the phenomena in extranuclear physics and they are mediated by the photon (γ), while Weak interactions are, for instance, responsible for neutron decays (the neutron lifetime τ is $\tau_n \sim 900\,\mathrm{s}$). This is the only interaction that involves neutrinos and that can change the flavours of particles. In the mathematical framework of the Standard Model, a Lagrangian equation describes the dynamics and kinematics of the elementary particles. The SM Lagrangian is the sum of the Quantum Chromodynamics (QCD) and the Electroweak Lagrangians, as outlined in the next Sections and as described in formula 1.

$$\mathcal{L}_{\mathrm{SM}} = \mathcal{L}_{\mathrm{EW}} + \mathcal{L}_{\mathrm{QCD}} \tag{1}$$

1.2 STRONG INTERACTIONS

Quantum chromodynamics (QCD) is the gauge theory which describes the strong interactions [4], mediated by eight massless particles called gluons. The matter fields in this theory are quarks carrying a quantum number called colour (and anticolour) which is conserved in strong interaction vertices and is represented by three states, called *red*, *green* and *blue*, analogous to the *charge* in electromagnetic interactions.
The gauge-invariant Lagrangian of QCD governs the dynamics of quarks and gluons and it is described in formula 2:

1 A partial and short outline of the SM theory is presented, for a complete introduction refer to [2], [3].

$$\mathcal{L}_{\text{QCD}} = -\frac{1}{4} F^a_{\mu\nu} F_{a\mu\nu} + \bar{\psi} \left(i\gamma^\mu D_\mu - m \right) \psi \tag{2}$$

where ψ is the Dirac spinor representing the fermion field and m is the fermion mass. The first part of the equation governs the dynamics of the system (quarks and gluons) and the second parts its kinematics. Because gluons carry colour, they can interact among themselves, as shown in the Feynman diagrams in Figure 2.

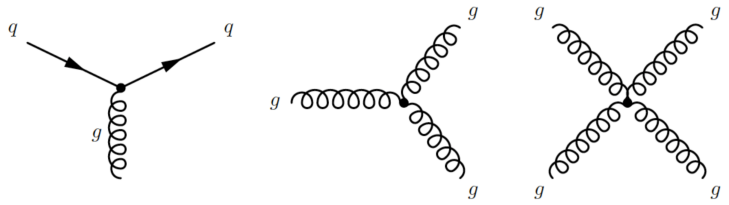

(a) Quark-gluon vertex **(b)** Three-gluon vertex **(c)** Four-gluon vertex

Figure 2.: Leading order QCD vertices, showing the interaction between a gluon and two quarks and the three- and four-gluon self-interaction vertices.

Due to this peculiarity, isolated quarks cannot be observed and this effect is called *confinement*: the strong force acting between two coloured quarks prevent them from being pulled apart. If enough energy is invested in trying to separate two coloured quarks, the energy in the gluon field can create another quark pair meaning that quarks can be only in bound composite colourless states such as baryons and mesons. For example, the protons which collide at the LHC are a bound state of quarks and gluons and it is crucial to physics analyses to understand the production cross section for a specific process that depends on the parton distribution function (PDF). Figure 3 shows the fraction of energy x carried by the parton, multiplied by the parton distribution function $f(x, Q^2)$, where Q is the transferred momentum and $Q^2 \in (10, 100^2)\,\text{GeV}^2$ for protons.

The QCD structure, namely the self interaction of the gauge fields, also leads to the behaviour of the strong coupling constant α_s, pictured in Figure 4, as a function of the transferred momentum Q of the interacting particles.

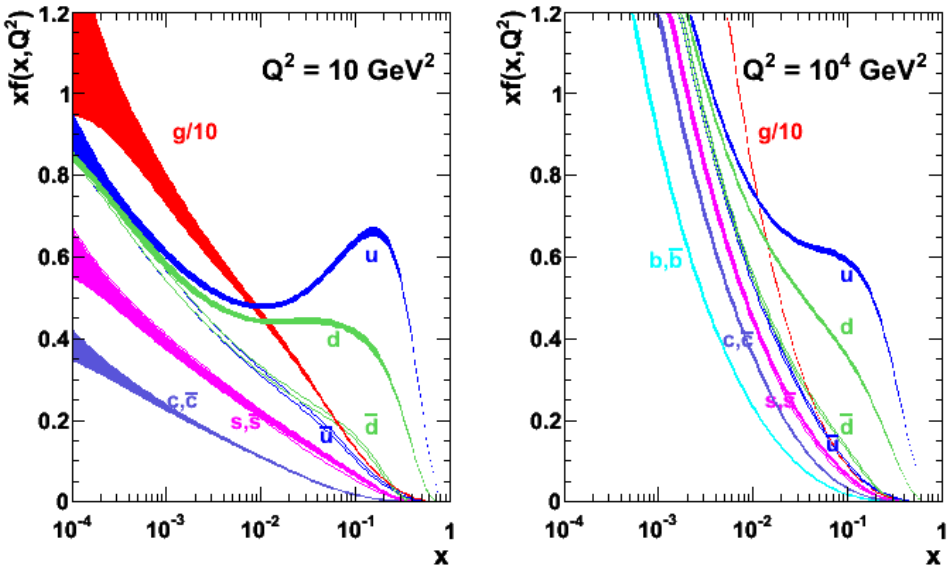

Figure 3.: Fraction of energy x carried by the parton, multiplied by the parton distribution function $f(x, Q^2)$ for protons [2].

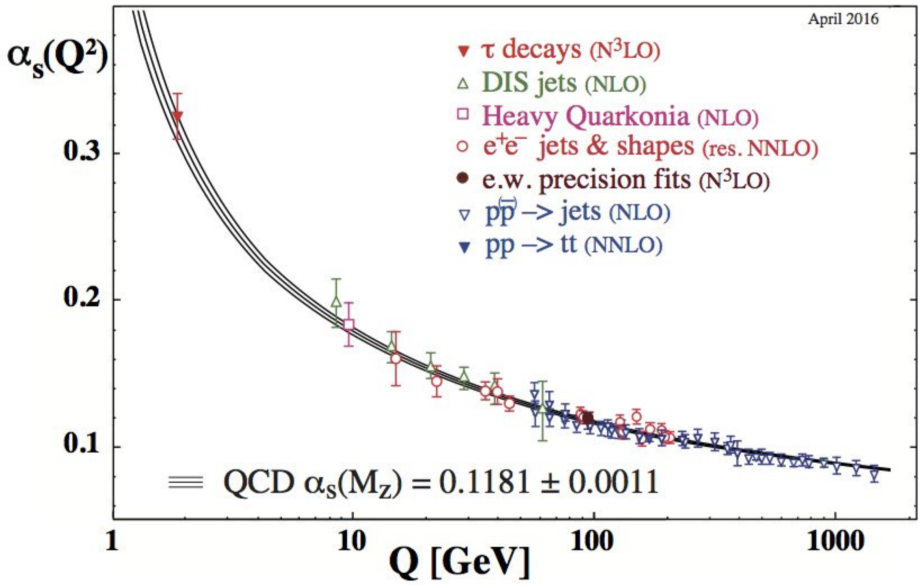

Figure 4.: α_s distribution as a function of the momentum transferred Q^2 [2].

As described in formula 3, as $Q^2 \to \infty$ quarks behave as free particles, while as the distances increases, $Q^2 \to 0$, the coupling $\alpha_s \to \infty$ and the quark confinement becomes more energetically convenient with respect to the free particles state.
The evolution of $\alpha_s\left(Q^2\right)$ is given by:

$$\alpha_s\left(Q^2\right) = \frac{12\pi}{\left(33 - 2n_f\right)\ln\left(Q^2/\Lambda_{QCD}\right)}, \tag{3}$$

where Λ_{QCD} is the energy scale of strong interactions (hundreds of MeVs) and n_f is the number of quarks with mass up to $\sqrt{Q^2}$.

1.3 ELECTROWEAK INTERACTIONS

1.3.1 *Electromagnetic Interactions*

Quantum Electrodynamics (QED) is a theory which describes phenomena involving charged particles and their interactions, mediated by the γ boson propagating the electromagnetic force.
Figure 5 shows the interaction between a photon and two fermions where the charge is always conserved in the vertex and the coupling is proportional to the electron charge.

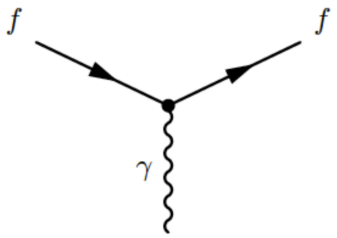

Figure 5.: Leading order vertex for QED: interaction between a photon and two generic fermions f.

1.3.2 *Weak Interactions*

In the early 1930', Fermi [5] provided a qualitative description of the theory of β decays of the neutron as a contact interaction of two vector currents, whose matrix element M is given in Equation 4.

$$M \propto G_F\left(\bar{n}\gamma^\mu p\right)\left(\bar{\nu}_e\gamma_\mu e\right) \tag{4}$$

where γ_μ are the Dirac γ matrices, $G_F = 1.1663787(6) \times 10^{-5}\,\mathrm{GeV}^{-2}$ is the Fermi coupling constant [1] and n, p, e, ν are the fermion fields of the neutron, proton, electron and neutrino respectively.
Weak interactions have a $V - A$ (vector-axial) structure to account for the parity-symmetry and charge-parity-symmetry violation, and this is achieved using the γ^5 Dirac matrix.

$$M \propto G_F \left(\bar{n}\gamma^\mu \left(1 - \gamma^5\right) p\right) \left(\bar{\nu}_e \gamma_\mu \left(1 - \gamma_5\right) e\right) \tag{5}$$

A generic weak field ψ can be decomposed into the left-handed component $\psi_L = \frac{1}{2}\left(1 - \gamma^5\right)\psi$ and into a right-handed component $\psi_R = \frac{1}{2}\left(1 + \gamma^5\right)\psi$.
The L and R subscripts refer to the left and right chirality eigenstates: the chirality is determined by whether the particle transforms in a right- or left-handed representation of the Poincaré group.
Substituting in Equation 5, it can be seen that only the left components of the fermion spinors enter into the weak interactions.
There are two types of weak interactions: *charged-current* interactions, mediated by particles that carry an electric charge ($W^\pm_\mu$ bosons) and *neutral-current* interactions, mediated by a neutral particle (the Z^0_μ boson).

1.3.3 *Electroweak Interactions*

In the 1960' Weinberg, Salam and Glashow proposed a unified model of the electroweak interactions [6], to do that it is necessary to define the minimal symmetry group able to describe both the weak and electromagnetic currents which is found to be $SU(2)_L \bigotimes U(1)_Y$, where the $SU(2)_L$ group acts on the left doublets of the weak isospin I_W. Quarks and leptons are classified in three generations and they are representations of $SU(2)_L$, as schematically shown in the following tables:

three left-handed doublets	*six right-handed singlets*
$Q_\alpha = (u_{L_\alpha}, d_{L_\alpha})$	$U_\alpha = u_{R_\alpha}$ $\quad$ $D_\alpha = d_{R_\alpha}$

Table 2.: Quarks as representations of $SU(2)_L$.
α is a flavour index: $u_\alpha = u, c, t$ and $d_\alpha = d, s, b$.

three left-handed doublets	*three right-handed singlets*
$L_i = (\nu_{L_i}, \ell_{L_i})$	$E_i = \ell_{R_i}$

Table 3.: Leptons as representation of $SU(2)_L$.
i is a flavour index: $i = e, \mu, \tau$.

In the lepton sector, there is no experimental evidence of right-handed neutrinos. Therefore, leptons are grouped in three doublets and three singlets.

A gauge-invariant Lagrangian can be written exploiting the minimal coupling and replacing in the kinetic term of the Lagrangian the ordinary derivative ∂_μ with the covariant derivative D_μ, defined as:

$$D_\mu = \partial_\mu + ig\frac{\vec{\tau}}{2}\vec{W}_\mu + ig^{'}\frac{Y}{2}B_\mu \tag{6}$$

where:

- $\vec{\tau}$, the Pauli matrices, and $\frac{Y}{2}$, the hypercharge, are the generators of the subgroup $SU(2)_L \bigotimes U(1)_Y$ and

$$Q = \tau^3 + \frac{Y}{2} \tag{7}$$

  is the electric charge;
- g and $g^{'}$ are two parameters which determine the couplings of a vector boson to a generic fermion. In terms of the electric charge the coupling constants g and $g^{'}$ are defined as:

$$Q = g\sin\theta_W = g^{'}\cos\theta_W \tag{8}$$

where θ_W is the weak mixing angle.
The resulting SM electroweak Lagrangian density is different for the quark (Q) and lepton sectors (LS):

$$\begin{aligned}\mathcal{L}_Q = &\sum_{\alpha,\beta=1}^{3} i\left(\bar{Q}_\alpha \not{D} Q_\beta\right)\delta_{\alpha,\beta} \\ &+ \lambda^U_{\alpha,\beta}\left(Q^\dagger_\beta H U_\alpha + U^\dagger_\alpha H^\dagger Q_\beta\right) + \lambda^D_{\alpha,\beta}\left(Q^\dagger_\beta H D_\alpha + D^\dagger_\alpha H^\dagger Q_\beta\right) \qquad (9)\\ \mathcal{L}_{LS} = &\sum_{\alpha,\beta=1}^{3} i\left(\bar{L}_\alpha \not{D} L_\beta\right)\delta_{\alpha,\beta} + \lambda^E_{\alpha,\beta}\left(L^\dagger_\alpha H E_\beta + E^\dagger_\beta H^\dagger L_\alpha\right)\end{aligned}$$

where f is a mathematical objects called Dirac *bispinor* and $\bar{f} = f^\dagger\gamma^0$ is its conjugate. In both equations, the first terms are the kinematic+gauge terms and they are diagonal, while the latter ones are the Yukawa terms. Since the lagrangian density is gauge-invariant, $\lambda^I_{\alpha,\beta}$ $(I = U, D, E)$ is an hermitian matrix that verifies the relation:

$$\lambda^I_{\alpha,\beta} = U^\dagger \lambda^I_{diag} U \qquad (10)$$

where λ^I_{diag} are real diagonal matrices with non negative eigenvalues.
Replacing (10) in the lagrangian density, we notice that only in the lepton sector a suitable redefinition of the ℓ_{R_i}'s is possible in order to simultaneously diagonalize the kinetic+gauge term and the Yukawa term. The result is:

$$\mathcal{L}_{LS} = \sum_{\alpha=1}^{3} i\left(\bar{L}_\alpha \not{D} L_\alpha\right) + \lambda^E_\alpha\left(L^\dagger_\alpha H E_\alpha + E^\dagger_\alpha H^\dagger L_\alpha\right) \qquad (11)$$

All terms are diagonal in flavour, so the individual family lepton numbers L_e, L_μ, L_τ are conserved in the Standard Model, neglecting neutrino masses.
In the quark sector it is not possible to redefine the matter fields in order to simultaneously diagonalise both the kinetic+gauge term and the Yukawa term in (9), because of the presence of the $V^{CKM}_{\alpha,\beta}$, the Cabibbo, Kobayashi, Maskawa matrix [11] [12]. Thus only the overall baryon number is conserved because in the quark sector the interaction eigenstates $d'_\alpha = V^{CKM}_{\alpha,\beta} d_\beta$ are a linear combination of flavour and mass eigenstates d_α. A detailed description of the CKM matrix is given in Section 1.4.

To introduce mass terms in Equations 9, a new $SU(2)$ doublet scalar field is required to activate the mechanism of spontaneous symmetry breaking.
According to spontaneous electroweak symmetry breaking of $SU(2)_L \times U(1)_Y$ into $U(1)_{em}$ [13] [14], there is a non-null vacuum expectation value for the Higgs $SU(2)_L$ doublet (H): $v \simeq 246\,\text{GeV}$. The Higgs coupling to fermions results in their mass terms and also there are the massive bosons $W^\pm_\mu$ and Z^0_μ

while the photon A_μ remains massless. Equation 12 shows how the physics fields A_μ (photon field), Z_μ (Z^0 field) and W_μ ($W^\pm$field) can be obtained from a combination of gauge fields.

$$\begin{aligned} A_\mu &= B_\mu \cos\theta_W + W^3_\mu \sin\theta_W \\ Z_\mu &= W^3_\mu \cos\theta_W - B_\mu \sin\theta_W \\ W^\pm_\mu &= \frac{W^1_\mu \mp i W^2 \mu}{\sqrt{2}} \end{aligned} \tag{12}$$

The measured values of the vector bosons masses are [1]:

$$\begin{aligned} m_W &= 80.385 \pm 0.015 \text{ GeV} \\ m_Z &= 91.1876 \pm 0.0021 \text{ GeV} \\ m_H &= 125.7 \pm 0.24 \text{ GeV} \end{aligned}$$

1.4 QUARK MIXING

Quarks have mass eigenstates and weak interaction eigenstates; weak interaction eigenstates are a linear combination of mass eigenstates. The CKM matrix is a unitary matrix which acts on the down flavour eigenstates and rotates them into the mass eigenstates as:

$$\begin{bmatrix} d' \\ s' \\ b' \end{bmatrix} = V_{\text{CKM}} \begin{bmatrix} d \\ s \\ b \end{bmatrix} = \begin{bmatrix} V_{ud} & V_{us} & V_{ub} \\ V_{cd} & V_{cs} & V_{cb} \\ V_{td} & V_{ts} & V_{tb} \end{bmatrix} \begin{bmatrix} d \\ s \\ b \end{bmatrix} \tag{13}$$

The CKM matrix describes the transition probability for a quark q_i to change its flavour into q_j and it is proportional to $\left|V_{ij}\right|^2$. The observed values of the V_{CKM} that measure the strength of the flavour-changing weak interaction are [1]:

$$V_{\text{CKM}} = \begin{bmatrix} 0.97427 \pm 0.00015 & 0.22534 \pm 0.00065 & 0.00351^{+0.00015}_{-0.00014} \\ 0.22520 \pm 0.00065 & 0.97344 \pm 0.00016 & 0.0412^{+0.0011}_{-0.0005} \\ 0.00867^{+0.00029}_{-0.00031} & 0.0404^{+0.0011}_{-0.0005} & 0.999146^{+0.000021}_{-0.000046} \end{bmatrix} \tag{14}$$

The elements of the CKM matrix are often parametrised using three rotation angles and a complex phase:

$$V_{\text{CKM}} = \begin{bmatrix} c_1 & -s_1c_3 & -s_1s_3 \\ s_1c_2 & c_1c_2c_3 - s_2s_3e^{i\delta} & c_1c_2s_3 + s_2c_3e^{i\delta} \\ s_1s_2 & c_1s_2c_3 + c_2s_3e^{i\delta} & c_1s_2s_3 - c_2c_3e^{i\delta} \end{bmatrix} \tag{15}$$

where $s_{ij} = \sin\theta_{ij}$, $c_{ij} = \cos\theta_{ij}$ and δ is a complex phase, necessary to account for $\mathcal{CP}$ violation in weak interactions with three quark generations, as detailed in the next Sections.
For completeness it is worth mentioning that the discovery of neutrino oscillations has proven that neutrinos have mass [7], [8]; therefore an analogous matrix can be defined in the lepton sector, *i.e.* the Pontecorvo-Maki-Nakagawa-Sakata (PMNS) matrix [9], [10].

1.5 DISCRETE SYMMETRIES: PARITY, CHARGE CONJUGATION AND CP

The parity inversion (denoted as $\mathcal{P}$), the charge conjugation (denoted as $\mathcal{C}$), and their combination $\mathcal{CP}$ are three important discrete symmetries in the Standard Model.
Parity is a quantum mechanical operator whose effect on a single particle wavefunction $\phi(\vec{r}, t)$ is described in Equation 16.

$$\hat{\mathcal{P}}\phi(\vec{r}, t) = \phi(-\vec{r}, t) \tag{16}$$

The parity operation basically consists in a reflection through a mirror, followed by a rotation of π around an axis defined by the mirror plane, as schematically shown in Figure 6.

Parity is a unitary operator: $\hat{\mathcal{P}}^2 = \mathbb{1}$, meaning that two consecutive applications of the parity operator result in the original state, as shown in Equation 17.

$$\hat{\mathcal{P}}^2\phi(\vec{r}, t) = \phi(\vec{r}, t) \tag{17}$$

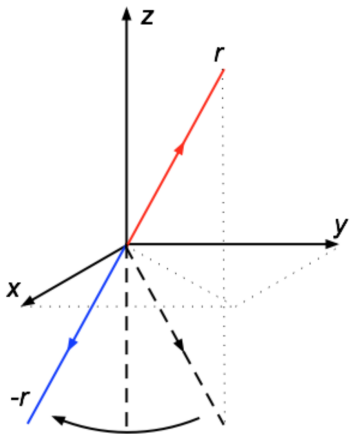

Figure 6.: Parity is equivalent to a reflection in an x, y mirror plus a rotation of 180° about the z axis.

This means that there are two possible eigenvalues P_a for this operator: there are objects which are even under parity, $P_a = +1$ (like scalars and axial vectors), the other are odd $P_a = -1$ under parity (like vectors and pseudoscalars). Focusing on Dirac particles, as the spin is not affected by a parity transformation, a left-handed particle becomes a right-handed particle under parity.
Parity is violated in weak interactions, *i.e.* $[\mathcal{P}, \mathcal{H}_W] \neq 1$, where H_W is the Hamiltonian of weak interactions.
The charge conjugation, $\mathcal{C}$, changes a quantum field ϕ into $\phi^\dagger$, where $\phi^\dagger$ has opposite $U(1)$ charges like baryon number, electric charge, lepton number and flavour quantum numbers. It changes a particle into its antiparticle, *i.e.* $e^- \to e^+$, $\gamma \to \gamma$ and it is an unitary operator: $\hat{\mathcal{C}}^2 = \mathbb{1}$. In particular, a left(right)-handed particle remains left(right)-handed after a charge conjugation transformation.
Also $\mathcal{C}$ is violated in weak interactions: $[\mathcal{C}, \mathcal{H}_W] \neq 1$.
Consider the combined action of the $\mathcal{C}$ and $\mathcal{P}$ transformations (known as $\mathcal{CP}$): it has the effect of transforming a particle into its own antiparticle while, at the same time, changing its chirality. Also $\mathcal{CP}$ is an unitary operator: $\hat{\mathcal{CP}}^2 = \mathbb{1}$.
The $\mathcal{CP}$ symmetry was supposed to be conserved in weak interactions until the observation of the $K_L^0 \to \pi^+\pi^-$ decays [15], which was the evidence that the $\mathcal{CP}$ symmetry is broken in the SM. Nowadays, $\mathcal{CP}$ violation has been observed in kaon and B meson decays (an example Feynman diagram of $\mathcal{CP}$ violation mixing in the neutral B meson system is given in Figure 7). The violation of $\mathcal{CP}$ translates into the presence of an irreducible phase in the CKM matrix, which hence cannot be transformed into a real matrix by a redefinition of the fields. Due to this additional phase, there are differences in the rates of processes involving particles and antiparticles.

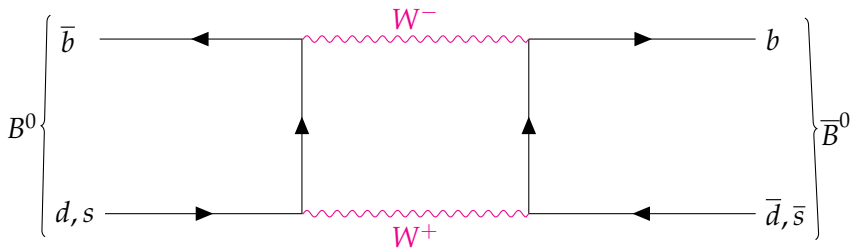

Figure 7.: An example of $\mathcal{CP}$ violation mixing in neutral B-meson system.

1.6 CP VIOLATION

$\mathcal{CP}$ violation can happen in three ways:

1. Direct $\mathcal{CP}$ violation: the probability of a particle A to decay in a particle X is different from the probability of its antiparticle $\bar{A}$ to decay in the antiparticle $\bar{X}$, $P(A \to X) \neq P(\bar{A} \to \bar{X})$, leading to a difference in the amplitudes $\Gamma(A \to X) \neq \Gamma(\bar{A} \to \bar{X})$;

2. Indirect, or $\mathcal{CP}$ violation in mixing: the probability of a particle A to oscillate into its own antiparticle $\bar{A}$ is different from the probability of $\bar{A}$ to oscillate into A, $P(A \to \bar{A} \to \bar{X}) \neq P(\bar{A} \to A \to X)$;

3. Interference of the two previous mechanisms.

Focussing on a neutral B meson system propagating in time, which is the most useful example for the purposes of this thesis, each particle will propagate as the mass eigenstate (either a heavy, B_H or light, B_L) which is a linear combination of flavour eigenstates, governed by a time-dependent Schroedinger equation 18:

$$\begin{aligned} |B_L\rangle &= p\,|B^0\rangle + q\,|\bar{B}^0\rangle \\ |B_H\rangle &= p\,|B^0\rangle - q\,|\bar{B}^0\rangle \end{aligned} \tag{18}$$

where p and q are complex coefficients and B_L and B_H have a mass difference Δm_B and a width difference $\Delta\Gamma \sim \frac{1}{\tau}$, where τ is the particle lifetime. The product $\Delta m_B \times \Delta\Gamma$ is a measure of the probability for a $\mathcal{CP}$ violating process to occur: for example the B^0 oscillation is more likely to happen with respect to the D^0 oscillation because in the first case the particle lifetime τ is longer than the oscillation period.
The neutral B meson wavefunction oscillates between the states B^0 and $\bar{B}^0$, as shown in the box diagram in Figure 7. The complex coefficients p and q have

phases which appear in the CKM matrix as $\mathcal{CP}$ violating terms. When evaluating a decay amplitude, only phase differences between multiple terms are relevant. The decay amplitude A_f of a particle ($\bar{A}_f$ of an anti-particle) can be written as 19:

$$\begin{aligned} A_f &= \sum_i A_i e^{(i\delta_i+\phi_i)} \\ \bar{A}_f &= e^{(2i\zeta_i+\zeta_f)} \sum_i A_i e^{(i\delta_i+\phi_i)} \end{aligned} \tag{19}$$

where A_i is the magnitude, $e^{(i\delta_i)}$ is the weak phase which violates $\mathcal{CP}$, $e^{(i\phi_i)}$ is the strong phase which does not violate $\mathcal{CP}$ and finally ζ_i and ζ_f are arbitrary phases, related to the flavour content of the initial and final states.

1.6.1 *Parameters of CP Violation in Decays*

The decay amplitudes defined in Equation 19 imply that $\mathcal{CP}$ occurs if $\left|A_f/\bar{A}_f\right| \neq 1$:

$$\left|\frac{A_f}{\bar{A}_f}\right| = \frac{\sum_i A_i e^{(i\delta_i+\phi_i)}}{e^{(2i\zeta_i+\zeta_f)} \sum_i A_i e^{(i\delta_i+\phi_i)}} \neq 1 \tag{20}$$

It is possible to define a $\mathcal{CP}$ asymmetry using the magnitude of the difference in amplitudes in Equation 21.

$$a_f = \frac{1-\left|A_f/\bar{A}_f\right|^2}{1+\left|A_f/\bar{A}_f\right|^2} = \frac{\left|A_f\right|^2-\left|\bar{A}_f\right|^2}{\left|A_f\right|^2+\left|\bar{A}_f\right|^2} \tag{21}$$

Equation 21 can be re-written in terms of the decay width of a process, using Fermi's Golden Rule: the width of a process is proportional to the square of its amplitude. Equation 22 shows $\mathcal{CPV}$ effects using asymmetries of differences in rates, such as the direct $\mathcal{CP}$ asymmetries measured in the analysis [16].

$$a_f = \frac{\Gamma\left(B^+ \to f\right) - \Gamma\left(B^- \to \bar{f}\right)}{\Gamma\left(B^+ \to f\right) + \Gamma\left(B^- \to \bar{f}\right)} \tag{22}$$

1.6.2 *Parameters of CP Violation in Mixing*

In a similar way, $\mathcal{CPV}$ effects can be investigated in mixing using meaningful parameters, such as in equation 23:

$$a_{sl} = \frac{1 - \left|\frac{p}{q}\right|^4}{1 + \left|\frac{p}{q}\right|^4} = \frac{|p|^4 - |q|^4}{|p|^4 + |q|^4} \tag{23}$$

which translates in the amplitude relation 24:

$$a_{sl} = \frac{\Gamma\left(\bar{B}^0(t) \to \ell^+ \nu X\right) - \Gamma\left(B^0(t) \to \ell^- \bar{\nu} X\right)}{\Gamma\left(\bar{B}^0(t) \to \ell^+ \nu X\right) + \Gamma\left(B^0(t) \to \ell^- \bar{\nu} X\right)} \tag{24}$$

a_{sl} is the quantity measured to evaluate $\mathcal{CP}$ asymmetries in [16].

1.6.3 *Parameters of CP Violation in Interference*

To measure $\mathcal{CPV}$ in the interference between mixing and decays the meaningful quantity is λ_f, defined as in equation 25:

$$\lambda_f = \frac{q}{p}\frac{\bar{A}_f}{A_f} \tag{25}$$

Asymmetries are measured in a time-dependent way, however the analysis presented in this thesis is a time-integrated analysis and it is not sensitive to this parameter.

1.7 CKM MATRIX AND $\mathcal{CPV}$

The CKM matrix can be parametrised using unitarity triangles, as the one shown in Figure 8, where the angles are related to $\left|V_{ij}\right|$ amplitudes and hence the $\mathcal{CPV}$ parameters. For example, the angle $\phi_3 = arg\left(\frac{-V_{ud}V_{ub}^*}{V_{cd}V_{bc}}\right)$ is sensitive to semi-leptonic decays of B-mesons, involving either the $b \to u\ell\nu$ process (related to $|V_{ub}|$), or $b \to c\ell\nu$ process (related to $|V_{cb}|$).
Moreover, the neutral B-meson mixing is sensitive to $V_{tb}V_{td}^*$ and $V_{tb}V_{ts}^*$ as shown in

Figure 7. These amplitudes are used to determine the yellow and orange rings in Figure 8 [1] which further constrain the CKM angles.

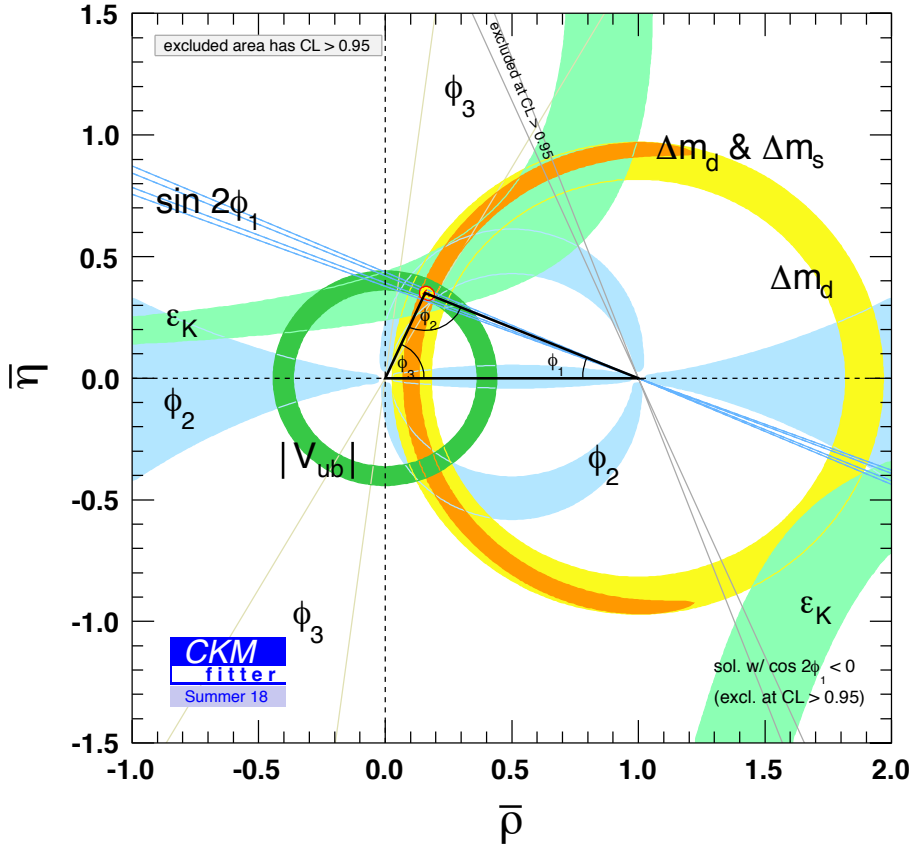

Figure 8.: Constraints on the unitarity triangle angles, following a global CKM fit in the $(\bar{\rho}, \bar{\eta})$ plane, using all modern experimental inputs. $\bar{\rho}$ and $\bar{\eta}$ are defined by the relation: $\sqrt{\bar{\rho}^2 + \bar{\eta}^2} = |V_{ud}/V_{us}V_{cb}|$ [17].

1.8 BARYOGENESIS AND ITS RELATION TO $\mathcal{CPV}$

The matter anti-matter asymmetry in the Universe (*i.e.* the excess of baryonic matter) is evident in everyday life: we are all made of cells, made up by atoms, containing protons and neutrons. Going from the common experience to more rigorous scientific observations: all the measurements performed by radioastronomy and cosmic ray telescopes indicate that all known galaxies in the observed universe,

are made of matter. Several astroparticle experiments (for instance, the PAMELA experiment on the Resurs-DK1 satellite [18] or the AMS-02 experiment on the International Space Station [19]) are currently looking for excess of anti-matter in the flux of cosmic rays but no evidence has been claimed so far.
Assuming that in the early universe, shortly after the big bang, there were equal numbers of baryons (N_B) and anti-baryons ($N_{\bar{B}}$) in thermal equilibrium, the annihilation processes in formula 26 would have happened at the same rate in both directions.

$$p + \bar{p} \rightleftharpoons \gamma + \gamma \tag{26}$$

Therefore, the baryon asymmetry can be defined by the rate η in Equation 27.

$$\eta = \frac{N_B - N_{\bar{B}}}{N_B + N_{\bar{B}}} \sim \frac{N_B}{N_\gamma} \tag{27}$$

where $\eta = 6.1^{+0.3}_{-0.2} \times 10^{-10}$ was measured by the WMAP experiment [20], proving the the baryon number B is strictly positive for the observed Universe.
Thus, even if the baryon number was zero at the beginning, at some point after the Big Bang, some dynamical process happened resulting in $\frac{dB}{dt} > 0$ (baryogenesis).
$\mathcal{CPV}$ is one of the conditions necessary to give rise to baryognesis, as outlined in the following.
In order to make the baryogenesis occur, Sakharov formulated three necessary conditions to be satisfied [21]:

1. Baryon number violating interactions (at least one must exist): in these processes a unequal number of baryons or anti-baryons can be produced (or destroyed);

2. $\mathcal{C}$ and $\mathcal{CP}$ symmetries must be violated: assuming that the first condition is satisfied, but $\mathcal{C}$ is conserved then the $\mathcal{C}$ conjugate of the above process would balance again the total number of baryons and anti-baryons. Even if there is $\mathcal{C}$ violation but not $\mathcal{CPV}$, a hypothetical B-violating process $X \to q_L q'_L$ could be re-balanced as shown in Equation 28

$$\Gamma\left(X \to q_L q'_L\right) + \Gamma\left(X \to q_R q'_R\right) = \Gamma\left(\bar{X} \to \bar{q}_L \bar{q}'_L\right) + \Gamma\left(\bar{X} \to \bar{q}_R \bar{q}'_R\right) \tag{28}$$

   and hence these processes must happen at a different rate and $\mathcal{CP}$ must be violated as well.

3. Departure from thermal equilibrium: even if the first two conditions happened, in thermal equilibrium every process would occur at an equal rate to its inverse process and the baryon numbers would be balanced again.

At present, all the $\mathcal{CPV}$ observations are not sufficient [22, 23, 24, 25, 26, 27] to explain the matter anti-matter asymmetry in the Universe and, given the abundance of top quark pair production at LHC, top physics could be a fertile field to investigate $\mathcal{CPV}$ in the B sector.

1.9 TOP QUARK

Since the bottom quark was observed in 1977, the existence of another quark with charge $2/3$ was expected to complete the isospin doublet. It took 23 years to discover the top quark at the FermiLab proton-antiproton collider, called Tevatron, at a centre of mass energy $\sqrt{s}$ of 1.8 TeV. The top quark, discovered by the CDF [28] and D0 experiments [29], has a short lifetime $\tau_t \sim 0.5 \times 10^{-24}$ s which is shorter than the hadronization time scale $\sim 10^{-23}$ s [1] and even shorter than the spin decorrelation time $\sim 10^{-21}$ s [1], providing the unique opportunity to study the properties of a bare quark.
The top quark is the heaviest elementary particle known in the framework of the SM, its large mass $m_t = 173.34 \pm 0.27(\mathrm{stat.}) \pm 0.71(\mathrm{syst.})$ GeV (m_t is the world average value [1]) is one of the fundamental parameters of the SM. It is significantly heavier than the bottom quark mass, which is the other third generation particle in the quark sector. Figure 9 shows a summary of the ATLAS and CMS direct m_t measurements performed at LHC, compared with LHC and Tevatron+LHC m_t combinations.

The CERN Large Hadron Collider (LHC), operating at a centre of mass energy of 13 TeV, can be considered a *top factory* because of its high rate production: about 500 top quark-pairs per minute are produced in LHC proton-proton collisions. Top quark physics is a fertile field to investigate New Physics (NP) thanks to its unique properties and, due to its large mass, it has a large coupling with the Higgs boson [31] and it may be the most likely particle to couple to NP at the TeV scale.

1.10 TOP QUARK PRODUCTION

The top quark pairs are mainly produced via strong interactions in gluon-gluon fusion at the LHC. Figure 10 shows the diagrams for leading order (LO) production of top quark pairs: gluon-gluon fusion and $q\bar{q}$ annihilation. The first process

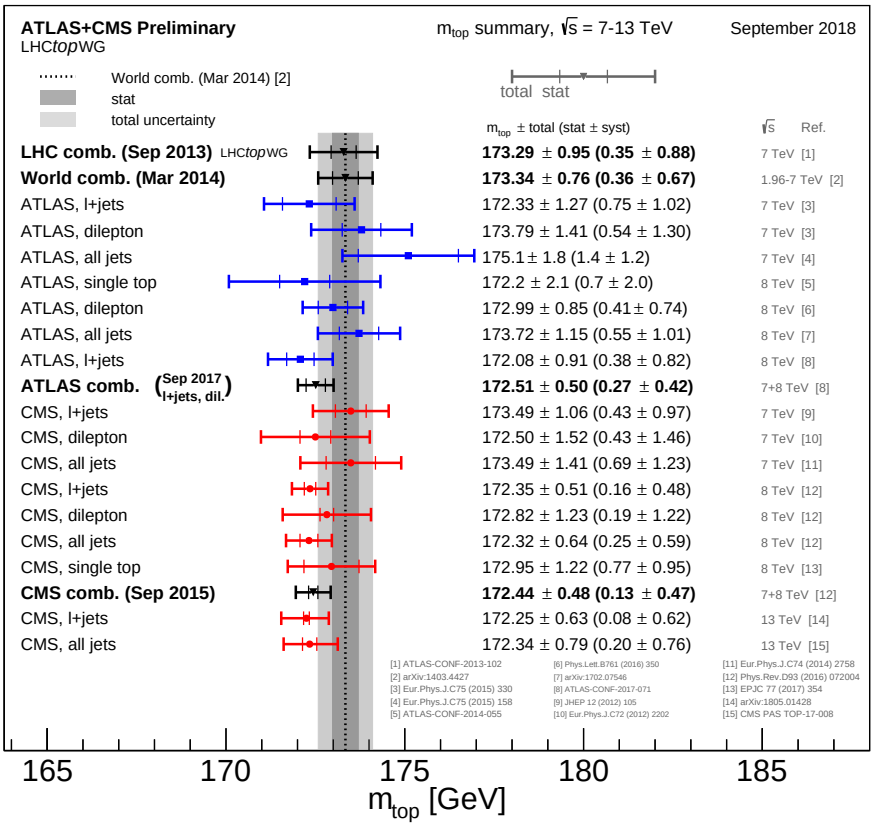

Figure 9.: m_t measurements performed with the ATLAS and CMS experiments at LHC, compared with LHC and Tevatron+LHC results. Statistics and systematic uncertainties are shown. [30]

occurs in $\sim$ 87% of the cases at the LHC because of the high $\sqrt{s}$ value and because both the colliding beams are made of protons, whose structure is shown in Figure 3. Since gluons dominate the parton distribution function of the proton up to high x, the gluon gluon fusion is the dominating process. The theoretical cross-section, calculated up to the next-to-next-to-leading-order (NNLO), for top-quark pair production at the LHC at $\sqrt{s} = 13\,\text{TeV}$ is $\sigma_{t\bar{t}} = 832^{+40}_{-46}\,\text{pb}$ [30], as shown in Figure 11.

Moreover, it is also possible to produce single top quarks through several processes, shown in the diagrams in Figures 12, 13, 14. Single top quark can be produced in electroweak processes, whereas the electroweak cross section production is less likely than the strong one. Indeed, single top cross sections in pp collisions at $\sqrt{s} = 13\,\text{TeV}$ are listed in Table 4.

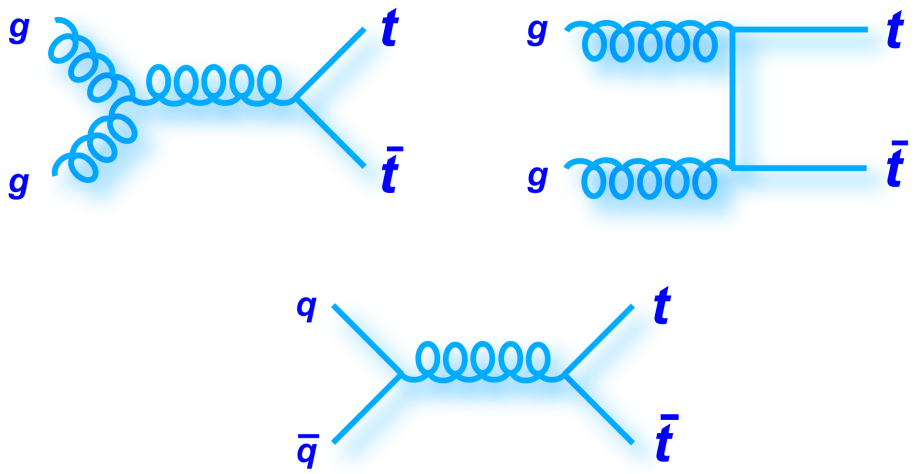

Figure 10.: LO Top quark pairs production Feynman diagrams. Top: gluon-gluon fusion processes. Bottom: $q\bar{q}$ annihilation process [32].

Process	Total cross section pb	Top cross section pb (%)	AntiTop cross section pb (%)
t channel	$216.99^{+9.04}_{-7.71}$	136.02 (62.68%)	80.95 (37.31%)
s channel	$10.32^{+0.40}_{-0.36}$	6.35 (61.53%)	3.97 (38.47%)
Wt channel	71.7 ± 3.85	35.85 (50.00%)	35.85 (50.00%)

Table 4.: Single top production cross sections, in pp collisions at $\sqrt{s} = 13\,\text{TeV}$ [30].

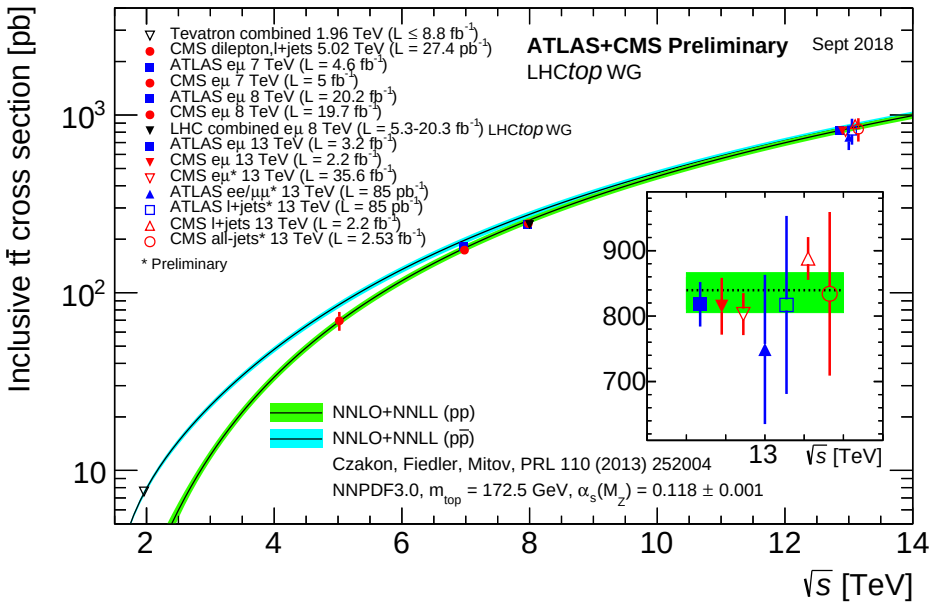

Figure 11.: Measurements of the top-pair production cross-section at LHC and Tevatron, as a function of the centre-of-mass energy compared to the NNLO QCD calculation [30].These measurements assume $m_t = 172.5\,\text{GeV}$.

1.11 TOP QUARK DECAY

Detectors can only measure top quark's decay products because the top quark decays before hadronizing and it can be studied as a bare quark.
The top quark predominantly decays into a W boson and a bottom quark ($t \to Wb$) because the CKM element $|Vtb|$ is very close to unity. For this reason the top quark decay amplitude $\Gamma(t \to Wb)$ can be evaluated using the formula in Equation 29.

$$\Gamma(t \to Wb) = \frac{G_F m_t^3}{8\pi\sqrt{2}} |V_{tb}|^2 \sim 1.74\,\text{GeV} \tag{29}$$

Figure 15 shows the Feynman diagram for the $t \to Wb$ process.

The final states for the leading pair-production process can be divided into three classes. The decay signatures of the top quark or the anti-top quark are classified according to the final states of the W boson and they are referred to as: hadronic, semi-leptonic and di-leptonic decay modes (see Figures 16). The relative decay probabilities are listed below [1] and summarised in Figure 17.

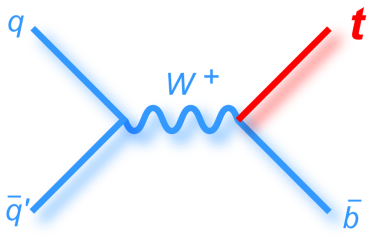

Figure 12.: LO single top production Feynman diagram, *s*-channel [32].

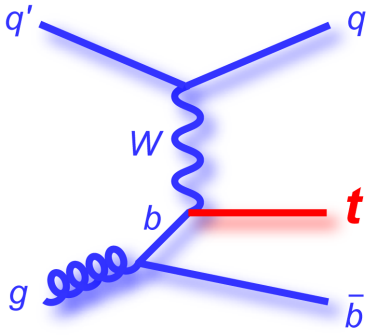

Figure 13.: LO single top production Feynman diagram, *t*-channel [32].

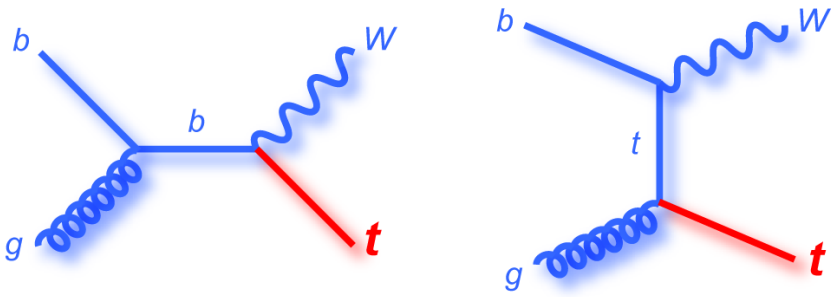

Figure 14.: LO single top production Feynman diagrams, *Wt*-channel [32].

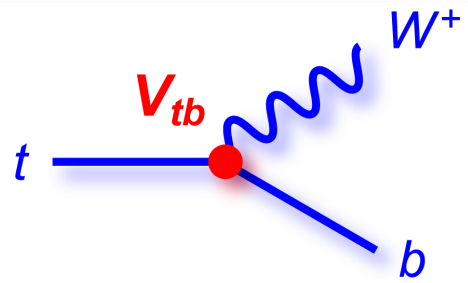

Figure 15.: $t \to Wb$ Feynman diagram, showing the coupling proportional to $|V_{tb}|$ [32].

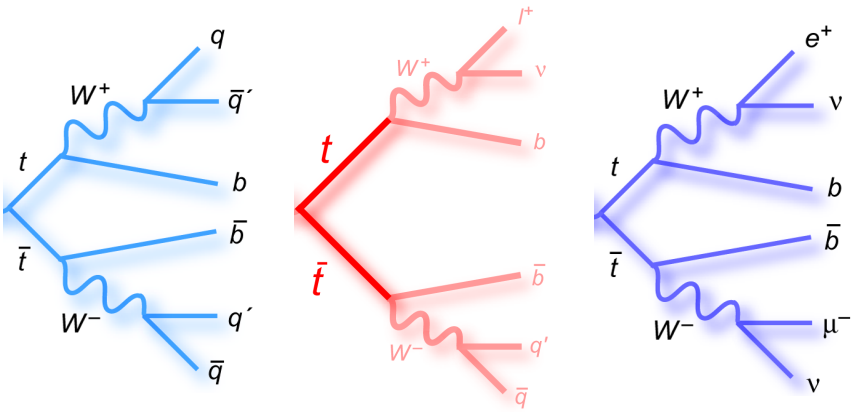

Figure 16.: From left to right: all hadronic, semi-leptonic and di-leptonic top pair decay Feynman diagram [32].

- All hadronic: $t\bar{t} \to W^+bW^-\bar{b} \to q\bar{q}'bq\bar{q}'\bar{b}$, 45.7%;
- Semi-leptonic: $t\bar{t} \to W^+bW^-\bar{b} \to q\bar{q}'b\ell^-\bar{\nu}\bar{b} + \ell^+\nu bq\bar{q}'\bar{b}$, 43.8%;
- Di-leptonic: $t\bar{t} \to W^+bW^-\bar{b} \to \ell^+\nu b\ell^-\bar{\nu}$, 10.5%.

In all the listed cases, the quarks in the final state evolve into jets of hadrons and $\ell = e, \mu, \tau$ leptons, assuming universality for lepton interactions.

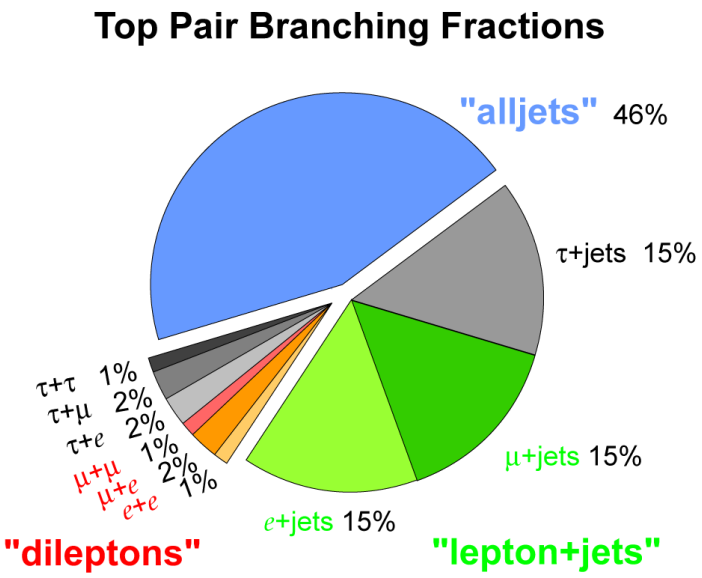

Figure 17.: Top quark pairs branching ratios [32].

2

ANALYSIS MOTIVATIONS AND OUTLINE

Nowadays, all the existing $\mathcal{CPV}$ measurements in the heavy-flavour sector are not sufficient to explain the observed matter-antimatter asymmetry in the Universe (as outlined in Section 1.8).
All these measurements are in good agreement with SM predictions but the inclusive like-sign dimuon charge asymmetry measurement, performed by the D0 experiment [36], observed a significant excess ($3.8\,\sigma$) from the SM. This result has not been confirmed by LHCb [33, 34] and BaBar [35] analysis, as discussed in Section 2.3.
The underlying idea of the measurement presented in this thesis is to exploit the large number of top-antitop pair events produced in pp collisions at the Large Hadron Collider (LHC) as a unique source of b-quarks that can be used to probe the CP violation in heavy-flavour mixing and decay.

2.1 ANALYSIS OVERVIEW AND $\mathcal{CPV}$ OBSERVABLES

Evidence for $\mathcal{CP}$ violation in weak interactions is well established in Particle Physics. Nevertheless, the most recent combination of all $\mathcal{CP}$ violation measurements is found to be insufficient to explain the size of the matter anti-matter asymmetry present in the Universe. The large number of top-antitop pair events produced in pp collisions at the Large Hadron Collider provides a unique source of b-quarks that can be used to probe the CP violation in heavy-flavour mixing and decay.
The measurement presented in this thesis focuses on semi-leptonic top-antitop events where one of the W-bosons decays hadronically and the other one decays leptonically, as shown in Figure 18. The charge of the lepton (electron or muon) from the W-boson tags the charge of the b-quark at production. In events where a muon is associated to the semi-leptonic decay of the b-quark (either directly or after a $b \to c$ hadronic transition), two charge asymmetries (CA) and several $\mathcal{CP}$ asymmetries, based on the charges of the lepton from the W-boson and this muon, can be measured. In $t\bar{t}$ semi-leptonic decays there are three classes of decay chains which produce two leptons of the same sign, given by the following left-hand side

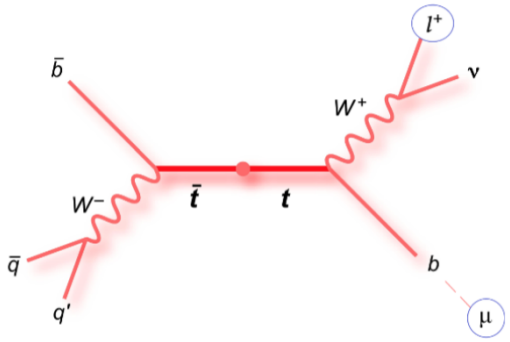

Figure 18.: Illustration of semi-leptonic same-top $t\bar{t}$ event.

Equations 30, and three classes of decay chains which produce two leptons of opposite sign in the final state, given by the right-hand side Equations 30 [39] [1]:

$$N_b : t \to \ell^+ \nu \left(b \to \bar{b}\right) \to \ell^+ \ell^+ X \qquad \widetilde{N}_b : t \to \ell^+ \nu b \to \ell^+ \ell^- X \tag{30a}$$

$$N_c : t \to \ell^+ \nu \left(b \to c\right) \to \ell^+ \ell^+ X \qquad \widetilde{N}_c : t \to \ell^+ \nu \left(b \to \bar{b} \to \bar{c}\right) \to \ell^+ \ell^- X \tag{30b}$$

$$N_{c\bar{c}} : t \to \ell^+ \nu \left(b \to \bar{b} \to c\bar{c}\right) \to \ell^+ \ell^+ X \qquad \widetilde{N}_{c\bar{c}} : t \to \ell^+ \nu \left(b \to c\bar{c}\right) \to \ell^+ \ell^- X \tag{30c}$$

These processes are sensitive to $\mathcal{CP}$ violation in $B_{d,s} - \bar{B}_{d,s}$ mixing, semi-leptonic b and c decays and $b \to c$ transitions.
Experimentally, it is possible to form charge asymmetries from the charge of the W-boson lepton and the muon from the semi-leptonic decay of the b quark, which are sensitive to $\mathcal{CP}$ violation. The measurement focuses on determining relative differences in the probabilities of an initial b or $\bar{b}$ to decay to either a positive or negative soft muon. These probabilities may be measured by considering the number of soft muons observed, where N^{ab} represents the number of soft muons observed in conjunction with a W-boson lepton of charge a and a soft muon of charge b. A total of four different probabilities are considered, as in Equations 31.

1 Note that $c\bar{c}$ here does not refer to resonant states.

$$P\left(b \to \ell^{+}\right) = \frac{N\left(b \to \ell^{+}\right)}{N\left(b \to \ell^{-}\right) + N\left(b \to \ell^{+}\right)} = \frac{N^{++}}{N^{+-} + N^{++}} = \frac{N^{++}}{N^{+}} \tag{31a}$$

$$P\left(\bar{b} \to \ell^{-}\right) = \frac{N\left(\bar{b} \to \ell^{-}\right)}{N\left(\bar{b} \to \ell^{-}\right) + N\left(\bar{b} \to \ell^{+}\right)} = \frac{N^{--}}{N^{--} + N^{-+}} = \frac{N^{--}}{N^{-}} \tag{31b}$$

$$P\left(b \to \ell^{-}\right) = \frac{N\left(b \to \ell^{-}\right)}{N\left(b \to \ell^{-}\right) + N\left(b \to \ell+\right)} = \frac{N^{+-}}{N^{+-} + N^{++}} = \frac{N^{+-}}{N^{+}} \tag{31c}$$

$$P\left(\bar{b} \to \ell^{+}\right) = \frac{N\left(\bar{b} \to \ell^{+}\right)}{N\left(\bar{b} \to \ell^{-}\right) + N\left(\bar{b} \to \ell^{+}\right)} = \frac{N^{-+}}{N^{--} + N^{-+}} = \frac{N^{-+}}{N^{-}} \tag{31d}$$

A same sign (SS), and opposite sign (OS) asymmetry are formed from the probabilities in Equations 32:

$$A^{ss} = \frac{P\left(b \to \ell^{+}\right) - P\left(\bar{b} \to \ell^{-}\right)}{P\left(b \to \ell^{+}\right) + P\left(\bar{b} \to \ell^{-}\right)} \qquad A^{os} = \frac{P\left(b \to \ell^{-}\right) - P\left(\bar{b} \to \ell^{+}\right)}{P\left(b \to \ell^{-}\right) + P\left(\bar{b} \to \ell^{+}\right)} \tag{32a}$$

$$A^{ss} = \frac{\left(\frac{N^{++}}{N^{+}} - \frac{N^{--}}{N^{-}}\right)}{\left(\frac{N^{++}}{N^{+}} + \frac{N^{--}}{N^{-}}\right)} \qquad A^{os} = \frac{\left(\frac{N^{+-}}{N^{+}} - \frac{N^{-+}}{N^{-}}\right)}{\left(\frac{N^{+-}}{N^{+}} + \frac{N^{-+}}{N^{-}}\right)} \tag{32b}$$

The CAs formulation in Equation 32 is necessary to normalise the measurement and not be affected by detector-related and other effects which could introduce spurious asymmetries, not related to the measurement. The most relevant among these absolute asymmetries are listed below:

- $t\bar{t}$ pair production charge asymmetry: the top and the anti-top quarks have different rapidity distributions because, in next-to-leading order (NLO) calculations for pp collisions at the LHC experiment, there are interferences between the tree- and 1loop-diagrams for $q\bar{q} \to t\bar{t}$ production [38]. Even if the $t\bar{t}$ production at LHC is dominated by gluon-gluon fusion, this effect has been measured to be $A_C = (0.9 \pm 0.5)$ %, at a centre of mass energy of 8 TeV, in ATLAS [38]. This effect has a (small) impact on the measurement presented in this thesis because the analysis introduces selection requirements on the pseudorapidity, η, and therefore the sampled data contain more anti-top quarks than top quarks, meaning that there will be more initial negatively charged W-boson leptons than positively charged.

- b-jet reconstruction: the event selection might be affected by any charge-dependency in the reconstruction of b-jets in ATLAS.

Asymmetries related to lepton reconstruction should, in principle be taken into account since they would lead to a different initial number of positive and negative W-boson leptons, but in ATLAS no such dependence has been observed.
The $\mathcal{CP}$ asymmetries are related to fundamental $\mathcal{CP}$ violation parameters [39] via Equations 33:

$$A^{ss} = r_b A^{b\ell}_{mix} + r_c \left(A^{bc}_{dir} - A^{c\ell}_{dir} \right) + r_{c\bar{c}} \left(A^{bc}_{mix} - A^{c\ell}_{dir} \right) \tag{33a}$$

$$A^{os} = \widetilde{r}_b A^{b\ell}_{dir} + \widetilde{r}_c \left(A^{bc}_{mix} + A^{c\ell}_{dir} \right) + \widetilde{r}_{c\bar{c}} A^{c\ell}_{dir} \tag{33b}$$

where, in addition, r_q is defined as $r_q \equiv \frac{N_q^{++}+N_q^{--}}{N^{++}+N^{--}}$, with $q = b, c, c\bar{c}$ and $N_q^{\pm\pm}$ are the corresponding numbers of events coming from same-sign equations and $\widetilde{r}_q$ are the corresponding fractions of events for the decay chains defined in different-sign equations, respectively (see Equations 34).

$$r_b = \frac{N_b}{N_b + N_c + N_{c\bar{c}}}, \qquad \widetilde{r}_b = \frac{\widetilde{N}_b}{\widetilde{N}_b + \widetilde{N}_c + \widetilde{N}_{c\bar{c}}}, \tag{34a}$$

$$r_c = \frac{N_c}{N_b + N_c + N_{c\bar{c}}}, \qquad \widetilde{r}_c = \frac{\widetilde{N}_c}{\widetilde{N}_b + \widetilde{N}_c + \widetilde{N}_{c\bar{c}}}, \tag{34b}$$

$$r_{c\bar{c}} = \frac{N_{c\bar{c}}}{N_b + N_c + N_{c\bar{c}}}, \qquad \widetilde{r}_{c\bar{c}} = \frac{\widetilde{N}_{c\bar{c}}}{\widetilde{N}_b + \widetilde{N}_c + \widetilde{N}_{c\bar{c}}}. \tag{34c}$$

Moreover, the $\mathcal{CP}$ asymmetries related to $B_q - \overline{B}_q$ mixing and direct $\mathcal{CP}$ violating b- and c-decays are defined in Equations 35.

$$A_{\text{mix}}^{b\ell} = \frac{\Gamma\left(b \to \overline{b} \to \ell^+ X\right) - \Gamma\left(\overline{b} \to b \to \ell^- X\right)}{\Gamma\left(b \to \overline{b} \to \ell^+ X\right) + \Gamma\left(\overline{b} \to b \to \ell^- X\right)}, \tag{35a}$$

$$A_{\text{mix}}^{bc} = \frac{\Gamma\left(b \to \overline{b} \to \overline{c} X\right) - \Gamma\left(\overline{b} \to b \to \overline{c} X\right)}{\Gamma\left(b \to \overline{b} \to \overline{c} X\right) + \Gamma\left(\overline{b} \to b \to \overline{c} X\right)}, \tag{35b}$$

$$A_{\text{dir}}^{b\ell} = \frac{\Gamma\left(b \to \ell^- X\right) - \Gamma\left(\overline{b} \to \ell^+ X\right)}{\Gamma\left(b \to \ell^- X\right) + \Gamma\left(\overline{b} \to \ell^+ X\right)}, \tag{35c}$$

$$A_{\text{dir}}^{c\ell} = \frac{\Gamma\left(\overline{c} \to \ell^- X_L\right) - \Gamma\left(c \to \ell^+ X_L\right)}{\Gamma\left(\overline{c} \to \ell^- X_L\right) + \Gamma\left(c \to \ell^+ X_L\right)}, \tag{35d}$$

$$A_{\text{dir}}^{bc} = \frac{\Gamma\left(b \to c X_L\right) - \Gamma\left(\overline{b} \to \overline{c} X_L\right)}{\Gamma\left(b \to c X_L\right) + \Gamma\left(\overline{b} \to \overline{c} X_L\right)} \tag{35e}$$

where X (X_L) denotes an inclusive hadronic final state without any lepton, and with both light and charm quarks (with light quarks only).
The number of events in each channel is given by Equation 36 [39]:

$$N_q^{\pm\pm}\left(N_q^{\pm\mp}\right) = \sigma_{t\bar{t}}\,\mathcal{L}\,\text{BR}\left(t\bar{t} \to b\bar{b}\,\ell\,\nu\,\text{had}\right)\,\epsilon_{\text{sel}}\,\epsilon_b^2\,\epsilon_{\text{A}}\,\mathcal{B}_q \tag{36}$$

where q refers to the various same- and different- sign top processes, $\sigma_{t\bar{t}}$ is the top-pair production cross section, $\mathcal{L}$ is the integrated luminosity , BR is the branching ratio and $\text{BR}\left(t\bar{t} \to b\bar{b}\,\ell\,\nu\,\text{had}\right) \sim 0.30$, ϵ_{sel} is the efficiency of selecting the lepton and the four jets, ϵ_b is the b-tagging efficiency (squared because we tag two b-jets) and ϵ_{A} is the b-charge association efficiency. Finally $\mathcal{B}_q$ is a factor which accounts for the relative probabilities of the top inclusive decay chains listed above for same sign and different sign leptons in the final states.
All the charge and $\mathcal{CP}$ asymmetries outlined in the previous sections are supposed to be zero in the framework of the SM, any significative deviation could be a hint of new physics.
The analysis presented in this thesis is based on the theoretical work published in the paper [39] and outlined above, this is a novel technique employed to test $\mathcal{CPV}$ in top quarks decays but other tests of $\mathcal{CPV}$ have been performed by other analysis teams and other experiments at collider experiments.
Sections 2.2 and 2.3 provide a brief review of some $\mathcal{CPV}$ measurements at collider experiments.
At present, only the D0 like sign dimuon asymmetry (see Section 2.3) has a 3.8σ

with respect to the SM expectations. The sensitivity of the charge and $\mathcal{CP}$ asymmetry measurement in B-hadron decays from top pair events performed in Run-1 was not sufficient to exclude the D0 measurement and one of the main goals for the Run-2 measurement is to improve the sensitivity. The results achieved by the CA and CPAs measurement in Run-1 are summarised in Section 6.5.

2.2 $\mathcal{CPV}$ MEASUREMENTS AT COLLIDER EXPERIMENTS

Several interesting $\mathcal{CPV}$ analysis were performed at collider experiments using B-hadrons semileptonic decays, especially at the LHC.
The CMS collaboration performed a measurement of the $\mathcal{CP}$ violating weak phase ϕ_s and the decay width differences using the decay channel $B_s^0 \to J/\psi\,\phi(1020) \to \mu^+\mu^- K^+K^-$ in pp collisions at $\sqrt{s} = 8\,\text{TeV}$ [40] with an integrated luminosity of $19.7\,\text{fb}^{-1}$. The angle ϕ_s is related to the elements of the CKM quark mixing matrix by the Equation 37:

$$\phi_s \simeq 2\phi_1 \tag{37}$$

where $\phi_1 = arg\left(\frac{-V_{cd}V_{cb}^*}{V_{td}V_{tc}}\right)$ was defined in Section 1.7. The measured value of ϕ_s is in agreement with the SM predictions.
Also the ATLAS experiment performed a measurement of the B_s^0 decay parameters in the $B_s^0 \to J/\psi\,\phi(1020)$ channel using an integrated luminosity of $14.3\,\text{fb}^{-1}$ collected by the ATLAS detector at $\sqrt{s} = 8\,\text{TeV}$ in pp collisions at the LHC, statistically combined with data from $4.9\,\text{fb}^{-1}$ collected at $\sqrt{s} = 7\,\text{TeV}$ [41]. Among the measured parameters there is also the $\mathcal{CP}$-violating phase ϕ_s, defined in Equation 37. The measured value of ϕ_s is in agreement with the Standard Model predictions.
Finally, the LHCb experiment measured $\mathcal{CP}$ asymmetries using B-hadrons semileptonic decays. In particular, the LHCb collaboration performed the measurement of the semileptonic $\mathcal{CP}$ asymmetry in $B^0 - \bar{B}^0$ mixing [33] and in $B_s^0 - \bar{B}_s^0$ [34] mixing, using data collected in pp collisions at a centre of mass energy of 7 TeV and 8 TeV corresponding to an integrated luminosity of $3.0\,\text{fb}^{-1}$. The flavour-specific (semileptonic) asymmetry is defined in terms of partial decay rates Γ as in Equation 38 and 39, where f is the final state of the B-hadron semileptonic decay.

$$a_{sl}^d = \frac{\Gamma\left(\bar{B}^0 \to f\right) - \Gamma\left(B^0 \to \bar{f}\right)}{\Gamma\left(\bar{B}^0 \to f\right) + \Gamma\left(B^0 \to \bar{f}\right)} \tag{38}$$

$$a_{sl}^{s} = \frac{\Gamma\left(\bar{B}_s^0 \to f\right) - \Gamma\left(B_s^0 \to \bar{f}\right)}{\Gamma\left(\bar{B}_s^0 \to f\right) + \Gamma\left(B_s^0 \to \bar{f}\right)} \tag{39}$$

The resulting measured values are $a_{sl}^{d} = (-0.02 \pm 0.19 \pm 0.30)\%$ and $a_{sl}^{s} = (0.39 \pm 0.26 \pm 0.20)\%$, both consistent with the SM predictions.

2.3 D0 LIKE SIGN DIMUON ASYMMETRY

The most updated measurement of the like sign dimuon asymmetry performed by the D0 collaboration exploited a data sample of $10.4\,\text{fb}^{-1}$ collected in Tevatron $p\bar{p}$ collisions [36]. In $p\bar{p}$ collisions, pairs of b and $\bar{b}$ quarks are produced symmetrically. b quarks hadronize into B and $\bar{B}$ particles, which can decay into final state muons through the direct decay chains: $b \to \mu^- X$ and $\bar{b} \to \mu^+ X$. The charge of the final state muon tags the flavour of b quarks at production, therefore in $b\bar{b}$ events there will be production of opposite-sign dimuon $\mu^+\mu^-$ pairs, without taking into account oscillations. Considering oscillations, on the other hand, means that the parent b quark could hadronize into a B^0 which could then oscillate into a $\bar{B}^0$ which then can lead to two like-sign muons in the final state, through the processes : $b \to \bar{b} \to \mu^+ X$ and $\bar{b} \to \mu^+ X$.
There is CP-violation if the rate $\Gamma\left(B_{(s)}^0 \to \bar{B}_{(s)}^0\right)$ is not equal to the rate $\Gamma\left(\bar{B}_{(s)}^0 \to B_{(s)}^0\right)$, leading to a sizeable charge asymmetry for the like-sign dimuons: $\Gamma\left(\mu^+\mu^+\right)/\Gamma\left(\mu^-\mu^-\right)$. These dimuon asymmetries are related to fundamental $\mathcal{CPV}$ parameters (see 1.6.2 and 1.6.1) using the Equations 40 and 41.

$$a_{sl}^{q} = \frac{\Gamma\left(\bar{B}_q^0 \to B_q^0 \to f\right) - \Gamma\left(B_q^0 \to \bar{B}_q^0 \to f\right)}{\Gamma\left(\bar{B}_q^0 \to B_q^0 \to f\right) + \Gamma\left(B_q^0 \to \bar{B}_q^0 \to f\right)} \tag{40}$$

$$a_{dir}^{q} = \frac{\Gamma\left(b \to \mu^- X\right) - \Gamma\left(\bar{b} \to \mu^+ X\right)}{\Gamma\left(b \to \mu^- X\right) + \Gamma\left(\bar{b} \to \mu^+ X\right)} \tag{41}$$

Figure 19 shows the D0 a_{sl}^{q} measurements, which are 3.8σ away from the SM expectations, compared to LHCb, Babar and Belle results. The neutral B-meson mixing is given by $a_{sl}^{b} = f_s a_{sl}^{s} + f_d a_{sl}^{d}$, where f_s and f_d are the fragmentation functions for B_s^0 and B_d^0 production respectively. a_{sl}^{b} is related to the parameter $A_{mix}^{b\ell}$ defined in Equation 35. Figure 20 shows the interpretation of the a_{dir}^{q} measurement, detailing the magnitude of direct $\mathcal{CP}$ violation in b and c decays required, assuming SM-like

neutral B-mixing. The single and double muon asymmetries are interpreted as the result of $\mathcal{CP}$ violation in the direct decays of B and D meson and thus they are related to the $A_{dir}^{b\ell}$ and $A_{dir}^{c\ell}$ parameters given in Equation 35.

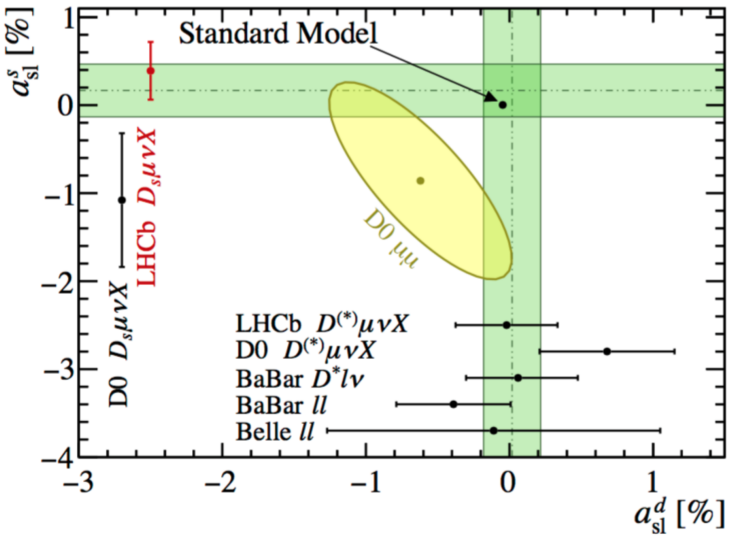

Figure 19.: a_{sl}^q measurements performed by D0, LHCb, Belle and Babar. The black dot represents the SM expectation value, the yellow ellipse are interpretation of the D0 dimuon observation, and finally the green bands are averages of previous measurements [34].

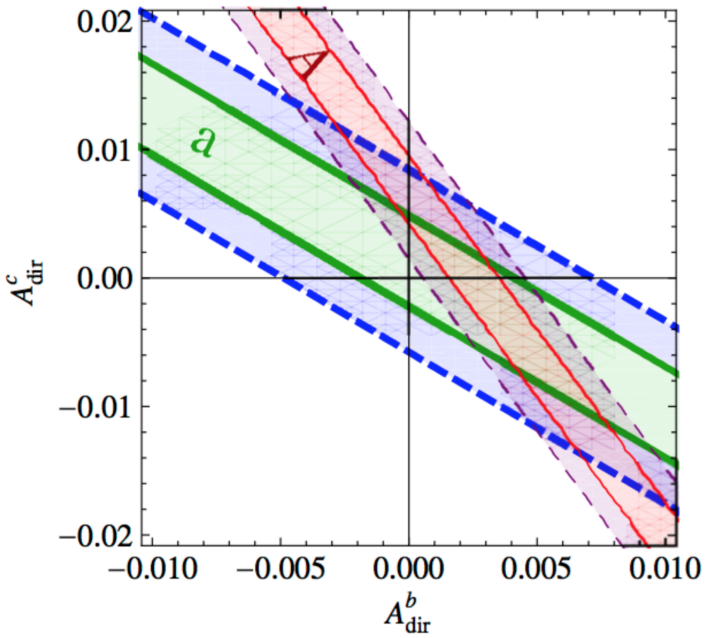

Figure 20.: Interpretation of the D0 dimuon (A^q_{dir}) and single muon (a^q_{dir}) measurements, showing the magnitude of direct $\mathcal{CP}$ violation in b and c decays required, assuming SM-like neutral B-mixing [46].

3

THE ATLAS DETECTOR AT THE LARGE HADRON COLLIDER

The measurements presented in this thesis were performed using data collected by the ATLAS detector in pp collisions during Run-1 and Run-2. In Run-1 the Large Hadron Collider (LHC) delivered proton collisions with a centre of mass energy ($\sqrt{s}$) equal to 8 TeV *and the data sample analysed here corresponds to an integrated luminosity of* $20.3\,\text{fb}^{-1}$ *(*2012 *data taking), while in Run-2 collision data were collected at* $\sqrt{s} = 13$ TeV *with an integrated luminosity of* $36.1\,\text{fb}^{-1}$ *(*2015 *and* 2016 *data taking).*
In this chapter there is a brief overview of the LHC and the ATLAS detector, focussing on the most relevant features for the analysis.

3.1 THE LARGE HADRON COLLIDER

The Large Hadron Collider (LHC) [47] is a storage ring where high energy proton or heavy ion beams circulate and collide.
With its 27 km ring of superconducting magnets, 14 TeV design centre of mass energy and $10^{34}\,\text{cm}^{-2}\text{s}^{-1}$ nominal luminosity, LHC is the largest and most powerful particle accelerator ever built in the world. It was built by the European Organisation for Nuclear Research (CERN) in the Geneva area, just across the French border and it first started the operations in 2008.
The LHC tunnel is located 100 m underground and it is the final stage of the particle acceleration mechanism, as shown in Figure 21.

Protons are produced using an electric field to ionise hydrogen atoms. Protons first pass through a Radio Frequency Quadrupole where packets start to form and then they enter the linear accelerator LINAC2 where an alternating radio frequency field accelerates particles up to 50 MeV and magnets squeeze the beam, focusing it in the transverse plane with respect to the direction of motion; particles are injected in the Proton Synchrotron Booster circular accelerator where they reach an energy of 1.4 GeV.
Proton acceleration continues in a larger circular accelerator: the Proton Synchrotron (PS), 628 m long, where the beam energy rises up to 26 GeV. The next step is achieved in the Super Proton Synchrotron (SPS) 7 km ring where the proton energy increases up to 450 GeV.

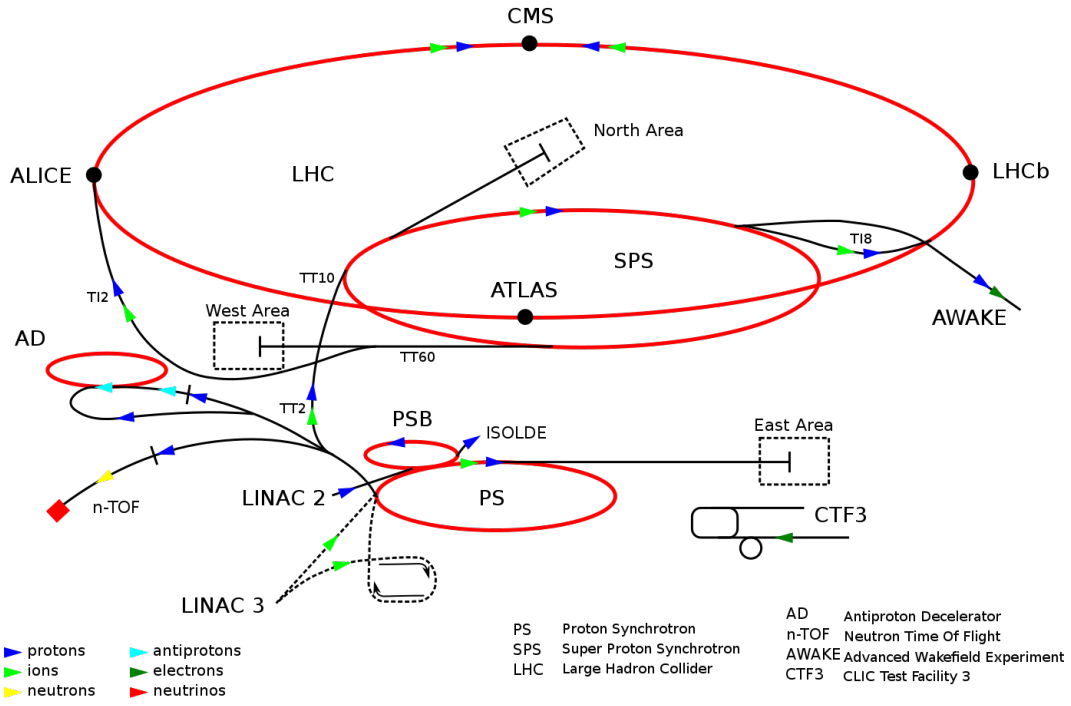

Figure 21.: CERN accelerator facility [48].

Protons are finally injected into the LHC where beams circulate in opposite directions into two parallel ultrahigh vacuum rings. Superconductive radio frequency (RF) cavities accelerate the protons to the desired centre-of-mass energy and superconducting dipole magnets bend the particle trajectory. The maximum magnetic field of the dipole is equal to 8.3 T and a schematic view of the LHC dipole magnets is shown in Figure 22 left. Moreover, 392 quadrupole magnets are installed to stabilise and focus the particle beams. The RF cavities and magnets operate in cryogenic conditions thanks to a complex cooling system that provides fluid helium, guaranteeing a temperature of about 1.9 K.

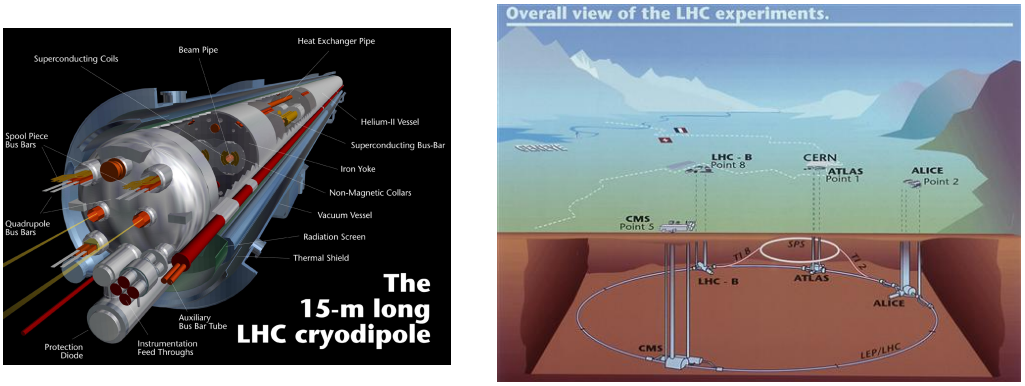

Figure 22.: Left: schematic view of an LHC dipole magnet, operated with a nominal current of 11700 A, producing a magnetic field of 8.3 T to bend charged particles along a circular trajectory.
Right: underground LHC ring and experiments [49].

Protons are organised in bunches containing $\sim 10^{11}$ particles each, with a minimum time spacing between two consecutive bunches of 25 ns.
After ramping up to the desired energy, the beams are squeezed and direct to collisions at the dedicated LHC major experiments, ATLAS [52], ALICE [53], CMS [54] and LHCb [55], as shown in Figure 22 right.

3.2 LHC LUMINOSITY IN RUN-1 AND RUN-2

For a given physics process, the number of events per second (rate, $R(t)$) produced at LHC is proportional to the production cross section (σ) times a factor $\mathcal{L}(t)$ called instantaneous luminosity (as shown in Equation 42) which depends on the collider parameters, as described in equation 43. The total number of events for a given process is obtained by integrating the luminosity: $\int \mathcal{L}(t)\, dt = L$

$$R(t) = \mathcal{L}(t) \times \sigma \tag{42}$$

$$\mathcal{L}(t) = \frac{N_b^2 n f}{4\pi\sigma_x\sigma_y} \tag{43}$$

where f is the frequency of bunch crossings, N_b the number of particles per bunch (1.1×10^{11}), n the number of bunches per beam (2200), σ_x, σ_y (19 μm) are the Gaussian beam profiles in the transverse plane with respect to the beam direction *i.e.* the effective area; all the parameters are quoted at the design luminosity of $10^{34}\,\mathrm{cm}^{-2}\mathrm{s}^{-1}$.
Increasing the energy and the luminosity is crucial to explore new physics and LHC started the Run-1 with an initial energy of $\sqrt{s} = 7$ TeV in 2011 and an integrated luminosity of $5.2\,\mathrm{fb}^{-1}$ collected by the ATLAS detector, ramping up to $\sqrt{s} = 8$ TeV in 2012 with an integrated luminosity of $20.3\,\mathrm{fb}^{-1}$ collected by the ATLAS detector. After Run-1 there was a Long Shutdown period (LS1), when experimental upgrades were performed. Figure 23 shows the LHC schedule from 2011, when Run-1 started, to the High Luminosity LHC (HL-LHC) programme. During Run-2, the

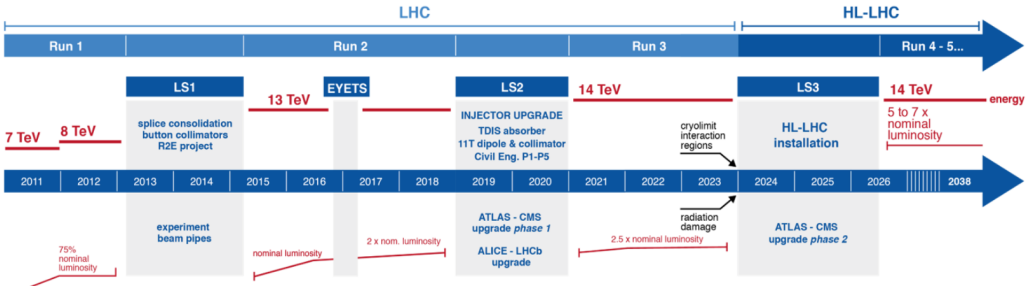

Figure 23.: LHC schedule from the year 2011 to the High Luminosity LHC (HL-LHC) programme [50].

LHC delivered proton-proton collisions at 13 TeV with a frequency of 40 MHz, corresponding to a bunch spacing of 25 ns. The ATLAS experiment collected $139.0\,\mathrm{fb}^{-1}$ during the 2015, 2016, 2017 and 2018 data taking. Figure 25 shows the ATLAS detector recording efficiency as a function of the integrated luminosity, throughout Run-1 and Run-2. The results presented in this thesis were performed using data collected by the ATLAS detector in pp collisions in 2012 (Run-1 measurement) and 2015-2016 (Run-2 measurement). In particular the calibration of the momentum imbalance based Soft Muon Tagger shown in Chapter 6 is performed with data collected during 2012, while all the studies concerning the 13 TeV analysis such as

the Kinematic Likelihood Fitter Implementation, Systematic Uncertainties evaluation and Results (Chapters 8, 9 and 10) are obtained applying the Object and Event Selections, outlined in Chapters 5 and 7, on 2015-2016 datasets.
Figure 25 shows the integrated luminosities collected by the ATLAS detector during these years.

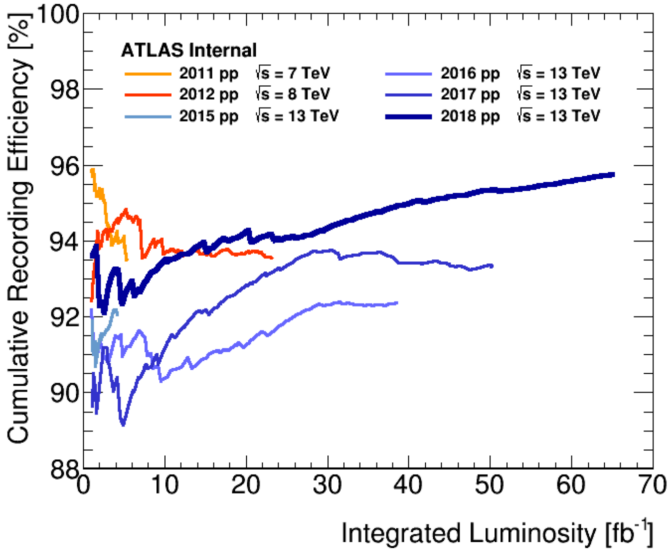

Figure 24.: Recording efficiency, expressed in percentage as a function of the integrated luminosity achieved by the ATLAS detector during Run-1 and Run-2. The efficiency is above the 90% [51].

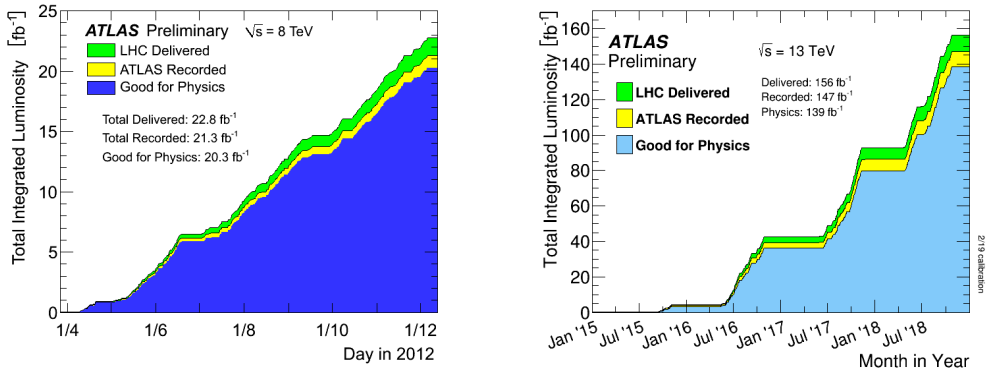

Figure 25.: Left: integrated luminosity recorded by the ATLAS detector during Run-1 at $\sqrt{s} = 8$ TeV in 2012. Right: integrated luminosity recorded by the ATLAS during Run-2 at $\sqrt{s} = 13$ TeV in $2015 - 18$. Several fractions of the run can be excluded from the physics analysis because the detector does not work properly, reducing the total amount of data, but the efficiency is typically above the 90% [51].

3.3 THE ATLAS DETECTOR

The particle detectors built around the LHC interaction points (IP) undergo very intense radiation doses and are designed to perform high precision measurements on a dense environment of high energetic particles delivered by LHC with high interaction rates. To face these experimental challenges detectors have to develop and exploit tools at the frontier of technology.
ATLAS (A Toroidal LHC ApparatuS) is one of the four major experiments instrumented in the LHC tunnel. It is a general-purpose particle detector designed to explore the full discovery potential of the LHC.
ATLAS is a forward-backward symmetric detector with a cylindrical geometry around the interaction point and its axis along the beam line. The overall detector, as shown in picture 26, is 44 m long with a radius of 25 m, weights over 7000 t and it is the largest single detector ever built in the world. The detector is made of successive concentric layers of dedicated instruments which identify and measure different features of the particles emerging from the pp collisions.

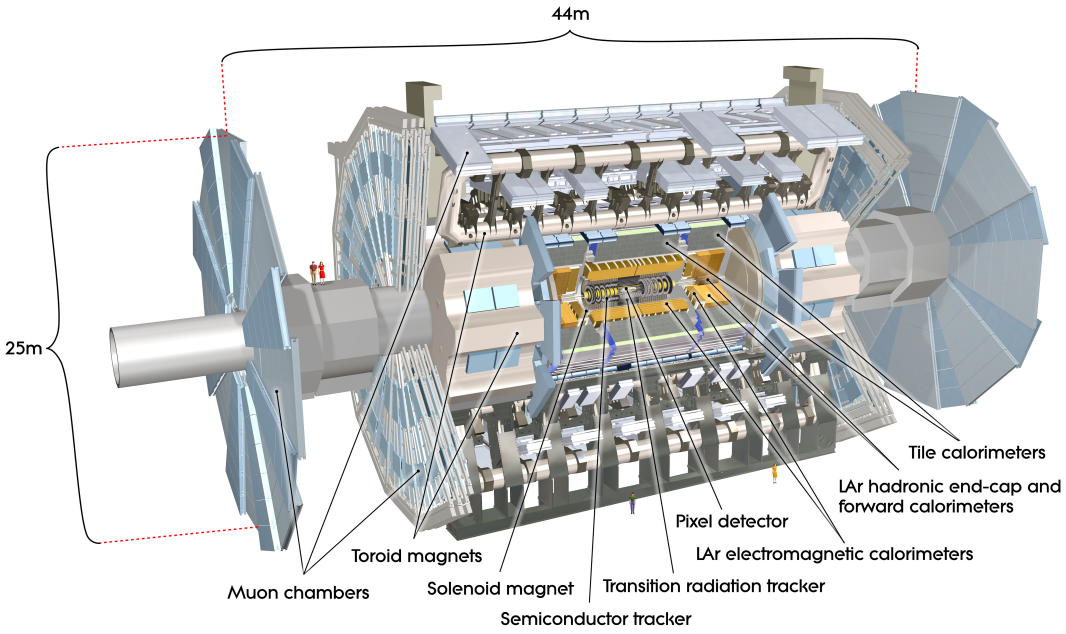

Figure 26.: The ATLAS detector, labelling the individual components [52].

It is useful to define a coordinate system which is the ATLAS standard one and will be adopted from now on. A right-handed system is adopted and the origin of the coordinate system is in the nominal interaction point, while the beam direc-

tion defines the z-axis and the $x - y$ plane is perpendicular to the beam line. The positive x-axis is defined as pointing from the interaction point to the centre of the LHC ring and the positive y-axis is defined as pointing to the surface. The positive z side of the detector is labelled as side-A, while the side-C is that with negative z. An azimuthal angle φ spans from $-\pi$ to π around the beam axis and the polar angle θ is the angle from the beam axis that spans from 0 to π in the $z - y$ plane. Since the polar angle θ is not a Lorentz invariant because it is susceptible to contractions in the z-direction, the rapidity y, defined in Equation 44, is used because differences in y are Lorentz invariant.

$$y = \frac{1}{2} \ln \left(\frac{E + p \cdot \cos\theta}{E - p \cdot \cos\theta} \right) \tag{44}$$

where E and p are respectively the energy and the momentum of the particle. At relativistic energies the pseudorapidity η tends to the rapidity in the limit of a mass-less particle and it is defined as $\eta = -\ln \tan\left(\frac{\theta}{2}\right)$. The total distance between two points can be calculated in the pseudorapidity-azimuthal angle space $\eta - \phi$ as $\Delta R = \sqrt{\Delta\phi^2 + \Delta\eta^2}$. The transverse momentum p_{T} , the transverse energy E_{T} and the missing transverse energy $E_{\mathrm{T}}^{\mathrm{miss}}$ are defined in the $x - y$ plane. The energy and the momentum in the $x - y$ plane are conserved in particle collisions and decays while the momentum in the z-direction cannot be fully reconstructed due to neutrino escaping from the detector and also due to the unknown initial parton momenta.

The overall detector is organised in several dedicated sub-detectors which provide different information. The variety of particles emerging from the interaction point interact with the matter in different ways, according to both the particles and the material properties. Each sub-detector is made of a specific material and focuses on the measurement of a different physics quantity: the charged particle tracks are reconstructed by the inner detector (ID) in the innermost layer of the detector, the electromagnetic (ECAL) and the hadronic (HCAL) calorimeters measure the energy of photons and electrons, and hadrons respectively, and finally the muon spectrometer (MS) detects the muons at the outer part of ATLAS. All these sub-detectors operate in an intense magnetic field provided by a solenoid and toroid magnetic systems which is designed to bend the charged particle trajectory and measure the particle momentum, while the forward detectors accomplish the luminosity measurement task along with the particle detection. The general performance figures of the ATLAS detector are listed in the table in Figure 27.

All the ATLAS sub-detectors were relevant for the measurement presented in this thesis so they will be described in details in the following sections.

Detector component	Required resolution	η coverage	
		Measurement	Trigger
Tracking	$\sigma_{p_T}/p_T = 0.05\%\ p_T \oplus 1\%$	± 2.5	
EM calorimetry	$\sigma_E/E = 10\%/\sqrt{E} \oplus 0.7\%$	± 3.2	± 2.5
Hadronic calorimetry (jets)			
barrel and end-cap	$\sigma_E/E = 50\%/\sqrt{E} \oplus 3\%$	± 3.2	± 3.2
forward	$\sigma_E/E = 100\%/\sqrt{E} \oplus 10\%$	$3.1 < \lvert\eta\rvert < 4.9$	$3.1 < \lvert\eta\rvert < 4.9$
Muon spectrometer	σ_{p_T}/p_T=10% at p_T = 1 TeV	± 2.7	± 2.4

Figure 27.: The design specifications for the intended precision of all ATLAS components. Energy and transverse momentum are expressed in GeV, Figure from [52].

3.3.1 *Magnet System*

The ATLAS magnet system is designed to provide a strong magnetic field and bend charged particles crossing the detector volume and operates at cryogenic temperatures (~ 4.6 K). The system, shown in Figure 28, is organised in four major components:

1. a barrel solenoid: it provides a 2 T axial magnetic field for the inner trackers, while minimising the radiative thickness to reduce multiple scattering and energy loss, which can affect the momentum and the energy measurements;

2. a toroid system: it consists of a barrel toroid and two end-caps toroids. The magnetic field generated in the usable detector area of about $12000\,\mathrm{m}^3$ has a peak in the coil windings of about 4.1 T, as shown in Figure 29 [57]. The toroid structure is open to minimise the uncertainty on the momentum measurements due to multiple scattering.
   - The barrel toroid is placed after the calorimeter system and consists of eight superconducting coils, providing a magnetic field of about 0.5 T to bend muons in the region $|\eta| < 1$ and thus measure their momentum;
   - The end-caps toroid's coils are smaller and forward-backward symmetric. They provide 1 T magnetic field to bend muons in the region $1.4 < |\eta| < 2.7$. In the transition region ($1 < |\eta| < 1.4$) the magnetic deflection is provided by a combination of barrel and end-cap.

3.3.2 *The Inner Detector*

The inner detector (ID) is in the ATLAS innermost region, it identifies and reconstructs the trajectories of charged particles produced in proton collisions. Thanks

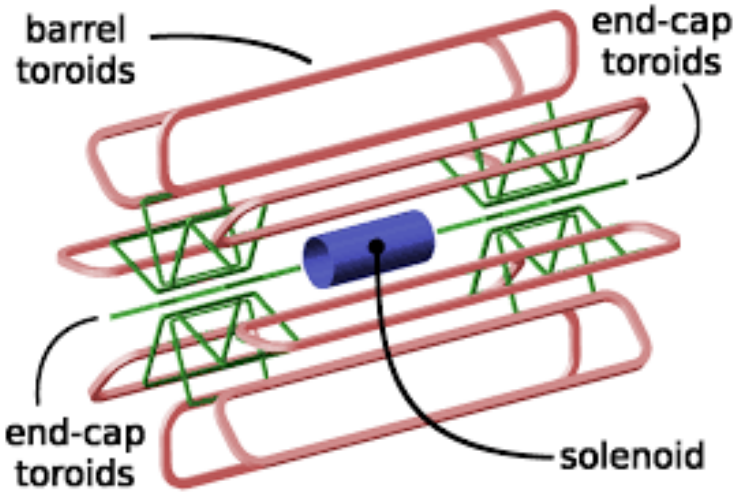

Figure 28.: Geometry of the ATLAS magnet system, Figure from [52]. Red and green lines show the physical coils.

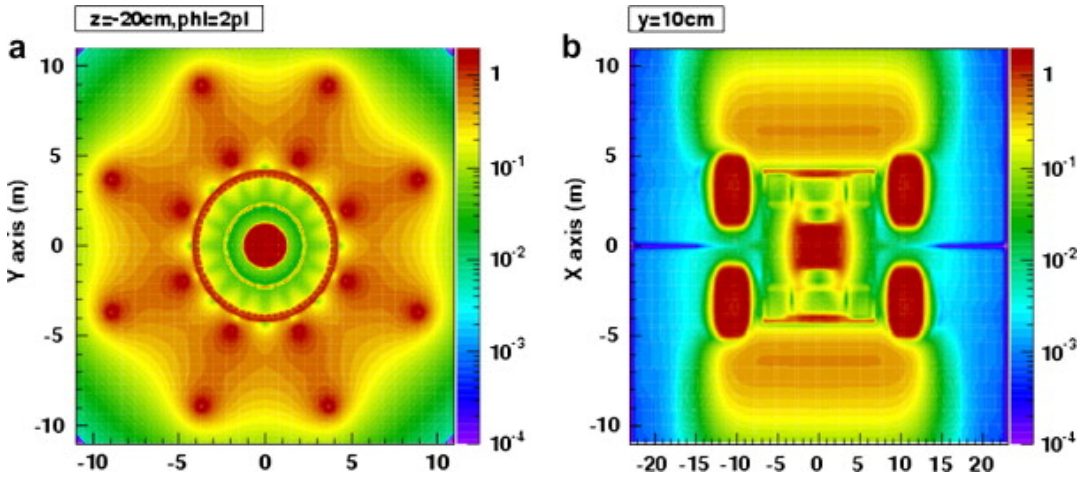

Figure 29.: Field of the ATLAS magnet system, Figure from [57]. The left plot shows the intensity of the magnetic field in the ATLAS detector in the transverse plane with respect to the beam axis, while the right plot shows the intensity of the magnetic field on the longitudinal plane.

to its fine granularity the ID also provides vertex and impact parameter measurements [58]. The ID is embedded in a 2 T magnetic field generated by a superconducting solenoid which bends the trajectories of charged particles and allows the measurement of their momentum. As shown in Figure 30, the ID extends over a length of 6.2 m with a diameter of 2.1 m and covers the $|\eta| < 2.5$ region. To achieve the required tracking precision three technologies are combined: pixel detectors, silicon micro-strip (semi-conductor) trackers (SCT) and a transition radiation detector.

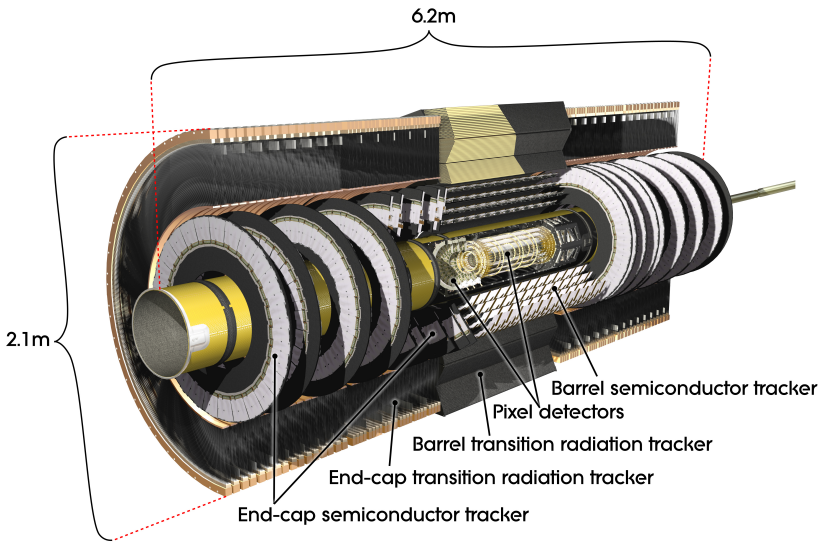

Figure 30.: A sketch of the ATLAS inner detector, labelling the individual components [52].

Figure 31 shows the components of the ID in the barrel region: they are arranged in concentric cylinders around the beam axis, while Figure 32 shows the tracker in the end-cap region: it is made of disks perpendicular to the beam axis.

During the Long Shutdown, a number of upgrades have been performed for the ATLAS ID and a significant upgrade concerns the installation of the Insertable B-Layer (IBL). IBL is an additional pixel layer close to the interaction point which provides high-resolution hits at small radius and an improvement on the tracking performances. It is useful to reconstruct the secondary vertices with a better precision and it contributes to improve the ATLAS b-tagging performances [56].

Pixel Detector

There are 1744 pixel modules organised in three barrel layers, containing approximately 67 millions of squared pixels, and three end-cap disks on each side, containing 13 millions of pixels, with about 80 million readout channels.

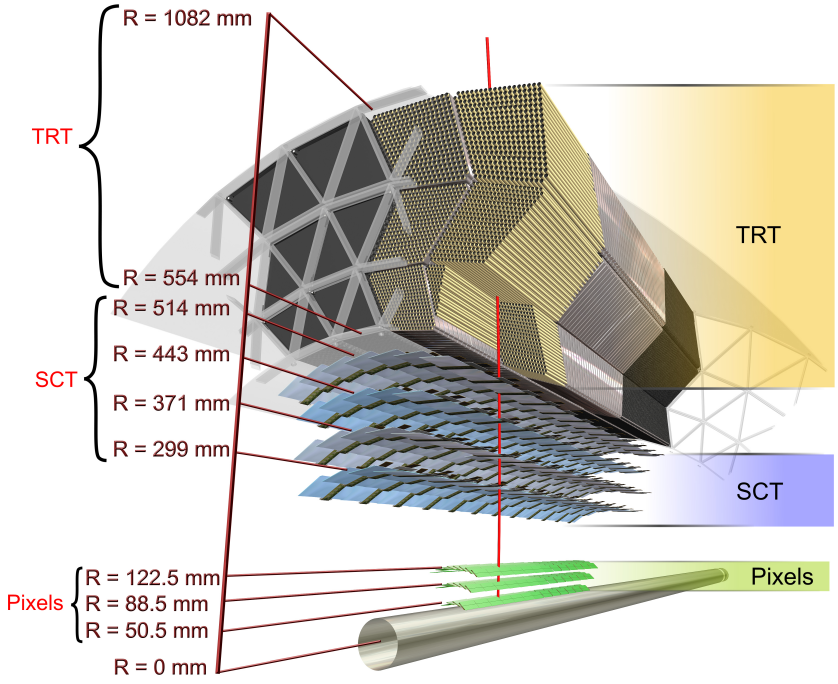

Figure 31.: The ATLAS barrel inner tracker (the IBL is not shown in this picture) [52].

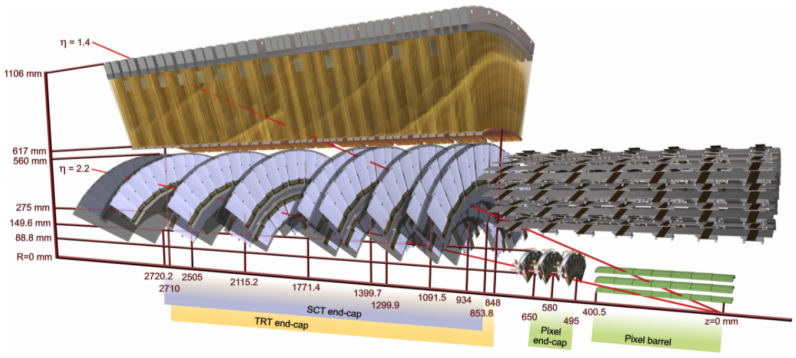

Figure 32.: The ATLAS end-cap inner tracker [52].

The IBL and the pixel detector [59] surround the beam pipe and it suffers from a massive radiation dose due to the approximately 1000 particles that will emerge from the collision point every 25 ns. To operate in such a high-radiation environment and perform high-precision measurements the pixel detector must be made of radiation-tolerant materials with fine granularity: the pixel size is $50 \times 400\,\mu\text{m}^2$ with intrinsic position resolutions of $10\,\mu$m in the $R-\phi$ plane and $115\,\mu$m in z for the barrel and $10\,\mu$m in the $R-\phi$ plane and $115\,\mu$m in R in the end-caps.
The pixel detector consists of three layers of oxygen-doped silicon wafers which are n-type extrinsic semiconductor. The passage of charged particles through the silicon generates electron-hole pairs that drift in opposite directions under a potential difference ranging from 150 V to 600 V (depending on pixel ageing) and are detected as hits.

Semiconductor Tracker

The semiconductor tracker (SCT) detector [60] is made of silicon strips ($6.36 \times 6.40\,\text{cm}^2$) and it is designed to provide track precision measurements and to contribute to the measurement of momentum, impact parameter and vertex position in the intermediate radial range, as shown in Figure 31.
Its working principle is very similar to the pixels. The full SCT detector contains $61\,\text{m}^2$ of silicon detectors, with 6.2 million readout channels. Each strip provides 2 hits and guarantees a spatial resolution of $16\,\mu$m in the $R-\phi$ plane and $580\,\mu$m in the z direction.

Transition Radiation Tracker

The transition radiation tracker (TRT) [61] is made of two components, based on different technologies: a tracker (based on straw tubes) and a transition radiation (TR) detector for pattern recognition.
When relativistic charged particles pass through inhomogeneous media they produce X-rays whose intensity is linearly proportional to the Lorentz factor $\gamma = \frac{E}{m}$ and hence provides information about both the mass and the energy. Transition radiation detectors are based on this physics phenomenon that allows to discriminate between lighter and heavier charged particles passing through several layers of material of different refraction indices. Typically only electrons reach the velocity which is needed to generate transition radiation thus the detection of a TR photon in ATLAS indicates the traversing of an electron.
The TRT is made of proportional drift tubes filled with a gas mixture of $Xe : CO_2 : O_2 = 70 : 27 : 3$. Each drift tube contains four straws. Straws consists of cylindrical negatively charged cathodes around singular ($31\,\mu$m diameter) anode wires. A polypropylene foil is placed between the straws to provide the material-transitions required to generate the transition radiation. A charged particle crossing a straw

ionises the gas and generates electrons which drift to the anode wire where electrons are multiplied in avalanche and produce a measurable signal. On the other hand also the transition radiation photons, created in one of the radiator layers, generate primary ionisation in the gas and this additional ionisation increases the electric pulse height obtained in the straw tube. Hence two independent thresholds are used to allow the detector to discriminate between tracking hits, which pass the lower threshold, and transition-radiation hits, which pass the higher threshold.
A charged particle will produce on average 35-40 hits and the generated electrical signals are then recombined to determine a particle's trajectory with a spatial resolution of 170 μm per straw tube.

3.3.3 *Calorimeters*

The purpose of calorimeter detectors is to measure the energy of the particles produced in pp interactions through the total absorption of particles. The signal produced in the detector volume is proportional to the total deposited energy. The ATLAS calorimeters are set to work alongside tracking detectors, provide a full ϕ cover and a larger pseudo-rapidity range coverage, up to $|\eta| \leq 4.9$ and provide fast signals ($\sim 10\,\mathrm{ns}$). The energy resolution of a calorimeter improves with higher energies and the ATLAS nominal values are expressed in the table in Figure 27.
The ATLAS detector employs both electromagnetic (ECAL) and hadronic (HCAL) sampling calorimeters: they are built alternating layers of absorber to induce particle interactions and active material (typically scintillators). Figure 33 shows a cut-view of the ATLAS calorimeter system.

Electromagnetic Calorimeter

Above a certain energy threshold (the so called critical energy E_c) the dominant process among the interactions of photons with matter is the production of e^+e^- pairs ($E_\gamma \geq 1\,\mathrm{MeV} = 2m_0^e \sim 1\,\mathrm{MeV}$) and these high energetic electrons will interact with the material producing bremsstrahlung radiation and therefore leading to more photons, producing an electromagnetic shower. At a given position x, the energy of an electron or positron is given by $E = E_0 e^{-\frac{x}{X_0}}$ and a meaningful parameter used to describe the depth of the electromagnetic shower is the radiation length X_0 that expresses the mean thickness (in $\mathrm{g/cm^2}$) after which the electron or positron energy is reduced by a factor $1/e$ of its initial energy, E_0. A calorimeter is required to be long enough to cover enough X_0 to absorb all the energy of the traversing particles.
Lead plates play as absorber in the ATLAS ECAL while Liquid argon (Lar) is the active medium [62]. The material choice is driven by the need to minimise X_0 in the absorber and have a fast and intrinsic radiation hard active medium. The ECAL

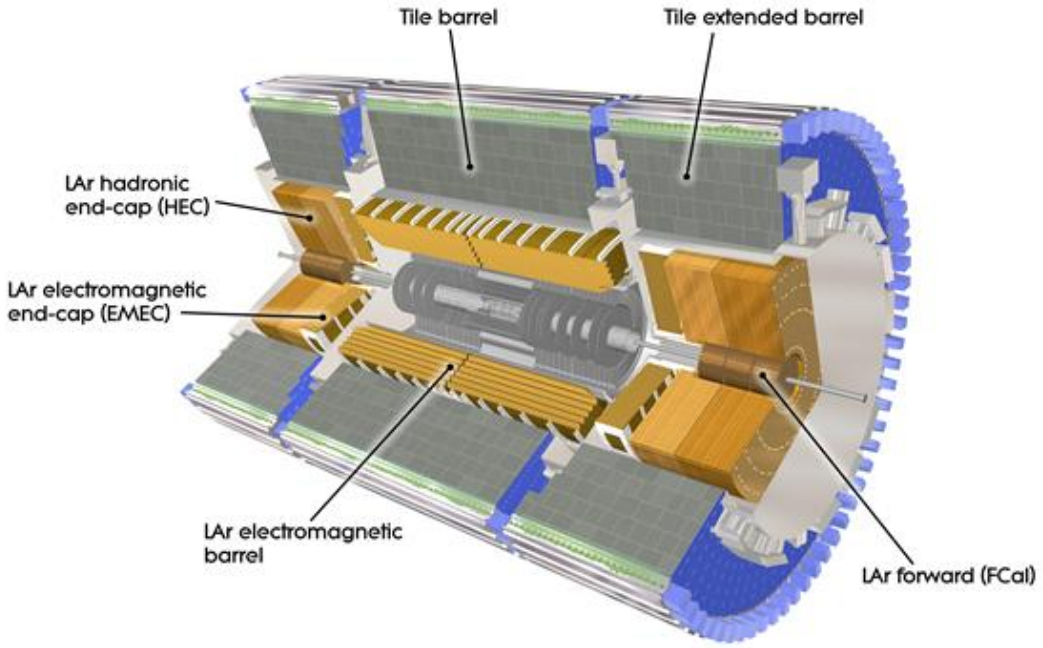

Figure 33.: Sketch of the ATLAS calorimeters [52].

consists of a barrel (EMB) and an end-cap (EMEC) calorimeter. The EMB system covers a pseudorapidity range of $|\eta| \leq 1.475$ and has a finer granularity with respect to the EMEC. The number of radiation lengths is $24\,X_0$ in the EMB and $26\,X_0$ in the EMEC. The EMEC is made of two concentric wheels covering the range $1.375 < |\eta| < 3.2$. The transition region between the EMB and the EMEC calorimeters, $1.37 < |\eta| < 1.52$, has a poorer performance because of the higher amount of passive material in front and it is called crack region. Electrons which are detected in that region are not considered in this thesis.

Hadronic Calorimeter

Hadrons with energies of the order of $\sim 100\,\mathrm{GeV}$ interact via inelastic scatterings with the nuclei of the material they are traversing. In these nuclear interactions, new particles are formed, producing a hadronic shower which is much larger and often travels much further than an electromagnetic shower and it is called a jet. Since pions are the lightest and most probable new particles produced in the interaction of hadrons with matter, the $\pi^0 \to \gamma\gamma$ decay gives rise to an electromagnetic shower within the hadronic one ($\sim 30\%$ of the total activity). The key material property for nuclear interactions is the interaction length λ_0.

The hadronic calorimeter wraps around the ECAL, it is divided into a barrel (TileCal) and two end-caps (HEC) calorimeters [63]. The TileCal consists of steel, as absorber, and plastic scintillators, as active material. The absorber choice aims at minimising the number of interaction lengths which is $\lambda_0 \sim 9$ in the TileCal. The HEC is divided in two wheels for each end-cap and it is composed of LAr and copper, covering up to $|\eta| < 3.2$. In the end-cap regions the total number of interactions lengths (including the EMEC) is $12\,\lambda_0$.

Forward Calorimeter

In the forward region ($3.1 < |\eta| < 4.9$), there is another type of LAr calorimeter: the Forward Calorimeter (FCAL) which is both ECAL and HCAL. It consists of copper rods inside an outer tube with $250\,\mu$m liquid Argon gap in between. This matrix is parallel to the beam axis. The number of interaction lengths is about $10\,\lambda_0$.

3.3.4 *Muon Spectrometer*

Muons are key particles in the analysis presented in this thesis and they are detected in both the ID and the muon spectrometer (MS). Muons travel more than all the other particles in the ATLAS detector because, whilst interacting electromagnetically, they are not absorbed in the calorimeters. Indeed, the energy loss per bremsstrahlung is proportional to E/m^2, muons interaction probability is $(200)^2$ times smaller than electrons. Moreover the energy loss due to ionisation is inversely proportional to the particle energy and so at the LHC collision energies the resultant muons could escape the detector, although they can be detected because they leave detectable hits in the ID and MS.
Figure 34 shows the ATLAS MS [64]: it consists of trigger and high-precision tracking systems provided by separate chambers and it measures tracks and momentum of muons through their magnetic deflection in the large superconducting toroid magnets. It is designed to have a resolution of $\sigma_{p_T} \sim 10\%$ for 1 TeV tracks.

Monitored Drift Tubes (MDT) and the Cathode Strip Chambers (CSC) are used for precision tracking, while Resistive Plate Chambers (RPC) and the Thin Gap Chambers (TGC) provide the trigger. The barrel region is instrumented with three cylindrical layers of chambers, while in the transition and end-cap regions the chambers are arranged in three planes perpendicular to the beam axis. MDTs provide a precision tracks measurement over most of the η range (they are both in the barrel and in the end-cap region) and CSCs are used for the same purpose at large pseudorapidity range ($2. < |\eta| < 2.7$). The trigger signal is supplied by RPCs in the barrel region, covering a pseudorapidity range $1.05 < |\eta| < 2.4$ while TGCs are installed in the end-cap regions and undergo an intense particle flux.

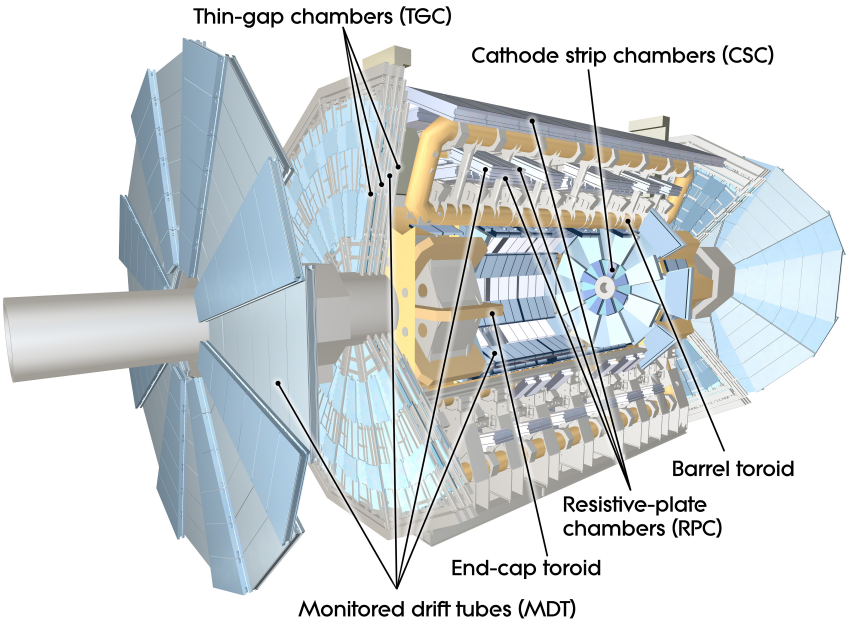

Figure 34.: Sketch of the ATLAS MS [52].

Monitored Drift Tubes

Each MDT chamber is made of two multi-layers of three or four (only in the innermost chambers) layers of drift tubes with a diameter of 3 cm operating with an $Ar/CO2$ gas mixture (93/7) at 3 bar absolute pressure. The operating gas was selected because of the good ageing properties.
The anodic central wire is gold plated tungsten and rhenium with a 50 μm diameter, held at high voltage, to collect the electrons generated by muons ionising the gas volume. The amount of charge collected is proportional to the energy deposited by the particle, the gas pressure and the potential of the wire. The measured drift time is converted to the drift distance using the $r - t$ relation of the mixture.
In total there are 1088 chambers and with this system of tubes assembly, a high level of operation reliability can be expected because the failure of a single tube does not affect the performances of most of the other tubes.
These chambers have a high spatial resolution (80 μm) and a typical drift time of 700 ns.

Cathode Strip Chambers

CSCs are radially-oriented multi-wire proportional chambers designed to provide high precision tracking in the detector region close to the beam pipe. Each chamber consists of arrays of positively-charged anode wires and negatively-charged

copper cathode strips within a gas ($Ar + CO_2$) volume. When muons pass through they ionise the gas creating electron-ion pairs: electrons drift to the anode while ions drift to the cathode generating an electric signal and, since anode and cathode strips are perpendicular, two coordinates can be measured with a typical spatial resolution is 40 μm in the radial direction and 5 mm in the longitudinal direction. The time resolution is about 7 ns.
The CSCs are divided in 16 sectors organised in two disks with eight chambers each (eight smalls and eight larges).

Resistive Plate Chambers

The RPCs are fast gaseous detectors located in the barrel region and consist two rectangular layers of gas gap, filled with a gas mixture of $94.74\%\, C_2H_2F_4 + 5\%\, isoC_4H_10 + 0.3\%\, SF_6$ (SF_6 is added to limit the charge avalanches in the chamber). The RPCs operating principle is also based on ionisation phenomena.
The RPC chambers are made of bakelite plates of 2 mm with a potential difference of 9.8 kV, readout by two orthogonal series of strips: the η-strips are parallel to the MDT wires and the ϕ-strips orthogonal to the MDT. Hence RPCs are able to provide bi-dimensional space coordinates with a good spatial resolution and with a time resolution of just 1 ns.
Due to their fast response, RPCs are used for the muon trigger in the barrel region.

Thin Gap Chambers

TGCs are multi-wire proportional chambers used for the muon trigger system in the end-cap region. A TGC chamber consists of a plane of closely spaced wires at positive high voltage, sandwiched between resistive grounded cathode planes. The gas mixture used for these chambers is $55\,\% CO_2$ and $45\%\, C_5H_{12}$. TGC chambers work at 2.9 kV and their time resolution is about 4 ns. They also provide a measurement of the muon track coordinate orthogonal to the one provided by the precision tracking chambers

3.3.5 *Forward Detectors*

In the very forward rapidity region there are four detectors which provide luminosity and proton-proton cross-section measurements: LUCID, ZDC, ALFA and AFP [52]. They are located at various distances from the interaction point along the z-axis and they are close to the beam pipe.

LUCID

LUCID is the acronym for Luminosity measurements Using Cherenkov Integrating Detector. Cherenkov radiation is a peculiar physics phenomenon due to a charged particle travelling in a medium at a speed that is faster than the speed of light in that medium.
LUCID consists of two detectors placed around the beam-pipe on both forward ends of the ATLAS detector at ± 17 m from the interaction point, respectively, and provides a pseudorapidity coverage of $5.5 < |\eta| < 5.9$. In each detector there are 16 photomultipliers (PMTs) and four quartz fibre bundles. Cherenkov light is produced in the quartz window and the resulting electrons are detected in the PMTs. The detector is composed of light material, which is radiation hard, and provide a fast response (~ 10 ns) from the moment a charged particle traverses the detector. Thus the detector is able to discriminate collisions coming from different bunch crossings (whose spacing is 25 ns) and LUCID can measure both the integrated luminosity and provide online monitoring of the instantaneous luminosity.

ZDC

The Zero Degree Calorimeter (ZDC) is located at an axial distance of ± 140 m from the interaction point and provides a coverage of the region $|\eta| > 8.3$. ZDC's main purpose is to trigger and measure the energy of the spectator neutrons dissociated from the colliding nuclei and it provides the absolute luminosity, with an accuracy of $\sim 5\%$, during the heavy ion physics program.

ALFA

ALFA (Absolute Luminosity For ATLAS), is a scintillating fibre tracker placed inside roman pots at a distance of ± 240 m from the IP. Its purpose is the measurement of the absolute luminosity via elastic proton-proton scattering at small angles.

AFP

The last detector is AFP (ATLAS Forward Proton) which is located 210 m away from the interaction point. It identifies events where one or two protons emerge intact from the proton-proton collisions.

3.3.6 *Trigger and Data Acquisition*

The trigger and data acquisition (TDAQ) system is one of the key elements for high-luminosity experiments in High Energy field, such as ATLAS. Only a small

part of the huge amount of data collected by LHC in each bunch crossing can be completely acquired and analysed. The ATLAS Trigger system filters all events reducing the information rate from $\geq 40\,\mathrm{MHz}$ to approximately $1\,\mathrm{kHz}$. It discards events which do not yield *interesting* physics, being the output of the vast majority of bunch collisions.
The trigger system has been changed substantially during the first long shutdown (LS1). Since the results presented in this thesis concern both Run-1 and Run-2 data taking, a brief introduction of both trigger systems will be given. For an overview of the Run-2 trigger, please refer to Chapter 4.
The ATLAS trigger during Run-1 was based on three stages, described in the next Sections.

Level-1 Trigger

The Level-1 (L1) is an hardware-based trigger and it represents the first filter on pp collisions. There are therefore two types of Level-1 triggers: calorimeter Level-1 (L1Calo) and muon Level-1 (L1Muon).
L1Calo uses physical signatures of electrons and photons in ECAL and jets in the HCAL, while L1Muon uses high-p_{T} muons in the MS, or large missing momentum to discriminate interesting events from the dominant background. Low-granularity information is required, coming from the MS RPC and TGC and the calorimeter subsystems. During Run-1 data taking, the L1 trigger had a latency of about $2.5\,\mu\mathrm{s}$ and reduced the output rate to $70\,\mathrm{kHz}$.
L1 trigger decision defines a physical region-of-interest (RoI) in the detector to be used as a seed in the next stage of the triggering system.

Level-2 Trigger

The Level-2 (L2) trigger is based on a processing farm and uses the RoI information to perform basic event reconstruction. The L2 reduces the rate from the L1 output up to $100\,\mathrm{kHz}$ to approximately $6.5\,\mathrm{kHz}$ within a processing time of $200\,\mathrm{ms}$.

Event Filter

The event filter (EF) is the final stage of the selection process. It manages the fully reconstructed event and runs in parallel over large computing farms. During Run-1 it was required to make a decision on each event within $1\,\mathrm{s}$ and to reduce the event rate up to $1\,\mathrm{kHz}$.

4

LEVEL 1 CALORIMETER TRIGGER EFFICIENCIES AND RATES OPTIMISATION

The optimisation of the rates and efficiencies of the Level 1 Calorimeter Trigger of the ATLAS detector is presented. To optimise the performance of the trigger efficiencies several options of the Level 1 Calorimeter Trigger configuration (such as filters and noise cuts) were tested with the goal of keeping the efficiency at a reasonable value (up to a drop of 5% is tolerable) while minimising the trigger rates, in view of the high-luminosity runs. The best configuration found corresponds to a drop of less than 1% in the trigger efficiency without any increase in the trigger rates.
This was done by simulating the trigger hardware in an offline analysis in order to be able to manipulate the default parameters and study the probe-electron response within the hardware. The signal efficiency is based on a $Z \rightarrow e^+e^-$ sample corresponding to an integrated luminosity of 1 pb^{-1}, while the rate results are based on an a sample consisting largely of very low p_T events, corresponding to an integrated luminosity of $2\,\mathrm{pb}^{-1}$. These studies exploit data collected by the ATLAS experiment in 2016 using $\sqrt{s} = 13$ TeV proton-proton collisions at the LHC.

4.1 MOTIVATIONS

As luminosity of the LHC beams is expected to increase significantly in the future, it has become a priority to reduce the rates of data taking to a reasonable level given the limited bandwidth, while at the same time keeping the physics signal efficiency the highest possible. During Phase-1 of the ATLAS experiment upgrade (see Figure 23) the instantaneous luminosity is expected to be $\mathcal{L} = 2 \times 10^{34}\,\mathrm{cm}^{-2}\,\mathrm{s}^{-1}$ and reach $\sim$ 55 interactions per beam crossing (μ), corresponding to a 25 ns bunch spacing at design energy.
The rates for most triggers, including the Calorimeters, will increase linearly with luminosity (which will be $\sim$ 33% higher than Run-2). As a consequence, the existing L1 system will not be able to provide low thresholds with acceptable rates for electron and photon triggers. Studies on the optimisation of the L1 trigger menus during Run-1 show that a reasonable figure of merit to gauge how severe is the

impact of the high luminosity pile-up on the performance of the ATLAS trigger system is the threshold corresponding to a 20 kHz trigger rate [66]. Figure 35 shows the predicted electromagnetic clusters threshold as a function of instantaneous luminosity, for a typical L1 trigger rate of 20 kHz: the energy threshold corresponding to the expected Phase-1 luminosity is shown to be above $40 - 45$ GeV. However, to preserve important physics signals it is mandatory to keep the thresholds below 30 GeV for the targeted 20 kHz rate.

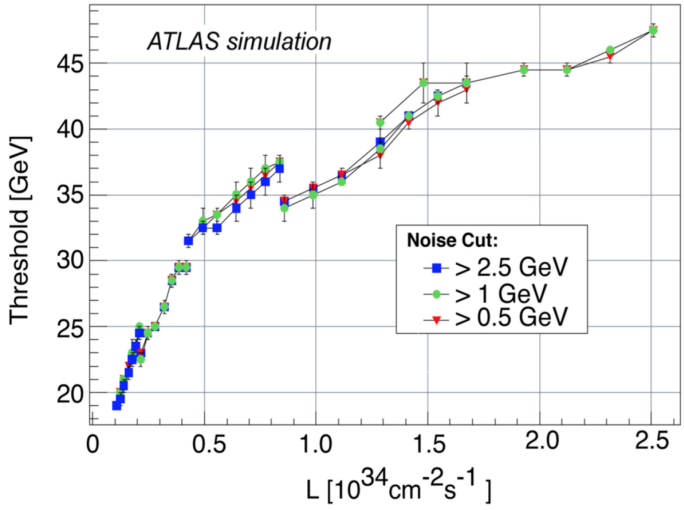

Figure 35.: Electromagnetic clusters threshold required to limit the Level-1 electromagnetic trigger rate to 20 kHz as a function of instantaneous luminosity. The different curves correspond to different levels of noise suppression threshold. Figure from [66].

The goal is to effectively reduce the overall rates and the Level 1 Calorimeter Trigger (L1Calo) plays a major role, since it is the first tier where the rate reduction takes place. A study about how the parameters of the hardware can be exploited to achieve this goal is presented in this chapter. Offline studies are performed to simulate the hardware and investigate the best configuration for the online parameters to maximise signal efficiency and minimise rates.

Via the offline analysis, it is possible to vary the noise and isolation parameter values, reconstruct new trigger objects and study whether a change will lead to an increase or reduction of efficiencies and rates. For efficiencies, a $Z \rightarrow e^+e^-$ sample is used, due to its relatively large production cross section and easily identifiable decays to leptonic final states which offer a clean experimental signature. Trigger rates were instead computed using a sample consisting largely of very low p_T events which are rarely used for physics analyses, but they constitute the majority of events the LHC delivers. This sample, enriched in very low p_T events, is called

enhanced minimum bias sample and it is extremely useful for studying trigger rates.

4.2 L1CALO REPROCESSING

The amount of data produced by the LHC during collisions is far higher than what can be viably stored; for a 25 ns bunch spacing, collision rates can reach up to 1 GHz. To compensate for this, the ATLAS detector utilises a two-stage trigger system, with the aim of recording as many signals of interest as possible. Figure 36 shows the ATLAS Trigger and Data Acquisition (TDAQ) system in Run-2 with emphasis on the components relevant for triggering [67]. The L1 system processes information from the muon detectors and calorimeters of ATLAS, reducing the incident bunch-crossing rate of 40 MHz to a rate of around 100 kHz. Events are stored in pipeline buffers for up to 2.5 µs while the trigger decision is made, before the results are passed on to the High Level Trigger (HLT) system. Consisting of a large cluster of computers, the HLT collectively forms the second level of the trigger system. At this stage, regions of interest (RoI) identified at L1 are passed through fast-reconstruction algorithms, outputting events at a rate of a few kHz. After the events are accepted by the HLT, they are transferred to local storage at the experimental site and exported to the Tier-0 facility at the CERN computing centre for offline reconstruction. L1Calo operates alongside L1 muon trigger (L1Muon)

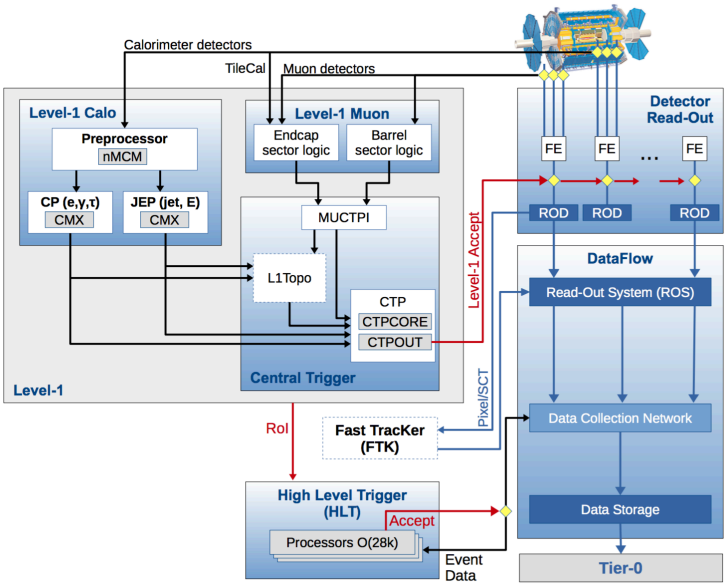

Figure 36.: A sketch of ATLAS TDAQ system, focusing on the trigger system [67].

and L1 topological trigger (L1Topo, new in Run-2) at L1 of the trigger system. Sec-

tion 4.2.1 describes the hardware structure of L1Calo, whilst Section 4.2.2 describes the means by which L1Calo can be simulated through software in the offline analysis.

4.2.1 *The Hardware Processing of L1Calo*

For a comprehensive overview of the ATLAS trigger system, refer to Ref. [69]. The ATLAS L1Calo is a pipelined digital system based on custom electronics with a fixed latency (dead time) of $\sim$1 µs plus $\sim$1.5 µs coming from cables transmission delays and the Central Trigger Processor (CTP) processing time. The L1Calo system is located entirely off detector in the service cavern called USA15. Input data comes from all the ATLAS electromagnetic and hadronic calorimeter cells, summed to about 7200 L1Calo trigger towers of reduced granularity. Table 5 describes the granularity of L1Calo, where η is the pseudo-rapidity and ϕ is the azimuthal angle.

Position	$\Delta\eta \times \Delta\phi$ [rad])
$\lvert\eta\rvert < 2.5$	0.1×0.1
$2.5 < \lvert\eta\rvert < 3.1$	0.2×0.2
$3.1 < \lvert\eta\rvert < 3.2$	0.1×0.2
$3.2 < \lvert\eta\rvert < 4.9$	0.4×0.4125

Table 5.: Trigger tower granularity for several $|\eta|$ slices and one quadrant in $\phi\,(0^\circ - 90^\circ)$.

L1Calo has three main sub-systems:

- Pre-Processor (PPr): it digitises the analogue calorimeter pulses, associates the trigger tower signals with the correct LHC bunch-crossing (BCID) and converts ADC counts to energy;
- Cluster Processor (CP): it identifies electrons, photons and single hadrons; the CP uses a 0.1×0.1 [rad] granularity and operates in the $|\eta| < 2.5$ region;
- Jet/Energy-sum processor (JEP): it does jet finding and energy sums; the JEP uses a 0.2×0.2 [rad] granularity, sums the electromagnetic and hadronic layers of L1Calo and operates over the whole of the ATLAS $|\eta| < 4.9$ region.

Both the CP and JEP processors work on the transverse energy (E_{T}) values in each of the electromagnetic (EM) calorimeter trigger towers and provided by the PPr. They all search for features in overlapping sliding windows and the final results are sent on cables to the CTP. The CP algorithms look for electron/photon (e/γ) and τ/hadron particles. Each CP consists of four crate systems and each of

them contains 14 Cluster Processor Modules (CPMs) and handles one calorimeter quadrant. The CP chips on each CPM are large FPGAs. CPMs carry out the e/γ and τ algorithms and count the multiplicity of successes, or hits, in the region covered by each module.

The e/γ algorithm searches for narrow, high-E_T showers in the EM calorimeters. The main background comes from a high rate of hadronic jets. Therefore, the characteristics used to discriminate between the electromagnetic and the hadronic showers and enhance the selection at L1 are to require transverse isolation, and that the showers should not penetrate to the hadronic calorimeter. The CP provides several sets of energy threshold and isolation conditions and each threshold can be chosen independently. Two Common Merger Modules (CMMs in Figure 37) receive via the backplane CPMs and jet energy modules (JEMs) results to be processed and summed over the entire crate. The CMMs use identical hardware but different firmware loads to process the results from the CPMs or JEMs. These final results are sent to the CTP.

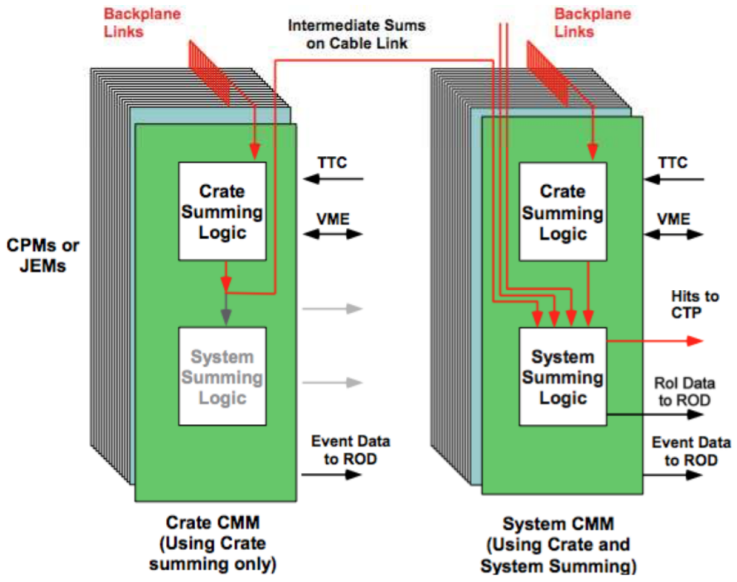

Figure 37.: CMM connectivity, including crate-level and system-level functionalities [69].

The increase in pileup in Run 2 results in higher occupancies in the calorimeter system. Consequently, the output data format has been extended from simple hit counts (used during Run1) to more descriptive Trigger Objects (TOBs) which include also the information for the topological trigger, *i.e.* η, ϕ and E_T of the candidate electron (see Figure 38). A TOB specifies a RoI along with its associated transverse energy, and its likelihood to be associated with a particle produced by

a collision. Figure 38 shows the elements of the algorithms, which are run for all possible sets of overlapping 4×4 trigger tower windows.

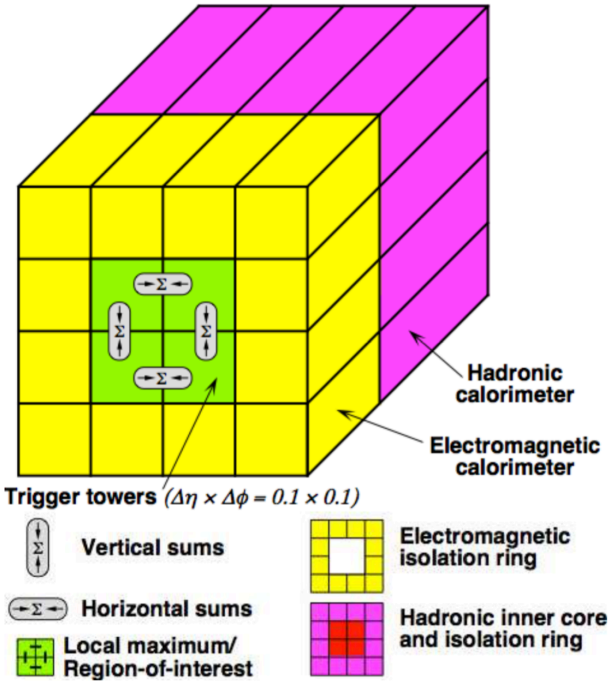

Figure 38.: Elements used for the e/γ and τ algorithms in CPMs. Consider the 2×2 trigger tower region at the centre of the 4×4 trigger tower window: in the EM calorimeter E_T values are summed for the towers in each of the four possible 1×2 and 2×1 pairs within the region, in order to find relatively narrow showers and the sum of the inner 2×2 region must be a local maximum compared to its eight overlapping nearest neighbours [69].

4.2.2 *Simulation and optimisation of the parameters for the L1Calo Simulation*

To simulate the L1Calo hardware the following procedure was implemented. It is performed in two steps:

1. trigger tower simulation
2. TOBs simulation

which allow to reprocess trigger towers varying the noise cuts and to reprocess TOBs changing the isolation cuts on CPMs.

Concerning the trigger tower simulation, the detailed procedure is the following:

1. access the database (DB): the initialisation uses COOL-derived values (COOL is the ATLAS-wide conditions database, also the acronym for: Condition Objects for LHC computing grid);
2. retrieve the database containers and remove dead or disabled channels;
3. get input trigger towers from input collection and copy ADC digits into a digit vector for reprocessing, with suitable granularity for the different $|\eta|$ regions listed in Table 5;
4. emulate finite-impulse-response (FIR) filter, bunch-crossing identification (BCID) and look up tables (LUT), and create and fill reprocessed trigger towers.

Since the calorimeter trigger tower pulses have rise times of the order of 50 ns and the LHC sampling rate is 40 MHz, i.e. 25 ns, there are several bunch-crossings in the width of a pulse. Hence it is of the utmost importance to find a robust way to associate trigger tower signals with the correct LHC bunch-crossing. The main method, used for normal unsaturated signals, is a digital pipelined finite-impulse-response (FIR) filter (see Figure 39).

These filters are used to sharpen the pulse before putting it through a peak finder. This is done by multiplying five consecutive samples by pre-defined coefficients and summing the resulting values. The coefficients are optimised for the pulse shape in each type of calorimeter. The FIR output results in $\sum_{i=1}^{5} a_i x_i$, where a_i are the coefficients expressed in 4 bits format, x_i are the values sampled by flash ADCs that digitise the pulses to 10-bit resolution, so the sum results in $\simeq$ 15 bits format. The peak finder then compares the sum with the values from the previous and following bunch-crossings, and looks for a maximum. When a peak is found the LUT is used to convert the output of FIR filtering into a transverse energy. There is a linear relation between the peaks and the signal energy and the LUT provides the calibration curve which is configured by two parameters:

- the slope;
- the offset where we can subtract the effect of pedestal and implement noise threshold.

Hence in the LUT simulation it is possible to implement the relative changes in the noise cuts for both the cluster and jet energy processor and then analyse the impact of these different noise cuts on the final efficiency and rates. Finally, the reprocessed trigger towers are stored in the so-called Trigger Elements (TEs), which represent a trigger-relevant object in the event.

To simulate TOBs, three further steps are required:

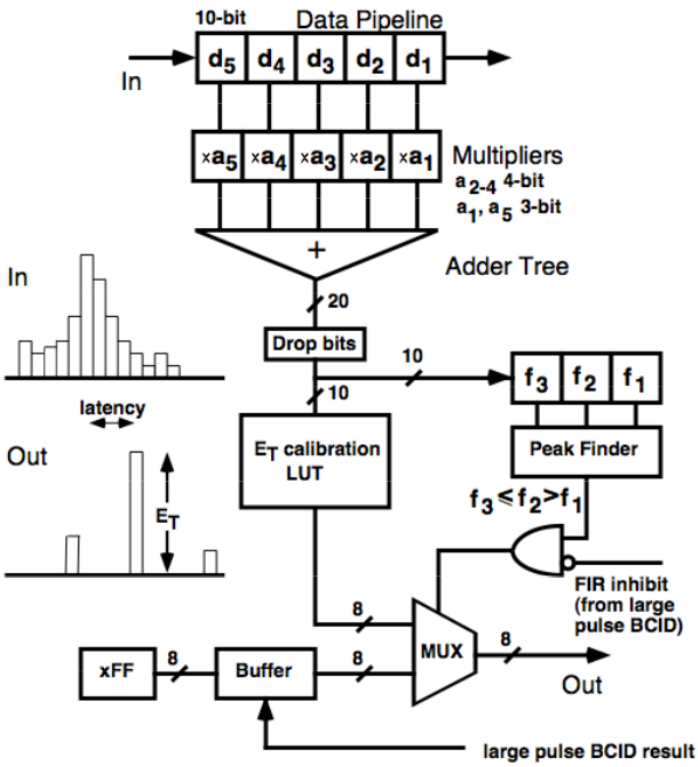

Figure 39.: Finite-impulse-response filter for identifying the bunch-crossing. A typical input pulse and resulting output are shown [69].

- receive trigger towers from TEs;
- form CPM Towers from trigger towers;
- store CPM Towers in the TEs.

A DataVector of CPMTowers is filled using a user-supplied vector of trigger towers, looping through all trigger towers present and adding their transverse energy and angular parameters values to CPMTowers. With these information the CPMs will be able to carry out the e/γ and τ algorithms and to count the multiplicity of successes, or hits, in the region covered by each module.

The optimisation of the parameters for the L1Calo Simulation required the implementation of an algorithm able to

- change noise cuts in trigger tower reprocessing, returning a linear LUT function;
- change isolation cuts in CPM reprocessing.

4.3 DATA SELECTION

Separate samples were used for the determination of trigger efficiencies and trigger rates. Both data samples contained events recorded by ATLAS in 2016. For efficiency calculations a data file called "L1CALO1 DxAOD" was utilised, whereas an enhanced minimum bias sample was utilised for the study of trigger rates. Full sample lists can be found in Appendix A.1.

4.3.1 *Electron-sample selection*

An electron sample is obtained via a $Z \to ee$ "tag and probe" analysis on data collected by the ATLAS experiment during 2016 and corresponding to an integrated luminosity of $1\,\mathrm{pb}^{-1}$: one electron is tagged with tight identification selections, the di-electron invariant mass is required to be consistent with the Z mass and a loose selection is applied to the second electron which is used for efficiency studies.

The selected events are required to have a di-electron invariant mass between 66 GeV and 116 GeV (see Figure 40). A requirement of at least one primary vertex is applied to each event, along with standard calorimeter cleaning at the calibration stage (for the terminology explanation refer to Chapter 5). To ensure a high level of data quality, events are required to originate from runs present in the Good Runs List (GRL).

The tag electron selection criteria follow (see Table 6):

- a logic OR among three separate HLT trigger requirements is applied to the tag electron;
- kinematic constraints on transverse momentum and pseudorapidity;
- the tag electron identification is performed applying Log Likelihood (LLH) and requiring a tight selection;
- tight isolation requirements are applied to the tag electron;
- match the tag electron to a fired trigger.

On the other hand, the probe electron has to satisfy the requirements (see Table 7):

- selected probe electrons are limited to the kinematic region: p_{T} greater than 7 GeV and a detector region with $|\eta| < 2.47$, the crack region of the electromagnetic calorimeter is excluded;
- the probe electron identification is performed applying Loose Likelihood (LLH) and requiring a medium selection;
- loose isolation requirements are applied to the probe electron;
- no trigger matching is required for the probe electron.

In combination these cuts assure a very good purity for the Z sample, with no background subtraction.

Selection	Requirement
HLT	HLT_e26_lhtight_nodo_ivarloose
	HLT_e60_lhmedium_nodo
	HLT_e140_lhloose_nodo
p_{T}	$p_{\mathrm{T}}^{e} > 27$ GeV
$\lvert\eta\rvert$	$\lvert\eta^{e}\rvert < 2.47$
	$(1.37 < \lvert\eta^{e}\rvert < 1.52$ excluded)
Identification	LooseLikelihood (LLH) Tight
Isolation	Tight
Trigger Matching	Required

Table 6.: Tag electron selection applied by the $Z \to ee$ Selector package. The superscript e refers to a quantity possessed by an electron.

Selection	Requirement
p_{T}	$p_{\mathrm{T}}^{e} > 7$ GeV
$\lvert\eta\rvert$	$\lvert\eta^{e}\rvert < 2.47$
	$(1.37 < \lvert\eta^{e}\rvert < 1.52$ excluded)
Identification	LooseLikelihood (LLH) Medium
Isolation	Loose
Trigger Matching	Not Required

Table 7.: Probe electron selection applied by the $Z \to ee$ Selector package. The superscript e refers to a quantity possessed by an electron.

From the selected di-electron events, a series of control plots were produced, shown in Figures 40 to 42. In all cases, the distributions present no anomalies and match well to expectation, suggesting that the obtained $Z \to ee$ sample obtained have sufficient purity (the background over signal ratio is less than 1%) to be used for trigger efficiency studies.

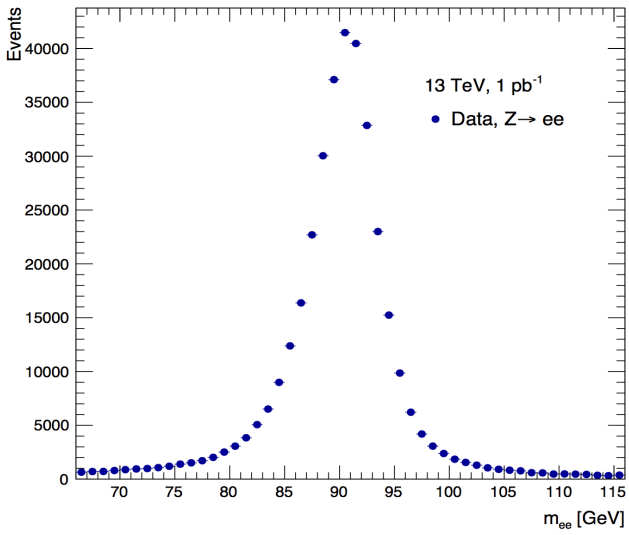

Figure 40.: Reconstructed invariant mass of the di-electron system, obtained from the $Z \to ee$ sample in 2016 data.

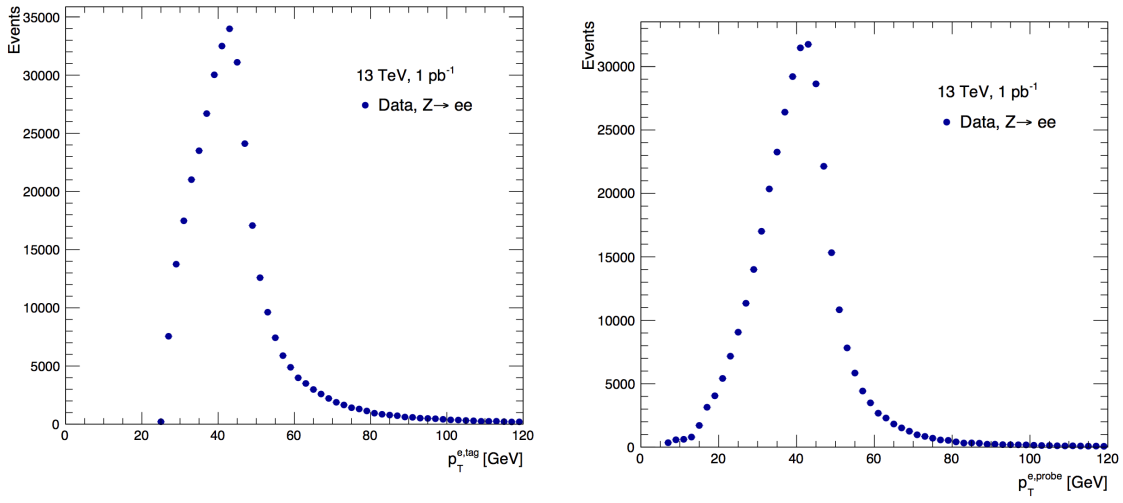

Figure 41.: p_{T}^{e} distributions for tag (left) and probe (right) electrons, obtained from the $Z \to ee$ sample in 2016 data.

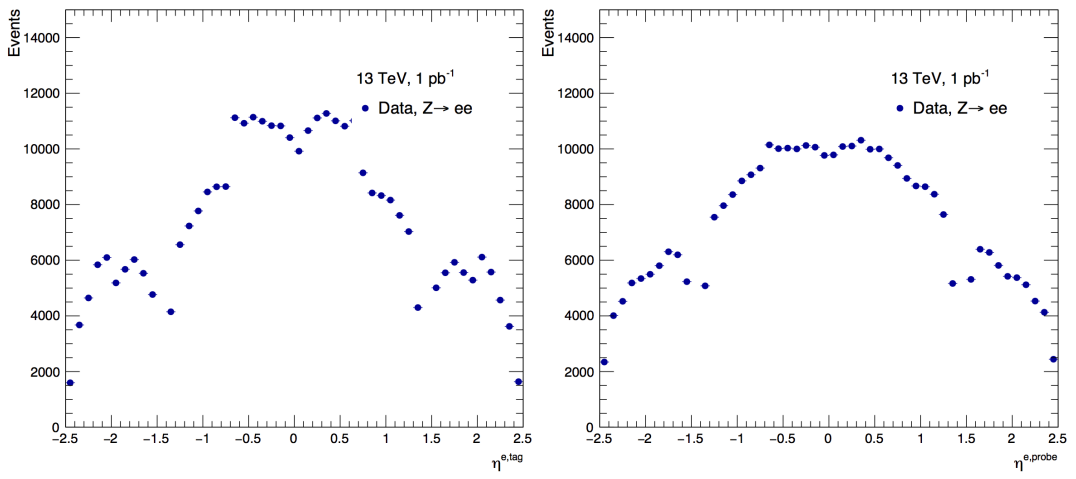

Figure 42.: η^e distributions for tag (left) and probe (right) electrons, obtained from the $Z \rightarrow ee$ sample in 2016 data.

Efficiency Calculation

Given the reconstruction of a tag electron, the efficiency of reconstructing a probe electron (as described in Table 7) can be measured in the $Z \rightarrow ee$ sample described above. The aim is measuring the trigger efficiency using the offline probe electron matched to a L1 TOB. The Trigger Object is associated to the probe electron requiring an angular matching. The complete selection on the associated TOBs is as follows:

- the angular separation between the TOB and the probe electron is required to be:
$$\Delta R = \sqrt{\Delta\phi^2_{e,TOB} + \Delta\eta^2_{e,TOB}} < 0.15 \quad (45)$$
where $\Delta\eta$ and $\Delta\phi$ are the differences between the TOB and probe electron in pseudorapidity and azimuthal angle respectively;
- the TOB must be reconstructed in a RoI of dimension $\Delta\eta \times \Delta\phi = 0.4 \times 0.4$. Most of the energy from an electron or photon is deposited in the second layer of the EM calorimeter and this corresponds to choosing a RoI type = 1;
- one of the trigger selections of interest listed below must be passed:
  1. EM15;
  2. EM15HI;
  3. EM20VHI;
  4. EM22VHI;
  5. EM24VHI;

where EM refers to the EM calorimeter, the number after the EM tag refers to the minimum transverse energy requirement (in GeV). The series of letters following that refers to different types and levels of isolation: 'I' refers to the EM ring isolation applied, where the EM energy is within an isolation ring surrounding the core 2×2 trigger towers; 'H' refers to the hadronic core isolation applied (E_{T}-dependent, no isolation for L1 $E_{\mathrm{T}} > 50\,\mathrm{GeV}$). Finally 'V' refers to η-dependent trigger energy threshold applied which follows the variation in η of the energy response (within $+2$ GeV to -3 GeV of the nominal threshold).

The electron efficiencies ε are obtained by considering the number of probe electrons associated to a TOB as defined above over the total number of probe electrons:

$$\varepsilon = \frac{\mathrm{N}\,(\text{Trigger Selection \&\& } \Delta R)}{\mathrm{N}\,(\text{all probe electrons})}. \tag{46}$$

Efficiencies can also be evaluated as a function of probe-electron p_{T}^{e} and η^{e}.

4.3.2 *Enhanced minimum-bias selection*

In order to assess the performance of the trigger system, a sample as much as possible representative of the LHC collisions is used. Since the majority of events coming from pp collisions at LHC consist of low p_{T} events (minimum bias events), trigger rate estimations are better performed with enhanced minimum bias samples. The aim is to get the best efficiency on signal keeping the overall rate as low as possible.

The "enhanced bias" events are processed using a simple selection. Each TOB is required to be reconstructed within a suitable RoI of the detector, *i.e.* in a RoI located in the first layer of the EM calorimeter. Then the trigger threshold lists are analysed and, if at least one TOB of the event passes a given threshold, the event is considered triggered by that trigger label.

The trigger threshold list used is the same as in 4.3.1: EM15, EM15HI, EM20VHI, EM22VHI and EM24VHI. All the events passing these triggers of interest are entered into the rate calculation. An effective trigger rate is defined as the number of events accepted by a specific trigger over the total number of events in the sample passing the simple RoI selection. Events from the "enhanced bias" sample have specific "enhanced bias" weights that factorise away the "enhanced" selection and correct effective rates to what is expected in "regular" data.

4.4 SIMULATION BIAS

As outlined in Section 4.2, a reprocessing procedure was implemented. The reprocessing procedure is performed in two steps: first simulate the creation of trigger towers and then simulate the processors. The aim here is to investigate how closely it is possible to simulate the online chain via an offline analysis, comparing the default objects and quantities with the reprocessed ones. This is aimed at giving us confidence in our procedure. However the studies of the parameter optimisation is done comparing exclusively the reprocessed objects and quantities obtained with the default parameters or with the changed settings. This procedure factorises away any reprocessing bias that is found in the following.

The comparison of the hardware response versus the offline hardware simulation is shown at various stages. There are two reprocessing steps: the first one creates the reprocessed trigger towers and the second one creates the modified processors. Finally it is possible to check the whole two-step procedure comparing the original TOBs with the ones generated by both the reprocessing steps.

The results show some bias in the simulation. However, as already stated, it does not affect the efficiency studies because reprocessed events are consistently used, factorising it out.

4.4.1 *Trigger tower and processor biases*

The first step considers the generation of the trigger towers within the reprocessing framework. A first check about the multiplicity of the trigger towers after this stage is shown in Figure 43. The top plot in figure 43 shows the multiplicity as it is obtained after the first reprocessing step while the bottom plots show the multiplicities in case of a minimum requirement on the transverse energy ($E_T > 0$) in the CP or in the JEP.

The second stage of reprocessing deals with processors: to check this step, we input the original non-reprocessed trigger towers (labelled here default trigger towers) and we obtain the reprocessed TOBs from the modified processors.

Figure 44 shows the transverse electromagnetic energy collected in the CPM in both linear (left) and logarithmic (right) scale, in order to show in detail both ends of the value range. The default TOBs are compared to the reprocessed ones obtained using the default trigger towers. Figure 45 shows the transverse hadronic energy collected in the jet energy processor, again in both linear (left) and logarithmic (right) scale. In both CP and JEP E_T plots, we have a non negligible bias due to the reprocessing, but we notice that this bias decreases for higher energies. Dashed lines in Figures 44 and 45 highlight the transverse energy region corresponding to the first EM threshold (15 GeV) that we apply in our efficiency and rate selections:

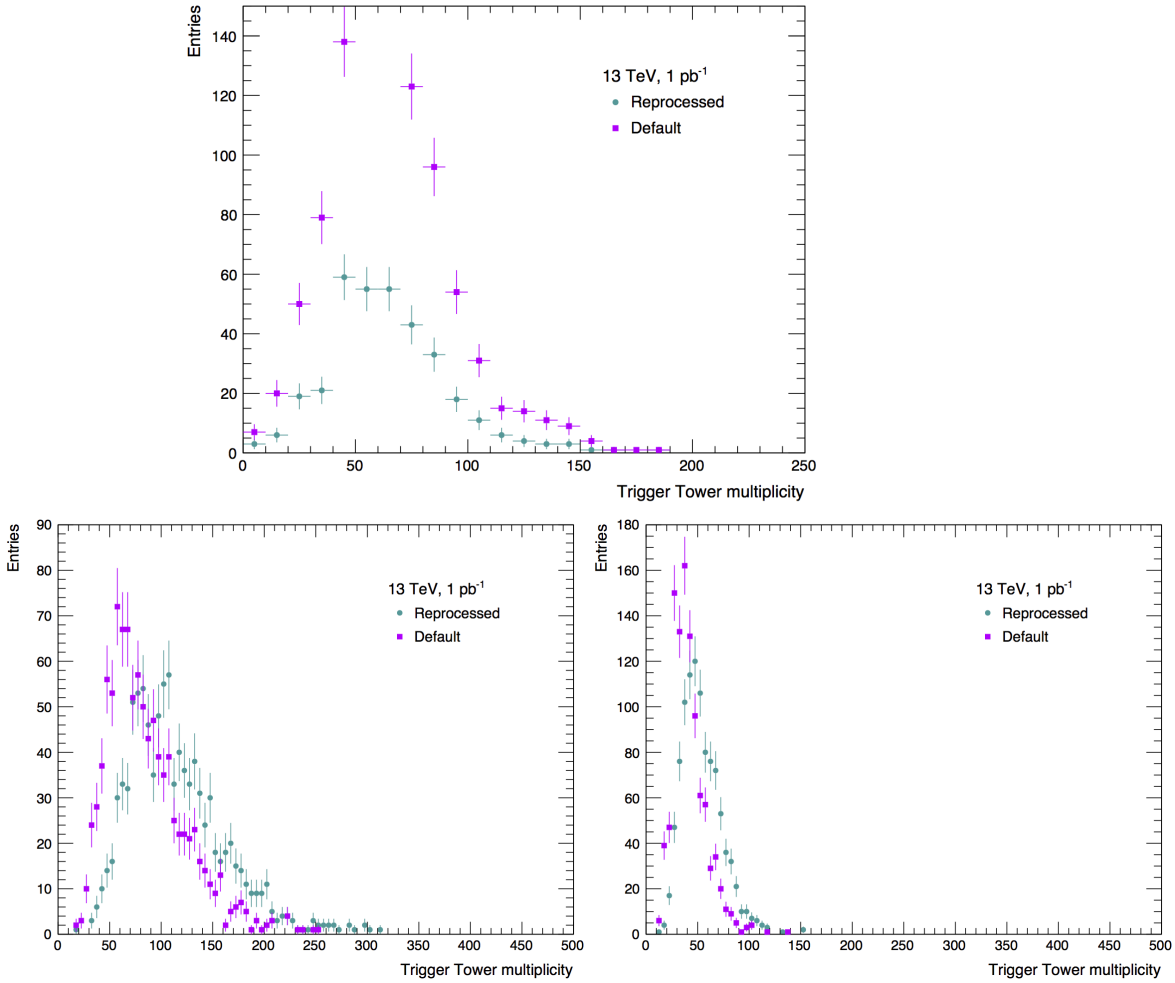

Figure 43.: Multiplicities for default and reprocessed trigger towers as it comes out of the first reprocessing step (top plot) and in case of a minimum requirement on the transverse energy ($E_T > 0$) in the CP (bottom-left) or in the JEP (bottom-right).

above this threshold the bias value is negligible, as shown in the log-scale plots in Figures 44 and 45.

4.4.2 *Full reprocessing bias*

Figure 46 shows the results of the total reprocessing procedure in TOB electromagnetic transverse energy and multiplicity. Here the reprocessed objects come from the reprocessing of both the trigger towers and the processors.

These reprocessed TOBs are used also to check the trigger efficiency (see equations 45 and 46) evaluated on the tag and probe sample. The trigger efficiency for the default and the reprocessed TOBs are evaluated versus the probe electron trans-

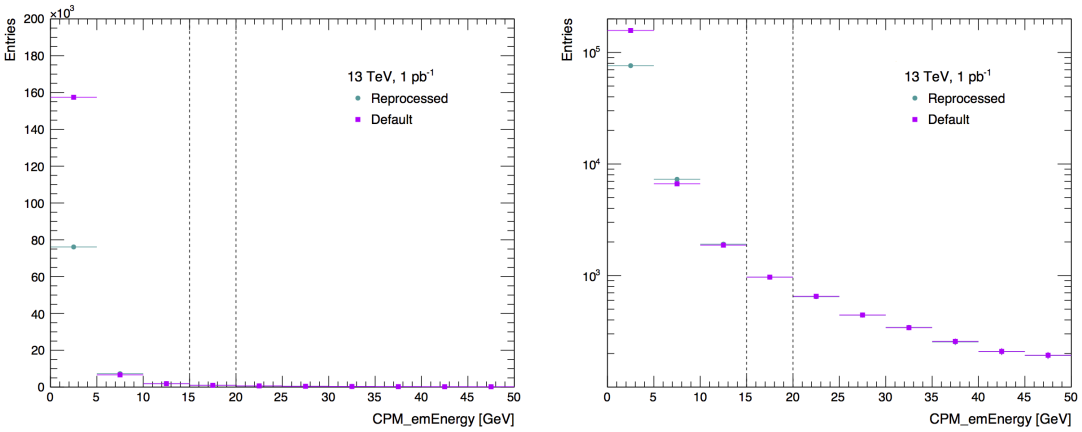

Figure 44.: Default and reprocessed CPM electromagnetic energy in linear (left) and logarithmic (right) scale. Here the reprocessed objects are obtained using the default trigger towers and applying only the second reprocessing step (modified processors).

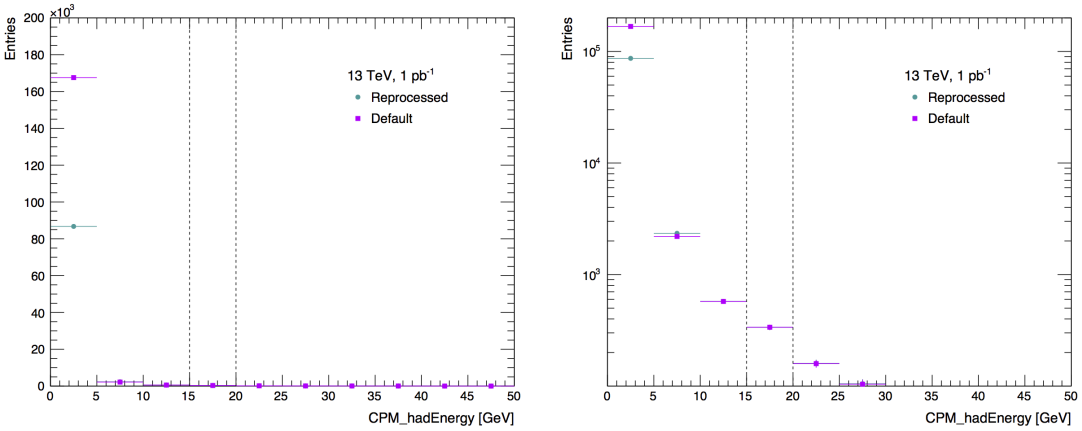

Figure 45.: Default and reprocessed CPM hadronic energy in linear (left) and logarithmic (right) scale. Here the reprocessed objects are obtained using the default trigger towers and applying only the second reprocessing step (modified processors).

verse momentum (Figure 47) and versus its η (Figure 48) from events selected with the various trigger selections listed in Section 4.3.1.

The full simulation bias is negligible in all trigger selections. This agrees with what observed in the previous section where it was shown that the bias in the different stages decreases consistently at energy values higher than the lower threshold adopted in the efficiency calculation.

However considering the efficiency versus η, two bins in the η central region show a significant deviation between the hardware and the simulation results. This happens consistently in all the considered trigger selections.

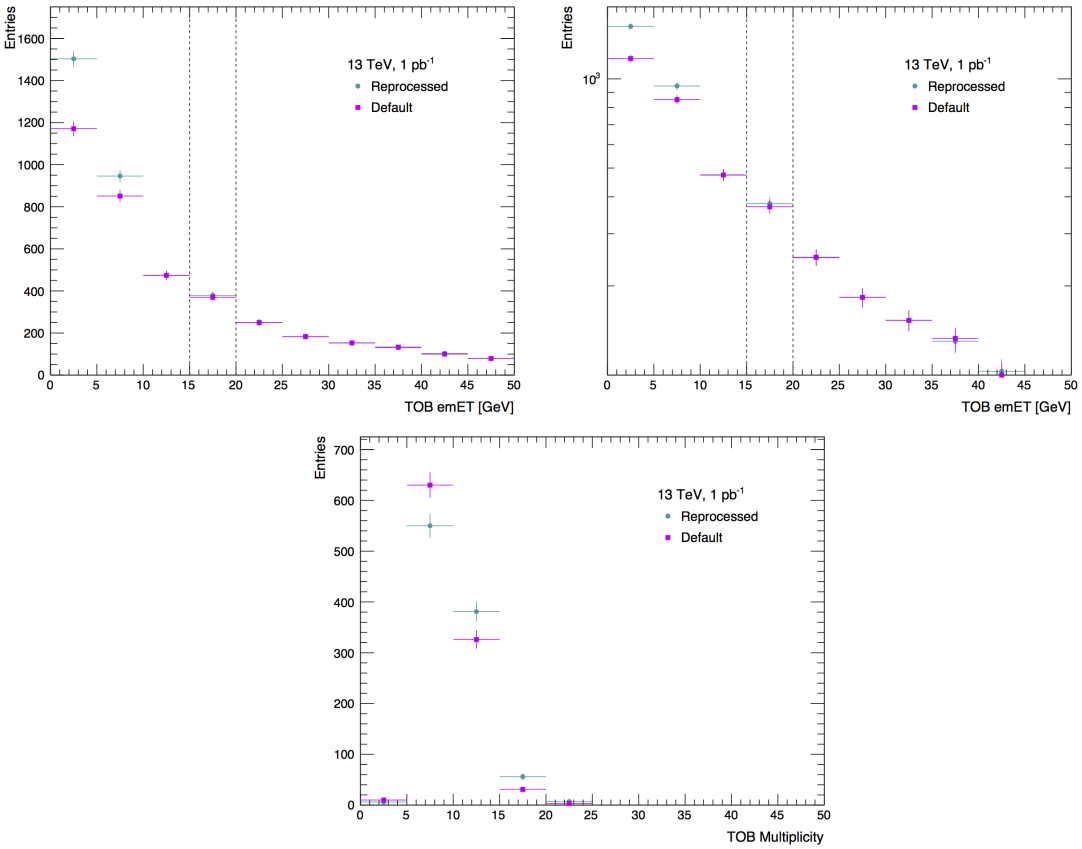

Figure 46.: Default and reprocessed TOB electromagnetic transverse energy in linear (up left) and logarithmic (up right) scale and TOB multiplicity (bottom). Here the reprocessed objects are obtained using the total reprocessing procedure.

Finally, an effective trigger rate calculation is performed for each trigger threshold for both the default and fully reprocessed TOBs: this is shown in Figure 49. The enhanced bias weights are not being applied to these rate calculations.

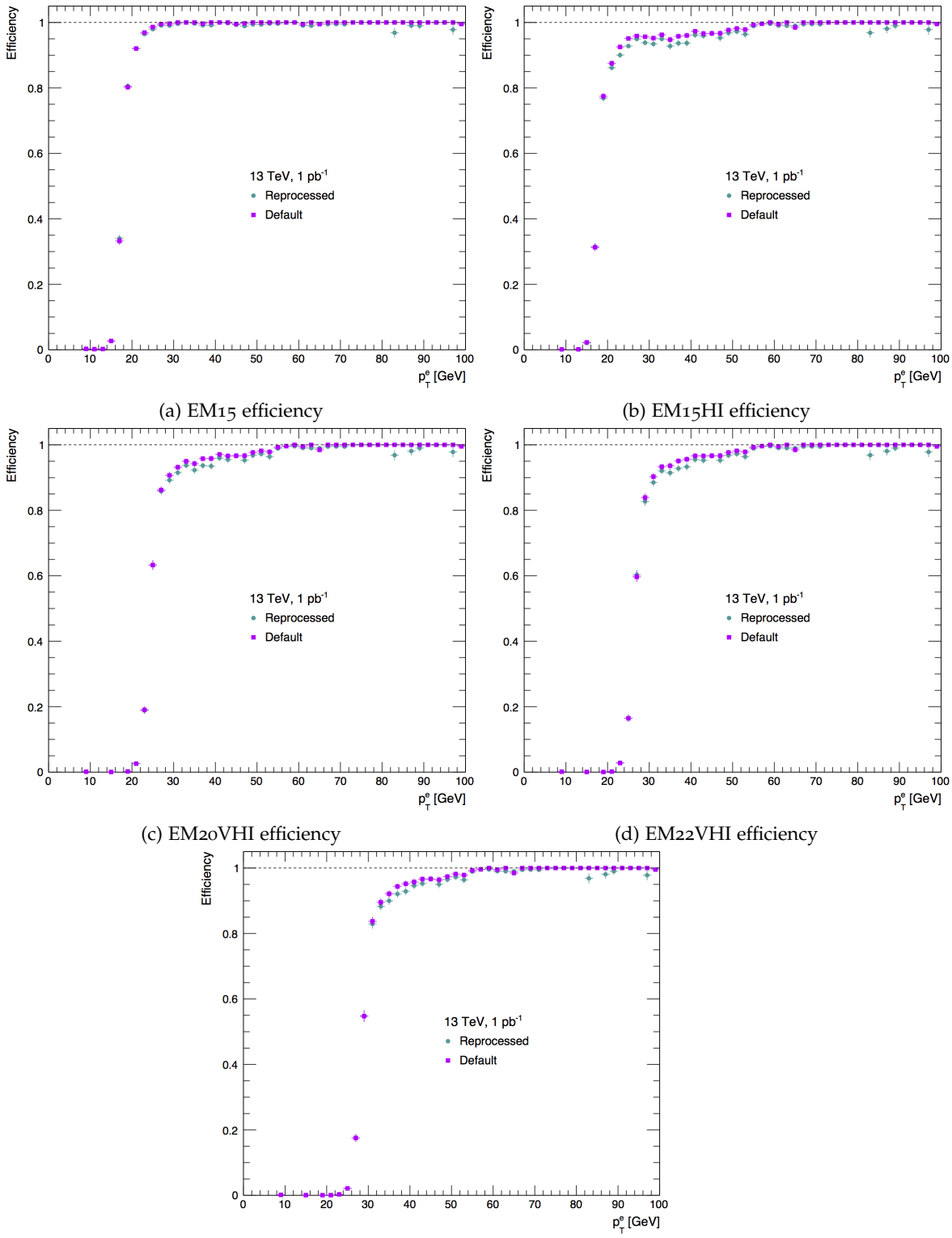

(a) EM15 efficiency

(b) EM15HI efficiency

(c) EM20VHI efficiency

(d) EM22VHI efficiency

(e) EM24VHI efficiency

Figure 47.: Trigger efficiencies for both default and reprocessed TOBs, as a function of the offline reconstructed probe electron p_{T}^{e} in the various trigger selections considered.

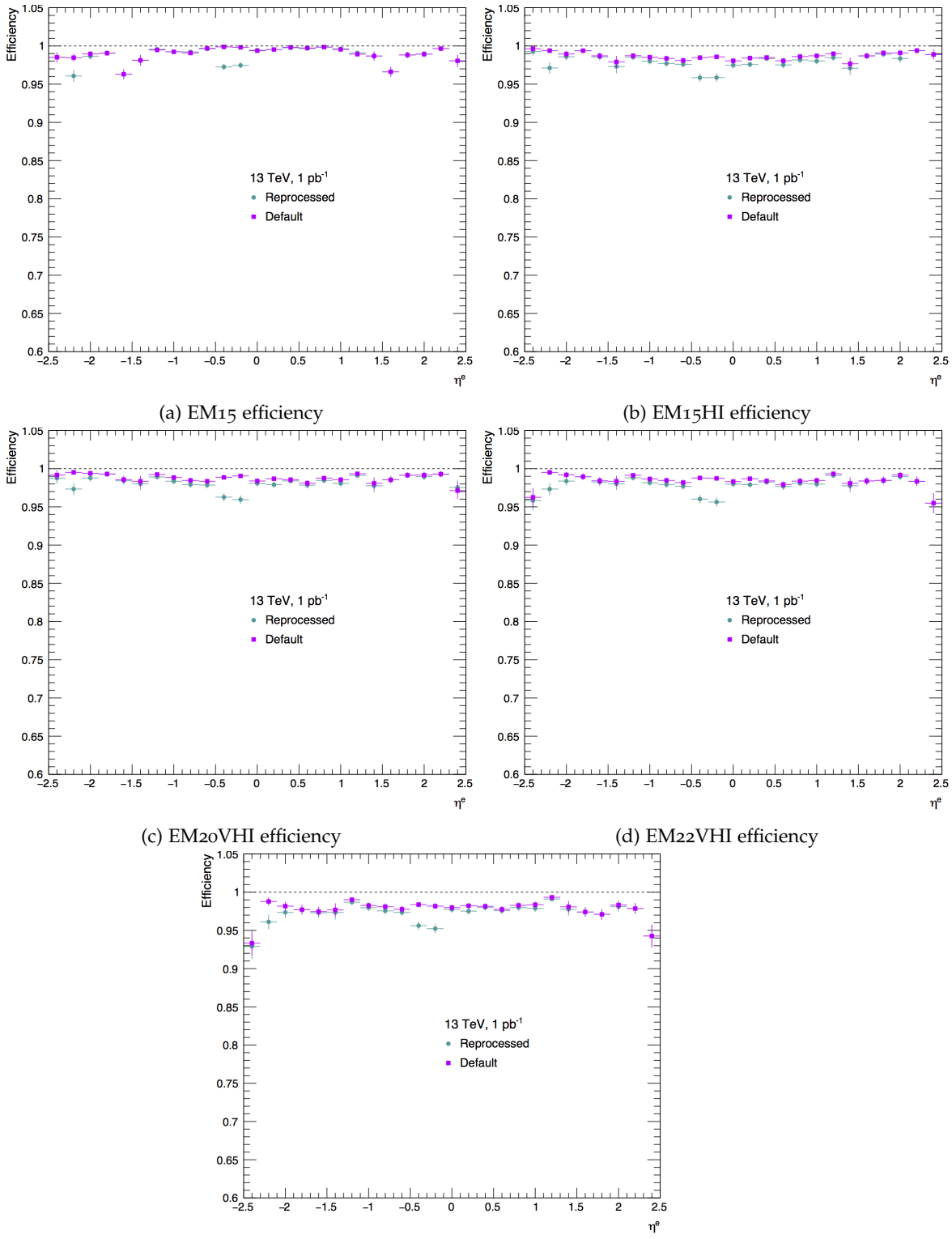

(a) EM15 efficiency

(b) EM15HI efficiency

(c) EM20VHI efficiency

(d) EM22VHI efficiency

(e) EM24VHI efficiency

Figure 48.: Trigger efficiencies for both default and reprocessed TOBs, as a function of the offline reconstructed probe electron η^e in the various trigger selections considered.

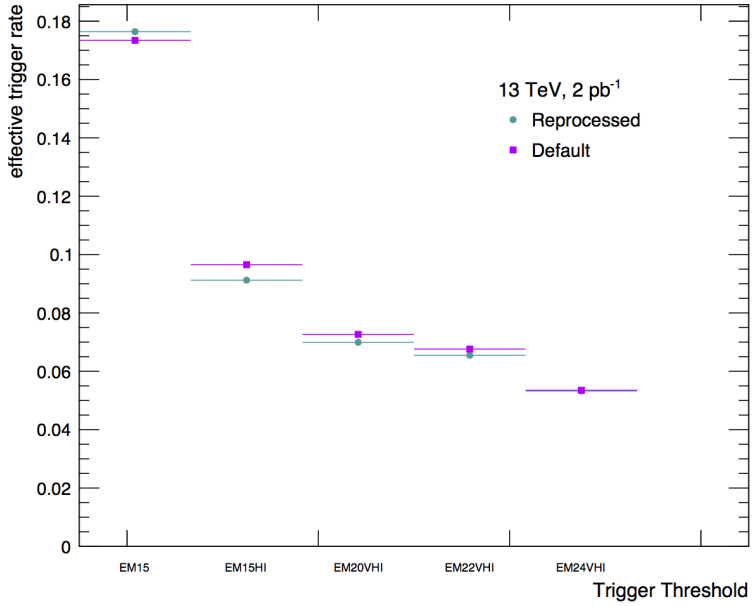

Figure 49.: Effective trigger rates for default and reprocessed TOBs (values reported in percentage), as a function of the various trigger thresholds considered. The enhanced bias weights are not being applied here.

4.5 NOISE SELECTION OPTIMISATION

Results from the optimisation of the noise selection are shown and summarised in this section. Noise cuts are applied in EM isolation rings, and for example the noise cut value $4.0k$ corresponds to 2 GeV. The goal of this study is to find optimal noise cut values to improve the efficiency while keeping the rate low. The efficiency as a function of offline reconstructed probe electrons p_{T}^{e} and η^{e} are shown for different noise cut values in the various trigger selections considered. The corresponding effective trigger rates are also obtained.

A first investigation involves a wide range of possible noise cuts around the current default one that corresponds to a $4.0k$ cut value: a check is performed from $2.0k$ to $8.0k$, in $2.0k$ steps. Figure 50 shows the efficiency as a function of the offline probe electron p_{T}^{e} for the different trigger thresholds and applying the different noise cuts. Reducing the value of the noise cut leads to higher LUT values in the isolation ring, while increasing noise cut value leads to lower LUT values in the isolation ring (see the last paragraph in 4.2.2). Hence little effect on the efficiency is seen in the EM15 trigger selection as there is no requirement on isolation. However in all the trigger labels, the turn-on region results in different efficiency values for different noise cuts, as expected.

Figure 51 shows the efficiency as a function of the offline probe electron η^{e}: for these efficiency calculations, the numerator consists of only probe electrons passing a p_{T}^{e} cut that depends on the specific trigger threshold analysed (in order to remove the efficiency turn-on region). The following p_{T}^{e} cuts are used for the listed trigger thresholds:

1. EM15, $p_{\mathrm{T}} > 20\,\mathrm{GeV}$;
2. EM15HI, $p_{\mathrm{T}} > 20\,\mathrm{GeV}$;
3. EM20VHI, $p_{\mathrm{T}} > 25\,\mathrm{GeV}$;
4. EM22VHI, $p_{\mathrm{T}} > 27\,\mathrm{GeV}$;
5. EM24VHI, $p_{\mathrm{T}} > 29\,\mathrm{GeV}$.

In addition to efficiencies, the calculation of the effective trigger rates on the enhanced minimum bias sample is done. Figure 52 shows the rates for the different trigger thresholds and applying the different noise cuts.

The efficiencies are summarised in Table 8 where the total efficiencies are p_{T}^{e} and η^{e} integrated. Again the numerator consists only of probe electrons passing the above-mentioned p_{T}^{e} cut that depends on the specific trigger threshold analysed. Table 9 shows the variation of the trigger efficiencies with respect to the default ($4.0k$) noise cut: the efficiency variation is defined as

$$\Delta_{\mathrm{eff}} = \frac{\mathrm{test}_{\mathrm{eff}} - \mathrm{default}_{\mathrm{eff}}}{\mathrm{default}_{\mathrm{eff}}}$$

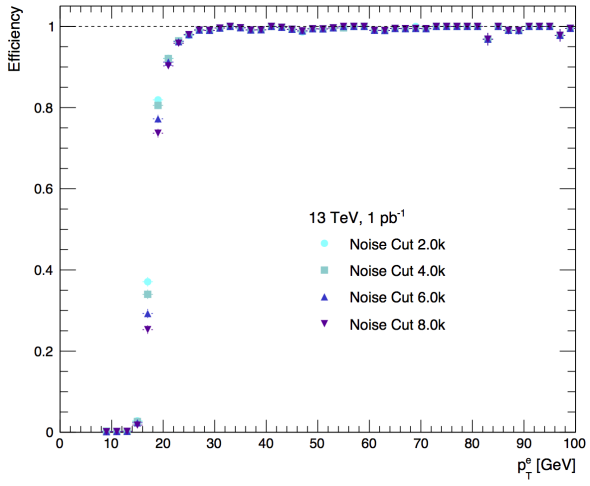

(a) EM15 efficiency

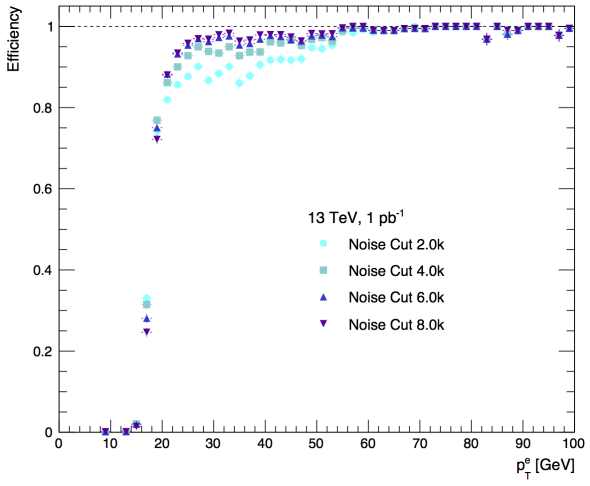

(b) EM15HI efficiency

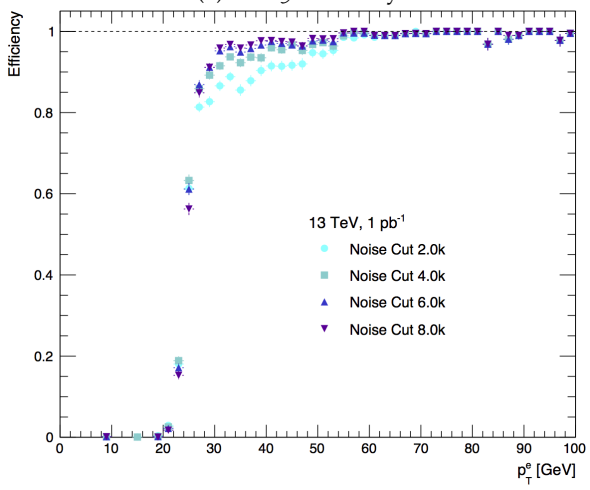

(c) EM20VHI efficiency

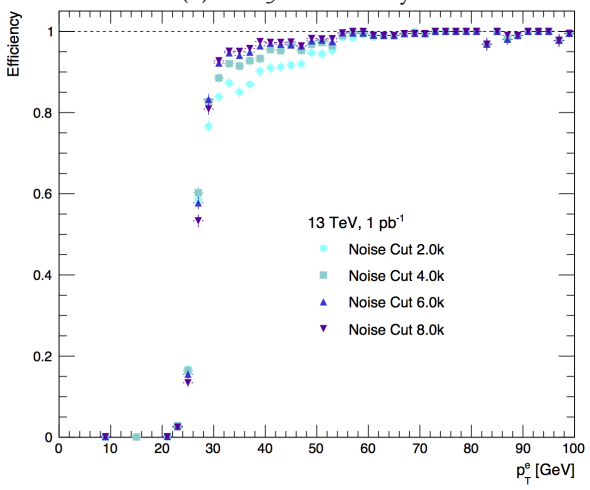

(d) EM22VHI efficiency

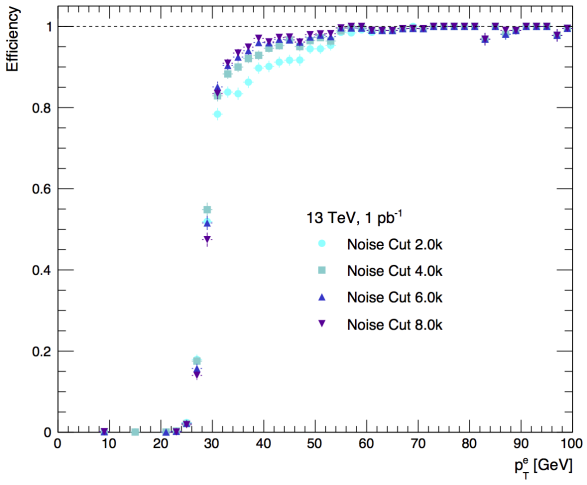

(e) EM24VHI efficiency

Figure 50.: Trigger efficiency for reprocessed TOBs as a function of the offline reconstructed probe electron p_{T}^{e} in the wide range of noise cuts.

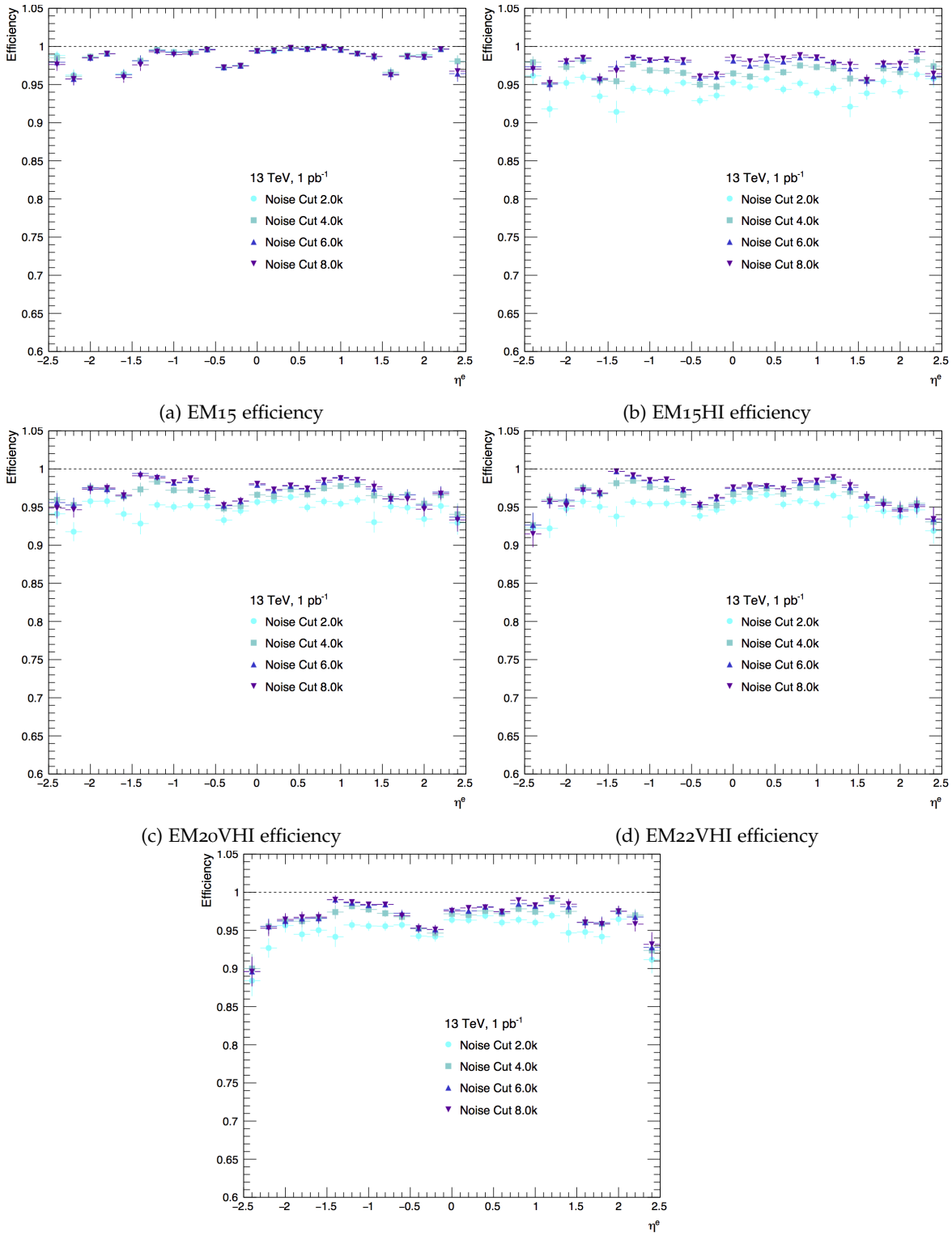

(a) EM15 efficiency

(b) EM15HI efficiency

(c) EM20VHI efficiency

(d) EM22VHI efficiency

(e) EM24VHI efficiency

Figure 51.: Trigger efficiencies for the reprocessed TOBs as a function of the offline reconstructed probe electron η^e in the wide range of noise cuts.

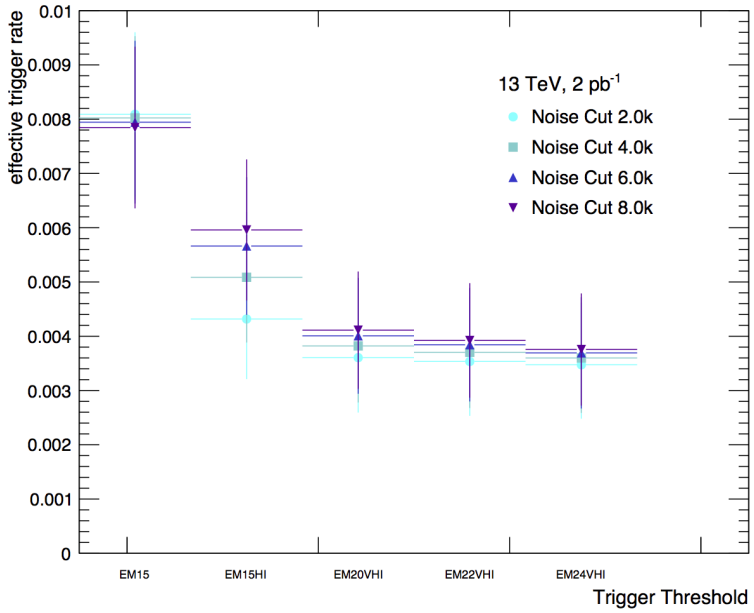

Figure 52.: Effective trigger rates (values in percentage) as a function of the analysed trigger thresholds in the wide range of noise cut values.

Table 8.: Trigger efficiency values as a function of the wide range of noise cut values. Efficiencies are calculated considering in the numerator only probe electrons passing a p_{T}^{e} cut that depends on the specific trigger threshold analysed (in order to remove the efficiency turn-on region). The values are given in percentage.

cut value	EM15	EM15HI	EM20VHI	EM22VHI	EM24VHI
2.0 k	99.28	95.44	95.60	95.61	92.65
4.0 k	99.28	97.34	97.27	97.27	93.20
6.0 k	99.28	98.16	97.93	97.93	94.81
8.0 k	99.26	98.42	98.12	97.12	94.99

Table 9.: Variation of the trigger efficiencies as a function of the wide range of noise cut values. The variation is evaluated as explained in the text with respect to the default (4.0*k*) noise cut shown in Table 8. Efficiencies are calculated considering in the numerator only probe electrons passing a p_{T}^{e} cut that depends on the specific trigger threshold analysed (in order to remove the efficiency turn-on region). The values are given in percentage.

cut value	EM15	EM15HI	EM20VHI	EM22VHI	EM24VHI
2.0 k	0	-1.95	-1.71	-1.71	-1.59
6.0 k	0	0.84	0.68	0.68	0.63
8.0 k	0.02	1.11	0.87	0.87	0.81

where $\text{default}_{\text{eff}}$ is the trigger efficiency calculated for the default 4.0k noise cut, while test_{eff} is the efficiency of the alternative noise cut being considered in the test. Since the aim is having the higher possible efficiency, the noise cut configurations giving a positive Δ_{eff} should be chosen.

The statistical uncertainty on the efficiencies is evaluated using the binomial distribution uncertainty:

$$\sigma_\epsilon = \sqrt{\frac{\epsilon(1-\epsilon)}{N_{\text{all probe electrons}}}}. \tag{47}$$

The obtained uncertainties on the efficiencies are in the range from 0.01% to 0.04%, hence the last significant digit of the values in the tables is the one affected by the statistical uncertainty.

Analogously the effective rates are summarised in Table 10 and the variation of such rates in Table 11. The rate variation is defined as

$$\Delta_{\text{rate}} = \frac{\text{default}_{\text{rate}} - \text{test}_{\text{rate}}}{\text{default}_{\text{rate}}}$$

where $\text{default}_{\text{rate}}$ is the effective trigger rate calculated for the default 4.0k noise cut, while $\text{test}_{\text{rate}}$ is the rate of the alternative noise cut being considered in the test. With the aim of having the lowest possible rates, the sign is inverted with respect to the efficiency variation: hence again noise cut configurations giving a positive Δ_{rate} should be considered.

Table 10.: Effective trigger rates as a function of the wide range of noise cut values. The values are given in percentage.

cut value	EM15	EM15HI	EM20VHI	EM22VHI	EM24VHI
2.0 k	0.81	0.43	0.36	0.35	0.35
4.0 k	0.80	0.49	0.38	0.37	0.36
6.0 k	0.79	0.57	0.40	0.38	0.37
8.0 k	0.78	0.59	0.41	0.40	0.38

Comparing the efficiency variations and the rate variations, the 2.0k noise cut results outside the zone of consideration as it corresponds to a loss in efficiency of more than 1%. Similarly the 8.0k noise cut corresponds to a significant increase in the rates hence it is not considered again.

Hence further studies are focused on a narrower range around the 4.0k default value and a finer step size: going from 3.0k to 5.0k, in 0.5k steps. Figure 53 shows the efficiency as a function of the offline probe electron p_{T}^{e} for the different trigger thresholds and applying the different noise cuts. Figure 54 shows the efficiency

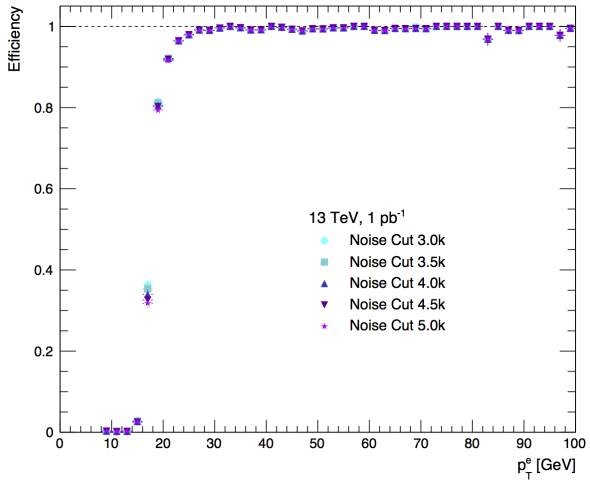

(a) EM15 efficiency

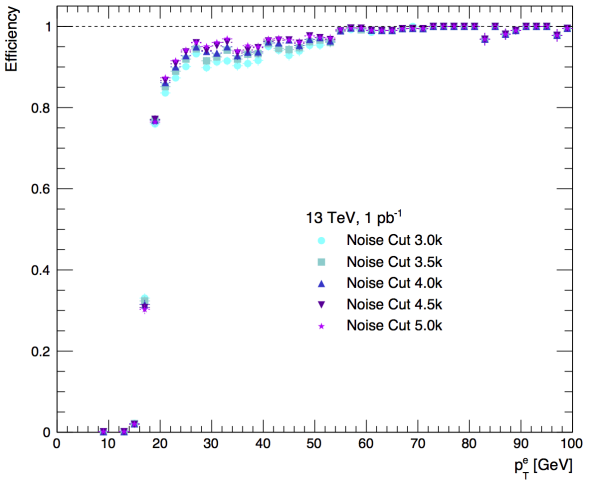

(b) EM15HI efficiency

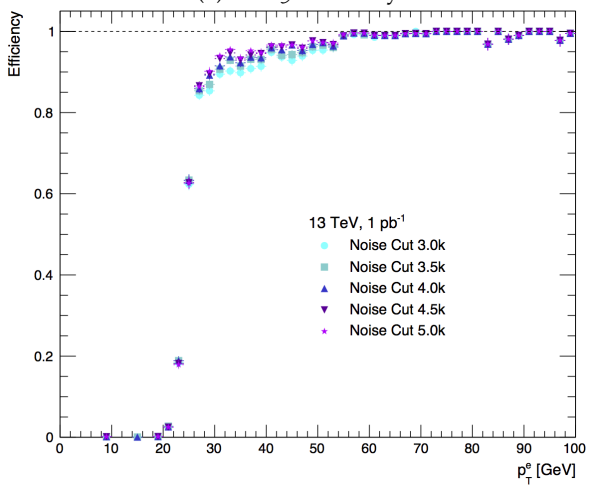

(c) EM20VHI efficiency

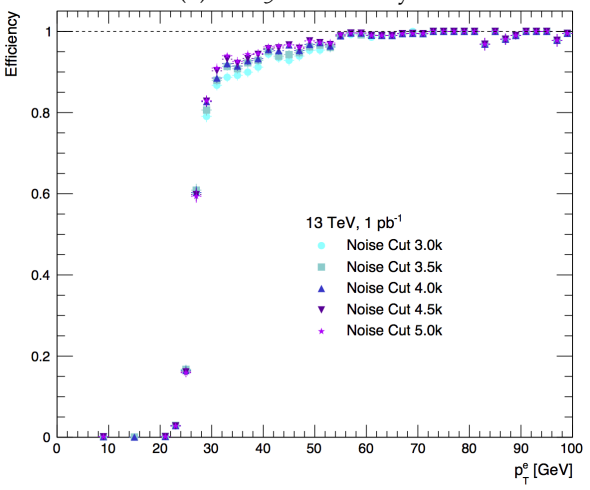

(d) EM22VHI efficiency

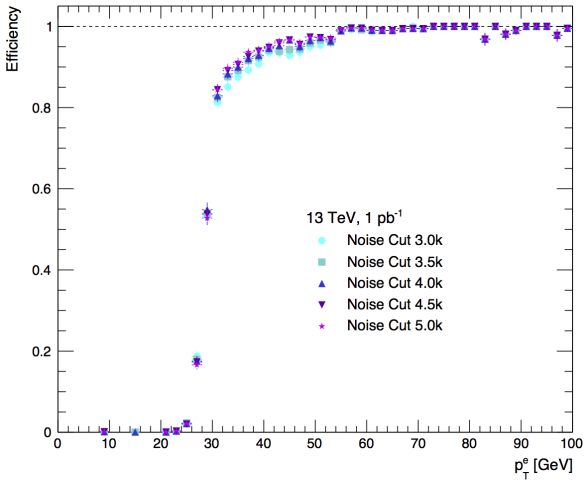

(e) EM24VHI efficiency

Figure 53.: Trigger efficiencies for reprocessed TOBs as a function of the offline reconstructed probe electron p_{T}^{e} in the narrow range of noise cuts.

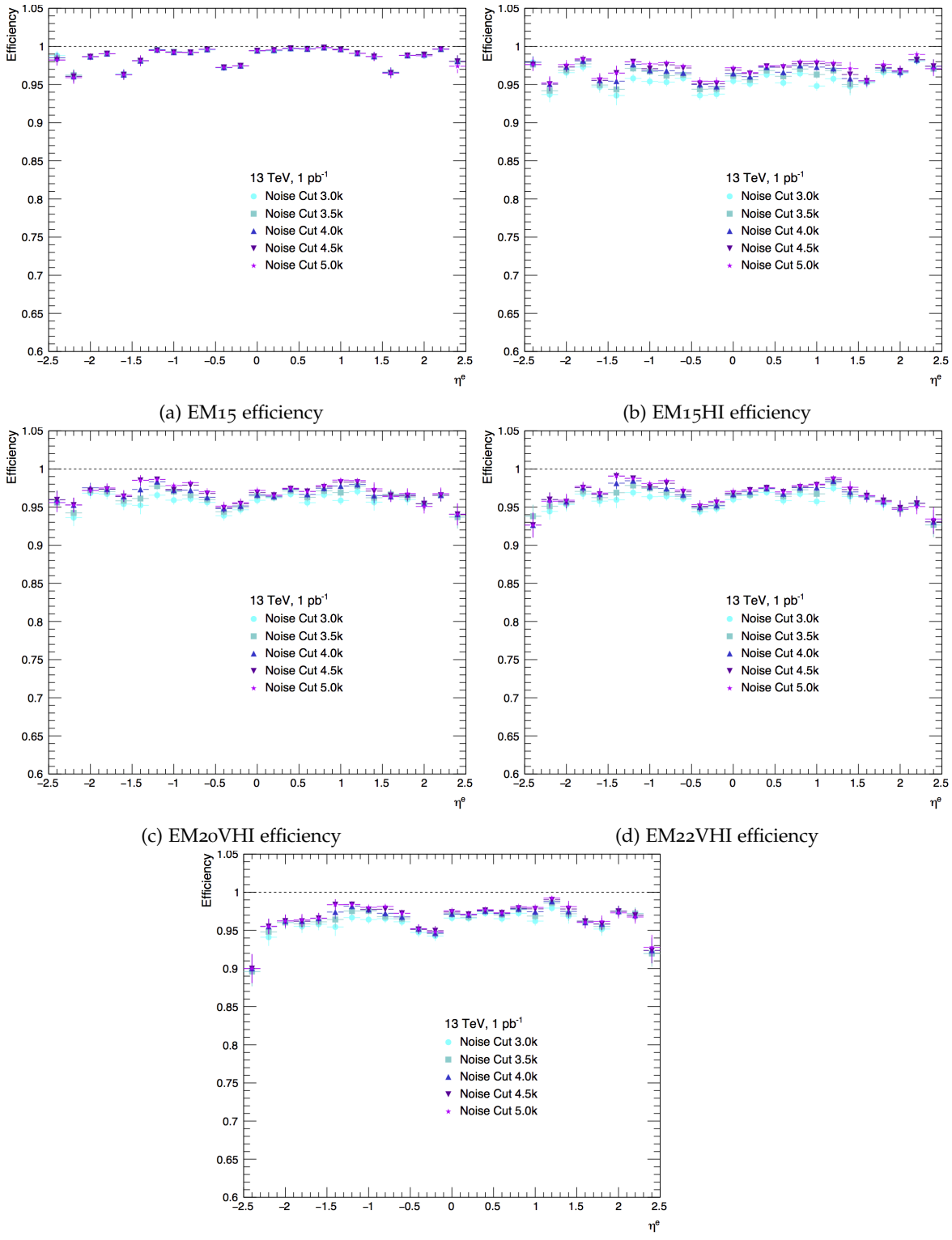

(a) EM15 efficiency

(b) EM15HI efficiency

(c) EM20VHI efficiency

(d) EM22VHI efficiency

(e) EM24VHI efficiency

Figure 54.: Trigger efficiencies for the reprocessed TOBs as a function of the offline reconstructed probe electron η^e in the narrow range of noise cuts.

Table 11.: Variation of the effective trigger rates as a function of the wide range of noise cut values. The variation is evaluated as explained in the text with respect to the default (4.0k) noise cut. The values are given in percentage.

cut value	EM15	EM15HI	EM20VHI	EM22VHI	EM24VHI
2.0 k	-0.83	15.11	5.64	4.55	3.47
6.0 k	0.97	-11.32	-4.87	-3.75	-2.59
8.0 k	2.20	-17.15	-7.62	-11.03	-4.34

as a function of the offline probe electron η^e: for these efficiency calculations, the numerator consists only of probe electrons passing the above-mentioned p_{T}^e cut that depends on the specific trigger threshold analysed. Also, the effective trigger rates on the enhanced minimum bias sample is calculated. Figure 55 shows the rates for the different trigger thresholds and applying the different noise cuts.

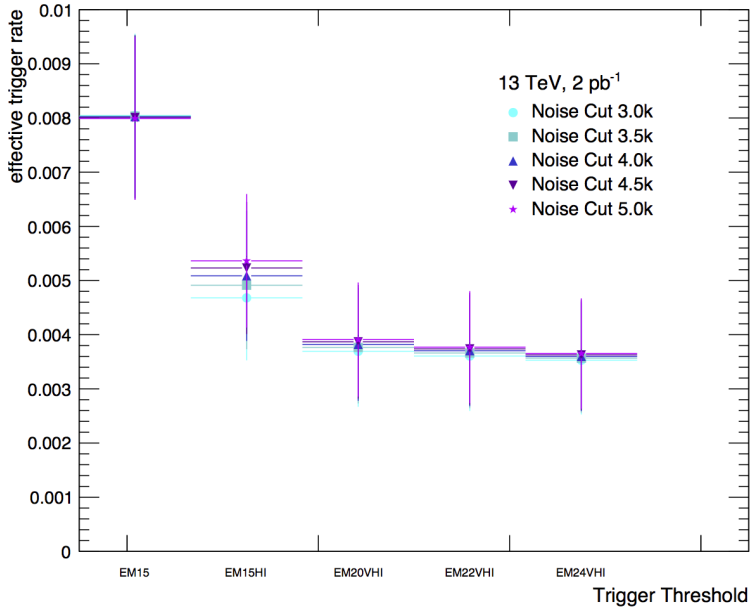

Figure 55.: Effective trigger rates (values in percentage) as a function of the analysed trigger thresholds in the narrow range of noise cut values.

Efficiencies are summarised in Table 12 where the total efficiencies are p_{T}^e and η^e integrated. Again the numerator is made of only probe electrons passing the trigger-dependent p_{T}^e cuts. Table 13 shows the variation of the trigger efficiencies with respect to the default (4.0k) noise cut with the efficiency variation defined above. Analogously the effective rates are summarised in Table 14 and the variation of such rates in Table 15.

Table 12.: Trigger efficiency values as a function of the narrow range of noise cut values. Efficiencies are calculated considering in the numerator only probe electrons passing a p_{T}^{e} cut that depends on the specific trigger threshold analysed (in order to remove the efficiency turn-on region). The values are given in percentage.

cut value	EM15	EM15HI	EM20VHI	EM22VHI	EM24VHI
3.0 k	99.28	96.35	96.43	96.40	93.27
3.5 k	99.28	96.94	96.92	96.87	93.70
4.0 k	99.28	97.33	97.27	97.20	93.96
4.5 k	99.28	97.61	97.50	97.41	94.12
5.0 k	99.28	97.81	97.65	97.57	94.18

Table 13.: Variation of the trigger efficiencies as a function of the narrow range of noise cut values. The variation is evaluated as explained in the text with respect to the default ($4.0k$) noise cut. Efficiencies are calculated considering in the numerator only probe electrons passing a p_{T}^{e} cut that depends on the specific trigger threshold analysed (in order to remove the efficiency turn-on region). The values are given in percentage.

cut value	EM15	EM15HI	EM20VHI	EM22VHI	EM24VHI
3.0 k	0	-1.01	-0.86	-0.82	-0.73
3.5 k	0	-0.69	-0.36	-0.34	-0.28
4.5 k	0	0.28	0.24	0.22	0.17
5.0 k	0	0.49	0.39	0.38	0.23

Table 14.: Effective trigger rates as a function of the narrow range of noise cut values. The values are given in percentage.

cut value	EM15	EM15HI	EM20VHI	EM22VHI	EM24VHI
3.0 k	0.80	0.47	0.37	0.36	0.35
3.5 k	0.80	0.49	0.38	0.37	0.36
4.0 k	0.80	0.51	0.38	0.37	0.36
4.5 k	0.80	0.52	0.39	0.37	0.36
5.0 k	0.80	0.54	0.39	0.38	0.35

Table 15.: Variation of the effective trigger rates as a function of the narrow range of noise cut values. The variation is evaluated as explained in the text with respect to the default (4.0*k*) noise cut. The values are given in percentage.

cut value	EM15	EM15HI	EM20VHI	EM22VHI	EM24VHI
3.0 k	0.00	7.84	2.63	2.70	2.78
3.5 k	0.00	3.92	0.00	0.00	0.00
4.5 k	0.00	-1.96	-2.63	0.00	0.00
5.0 k	0.00	-5.88	-2.63	-2.70	2.78

Considering the efficiency variations and the rate variations, a 3.5 k noise cut would correspond to a minimal loss in efficiency (less that 1%, the maximum tolerable drop in the efficiency is 5%), while not increasing the rates.

These results are obtained from noise cut studies only, but there is a correlation between noise cuts and isolation cuts so the QMUL group future plan foresee a two-variable study.

5

OBJECT RECONSTRUCTION IN ATLAS

The huge variety of physics processes produced by pp collisions at LHC require an excellent object reconstruction. Each particle traversing the ATLAS detector leaves an unique signature in the various detector sub-systems.
High-level objects, such as electron or muon candidates, are reconstructed from the digitised detector response through a process that is commonly referred to as object reconstruction.
This Chapter focuses on the reconstruction of the physics objects used in this analysis, such as vertices, electrons, muons, jets and neutrinos.
The objects definition changed going from Run-1 to Run-2 because of the luminosity increase and the ATLAS detector upgrade. The baseline description of the object reconstruction given in this Chapter is settled on the Run-2 definitions, however references to the Run-1 objects definition will be given, if appropriate. In this thesis, the Run-1 objects definition is used only for the calibration of the mistag rate of the momentum imbalance based soft muon tagger performed for the 8 TeV data set analysis, detailed in Chapter 6.

5.1 TRACKS AND VERTICES RECONSTRUCTION

In the ATLAS detector the reconstruction of the trajectories of charged particles, the measurement of their transverse momentum and impact parameters, and the determination of the position of the hard scatter interaction point is performed by the Inner Detector (ID), as described in Section 3.3.2.
Charged particles traversing the ID solenoidal magnetic field follow helicoidal trajectories that can be parametrised by the five parameter vector in formula 48:

$$\tau = \tau\left(d_0, z_0, \phi, \theta, q/p\right) \tag{48}$$

where d_0 is the transverse impact parameter and z_0 is the longitudinal impact parameter, defined respectively as the distance from the point of closest approach to the reconstructed position of the pp interaction vertex in the transverse plane and along the z axis. The ϕ is the azimuthal angle and θ is the polar angle, q/p is the ratio between the charge and the particle momentum and it defines the orientation and the curvature of the helix trajectory in the ID. Figure 56 shows a graphical view of the track parameters described above. Figure 57 shows the experimental

resolution on the d_0 and z_0 parameters in Run-1 and Run-2 (including the IBL detector).

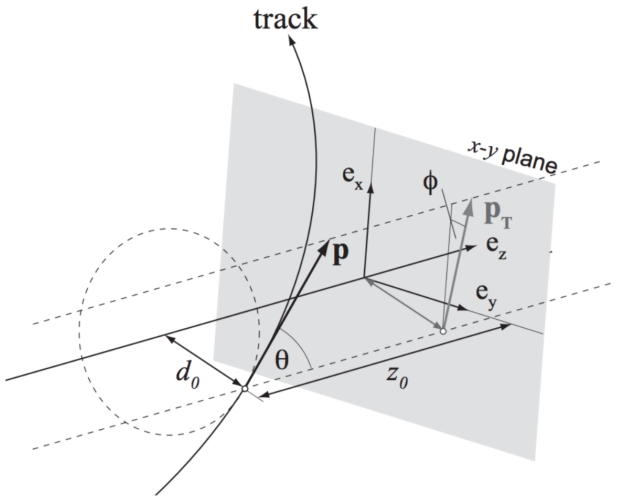

Figure 56.: Sketch of a charged particle trajectory in the ID with the representation of the track parameters considered [52].

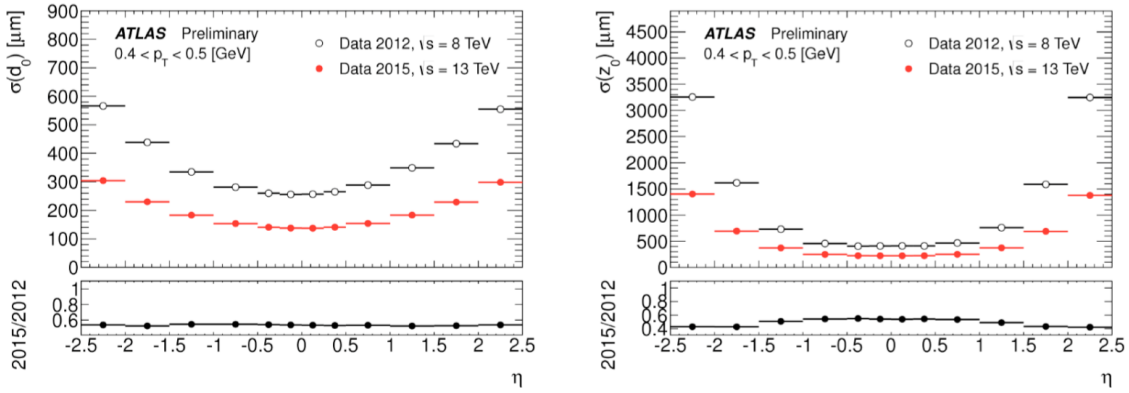

Figure 57.: Comparison between the experimental resolution on the impact parameters in 2012 (Run-1) and 2015 (Run-2) [70] [71].

The tracks associated to charged particles in the ID are reconstructed using a set of sequential algorithms [72]. The ATLAS ID tracking system covers two sequences: the primary inside-out track reconstruction and a consecutive outside-in tracking, with the goal of identifying and discriminating tracks originating from the proton-proton hard scatter (the so called primary tracks), from the decays of long-lived

particles (the so called secondary tracks) and from the interaction of particles with the material (the so called conversion tracks). Since secondary tracks have larger impact parameters with respect to the primary tracks, d_0 and z_0 are useful parameters to distinguish between prompt and non prompt leptons.
Primary tracks are required to have $p_T > 400\,\text{MeV}$ and to be reconstructed in the region $|\eta| < 2.5$, using an inside-out algorithm. Three-point seeds in the silicon detectors (Pixel and SCT) start the inside-out algorithm and moves away from the interaction point adding hits in a spatial window defined by the seed direction. A combinatorial, iterative algorithm called the Kalman filter [73] adds hits to the track candidate (or rejects them), based on projection of earlier measurements and the current measurement. At this stage, the filter creates multiple track candidates per seed if a cluster (*i.e.* an energy deposit) is shared by many tracks. These ambiguities in the track candidates are resolved using an appropriate track score definition which orders the tracks according to their individual scores: highest scores are assigned to the candidates that are more likely to correctly represent the trajectory of a charged primary particle. After that, tracks are extended into the TRT.
On the other hand, the outside-in tracking starts from segments reconstructed in the TRT and then adds information from the inwards detectors adding silicon hits to the track. this method is designed to reconstruct mainly secondary tracks.
Figure 58 shows the linear increase of the average number of reconstructed vertices as a function of the average number of bunch crossings per interaction μ. This means that in the dense LHC environment it is very challenging to distinguish between the pp interaction vertex (primary vertex) and pile-up vertices.

Reconstructed tracks are associated to a particular vertex candidate using a χ^2-based iterative vertex finding algorithm [74]. The primary vertex is defined as the reconstructed vertex with the largest associated transverse momentum: $\sum_i^{N_{\text{tracks}}} \left(p_T^i\right)^2$, where N_{tracks} is the number of tracks associated to the vertex and $\left(p_T^i\right)$ is the transverse momentum of the i-th track. Figure 59 shows the resolution on the so obtained primary vertex along the z-axis.

5.2 ELECTRON RECONSTRUCTION

The analysis presented in this thesis focuses on semileptonic $t\bar{t}$ events, reconstructed with the ATLAS detector, and electrons are used as prompt leptons in the leptonic branch of the $t\bar{t}$ system.
Electron candidates (both electrons and positrons are here referred to as electrons) are reconstructed using energy deposits (clusters) in the electromagnetic calorimeter (EM) associated to reconstructed tracks in the ID. Electron candidates are identified in the ATLAS detector central region $|\eta| < 2.47$, while electron candidates

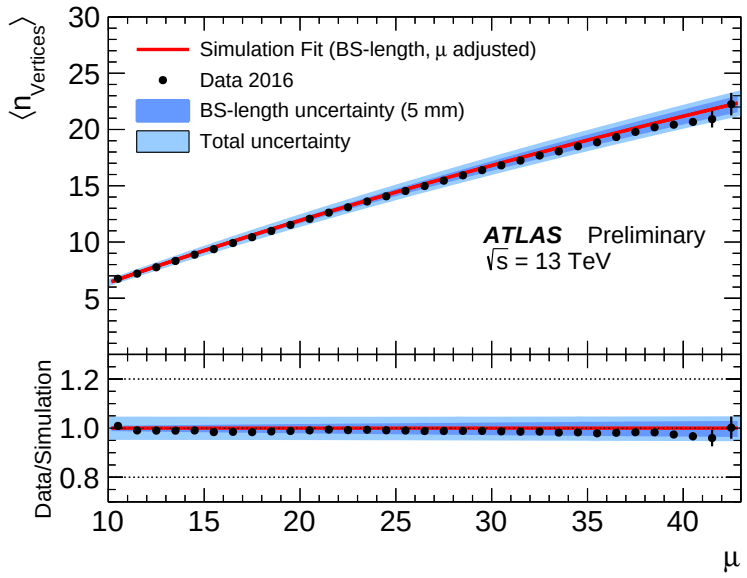

Figure 58.: Distribution of the average number of reconstructed vertices as a function of μ. The solid curve represents the result of a fit to the simulation of minimum-bias events, while dots represent a subset of zero-bias data collected in 2016 with $\sqrt{s} = 13\,\text{TeV}$. BS-length is the beam-spot length [71].

in the region $1.37 < |\eta| < 1.52$ (the so called calorimeter *crack region*) are not reconstructed because of the presence of infrastructures for cooling, support and services.

Clusters in the EM are reconstructed using a sliding window technique [75] that performs a sum over the calorimeter cells energy deposits in a window of 3×5 towers with a size of 0.025×0.025 in the $\eta \times \phi$ region, corresponding to the EM calorimeter granularity (for further details see the Chapter 4).

Once clusters ($E_T > 2.5\,\text{GeV}$) are reconstructed, they are used to identify a Region of Interest in the ID where a track reconstruction algorithm is performed. This is a two-steps reconstruction algorithm that proceeds with a pattern recognition and track fit [76], [77]. Among all the successfully fitted tracks, only the one that best matches the calorimeter cluster is chosen and finally the electron candidate is built while electron candidates without any associated precision hit tracks are removed and considered to be photons. Moreover, in Run-2, electron measurements are performed by requiring the track associated with the electron to be compatible with the pp primary vertex, with the aim of reducing the background from conversions and secondary particles.

The electron particle identification exploits a likelihood-based (LLH) method: it is a multivariate analysis (MVA) technique that simultaneously evaluates several prop-

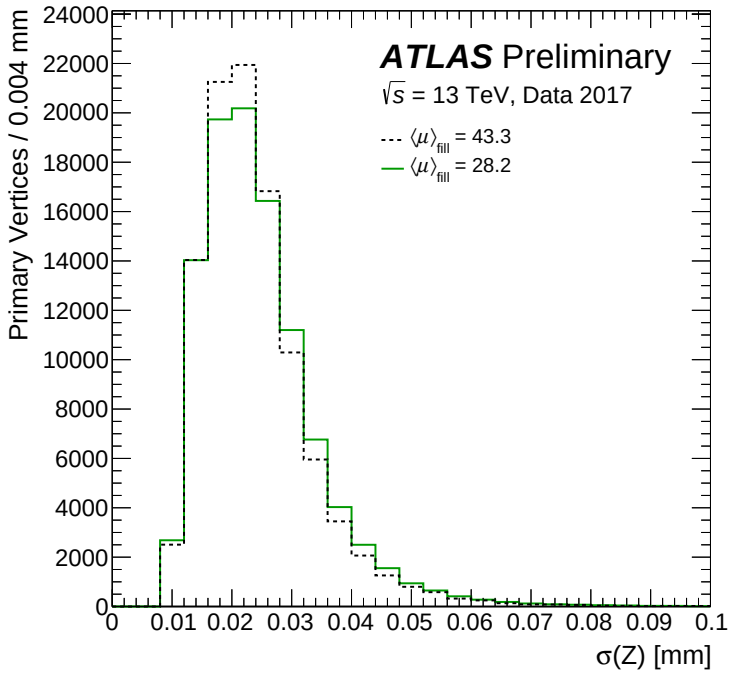

Figure 59.: Resolution of Z-position as obtained from the vertex fit of the reconstructed vertices with the highest $\sum_i^{N_{\text{tracks}}} \left(p_T^i\right)^2$ value for a given event, in two fills with different average μ, taken at different points in 2017 [71]. The ATLAS ID and its Pixel system was described in 3.3.2.

erties of the electron candidates to discriminate electrons from other particles.
The *LLH* discriminants have a set of three working points called Loose, Medium, and Tight [79], in order of increasing background rejection. The *LLH* Loose criteria are optimised to discriminate electrons from charged pions, while Medium and Tight selections evaluate additional variables in order to reject electrons originating from semi-leptonic decays of heavy flavour hadrons or photon conversions. The most widely used variables in *LLH* discriminants are: the shower width, the lateral width of the electromagnetic shower, the ratio of the transverse energy in the hadronic over the electromagnetic calorimeters, the total number of hits in the Inner Detector subsystems (Pixels, SCT, TRT), the transverse impact parameter.
Figures 60 and 61, for Run-1 and Run-2 respectively, show the *LLH*-based electron identification working point efficiencies. Concerning Run-2, the signal efficiencies for electron candidates with $E_{\mathrm{T}} = 25\,\mathrm{GeV}$ are in the range from 78 to 90%, depending on the operating point, and increase with E_{T} and varies with η, because the distributions of electron shower shapes depend on the amount of material the electrons traverse in the detector.

5.3 MUON RECONSTRUCTION

Reconstructed muons are key elements of the analysis presented in this thesis because they are used as both prompt leptons and soft muons in $t\bar{t}$ semileptonic events.
At a first stage, muon reconstruction is performed independently in the Inner Detector (ID) and in the Muon Spectrometer (MS). Then the information from individual sub-detectors is combined to reconstruct the muon tracks. Although muons in the ATLAS detector traverse about 100 radiation lengths of material, mainly instrumented by the electromagnetic and hadronic calorimeters, they release a small amount of energy in their path from the ID to the MS. Typically, muons produced in pp collisions at LHC have energies in a range from 10 GeV to 1 TeV and they can be treated as Minimum Ionizing Particles (MIP) since they deposit a minimum amount of energy in the calorimeter systems (about 3-4 GeV).
Muon candidates are reconstructed in the ID like any other charged particles, as described in Section 5.1.
In the MS, muon reconstruction starts searching for hit patterns in each muon detector system in order to form segments. Each muon chamber is analysed: MDT chambers information feed a particular pattern recognition algorithm, called Hough transform [80], that is used to search for hits aligned on a trajectory in the bending plane of the detector (muons traverse the ATLAS toroidal magnetic field in the MS). Then, MDT segments are reconstructed performing a straight-line fit to the hits found in each layer. RPC and TGC are mainly used for trigger purposes but

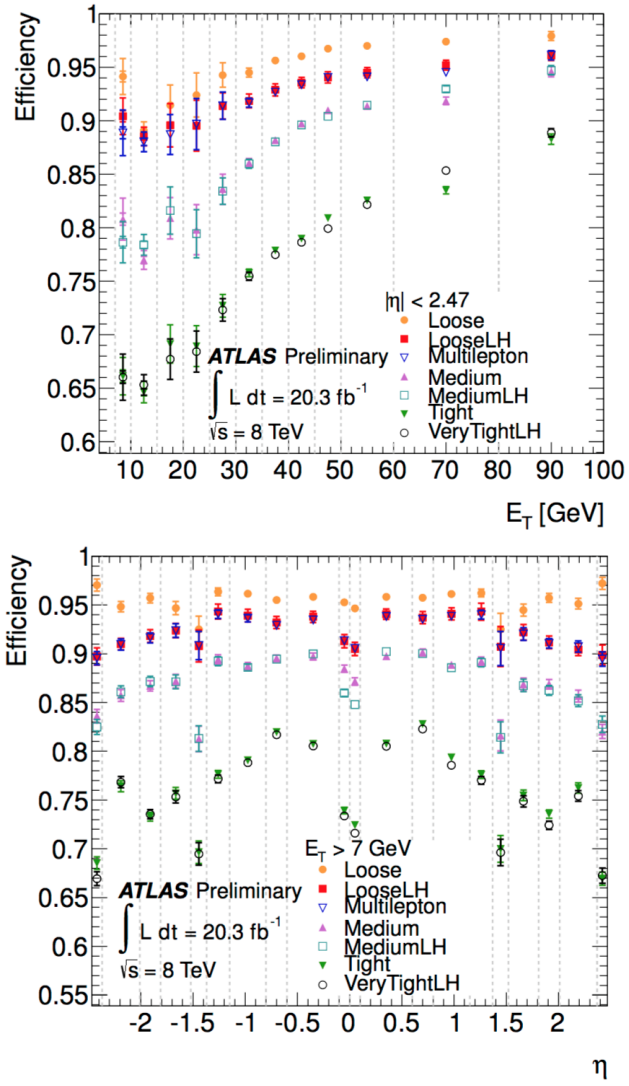

Figure 60.: Measured electron reconstruction and identification efficiency for the cut-based and LLH working points, as a function of E_T and η for the 2012 dataset. The efficiency is measured using a $Z \to ee$ simulated sample. Figures from [78].

their hits also help in measuring the coordinate orthogonal to the bending plane. In the CSC detector, segments are built using a separate combinatorial search in both the η and ϕ detector planes.

Finally, muon track candidates are built fitting all the hits from the different segments in the different detector layers, using the χ^2 method: generally, at least two matching segments are required to build a track, but in the barrel-endcap transition region a single high-quality segment can be used to build a track.

In Run-2, the combined ID and MS information is used to reconstruct muons and to define four different muon types [81]:

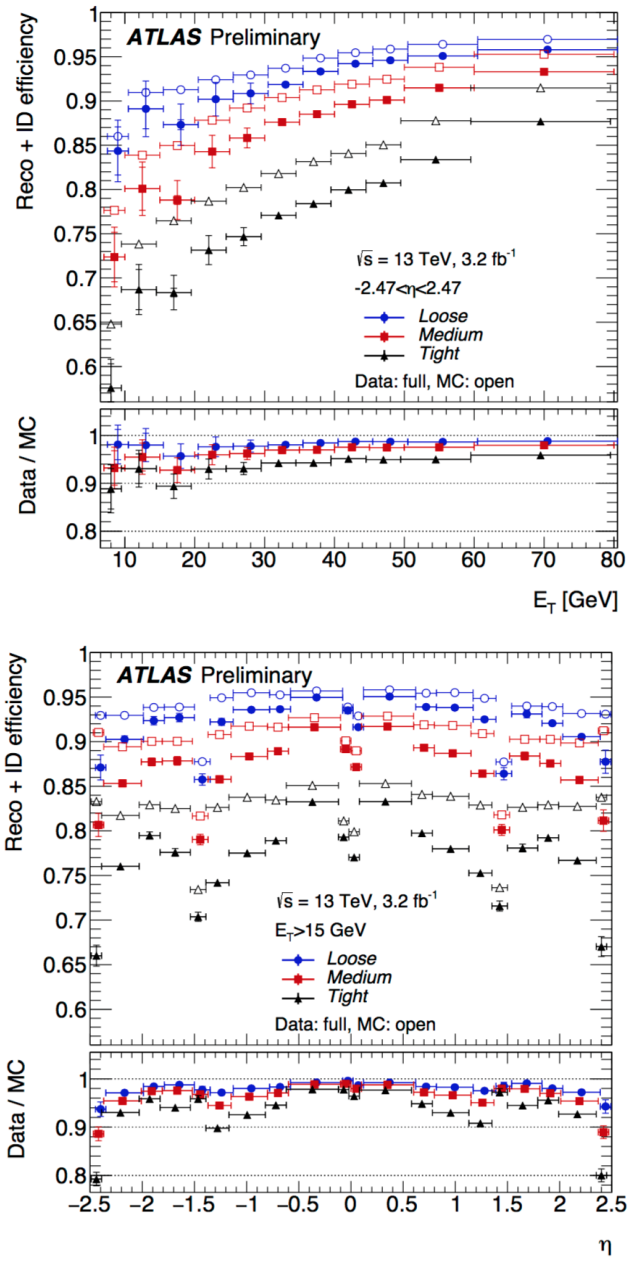

Figure 61.: Measured electron reconstruction and identification efficiency for the three *LH* working points as a function of E_T and η for the 2015 dataset. The efficiency is measured using a $Z \to ee$ simulated sample. Figures from [79].

- **Combined (CB) Muons**: first track reconstruction is performed independently in the ID and MS sub-detectors, then a global fit is performed using hits from both the ID and the MS to form a combined track. The global fit procedure follows an outside-in pattern recognition and starts with the hits in the MS,

where the track density is much smaller if compared to the ID, and then the tracks are extrapolated inward and matched to the ID tracks.

- **Segmented Track (ST) Muons**: a muon is classified as an ST muon if a track in the ID, once extrapolated to the MS, it is associated with at least one track segment in the MDT or CSC chambers. These muons are exploited when muons cross only one layer of MS chambers, either because of their low p_{T} or because they fall in regions with a reduced MS acceptance.

- **Calorimeter Tagged (CT) Muons**: tracks in the calorimeter and ID are used: a track in the ID is identified as a muon if it can be matched to an energy deposit in the calorimeter compatible with a MIP particle. These muons have the lowest purity but they recover acceptance in the $|\eta| < 0.1$ region where the ATLAS MS is only partially instrumented (due to cabling and services).

- **Extrapolated (ME) Muons**: only MS tracks are used to reconstruct the muon trajectory and a loose requirement on compatibility with originating from the interaction point is required. In the central region, the muon is required to traverse at least two layers of MS chambers, but three layers are required in the forward region to provide a track measurement. ME muons are used to extend the acceptance for muon reconstruction into the region where there is no ID coverage ($2.5 < |\eta| < 2.7$).

Muon identification is split in four selections: Loose, Medium, Tight and High-p_{T}. Muons selected by Medium are all selected by Loose, and Tight muons are all selected by Medium. Increasing quality requirements are applied to muons in order to suppress background, mainly from pion and kaon decays in flight, while selecting prompt muons with high efficiency. It is also important to guarantee a robust momentum measurement using specific requirements on the number of hits in the ID and MS. For the ID, the quality cuts require:

1. at least one Pixel hit
2. at least five SCT hits
3. fewer than three Pixel or SCT holes (a hole is defined as an active sensor traversed by the track but containing no hits)
4. at least 10% of the TRT hits originally assigned to the track are included in the final fit (for $|\eta|$ between 0.1 and 1.9)

The muon identification categories are defined as follows:

- **Loose**: the aim of Loose identification criteria is to maximise the muon reconstruction efficiency while providing good-quality muon tracks. All muon

types are used in this category. CB and ME tracks are required to have ≥ 3 hits in at least two MDT layers, except for tracks in the $|\eta| < 0.1$ region, where tracks with at least one MDT layer but no more than one MDT hole layer are allowed. On ME tracks there is the constraint to have at least three MDT/CSC layers, and are employed only in the $2.5 < |\eta| < 2.7$ region to extend the acceptance outside the ID geometrical coverage. The usage of CT and ST muons is restricted to the $|\eta| < 0.1$ region. About 97.5% of the Loose muons are combined muons in the region $|\eta| < 2.5$, about 1.5% are CT and the remaining 1% are reconstructed as ST muons.

- **Medium**: the Medium identification criteria are the baseline selection for muons in ATLAS. This category minimises the systematic uncertainties associated with muon reconstruction and calibration. Only CB and ME tracks are used as Medium muons. The requirements on CB and ME muons are the same as for Loose muons, moreover a loose selection on the compatibility between ID and MS momentum measurements is applied to suppress the contamination due to hadron backgrounds misidentified as muons. More precisely, the q/p significance is required to be less than seven. In the pseudo-rapidity region $|\eta| < 2.5$, about 99.5% of the muons classified as Medium originate from the outside-in combined reconstruction strategy. Medium muons have an identification efficiency measured to be above 95% on a $t\bar{t}$ sample [81], for muons with a transverse momentum greater than 4 GeV.

- **Tight**: Tight muons are selected to maximise the purity of muons, but they have the lowest efficiency. Only CB muons with hits in at least two stations of the MS and satisfying the Medium selection criteria are exploited. The χ^2 method is considered when fitting the combined tracks, to remove pathological tracks. To ensure stronger background rejection in the p_{T} region where the misidentification probability is higher (muons below 20 GeV), a two-dimensional cut on the q/p significance and on the absolute value of the difference between the transverse momentum measurements in the ID and MS divided by the p_{T} of the combined track (the so called ρ') variables is performed. Tight muons have an identification efficiency measured to be above 90% on a $t\bar{t}$ sample [81], for muons with a transverse momentum greater than 4 GeV.

- **High-p_{T}**: High-p_{T} muons maximise the momentum resolution for tracks with transverse momentum above 100 GeV. In this criteria, CB muons passing the Medium selection and having at least 3 hits in three MS stations are selected. Specific regions of the MS where the alignment is suboptimal are vetoed, as a precaution. This constraint on MS stations, improves the p_{T} resolution of

muons above 1.5 TeV by approximately 30%, while reducing the reconstruction efficiency by about 20%.

The muon reconstruction efficiency in the region $|\eta| < 2.5$ is calculated with a tag-and-probe method, using standard and well known decays such as $Z \to \mu\mu$ and $J/\Psi \to \mu\mu$ to cover a broad muon transverse momentum spectrum. The tag is a muon reconstructed in either the MS or the ID and it is used to test the probe muon reconstructed in the other system (ID or MS). During the shutdown between the LHC Run-1 and Run-2 (LS1), the MS was completed adding the last missing chambers in the transition region between the barrel and the endcaps ($1.0 < |\eta| < 1.4$). Four RPC-equipped MDT chambers were also installed inside two elevator shafts to improve the acceptance in that region compared to Run-1. Some of the new MDT chambers are made of tubes with a smaller radius compared to the ones used in the rest of the detector, allowing the detector to cope with higher rates.
Figures 62 and 63 show the reconstructed efficiency for muons in Run-1 and in Run-2, respectively. In Figure 62, the drop in efficiency for CB muons at $|\eta| \sim 1.2$ corresponds to the transition region between the barrel and the endcap region where only one layer of MS chambers is present. This feature was recovered in Run-2, thanks to the addition of extra muon chambers during the LS1.

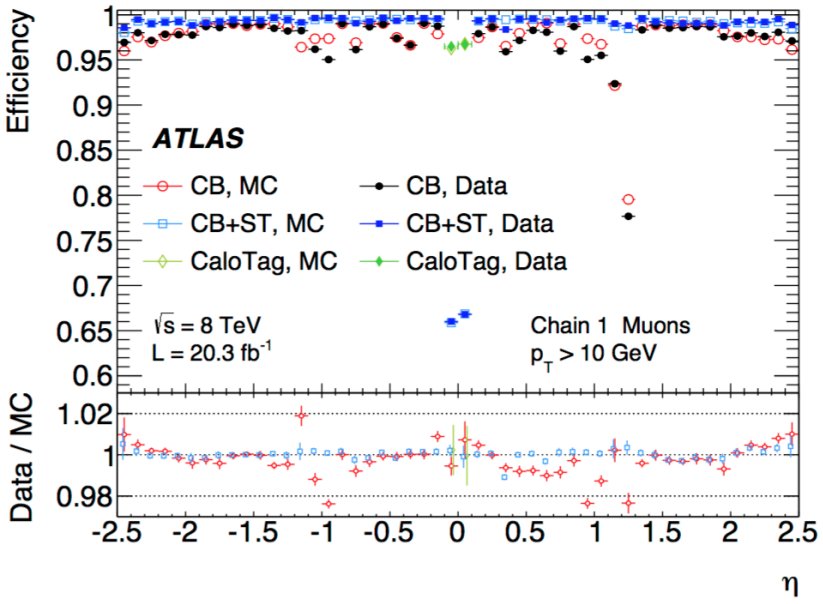

Figure 62.: Muon reconstruction efficiency as a function of η for different type of muons reconstructed in Run-1. For details on the muon reconstruction and identification algorithms in Run-1, refer to [82].

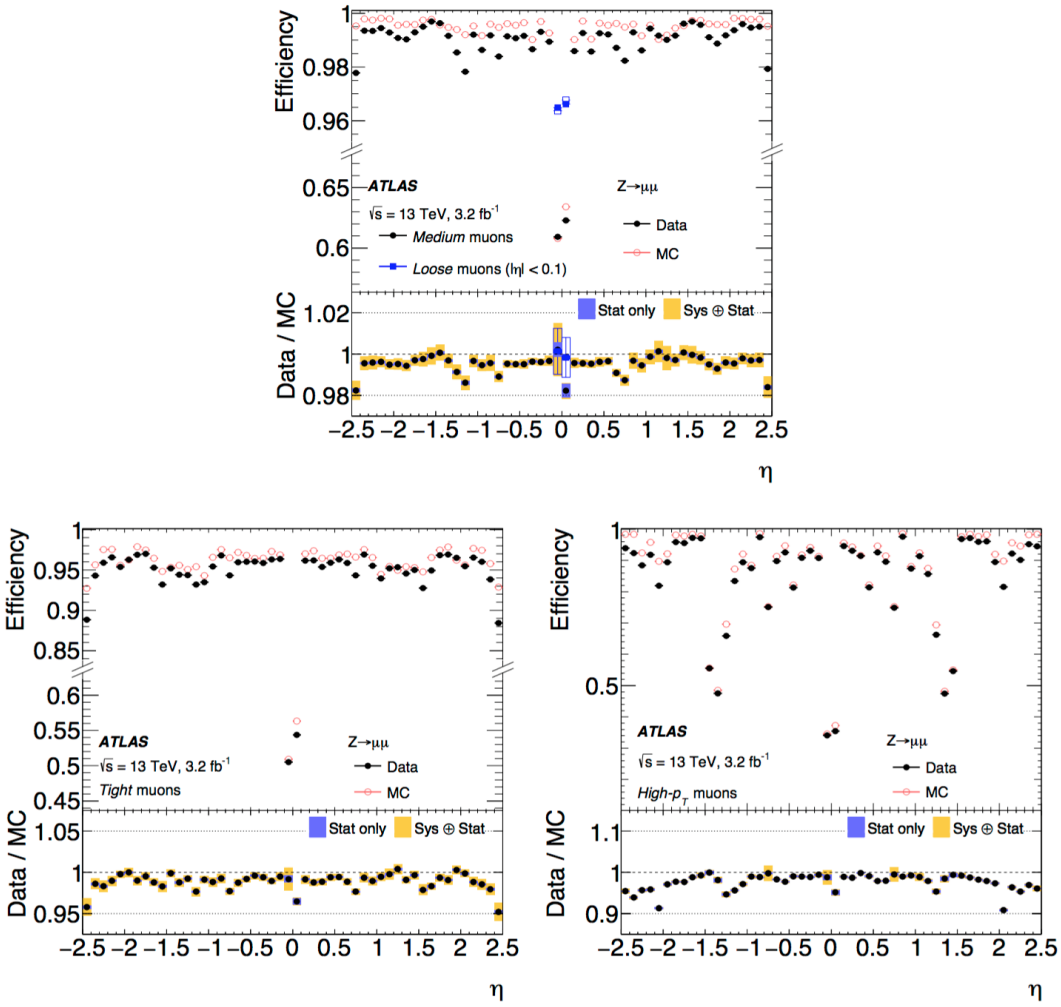

Figure 63.: Muon reconstruction efficiency as a function of the pseudorapidity η, measured in $Z \to \mu\mu$ events for muons with $p_{\mathrm{T}} > 10\,\mathrm{GeV}$ shown for Medium (top), Tight (bottom left), and High-pT (bottom right) muon selections in Run-2 at 13 TeV. The top plot also shows the efficiency of the Loose selection (squares) in the region $|\eta| < 0.1$ where the Loose and Medium selections differ significantly. The error bars account only for the statistical uncertainty. Panels at the bottom show the ratio of the measured to predicted efficiencies, with statistical and systematic uncertainties. Figure from [81].

5.4 JETS RECONSTRUCTION

Most of the LHC pp interactions result in quarks and gluons that undergo a fragmentation and a hadronisation process, respectively, responsible for a narrow cascade of partons and for the formation of colourless hadrons. These processes result in the formation of cones of particles, known as jets, around the direction of the original object. Jet reconstruction is one of the key points of this analysis. Jets have a hadronic and an electromagnetic component (due to $\pi^0 \to \gamma\gamma$ decays) and they are detected in both the hadronic and electromagnetic ATLAS calorimeters, where they release energy deposits associated with collimated charged particle tracks reconstructed in the ID.
The ATLAS jet reconstruction process is a sequential topological cluster algorithm that builds three dimensional clusters from the energy deposits in the calorimeter cells [83]. The reconstruction starts with the identification of seed cells, characterised by a total energy at least 4σ above the noise level (electronic and pile-up signals). If close-by cells have an energy significance greater than 2σ, they are iteratively added to the cluster, increasing its size. The resulting topo-cluster energy is the sum of all the considered calorimeter cells and points to a direction calculated averaging η and ϕ of the constituent cells.
Reconstructed jets have to satisfy several experimental and theoretical requirements, among them the most important are:

- Infrared Safety: the number of reconstructed jets has to be insensitive to the effects of soft gluon emissions not originated by the hard scatter. For example, if there is a low energy cluster between two energy clusters, the jet reconstruction algorithm has to be able to define them as two separate objects, as shown in Figure 64.

- Collinear Safety: the number of reconstructed jets must be independent from the effects of collinear splittings, as shown in Figure 65.

The *anti-k_T* sequential clustering algorithm [84] used in this physics analysis satisfies the above conditions. It works iteratively merging together the calorimeter deposits, depending on the distance $d_{i,j}$ between them and from the beam line $d_{i,B}$ defined as:

$$d_{i,j} = \min\left(\frac{1}{k_{Ti}^2}, \frac{1}{k_{Tj}^2}\right)\frac{\Delta R_{i,j}^2}{R^2} \qquad d_{i,B} = \frac{1}{k_{Ti}^2} \tag{49}$$

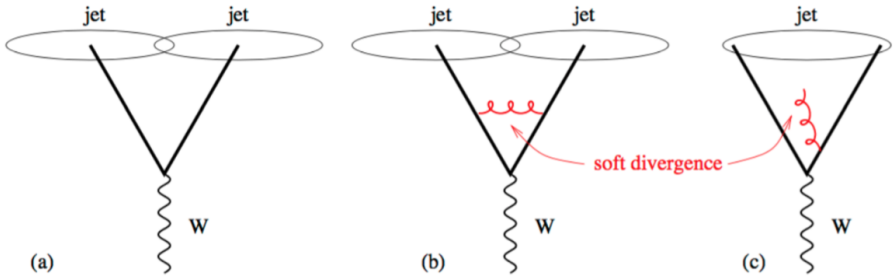

Figure 64.: When applying the jet reconstruction algorithm, the initial two jets (a) remain as two jets with an infrared safe algorithm (b), but converge to a single jet when reconstructed using an infrared unsafe algorithm (c).

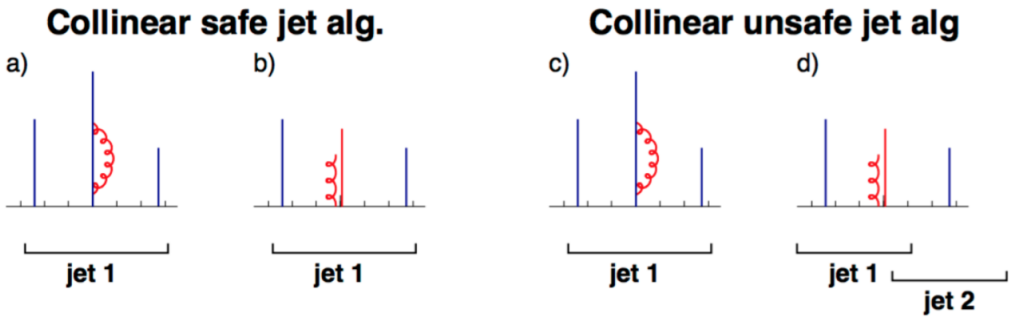

Figure 65.: A representation of a collinear safe (left) and unsafe (right) algorithm. The vertical lines represent partons with the height proportional to their transverse momentum, the rapidity is on the horizontal axis.

where $R^2 = \left(\eta_i - \eta_j\right)^2 + \left(\phi_i - \phi_j\right)^2$ and $k_{Ti,j}$, $\eta_{i,j}$ and $\phi_{i,j}$ are the transverse momentum, the pseudorapidity and the azimuthal angle of the topological clusters i and j, respectively. The *anti-k_T* proceeds with the following steps:

1. define the distance $d = \min\left(d_{i,j}, d_{i,B}\right)$
2. if the minimum value is $d = d_{i,j}$, then combine i and j into a single object and repeat the first step
3. if the minimum value is $d = d_{i,B}$, consider i as a final jet.

The recombination starts from the hardest object, ensuring that energy deposits due to soft radiation will be merged to the hard object before being clustered among themselves, resulting in a reconstructed jet unaffected by soft radiation. In this analysis the parameter R is equal to 0.4, which defines the size of the jet cone and the minimum distance between two un-merged jets.
The energy of reconstructed jets has to be calibrated to the truth energy of the corresponding jet of stable hadronic particles. This process is based on a combination of simulated Montecarlo samples and data driven techniques. The calibration accounts for several experimental effects, such as: calorimeter non compensation, dead material in the detector, leakages due to showers reaching the outer areas of the calorimeters, energy deposits below noise thresholds, pile-up and out-of cone effects (fraction of energy lost due to low energy particles deflected at large angle by the electromagnetic field and not reconstructed in the jet cone). The calibration process results in the so called Jet Energy Scale uncertainties which is usually one of the major systematic uncertainty in physics analyses.
Moreover, there is a second calibration that uses the local cell signal weighting (LCW) method [83] to classify the topo-clusters as electromagnetic or hadronic clusters, depending on their shower properties and apply Montecarlo based simulations to the energy deposits due to hadronic calorimetric showers.

5.4.1 *b-tagging*

The identification of b-originating jets is of primary importance for the analysis presented in this dissertation, because CAs and CPAs must be measured using soft muons genuinely coming from heavy hadron decays. Various algorithms are employed in ATLAS to reconstruct b-jets, most of them are based on the information from the reconstructed tracks with large impact parameters and displaced secondary vertices in the ID, as shown in Figure 66.

These techniques take advantage of the relatively long lifetime of B-hadrons, which is of the order of 1.5 ps, meaning that a B-hadron with $p_{\mathrm{T}} = 30\,\mathrm{GeV}$ will have a mean flight path length $< l >= \beta\gamma c\tau$ of the order of 3 mm in the transverse

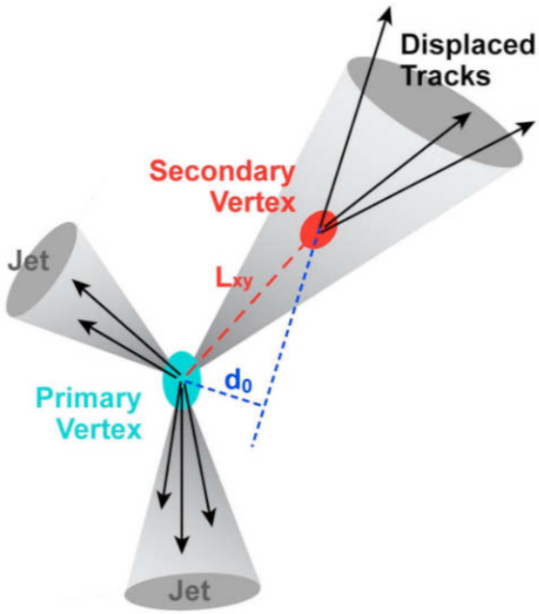

Figure 66.: A sketch of two light jets, emerging from the primary vertex and one b-jet, originating from a secondary vertex. The flight path and the transverse impact parameter d_0 (reconstructed in the $r\phi$ plane) are also shown in red and blue, respectively [85].

direction before decaying.
In ATLAS, the most commonly used b-tagging method is a Multi-Variate technique that merges impact parameters and displaced vertex information. The unique feature of this analysis is the usage of an alternative b-tagging technique called Soft lepton Tagging that tags reconstructed jets as heavy flavour (HF) jets exploiting the $b(c) \to \mu$ semi-leptonic branching ratio ($\sim 21\%$).

Multi-Variate Techniques

The Multi-Variate techniques (MV) take inputs from other algorithms. The first class of algorithms (JetProbe and IP3D [86]) exploits the impact parameter information, while the second class of algorithms is explicitly based on the displaced vertex reconstruction. The SV1 and SV2 algorithms fall in the second category: they consider secondary vertex information and additional variables such as the ratio of the energy associated to the tracks in a jet to the energy assigned to tracks associated with the primary vertex. These parameters are then combined in a likelihood fit to improve the tagger performance.
Finally the JetFitter [87] algorithm is used, aiming at reconstructing the complete b-hadron decay chain.
During Run-1 the Multi-Variate technique (so called MV1) was based on a neural network approach [88] to discriminate b-originating jets from light (u, d, s-quark or gluon jets) and c-jets. The working points calibrated at $\sqrt{s} = 8\,\text{TeV}$ for the MV1 tagger are shown in Table 16 [85].

Tagger	b-jet efficiency (%)	purity (%)	c-jet rejection factor	LF-jet rejection factor
MV1	70	92.28	4.97	136.66
MV1	80	85.41	3.08	25.18
MV1	85	76.86	2.38	9.66

Table 16.: Working Points (WP) for the MV1 tagger, calibrated by ATLAS for Run-1.

In Run-2 an improved MVA method, based on a Boosted Decision Tree algorithm (BDT), is adopted. Figure 67 shows the MV1 light flavour rejection rate, as a function of the b-tagging efficiency.
The new approach, called MV2 [89] [90], improves the MV1 performances, taking advantage also from the new IBL layer information. The main inputs, obtained from the three basic algorithms (IP3D, SV and JetFitter), and fed to MVA algorithms are:

1. the jet transverse momentum
2. the invariant mass of tracks at the secondary vertex
3. the number of tracks from the secondary vertex

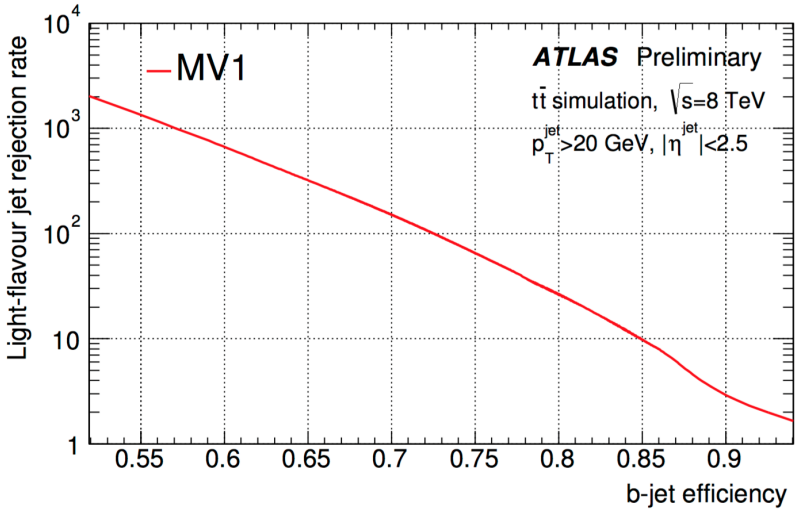

Figure 67.: *b*-jet tagging efficiency versus light-flavour jet rejection for the three working points of the MV1 *b*-tagging algorithm, evaluated on $t\bar{t}$ events. Figure from [85].

4. the distance between the primary and secondary vertices
5. the distance between the primary and secondary vertices, divided by their uncertainties

Three different MV2 variables are available: MV2c00, MV2c10 and MV2c20, indicating the *c*-jet fraction in the training, 0%, 10% and 20% respectively (*i.e.* in MV2c20, the background sample is composed of 20% (80%) *c*- (light-flavour) jets.
Figure 68 shows the light-jet rejection as a function of the *b*-tagging efficiency for the optimised MV2c00, MV2c10 and MV2c20 *b*-tagging algorithms. The rejection is defined as the reciprocal of the fraction of light-jets sample that pass the *b*-tagging algorithm requirements in a background sample.

The tagger adopted in this thesis is MV2c10 and the efficiency calibrations of this algorithm are performed with fixed thresholds (or working points) of the tag weights computed by the *b*-tagging algorithms, as shown in Table 17. These WP are defined using a single cut value on the MV2 output distribution. In this analysis the MV2c10 algorithm with a 77% working point will be used, as stated in 7.2.3.

weight-cut (%)	*b*-jet efficiency (%)	purity (%)	*c*-jet rejection factor	τ jet rejection	LF-jet rejection factor
0.8529	59.99	96.68	16.16	53.47	276.16
0.6455	70.00	93.55	7.09	17.25	119.69
0.3706	77.00	89.81	4.21	8.09	57.90
-0.1416	84.99	82.31	2.47	3.75	18.97

Table 17.: Working Points (WP) for the MV2c10 tagger, calibrated by ATLAS for Run-2.

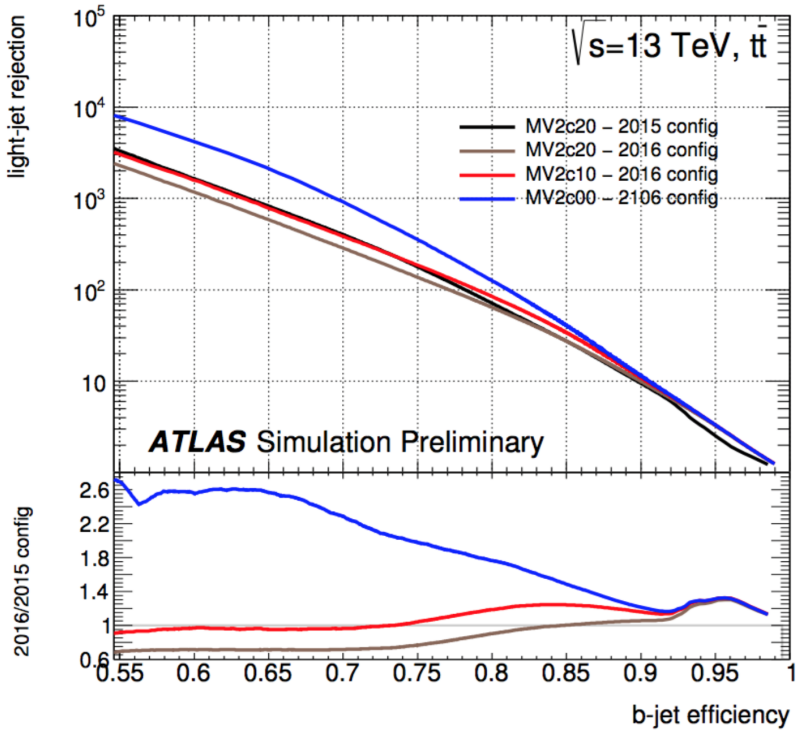

Figure 68.: b-jet tagging efficiency versus light-flavour jet rejection for the three MV2 b-tagging algorithm evaluated on $t\bar{t}$ events. In the 2016 configuration the Montecarlo simulation has been adjusted to better represent the data conditions expected in 2016 (pileup profile for 2016 data-taking). Figure from [89].

Soft Lepton Tagging

Soft lepton taggers identify reconstructed jets as HF-originating jets, exploiting the final state lepton in the jet decay chains. The resulting electron or muon is collinear with the jet axis and usually has a wide p_{T} distribution. A soft muon tagging (SMT) technique is adopted in this dissertation and this choice will be justified in details in Chapter 6. This is one of the unique features exploited by the analysis presented in this thesis.
The SMT definition in Run-1 [91] was based on STACO combined muons, which consisted of a statistical combination of an ID and a MS track in a combined track [82]. A detailed description of the SMT algorithm adopted in Run-1 will be given in Chapter 6, that will be entirely dedicated to this technique.

In Run-2 STACO muons are not supported and soft muons are defined using Tight muons (refer to Section 5.3 for the Tight muon definition).

5.5 MISSING TRANSVERSE MOMENTUM RECONSTRUCTION

In semileptonic $t\bar{t}$ events, missing transverse momentum is expected from the leptonically decaying W boson.
Neutrinos are the only Standard Model particles that do not interact within the detector volume, they escape undetected and hence they cannot be reconstructed. Neutrinos can only be detected by indirect information: in pp collisions, the four-momentum component orthogonal to the beam axis is zero before the protons interaction and this quantity has to be conserved also in the final state. An imbalance in the total measured transverse momentum in the final state indicates the presence of an invisible particle in the event and, in the framework of the Standard Model, neutrinos are the only viable candidates.
This missing transverse momentum is defined as the negative vectorial sum of all the reconstructed objects transverse momenta [92]. The magnitude of the missing transverse momentum is calculated using the reconstructed transverse momentum of electrons, muons, taus, photons, jets and the soft terms detected in the ID, in the calorimeter systems or a combination of both, as in formula 50.

$$E_{\mathrm{T}}^{Miss} = -\left(\sum_{e} p_{\mathrm{T}}^{e} + \sum_{\mu} p_{\mathrm{T}}^{\mu} + \sum_{\tau} p_{\mathrm{T}}^{\tau} + \sum_{\gamma} p_{\mathrm{T}}^{\gamma} + \sum_{jets} p_{\mathrm{T}}^{jets} + \sum_{\mathrm{Soft}} p_{\mathrm{T}}^{\mathrm{Soft}}\right) \tag{50}$$

$p_{\mathrm{T}}^{\mathrm{Soft}}$ is composed by detector signal objects not associated with any hard object reconstructed in the detector that can arise from ID tracks or calorimeter cells.

Part II.

Run-1 analysis

6

CALIBRATION OF THE MISTAG RATE OF THE SMT

This chapter focuses on the calibration of the mistag rate of the momentum imbalance based Soft Muon heavy flavour Tagging (SMT) algorithm, performed with data collected by the ATLAS detector during 2012*. The SMT has a lower tagging efficiency than vertex based tagging algorithms due to the relatively small branching ratio of b-hadrons decaying to muons, however it is a feature exploited by many physics measurements.*
The first measurement of charge and $\mathcal{CP}$ asymmetries in heavy flavour b- or c-decays from top-antitop lepton+jets events, using the data collected with the ATLAS detector during Run 1 *of the LHC, is also shown in Section 6.5.*

6.1 THE MOMENTUM IMBALANCE BASED SOFT MUON TAGGER

An important feature of many physics analyses in the ATLAS collaboration programme is the determination of the flavour of a jet. The identification of heavy flavour (HF) jets is a crucial component of the analysis presented in this thesis.
The most common strategies developed and adopted by the ATLAS physicists to discriminate between HF and light flavour (LF) originating jets rely on a characteristic feature of the b and c hadrons: b-hadrons have a relatively long life time ($\tau \sim 10^{-12}$ s) if compared to other hadrons and they travel a greater distance (d) in the ATLAS Detector (namely, in the beam pipe) than other hadrons. The decay products of b-hadrons point back to a vertex which is displaced from the beam interaction point by a measurable distance ($d \sim$ a few mm) and the measured distance between reconstructed primary and secondary vertices can be used to identify the jet as a b-jet. The particular features exploited by MVA techniques to identify b-jets are detailed in Section 5.4.1.
In contrast to the displaced vertex tagger, the Soft Lepton tagging (SLT) uses the semi-leptonic decays of the b and c hadrons into leptons (electrons and muons) which usually have low-p_T and are collinear with the HF jet axis. The branching ratios of the decay chains $b \to \ell$ and $b \to c \to \ell$ is $\approx 21\%$ and the SMT algorithm is complementary to the other taggers because it does not make use of any vertexing

information and it is sensitive to a different set of b-tagging systematic uncertainties, however the method suffers from a lower tagging efficiency if compared to the displaced vertex techniques. Moreover, the SLT exploits a slightly different data sample, the one coming from semi-leptonic b-hadron and charm-hadron decays, with respect to the other taggers.
Soft electron tagging would require the reconstruction of a low energy EM shower aligned with a jet but the jet itself has EM components in the ECAL and it would be very challenging to distinguish the two. For this reason, this technique is not utilised at ATLAS. On the other hand, a soft muon produced from a semi-leptonic b-decay will traverse all the ATLAS detector and reach the MS losing only a small amount of energy per ionisation. The fractional difference in momentum between the candidate track in the ID and the MS will be very small and the muon tracks will be collinear with the HF-originating jet axis.
The SMT draws on the momentum imbalance (MI) between a muon track measured in the Inner Detector (ID) and a track in the Muon Spectrometer (MS) extrapolated back to the ID (ME), defined in the equation 51.

$$\mathrm{MI} = \frac{p^{\mathrm{ID}} - p^{\mathrm{ME}}}{p^{\mathrm{ID}}} \tag{51}$$

Where p^{ID} and p^{ME} are the magnitude of 3-momenta of the muons.
Light charged mesons ($\pi^{\pm}$ and $K^{\pm}$) decay predominantly into muons and thus contribute significantly to a sample of jets with associated muons. Since these light charged mesons have a long lifetime ($\tau \sim 10^{-8}$ s), a small fraction of those mesons decay between the end of the ID volume and the entrance of the muon system. In cases when the ID measures the track parameters for the meson, the MS is sensitive to the track of the muon produced in the decay, giving rise to an enlarged momentum imbalance. As shown in figure 69 (left), the muon decaying from a light meson gets a kink in its trajectory. For kinematic reasons (momentum conservation) the muons gets part of the mother momentum and curves more in the magnetic field because of the rigidity equation 52, resulting in a fractional difference in momentum between a track candidate as measured in the ID, and as measured in the MS.

$$BR = \frac{p}{e} \tag{52}$$

Where R is the radius of curvature, B is the magnetic field applied in the ATLAS detector, p is the 3-momentum of the charged particle and e is its charge.

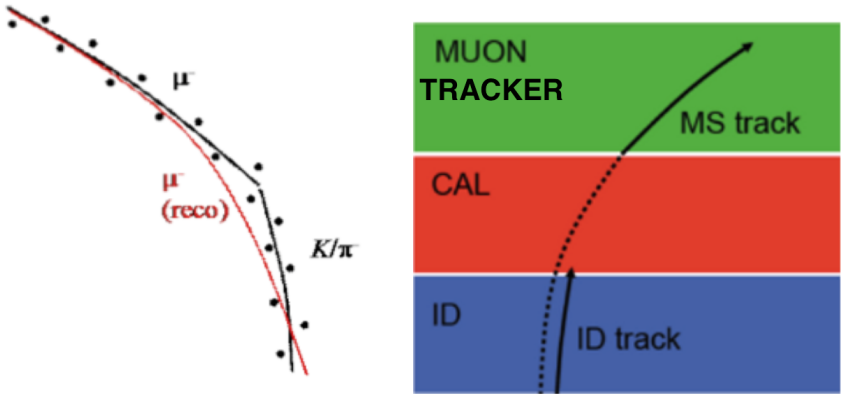

Figure 69.: Left: Muon decaying trajectory, kinked with respect to the mother particle trajectory. Right: sketch of the muon candidate trajectories in the ID, in the calorimeter and in the MS detector [91].

As shown in figure 70, tracks in the MS aligned with ID tracks associated to true HF hadrons and their decays have a small fractional difference in momentum and a smaller value of MI, while other hadrons show a larger fractional difference in momentum and a larger value of MI.

Jets selected using the MI parameter allow good light-jet rejection. Since there are differences in the performance of the tagger when applied to data and to MC simulations and also the amount of light mesons in the MC generator might be different from data, a calibration is required and this results in a set of scale factors (SF) to account for such differences.
However there are events where the SMT algorithm mistakenly tags a LF-originating jet as an HF jet and this is known as mistag rate.

6.2 MEASUREMENT OF THE MISTAG RATE

This chapter describes my work in the calibration of the mistag rate of the SMT, while the calibration of the efficiency of the SMT was performed elsewhere. As the SMT depends only on quantities related to muon tracks, the calibration of the tagger was performed using isolated $J/\Psi \to \mu\mu$ low-p_T muons and $Z \to \mu\mu$ high-p_T muons. For a more comprehensive overview of these studies refer to [91].
The mistag rate is defined as the fraction of jets originating from gluons and light-flavour (LF) which are mistakenly tagged by the SMT algorithm. Sources of mistag rate may be both physical and instrumental. The first category includes decays in flight of light hadrons like pions and kaons with a high-p_T, while another contribution is due to instrumental effects like *punch-through* of hadrons through the

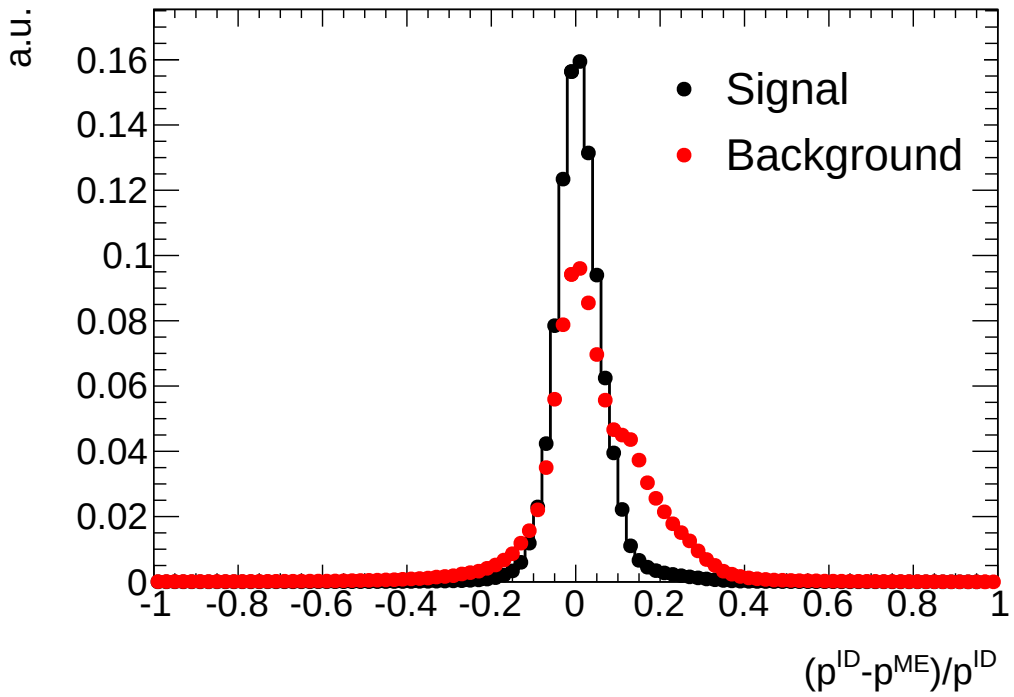

Figure 70.: Momentum imbalance distribution for 'signal' soft muons, and 'fakes' from the decay of non-b-hadrons, *i.e.* LF-jets from of u-, d- or s-quarks, using $t\bar{t}$ MC simulations. The areas under each distribution has been normalised to unity.

calorimetry (known as fake muons) and nuclear interactions of the constituents of hard jets with the material in the calorimeters, which create high-p_T muon tracks in the Muon Spectrometer (MS).
The mistag rate is studied as a function of the p_T of the jet under consideration, in order to determine if there is a dependence on the jet kinematics. A full study of the mistag rate dependence on pileup is also undertaken. There is no observed η dependence so the mistag rate is evaluated over the full pseudorapidity region $|\eta| < 2.5$.
The mistag rate is calibrated using a W+Jets estimation method for low-p_T jets and a dijet method for high-p_T jets. This Chapter focuses on the high-p_T jets. At low-p_T, the di-jet method suffers from low data statistics, originating from large trigger prescales, as well as large systematic uncertainties due to the b-to-c jet fraction estimated from the simulation. These uncertainties reduce significantly at high-p_T and the dijet method can extend to the TeV scales. The W+Jets estimation method only covers jets up to a p_T of around 150 GeV, however, it provides an abundance of data statistics that are triggered via unprescaled muon triggers. The two methods have different kinematic ranges and they are complementary in determining the mistag rate and provide SFs.

6.3 HIGH-p_T MISTAG RATE WITH THE DI-JET METHOD

The mistag rate is measured in both collision data and MC simulation from an inclusive sample of QCD multi-jet events. Numerous jets in a multi-jet event may fake a lepton or produce a real charged lepton and they may satisfy SMT tagging requirements. Since it is extremely rare that a muon is misidentified as a jet in the ATLAS detector, fakes mainly come from muons originated by light hadrons.
The sample is selected following the requirements in Section 6.3.1. Section 6.3.2 describes the di-jet sample and its features in the simulation. A method which relies almost completely on data inputs is applied to data in order to isolate light flavour-originated jets and evaluate the corresponding mistag rate. The method is described in Section 6.3.3. Section 6.3.4 discusses the systematic uncertainties. The results and the comparison of the mistag rate with MC expectations for a truth-selected sample of LF jets are provided in Section 6.3.5, together with a discussion on the associated systematic uncertainties.

6.3.1 *Data and MC samples and selections*

Samples

The following samples are used to determine the mistag rate in data and the expected one in MC simulation:

- Collision data:
  - Data are taken from a multi-jet dataset recorded by the ATLAS detector during 2012, in Run-1 with a centre of mass energy $\sqrt{s} = 8$ TeV.
  - Only data taken when the full ATLAS detector is working properly are taken into consideration, given the need of all detector components in this analysis (tracking/vertexing, calorimetry for the jets and muon spectrometer for the tagging muon). In order to guarantee a good quality of the data, only data collected when the ATLAS detector is fully operational are considered, these datasets are recorded in the so called Good Run List (GRL). The GRL provides information about the status of the LHC (*i.e.* if there is a stable beam) and about the ATLAS detector status during the operations.
  - The data are selected on-line using a logical OR of several jet triggers. Each component in this jet trigger chain requires at least a jet above a certain transverse energy (E_{T}) threshold at the Event Filter (EF). Jets are reconstructed using the $anti\text{-}k_T$ algorithm with topological cell energy clusters as signal input with a radius of $R = 0.4$. Jets with transverse energy (E_{T}) from above 15 GeV up to 1 TeV are analysed.
    The three lowest transverse energy triggers are selected at L1 by a random pre-scaled trigger and are chosen because of their wider acceptance at low jet p_T with respect to the L1-jet-trigger seeded signatures, but are very highly pre-scaled. The higher energy triggers guarantee access to the higher p_T region but with a lower pre-scale.
- MC simulation:
  - An inclusive sample of di-jet events simulated with the MC generator Pythia8+EvtGen (as described in Section 7.1) was used. This analysis covers a wide p_T range, so the MC simulation is divided into different truth p_T samples. Jets are ordered according to their truth-p_T and grouped in five slices, labelled from J0 to J4. These five samples are combined and the correct shapes for the jet p_T spectra are obtained by applying the event weight (stored on an event-by-event basis) and then normalising each JX sample to the corresponding cross section, filter efficiency, number of events, (taken from the ATLAS Metadata Interface

AMI) and the luminosity of the data sample under consideration.
A final MC quality cut requiring (p_TAvg/leading truth p_T) < 1.4, where p_TAvg refers to the mean di-jet p_T described by formula 53, is applied to remove some events in the low-p_T region which do not follow an exponentially decreasing distribution as expected (see the J0 curve in Figure 71). This cut is used to minimise the impact of energy fluctuations and detector resolution related to detector resolution effects. It is possible that either the leading jet p_T is overestimated or the subleading jet p_T is underestimated. However, the cut on the average value mainly compensates this effect.

$$p_{\mathrm{T}}\mathrm{Avg} = \frac{p_{\mathrm{T}}^{(\mathrm{LJ})} + p_{\mathrm{T}}^{(\mathrm{SJ})}}{2} \tag{53}$$

$p_T{}^{(\mathrm{LJ})}$ is the transverse momentum of the leading jet while $p_T{}^{(\mathrm{SJ})}$ refers to the subleading jet.

– simulated events have to pass the same trigger combination as collision data.

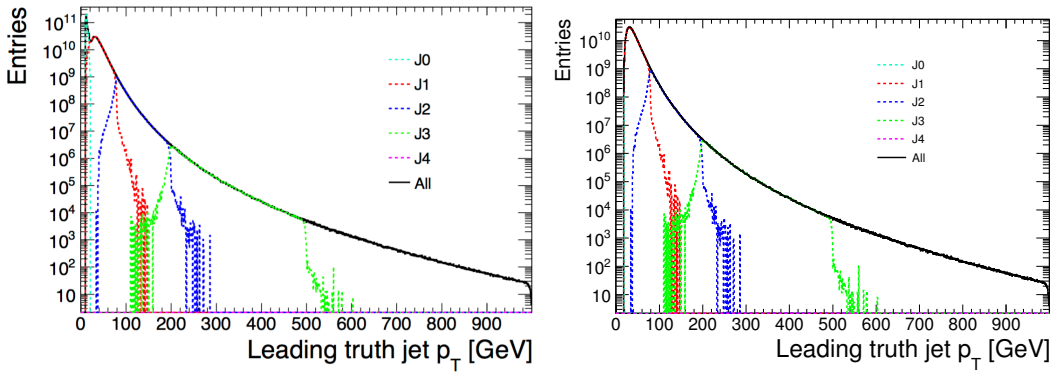

Figure 71.: Left: Leading truth jet p_T before quality cut applied. Problematic events in the J0 sample are visible at low jet p_T (the light blue spike). Right: Leading truth jet p_T after quality cut applied. Problematic events are removed.

Selections

In both data and simulation pre-selections are applied to guarantee good quality of the events. In particular, no errors in the LAr calorimeter should be present [93]. The ATLAS detector records and reconstructs jets that can originate from either a hard scatter proton-proton collision or a non-collision background processes such

as beam-induced backgrounds, cosmic particles and detector noise. Since both collisions and background jets can be reconstructed as physics objects in the detector, it is crucial to have a set of selection criteria that can distinguish between them. The development and implementation of these criteria is generally known as jet cleaning in ATLAS. The jet cleaning is applied to both MC simulations and data events. Only events containing at least one reconstructed primary vertex or one pile-up vertex, with at least 5 tracks associated, are selected.
A jet is considered *taggable* if it satisfyes the requirements:

- $p_T > 15\,\text{GeV}$
- $|\eta| < 2.5$
- |JVF[1]| > 0.5 (for jets with $p_T < 50\,\text{GeV}$)
- it does not overlap with an electron of $E_\text{T} > 25\,\text{GeV}$, $|\eta| < 2.5$, calorimeter-based isolation energy in $\Delta R < 0.2$ less than 3.5 GeV. The overlap is defined as $\Delta R(e, j) < 0.2$.

The SMT algorithm is run on all jets passing the above selections.

SMT selection cuts

In this section there is a summary of the selection cuts applied to the muon in order to use it for jet tagging. The selections are summarised in Table 18 where the first two requirements focus on the muon definition criteria.The other selections follows the muon quality recommendations from the Muon Combined Performance (MCP) group [95] and with the addition of specific cuts re-optimised for the MI version. The last four requirements are selections on the kinematic range and the impact parameters and their resolutions: d_0 is the distance of closest approach of the track to the primary vertex in the x-y plane, and z_0 is the equivalent shift along the z-axis (as shown in Figure 72). The final tagging cut requires MI < 0.1. The $|d_0|$ and $|z_0 \cdot \sin(\theta)|$ cuts are applied to suppress secondary and spurious tracks originated in the nuclear interactions of the hard scatter products with the beampipe and the tracking detectors; or badly measured track with kink from a hadronic interactions. The $|z_0 \cdot \sin(\theta)|$ cut is also effective in suppressing tracks from different vertices at high instantaneous luminosity.

From now on the jet pre-tag level is defined as the jet selection before the SMT tagging decision.

1 The Jet vertex fraction (JVF) variable is defined as the scalar transverse momentum (p_T) sum of the tracks that are associated to the jet and originate from the hard-scatter vertex divided by the scalar p_T sum of all associated tracks [94].

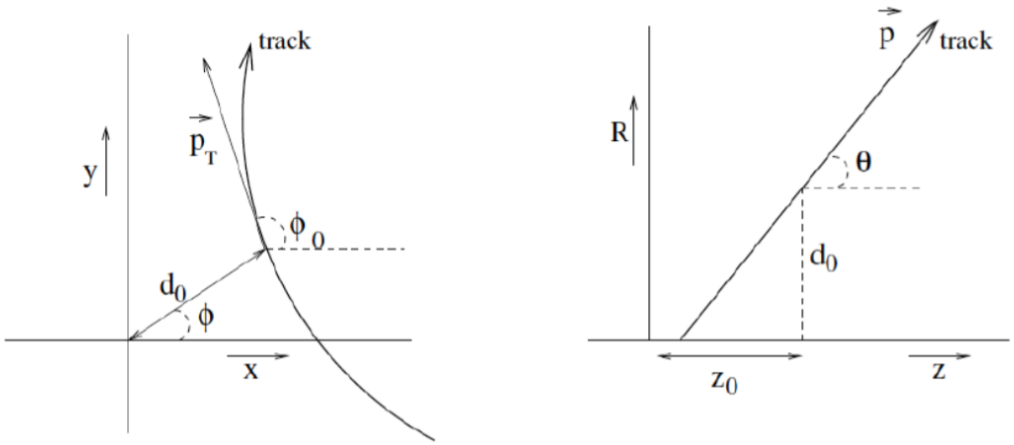

Figure 72.: Sketch of the track parameters in the transverse plane (left) and RZ-plane (right), as defined in the ATLAS tracking frame.

Muon collection and type	MCP quality cuts	Flavour tagger specific cuts
STACO collection	N(Pixel hits) + N(crossed dead Pixel sensors) $>$ 0	$p_T >$ 4 GeV
Combined muon	N(SCT hits) + N(crossed dead SCT sensors) $>$ 4	$\lvert d_0 \rvert <$ 3 mm
	N(Pixel holes) + N(SCT holes) $<$ 3	$\lvert z_0 \cdot \sin(\theta) \rvert <$ 3 mm
	If 0.1 $< \lvert\eta\rvert <$ 1.9: N(TRT hits) + N(TRT outliers) $>$ 5	$\Delta R(\mu, j) <$ 0.5
	N(TRT outliers) $<$ 0.9 [N(TRT hits) + N(TRT outliers)]	

Table 18.: Selection requirement applied to the jets. $\Delta R(\mu, j)$ is defined as $\Delta R = \sqrt{(\Delta\eta)^2 + (\Delta\phi)^2}$, in case of ambiguities, the muon is associated to the closest jet only.

Re-weighting of p_T and η spectra in MC simulations

The Pythia di-jet MC simulation is not expected to describe the jet kinematics of the data in an accurate way. Both jet p_T and η are different in data and simulation already at the pre-tag level. Furthermore trigger pre-scaling is applied to data but not to MC simulation. The jet p_T spectrum at pre-tag level is shown in Figure 73. The peaks visible in the p_T spectrum in data correspond to the activation of the various trigger thresholds affected by a lower pre-scale factor. The pre-tag distributions of η and the average number of interactions per bunch crossing, μ, are displayed in Figure 74.

The re-weighting procedure is applied to the events such that the jet p_T and η distribution in MC simulations match the corresponding ones in data at pre-tag level. In particular, the re-weighting factor is evaluated from a bi-dimensional comparison in the p_T-η phase space of jets in data and MC simulations, applied after the MC simulation has been re-weighted to pileup using a 1-D distribution of $\bar{\mu}$, on an event-by-event basis depending on which trigger is activated. The resulting dis-

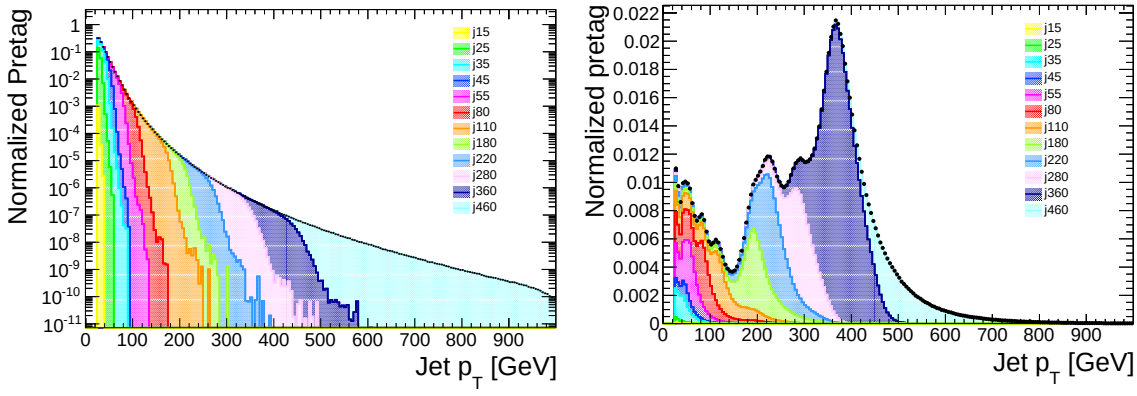

Figure 73.: The leading and sub-leading jet p_T distribution for individual triggers in MC simulation (left) and data (right) in di-jet events at the pre-SMT tag level. The black dots represent the total distribution across all triggers.

tributions of re-weighted jet kinematics at pre-tag and tag-level in MC simulations are shown in comparison to data in Figures 75 to 77.

Even with the rescaling there remains a discrepancy for low p_T jets at SMT-tagged level; the overall outcome being that the jets are softer in data than simulation, as shown in Figure 76. Furthermore it can be seen from Figure 78 that for very low p_T (less than 60 GeV) the leading/sub-leading jets are highly imbalanced, in particular the sample in p_T below 40 GeV consists almost entirely of sub-leading jets. How well balanced the jets are will affect the SMT tagging rate, since in the decay of a $b-$ or $c-$jet to a muon there will also be a neutrino present, thus high MET. This will correspond to a lower energy jet, and since, by definition, sub-leading jets have a lower energy, a sample rich in sub-leading jets will have an enhanced SMT rate. If the trigger for the event is much higher than the lower bound of the p_T range of the bin, all jets for this bin will be sub-leading and thus there will be an enhancement in the number of SMT-tagged jets and a trigger bias will be introduced. To remove this, a further requirement is imposed: for each p_T bin only events triggered by a jet with p_T lower than or equal to the lower p_T bound are included. This ensures that the SMT rate is not tested in a pool of jets which is artificially enriched in heavily unbalanced di-jets.

6.3.2 *Determination of the Mistag Rate in Simulation*

The expected mistag rate is extracted in MC simulations from reconstructed jets originated by LF decays, using truth-level information. In this analysis simulated jets are categorised according to their true origin into four classes: b, c, LF and τ jets, using the truth information available in the ATLAS software called Athena for

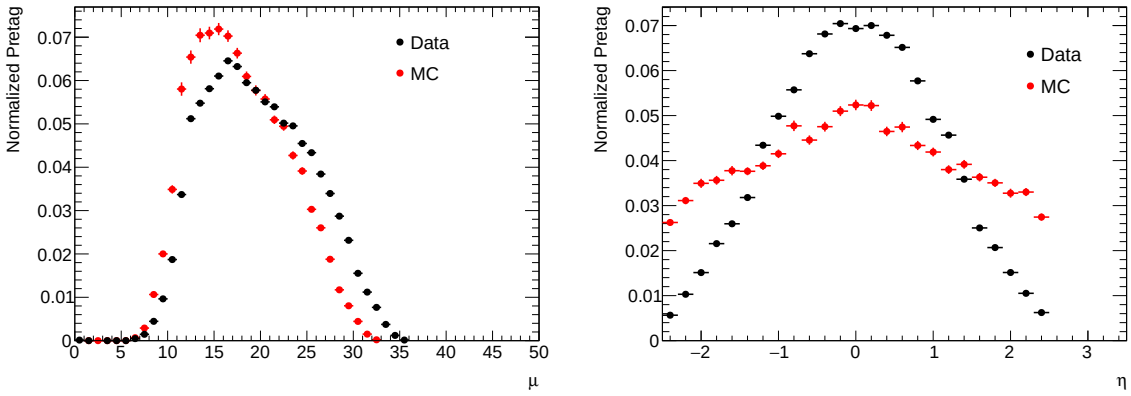

Figure 74.: Left: Comparison of the distribution of the number of interactions per bunch crossing ($\bar{\mu}$) for MC simulation (red line) and data (black dots), before any reweighting. Right: Comparison of the jet η distributions in MC simulation (red line) and data (black dots) at the pre-SMT tag level.

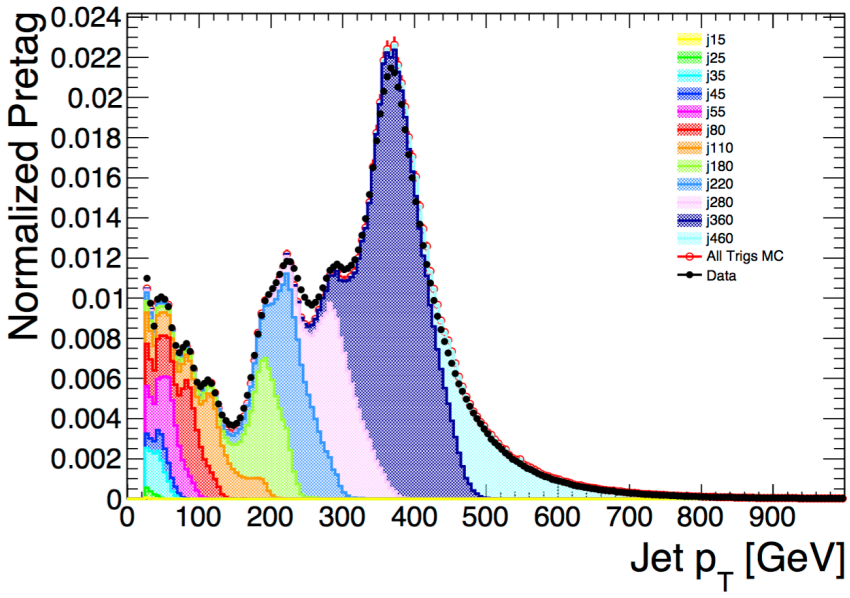

Figure 75.: Jet p_T distribution (leading and sub-leading jet) after re-weighting for each trigger in MC simulation.

each jet in the collection.
The mistag rate is defined as:

$$\varepsilon^{MC}_{LF,SMT} = \frac{N(SMT\ tagged\ LF\ jets)}{N(taggable\ LF\ jets)} \tag{54}$$

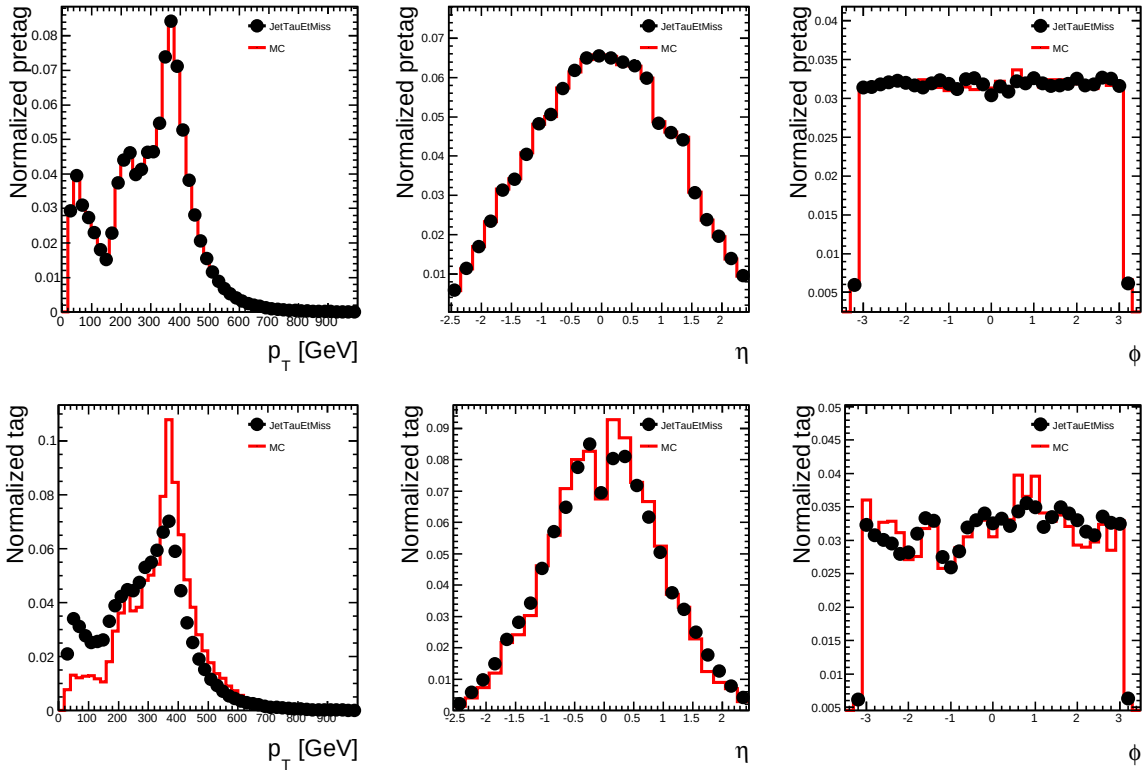

Figure 76.: Comparison of kinematic quantities (left to right: p_T, η and ϕ) after the MC jets have been re-weighted to pre-tag level p_T, η and $\bar{\mu}$ in data. Top: pretag level jets. Bottom: SMT tagged jets. The MC simulation and the data are normalized separately to unit area.

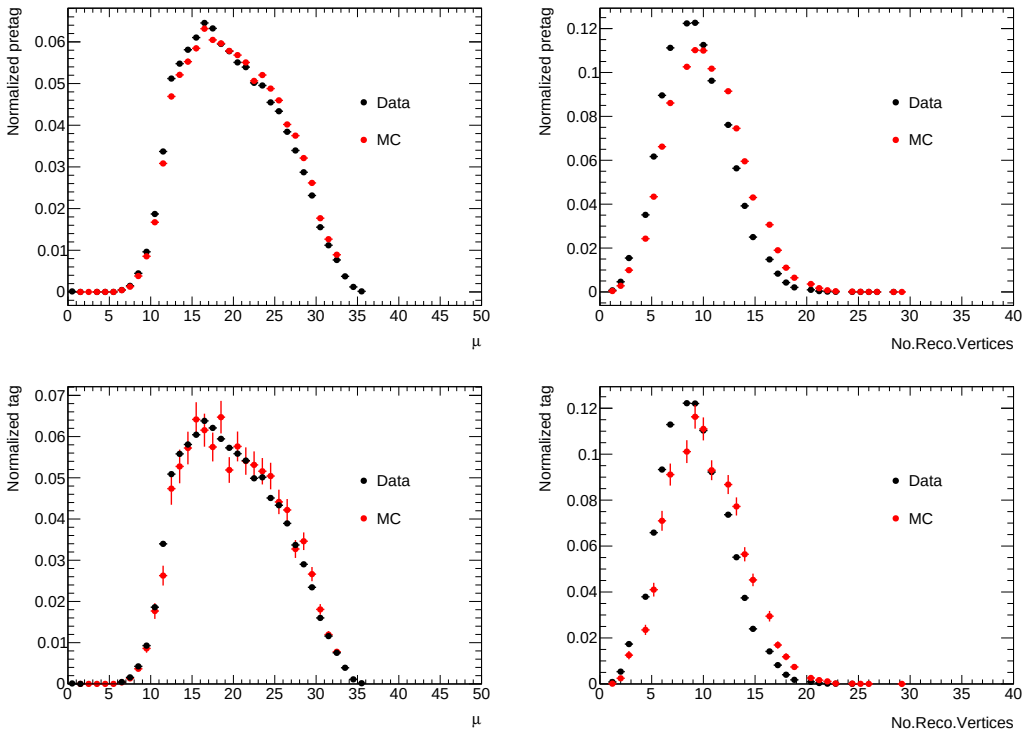

Figure 77.: Comparison of number of interactions per bunch crossing (left) and number of pp interaction vertices (right) for pretag (top) and SMT tagged (bottom) events. The MC simulation and data are normalized separately to unit area.

p_T range [GeV]	$\varepsilon^{MC}_{(LF,SMT)}$ [10^{-3}]
25–35	1.29 ± 0.25
35–45	1.37 ± 0.16
45–55	1.92 ± 0.16
55–80	2.60 ± 0.12
80–110	3.26 ± 0.20
110–140	4.88 ± 0.21
140–180	6.01 ± 0.29
180–220	6.78 ± 0.50
220–280	8.01 ± 0.46
280–360	10.81 ± 0.52
360–460	11.46 ± 0.42
460–500	12.73 ± 0.71
500–1000	16.49 ± 0.50

Table 19.: Mistag rate of the SMT in simulation for LF-originated jets selected at truth level ($\varepsilon^{MC}_{LF,SMT}$) in events with at least one taggable jet, for jets binned by reconstructed jet p_T and integrated over all η. All triggers up to the lower boundary of the p_T bin are considered. Statistical uncertainties are of the order 10^{-5} or smaller and only systematic uncertainties are shown in this table.

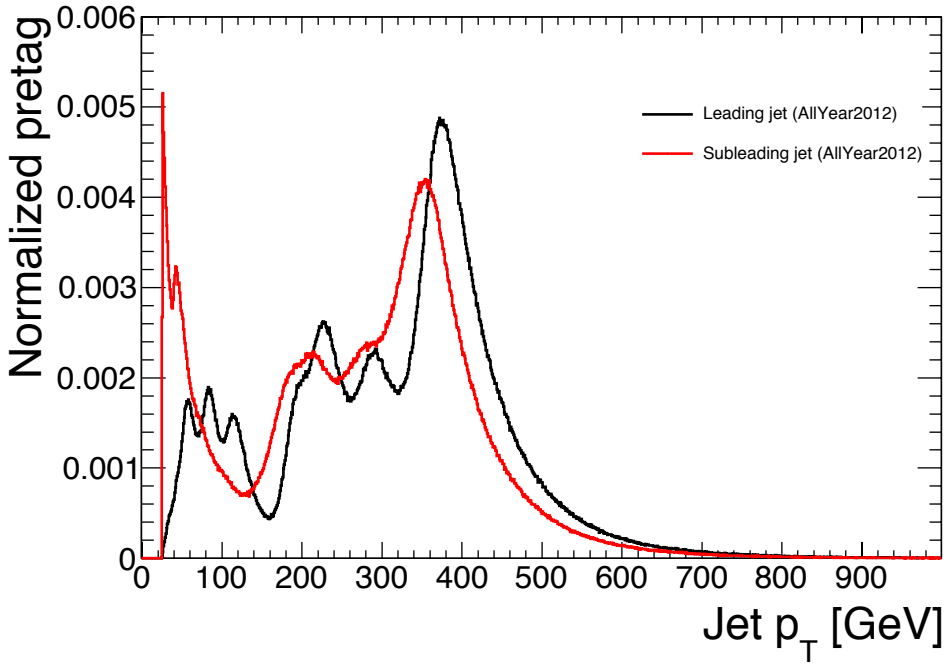

Figure 78.: Leading (black) and sub-leading (red) p_T distributions in data for jets before SMT tagging.

The values of $\varepsilon^{MC}_{LF,SMT}$ as a function of jet p_T are reported in Table 19.

The fake rate increases with the jet p_T presumably due to the fact that high energy LF-jets are expected to produce on average higher p_T muons and tracks which in turn have a lesser imbalance in momentum between the ID and MS than decays in flight of lower p_T mesons. Figure 79 shows the SMT muon p_T, the jet p_T and the momentum imbalance distributions for di-jet data and MC light-flavour simulations.

6.3.3 *Determination of the Mistag Rate in Data*

The MC simulation is not expected to model perfectly the fragmentation of light flavour quarks and the decay of light flavour hadrons, nor to model accurately all processes creating fake tags, like nuclear interactions and punch-through of (mainly) light mesons. Therefore the goal is to measure the SMT mistag rate relying on data information as much as possible.

A method based on a system of equations is used in order to extract the mistag rate from quantities measured in data. In this analysis the SMT is the tagger to calibrate and a lifetime tagger (LT) based on secondary vertex information is used as an auxiliary tagger to select an enhanced sample of LF-originated jets in data.

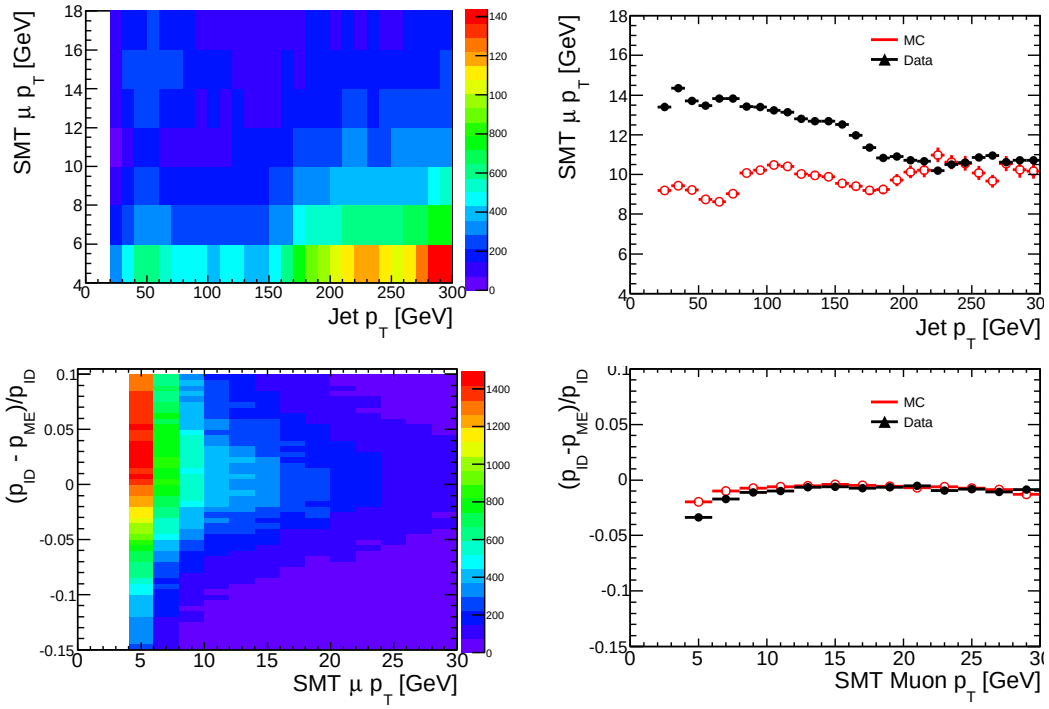

Figure 79.: Top left: 2D contour plot of the p_T of the SMT muon as a function of the jet p_T in data. Top right: profile of the SMT muon p_T against jet p_T for both data and MC simulation. Bottom left: 2D contour plot of the MI vs SMT μ p_T in data. Bottom right: profile of the MI vs SMT μ p_T for both data and MC simulation. In the profiles, red circles represent di-jet simulation and black circles are data.

Looking at events with two, and only two, jets passing all the selection of Section 6.3.1 we form two ensembles of events: in the first there are all events in which at least one jet is **not** HF-tagged by the LT of choice (single veto); in the second category there are events in which both jets are **not** HF-tagged by the LT (double veto).
Given that the LT efficiency to tag HF-originated jets, $\varepsilon_{HF,MV1}$, is not 100%, then in the first sample there is a contamination from HF pair production ($b\bar{b}$ and $c\bar{c}$). In the second sample the rate of HF-originated jets is expected to be further suppressed. The amount of HF in the double veto sample largely determines the magnitude of the uncertainty associated with the measurement of the mistag rate. Therefore, it is important to choose a LT with a high HF tagging efficiency (highest available HF rejection in the veto). The lifetime tagger that is used in this case is MV1 at nominal 80% efficiency, using the working point $w(MV1) \geq 0.3511$ as the veto [85].
The number of jets in data which are tagged by the SMT in each of the two above samples is given by Equation 55,

$$N^{(1)}_{data,SMT} = N^{(1)}_{data}[(\varepsilon_{HF,SMT} \cdot f_{HF}) + (\varepsilon_{LF,SMT} \cdot [1 - f_{HF}])] \tag{55a}$$
$$N^{(2)}_{data,SMT} = N^{(2)}_{data}[(\varepsilon_{HF,SMT} \cdot f'_{HF}) + (\varepsilon_{LF,SMT} \cdot [1 - f'_{HF}])] \tag{55b}$$

where $N^{(1)}_{data}$ ($N^{(2)}_{data}$) is the number of selected jets in events of the type single (double) veto, $N^{(1)}_{data,SMT}$ ($N^{(2)}_{data,SMT}$) is the number of selected jets in events of the type single (double) veto, which are also tagged by the SMT. The $\varepsilon_{LF,SMT}$ is the unknown SMT mistag rate, $\varepsilon_{HF,SMT}$ is the SMT tagging efficiency for HF and f_{HF}, f'_{HF} are the fractions of heavy flavour jets in the single- and double-vetoed samples, respectively. The f'_{HF}, i.e. the heavy flavour component of the double-vetoed sample, can be related to the heavy flavour component in the single-vetoed sample f_{HF} by defining the ratio $R_{HF,MV1}$ in Equation 56:

$$R_{HF,MV1} = 1 - \frac{f'_{HF} N^{(2)}_{data}}{f_{HF} N^{(1)}_{data}} = 1 - \frac{N^{(2)}_{HF}}{N^{(1)}_{HF}}, \tag{56}$$

hence solving the system of equations in 55 for the SMT mistag rate (see Appendix)

$$\varepsilon_{LF,SMT} = \frac{[N^{(1)}_{data,SMT} \cdot (1 - R_{HF,MV1}) - N^{(2)}_{data,SMT}]}{[N^{(1)}_{data} \cdot (1 - R_{HF,MV1}) - N^{(2)}_{data}]} \tag{57}$$

The ratio $R_{HF,MV1}$ is not known in data and is taken from simulation for each of the p_T bins for which the mistag rate is extracted. It takes into account the HF tagging scale factors (SF_{HF}) for the efficiency modelling of the MV1 tagger. SF_{HF} are corrections applied to MC simulations to reproduce data [85]. Heavy flavour (b-

and c-) jets are scaled according to their flavour using truth matching. Any HF jet that is MV1 tagged is scaled by the MV1 efficiency factor for that flavour whereas any jet not MV1 tagged is scaled by the inefficiency factor.
The plot in Figure 80 shows the fraction of heavy flavour events in the single and double vetoed samples, according to the simulation. The single veto sample has an heavy flavour fraction of about 30% of the jets, whereas the double vetoed sample has a heavy flavour contamination of just below 10%.

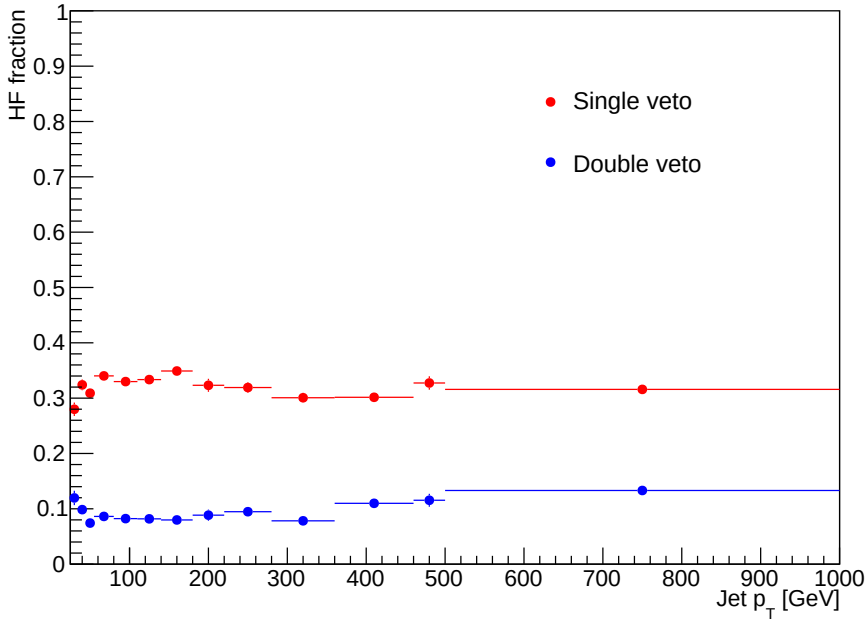

Figure 80.: Fraction of heavy flavour jets in the single and double MV1-vetoed di-jet samples, from MC simulation.

6.3.4 *Systematic uncertainties*

The main causes for systematic uncertainties in the measurement of $\varepsilon_{LF,SMT}$ arise from both the use of MV1 as an advanced lifetime tagger and the residual heavy flavour component in the samples.
The HF sample, from which $R_{HF,MV1}$ is obtained, is made up of b- and c-jets selected at truth level. Each HF jet is scaled using the MV1 scale factor, taking into account whether the jet is b- or c-originating.
The systematic uncertainty associated with $R_{HF,MV1}$ originates from MV1 algorithm calibration efficiency and it is calculated independently for c- and b-jets us-

ing the eigenvector variation method in which the scale factor for MV1 for c-(b-)jets is increased by $\pm\sigma$ (where σ is the uncertainty on the scale factor applied to each HF jet). There are 10 eigenvector variations (because the MV1 calibration was performed in 10 p_T bins) for b-jet and 6 for c-jets (because the MV1 calibration was performed in 6 p_T bins, each yielding a new measurement of the HF efficiency). Uncertainties due to the MV1 calibration for jets above 300 GeV are derived by extrapolating back from lower p_T.
The fraction of b-originated jets over the total HF-jets in the Pythia di-jet MC is assigned a systematic uncertainty by varying the nominal fraction by factors of 0.5 and 2.0. Similarly, the overall heavy flavour content is also varied by factors of 0.5 and 2.0. In addition to these systematic uncertainties, due to the heavy flavour sample composition, other uncertainties are considered: the momentum imbalance scale factors, the muon reconstruction ID scale factors and the MV1 scale factors (including that from the bias as described in section 6.3.4) and they were added in quadrature with the statistical uncertainties.
The values of $R_{HF,MV1}$ and the associated uncertainties are shown in the table 20 and Figure 81.

p_T[GeV]	$R_{HF,MV1}$
25–35 GeV	$0.529^{+0.019}_{-0.022}$
35–45 GeV	$0.504^{+0.013}_{-0.013}$
45–55 GeV	$0.521^{+0.019}_{-0.016}$
55–80 GeV	$0.548^{+0.018}_{-0.015}$
80–110 GeV	$0.572^{+0.018}_{-0.016}$
110–140 GeV	$0.570^{+0.019}_{-0.016}$
140–180 GeV	$0.567^{+0.022}_{-0.020}$
180–220 GeV	$0.561^{+0.025}_{-0.022}$
220–280 GeV	$0.555^{+0.026}_{-0.024}$
280–360 GeV	$0.553^{+0.025}_{-0.022}$
360–460 GeV	$0.554^{+0.020}_{-0.020}$
460–500 GeV	$0.539^{+0.019}_{-0.018}$
500–1000 GeV	$0.543^{+0.018}_{-0.018}$

Table 20.: $R_{HF,MV1}$ in simulation and including uncertainties from the MV1 calibration and the heavy flavour composition of the samples.

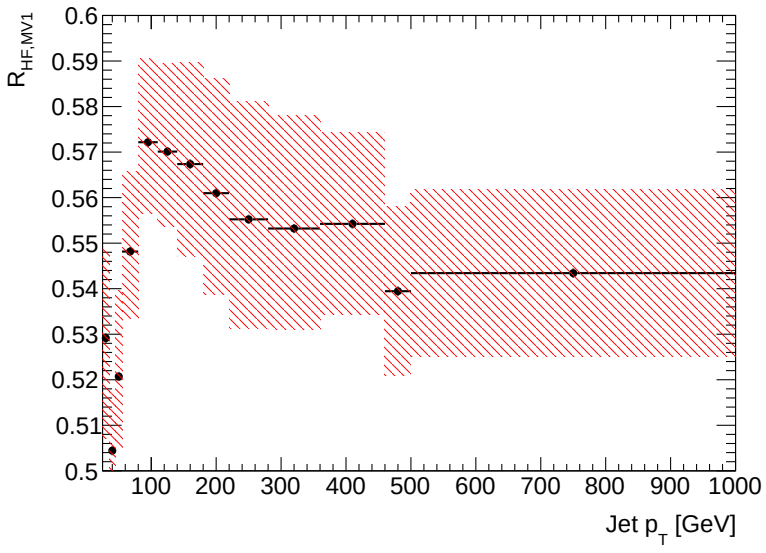

Figure 81.: The values of R_{HF} as a function of p_T. The error band includes systematic uncertainties from the MV1 and the heavy flavour composition of the samples.

Bias of the method from MV1 veto

In order to verify (and quantify) a possible bias of the mistag rate estimation arising from usage of the single and double veto events with respect to the true mistag rate in our sample, it is possible to rely on MC simulation. The assumption is that the same *relative* bias observed in the simulation is also present in data. The bias is defined as:

$$\delta = \frac{\varepsilon_{\mathrm{LF},SMT,true} - \varepsilon_{\mathrm{LF},SMT,MV1\ veto}}{\varepsilon_{\mathrm{LF},SMT,true}}, \tag{58}$$

where $\varepsilon_{\mathrm{LF},SMT,true}$ is the fake rate of the SMT (tagging rate of light-flavour jets) in the simulation with truth matching, and $\varepsilon_{\mathrm{LF},SMT,MV1\ veto}$ is the fake rate of the SMT (tagging rate of light-flavour jets) in the simulation with truth matching but only for jets which have a MV1-veto. This fake rate is evaluated for events with at least one taggable jet as a function of the jet p_T (for the central and forward regions in η). The bias is shown in Figure 82.

The requirement of an MV1 veto is seen to introduce a bias of -0.5%, which is negligible compared to the method uncertainties.

Bias of the method from heavy flavour composition

The set of Equations 55 assumes the same efficiency $\varepsilon_{HF,SMT}$ for both the single-veto and the double-veto sample. Since the samples contain a different mix of bot-

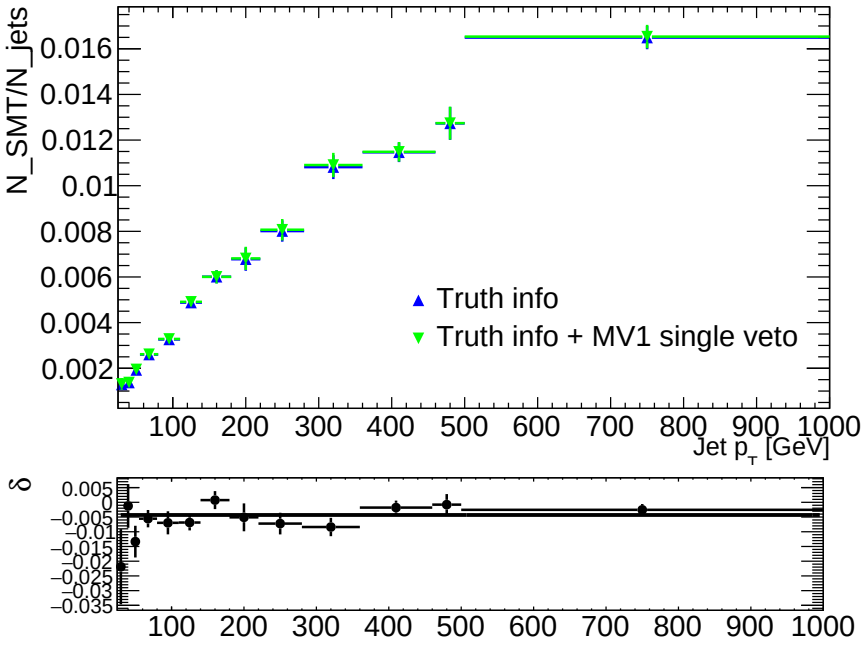

Figure 82.: Top: Mistag rate in MC events with at least one taggable jet, for LF-originated jets selected at truth level (blue triangles) and selected at truth level and with MV1 weight $w < 0.3511$ (MV1 vetoed, green triangles). Bottom: Bias, δ, as a function of jet p_T .

tom and charm, this assumption is only an approximation. Indeed a closure test performed on MC simulated di-jets shows a bias originating from the different $\varepsilon_{HF,SMT}$ for the two samples. Figures 83 and 84 show the bottom to charm ratio in the single and double veto samples and the average SMT efficiency on those heavy flavour events. The double veto action suppresses primarily bottom quarks, reducing the ratio. The SMT efficiency shown is an average over the b and c mixture of the sample.

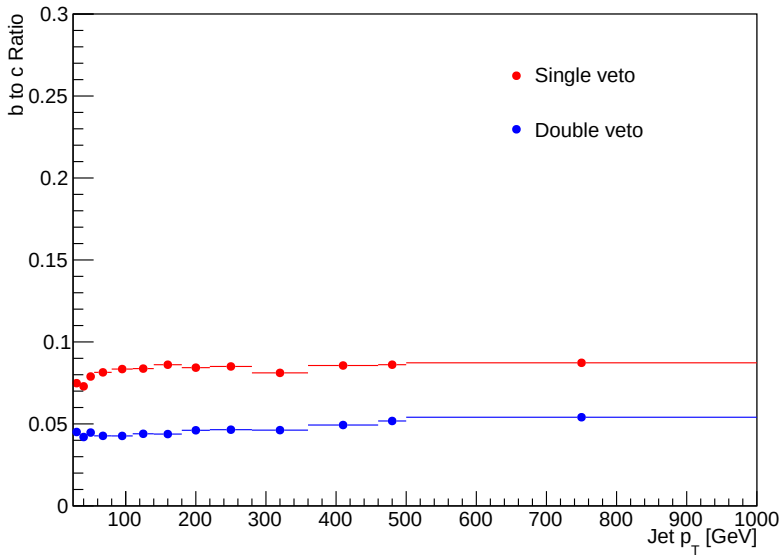

Figure 83.: The bottom to charm ratio in the single and double veto samples.

The plots in Figure 85 show the closure test of the Equations 55. In the variations plotted, the heavy flavour component has been doubled and halved both in the b to c content and in absolute value with respect to the light flavour component of the samples. The correction, in absolute value, is of about $1.4\,10^{-3}$ and is independent of the actual fake rate, as indicated in Figure 85 (right plot), being dependent instead only on the HF composition of the sample. The independence on the fake rate is deduced both from the p_T dependence, which corresponds also to a span of fake rate values changing by an order of magnitude from 0.001 to nearly 0.02, and from a test in which we increased by 3 the simulated fake rate for all p_T bins. A bias correction magnitude will be applied to the measurement in the data.

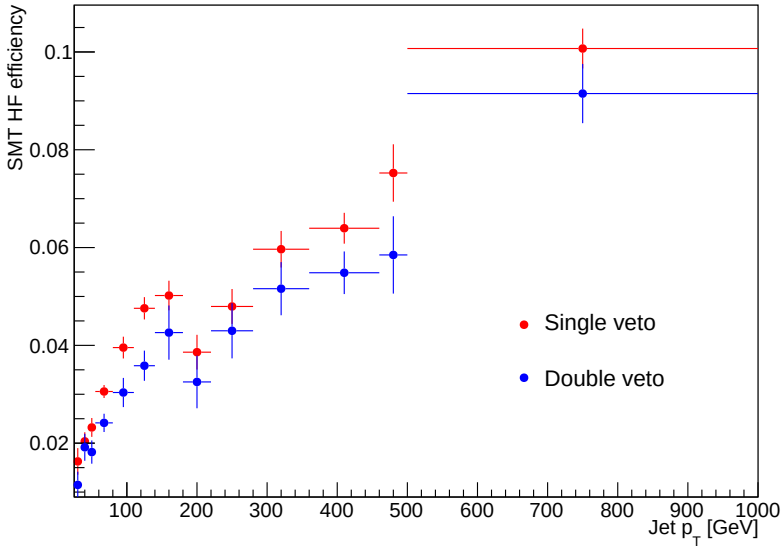

Figure 84.: The efficiency of the SMT on the heavy flavour events present within the single and double veto samples.

6.3.5 *Results*

The mistag rate $\varepsilon^{data}_{LF,SMT}$ is measured on data using Equation 57. The values for $N^{(1,2)}$, $N^{(1,2)}_{SMT}$, the corresponding mistag rates for data and simulation and scale factors are presented in Table 21 and in graphical form in Figure 86. The negative value of the first bin is possible due to the combined effect of a low R_{HF} and an excess in the number of tagged jets in the single veto sample but is well within statistical uncertainties. The scale factor is defined as follows:

$$SF_{LF,SMT} = \frac{\varepsilon^{data}_{LF,SMT}}{\varepsilon^{MC}_{LF,SMT}}. \tag{59}$$

The values of the closure bias from the heavy flavour composition are also included in the Table 21 (Offset).

6.3.6 *Study of the dependence on multiple interactions and pile-up*

In order to apply the mistag rate measurement and scale factor to other datasets, the mistag rate dependence on the number of interactions and pileup at the detector (especially tracking) level was studied.

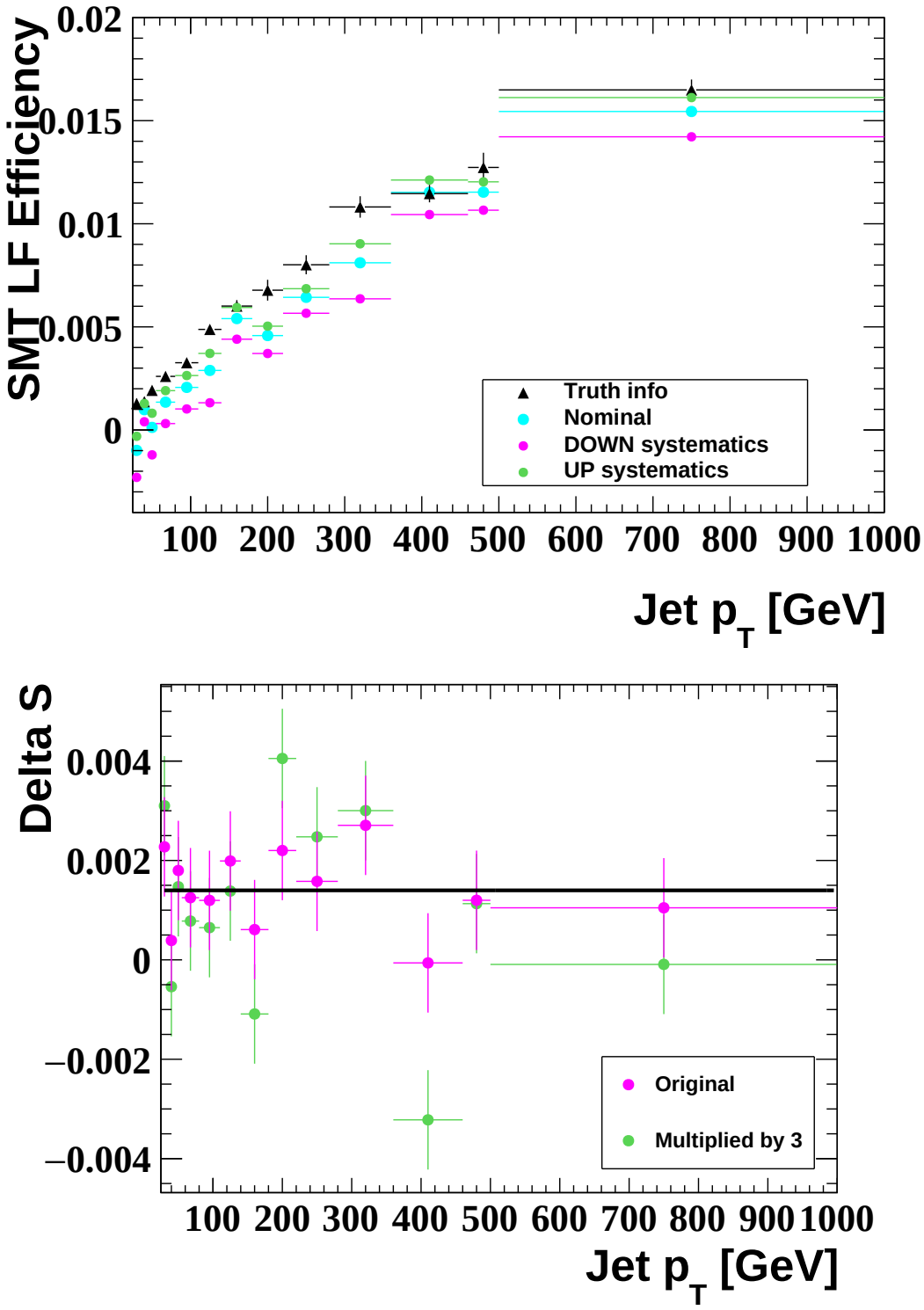

Figure 85.: Closure test of the di-jet method, showing a bias with respect to the truth light flavour tag rate. The plot on the right reports the difference between measured and true fake rate. As additional test test, the true fake rate has been also increased entirely by a factor of three across all p_T bins.

p_T [GeV]	$N^{(1)}$	$N^{(2)}$	$N^{(1)}_{SMT}$	$N^{(2)}_{SMT}$	$\varepsilon^{Data}_{(LF,SMT)}$ [10^{-3}]	Offset [10^{-3}]	$SF_{Data/MC}$
25–35	3753	2883	20	9	$-0.38 \pm 2.97^{+0.44}_{-0.36}$	$2.27^{+1.65}_{-1.22}$	$1.48^{+2.59}_{-2.58}$
35–45	18773	14543	121	57	$-0.58 \pm 1.53^{+0.33}_{-0.32}$	$0.39^{+1.16}_{-1.05}$	$-0.13^{+1.39}_{-1.39}$
45–55	23894	18500	157	81	$0.82 \pm 1.24^{+0.41}_{-0.35}$	$1.80^{+1.67}_{-1.21}$	$1.36^{+1.00}_{-1.01}$
55–80	87204	66651	787	362	$0.23 \pm 0.76^{+0.46}_{-0.48}$	$1.25^{+1.44}_{-1.15}$	$0.57^{+0.60}_{-0.61}$
80–110	114707	86388	1289	621	$1.86 \pm 0.69^{+0.69}_{-0.51}$	$1.20^{+1.45}_{-1.16}$	$0.94^{+0.47}_{-0.48}$
110–140	130799	97457	1753	819	$1.58 \pm 0.74^{+0.74}_{-0.70}$	$1.99^{+1.86}_{-1.30}$	$0.73^{+0.38}_{-0.39}$
140–180	80817	59729	1097	568	$3.76 \pm 0.94^{+0.94}_{-0.69}$	$0.61^{+1.42}_{-1.15}$	$0.73^{+0.29}_{-0.29}$
180–220	416223	306153	4554	2541	$4.39 \pm 0.37^{+0.37}_{-0.53}$	$2.20^{+1.34}_{-1.11}$	$0.97^{+0.20}_{-0.20}$
220–280	754508	548355	8847	5050	$5.24 \pm 0.30^{+0.57}_{-0.57}$	$1.58^{+1.27}_{-1.09}$	$0.85^{+0.17}_{-0.17}$
280–360	826344	588785	10674	6225	$6.63 \pm 0.48^{+0.87}_{-0.56}$	$2.71^{+2.02}_{-1.37}$	$0.86^{+0.17}_{-0.17}$
360–460	2650000	1830000	41262	24178	$8.91 \pm 0.21^{+0.56}_{-0.52}$	$-0.06^{+1.50}_{-1.20}$	$0.77^{+0.13}_{-0.13}$
460–500	372866	250382	6711	3950	$10.91 \pm 0.68^{+0.65}_{-0.60}$	$1.20^{+1.36}_{-1.16}$	$0.95^{+0.12}_{-0.12}$
500–1000	515188	334595	10858	6233	$12.82 \pm 0.70^{+0.83}_{-0.74}$	$1.05^{+1.63}_{-1.26}$	$0.84^{+0.11}_{-0.11}$

Table 21.: Left to right: Number of jets in the single ($N^{(1)}$) and double ($N^{(2)}$) veto samples at pretag level; Number of jets tagged by the SMT momentum imbalance algorithm in the single ($N^{(1)}_{SMT}$) and double ($N^{(2)}_{SMT}$) veto samples; Mistag rate in data ($\varepsilon^{Data}_{(LF,SMT)}$) with statistical (the first set) and systematic (the second set) uncertainties; Offset for closure bias test (Offset); Scale factor ratio (bias corrected) of mistag rate in data to simulation ($SF_{Data/MC}$) with the total statistical and systematic uncertainty.

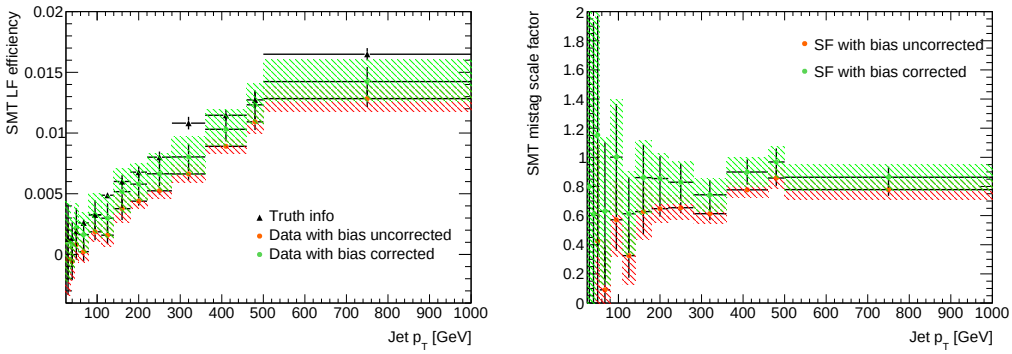

Figure 86.: Mistag rate in data (black dots) and simulation (red and green) as a function of the jet p_T, integrated over all η. The uncertainties in black are statistical only and in red and green bands are including systematic. The right panel shows the ratio between data and MC simulation.

Given the SMT only relies on a well reconstructed and identified muon track and there is little dependence of muon tracking on pileup, we have reason to believe that pileup and multiple interactions (MI) should not affect the mistag rate. To test this, the dataset is divided up into 5 bins in $< \mu >$ (the number of interactions per bunch crossing) and 4 bins in the number of reconstructed vertices (No.Reco.Vertices). The plots in Fig. 87 and Fig. 88 show the efficiency of MV1 as a function of the average number of interactions and of the number of reconstructed vertices. The behaviour is consistent with no dependence. The plots in Fig. 89 show the SMT fake tagging efficiency as a function of the number of vertices and number of interactions measured in data and from the truth simulation. The ratio of the efficiencies, i.e. the scale factor, is shown in Fig. 90. The SF is independent on the number of reconstructed vertices, while a small trend is visible as a function of the number of interactions, i.e. the fake rate increases slightly with more pile-up but it is negligible.

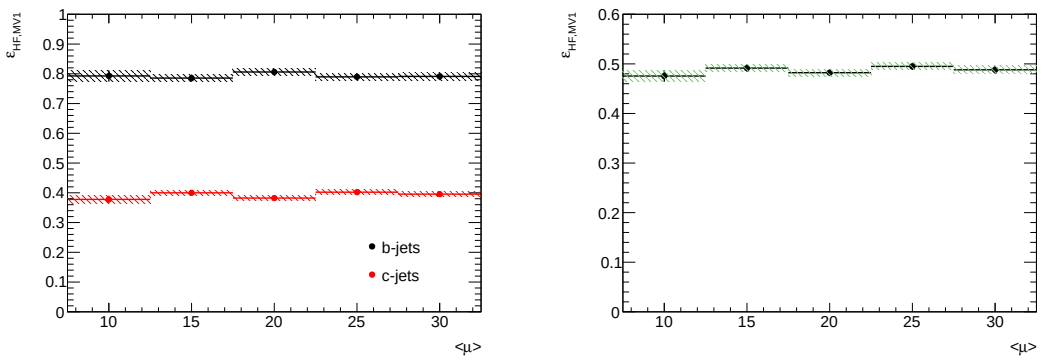

Figure 87.: Efficiency of tagging heavy flavour jets with MV1 in sumulation as a function of the average number of interactions, $< \mu >$. Left: b- and c- jets; Right: all heavy flavour jets.

6.3.7 *Complementarity of the W+jets and Di-jets fake rate evaluations*

The complementarity of the W+jets and di-jets method are evident considering that for di-jets there are very large trigger prescales in the region $p_T < 140$ GeV, while the W+jets estimate is optimal below 100 GeV. More coarsely-binned scale factors are given in Table 22 and presented in Figure 91 alongside the W+jets estimates. Here, statistical and systematic uncertainties have been combined in quadrature. The W+jets and the di-jets method are in agreement within the errors and they can be used in the low-p_T and high-p_T regions respectively, since they are two complementary methods. These methods were used in the measurements of charge

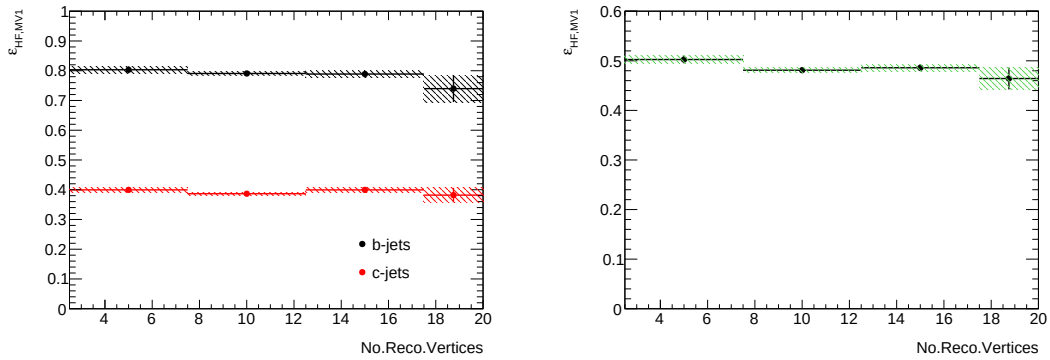

Figure 88.: Efficiency of tagging heavy flavour jets with MV1 in simulation as a function of the average number of reconstructed vertices. Left: *b*- and *c*- jets; Right: all heavy flavour jets.

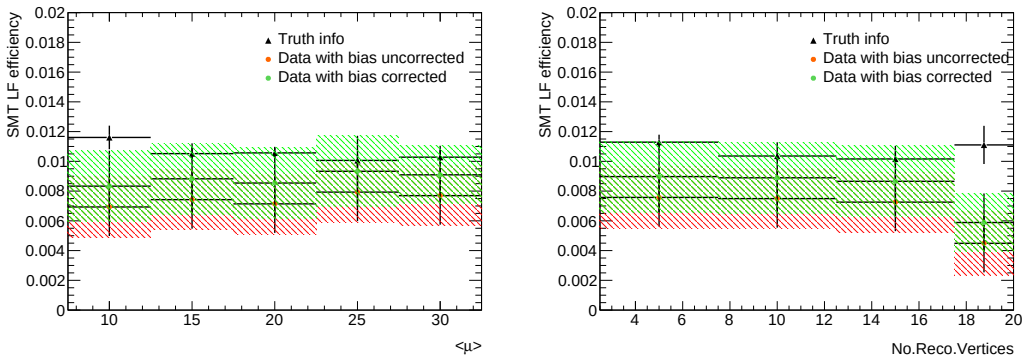

Figure 89.: SMT fake efficiency for data and MC simulation as a function of the average number of interactions, $< \mu >$ (left) and the average number of reconstructed vertices (right).

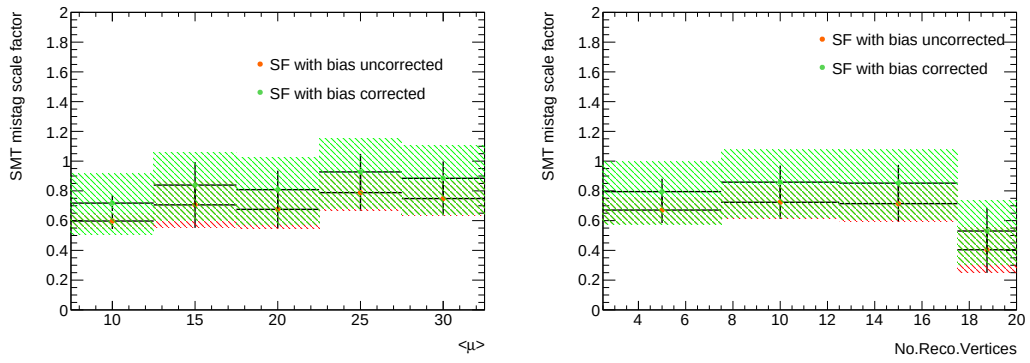

Figure 90.: Scale factor of the SMT fake efficiency between data and MC simulation as a function of the average number of interactions, $< \mu >$ (left) and the average number of reconstructed vertices (right).

and $\mathcal{CP}$ asymmetries in b-hadron decays using top-quark events collected by the ATLAS detector in pp collisions at $\sqrt{s} = 8$ TeV [16].

p_T range [GeV]	f_{HF} [%]	f'_{HF} [%]	$\varepsilon^{MC}_{(LF,SMT)}$ [10^{-3}]	$\varepsilon^{Data}_{(LF,SMT)}$ [10^{-3}]	$SF_{Data/MC}$
25–80	21	16	2.24 ± 0.09	$0.15 \pm 1.03^{+0.43}_{-0.42}$	$0.66^{+0.86}_{-0.78}$
80–140	23	18	4.16 ± 0.15	$1.72 \pm 0.72^{+0.58}_{-0.56}$	$0.80^{+0.46}_{-0.37}$
140–220	16	11	6.60 ± 0.39	$4.28 \pm 0.46^{+0.71}_{-0.72}$	$0.94^{+0.22}_{-0.18}$
220–360	13	10	9.81 ± 0.37	$5.94 \pm 0.30^{+0.02}_{-0.07}$	$0.83^{+0.17}_{-0.13}$
360–500	11	9	11.63 ± 0.38	$9.14 \pm 0.25^{+0.05}_{-0.02}$	$0.83^{+0.12}_{-0.10}$
500–1000	12	9	16.49 ± 0.50	$12.82 \pm 0.70^{+0.71}_{-0.85}$	$0.90^{+0.11}_{-0.10}$

Table 22.: Left to right: $\varepsilon_{LF,SMT}$ in MC, $\varepsilon_{LF,SMT}$ in data with statistical (the first set) and systematic (the second set) uncertainties, and the ratio $SF_{Data/MC}$ with combined statistical and systematic uncertainties as a function of jet p_T. The closure bias has been corrected in the Scale Factor. The f_{HF} and f'_{HF} are the fractions of heavy flavour defined in Eq. 55. The approximate values are calculated from data using the same equation and the simulated $\varepsilon_{HF,SMT}$.

6.4 CONCLUSIONS ON THE RUN-1 SMT MISTAG RATE CALIBRATION

The results of the calibration of the efficiency and mistag rate of the Soft Muon Flavour Tagger in its momentum imbalance version have been presented.

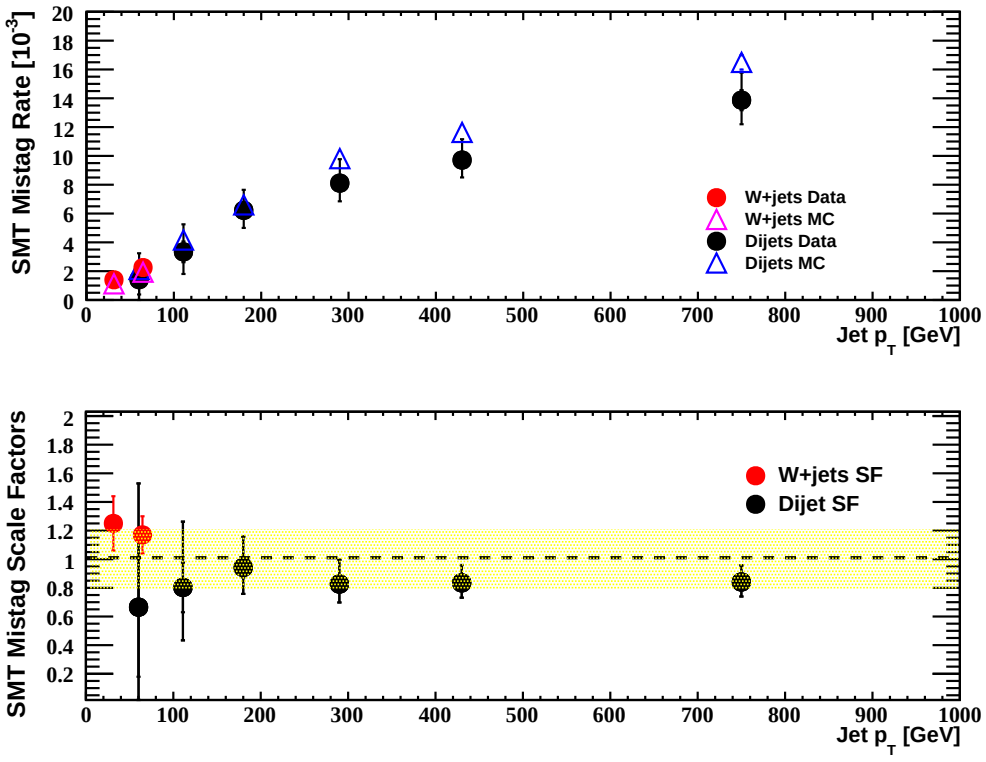

Figure 91.: Coarsely-binned mistag rate in data (black dots) and simulation (blue) as a function of the jet p_T , integrated over all η. The uncertainties include statistical and systematic. The lower panel shows the ratio between data and MC simulation for both the di-jet and the W+jets methods.

In this Chapter, the calibration of the mistag rate has been shown as performed with a dijet inclusive sample. The mistag rate is of order 10^{-3} for jets below 100 GeV to 10^{-2} at around and over 500 GeV in both data and MC simulation; the agreement between data and simulation is within 20%, which is remarkably good considering that the SMT mistag rate is the result of light-flavour fragmentation physics and detector mis-reconstruction. The data to MC scale factor is given binned in p_T of the jets.
The HF overall fraction and composition (b, c) dominates the uncertainty on the SFs at low p_T while the MV1 efficiency dominates the uncertainty at high p_T.
In all the performed studies there is no dependence of the mistag rate and SFs on multiple interactions and pile-up.

6.5 MEASUREMENT OF CHARGE AND $\mathcal{CP}$ ASYMMETRIES AT 8 TeV

The calibration of the mistag rate of the SMT was a key element for the measurements of charge and $\mathcal{CP}$ asymmetries in B-hadron decays using top-quark events collected by the ATLAS detector during Run-1, published in this paper [16].
The Run-1 analysis proceeds as follows, and the Run-2 analysis is based on the same guidelines:

1. The analysis first performs a "standard" $t\bar{t}$ lepton+jets events selection, using objects reconstructed by the ATLAS detector [52].

2. Events are selected in which a jet is b-tagged with both a displaced vertex based algorithm and a soft muon tagger algorithm, called SMT. Since the measurement presented in this thesis focuses on CAs in heavy flavour mixing and decays, double tagging is required to reduce the contribution from soft muon not originating from heavy hadrons decays, *i.e.* reduce the component of soft muons coming from light-jets which can spoil the measurement.

3. The inclusive $t\bar{t}$ cross section is measured to demonstrate that the data is well understood.

4. A kinematic likelihood algorithm, the KLFitter [96], is performed to fully reconstruct the $t\bar{t}$ system.

5. The KLFitter determines if an SMT muon comes from the same- or different-top quark than the lepton from the W-boson decay. This allows a precise determination of the initial charge of the b.

    a) For same-top SMT muons : $W^{\pm} \rightarrow b^{\mp}$

b) For different-top SMT muons : $W^{\pm} \rightarrow b^{\mp}$

6. Charge asymmetry input distributions are measured in the data.

7. Background is subtracted and the data are unfolded to the fiducial volume.

The data are separated into same- and different-top-like SMT muons, as illustrated in Figure 92, by a kinematic likelihood fitter (KLFitter), detailed in Chapter 8. The KLFitter places Breit-Wigner mass constraints on the top-quark and W-boson masses, and permutes reconstructed jets into each possible position in the leading order parton representation of the $t\bar{t}$ system. If a reconstructed b-tagged jet is mapped by the KLFitter to be in a leptonic b-jet position, then the SMT muon is considered to be same-top-like, whereas if the b-tagged jet is mapped to the KLFitter hadronic b-jet position then the SMT muon is considered to be different-top-like. The yield of SMT muons, that are designated as same-top-like is shown in

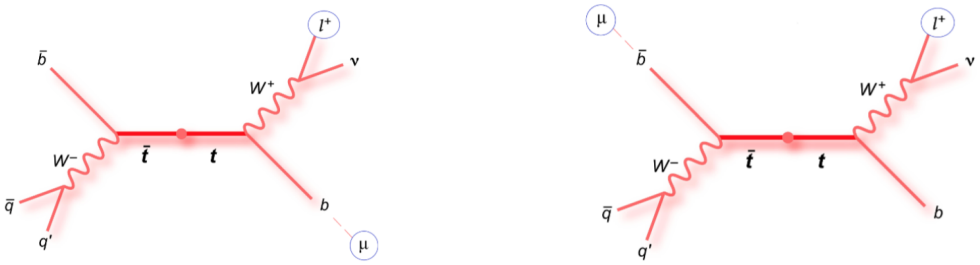

Figure 92.: Illustration of same- and different-top SMT muons.

Figures 93 while those designated as different-top-like is shown in Figure 94. For different-top-like SMT muons, the sign of the W-boson lepton has been reversed in order to consistently represent the charge of the b-quark at production in both the same- and different-top scenarios. The observed data are then combined and unfolded to the particle level.

The decay-chain fractions are obtained from simulation at the particle level. They can be used in conjunction with the observed charge asymmetries in order to extract the various $\mathcal{CP}$ asymmetries. The largest uncertainties in the decay-chain fractions come from the hadron-to-muon branching ratio and the parton shower. The data and MC predictions are compatible with zero and with the SM predictions, as shown in Table 23.

$\mathcal{CP}$ asymmetries are measured in b-hadron decays using top-pair events in 8 TeV ATLAS data. Also a measurement of A_{dir}^{bc} is performed, which improves the existing 2σ limit on $A_{\text{dir}}^{c\ell}$ and provides an equivalent 2σ limit on A_{dir}^{bc}. All reported results are found to be consistent with the Standard Model. The largest uncertainty on all reported asymmetries is statistical. With the Run 2 ATLAS dataset, the statistical

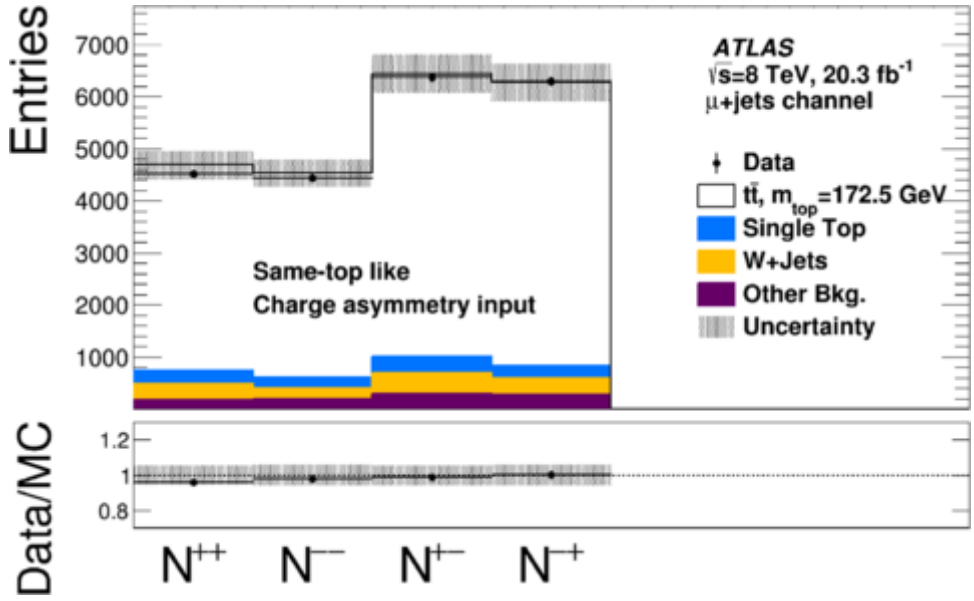

Figure 93.: Same-top like charge pairings distribution in the muon-channel (the electron channel is similar). The hashed area represents all the experimental systematic uncertainties as well as the b-hadron production and hadron-to-muon branching ratio uncertainties. The lower panel of the distributions show the ratio of the data divided by the simulation [16].

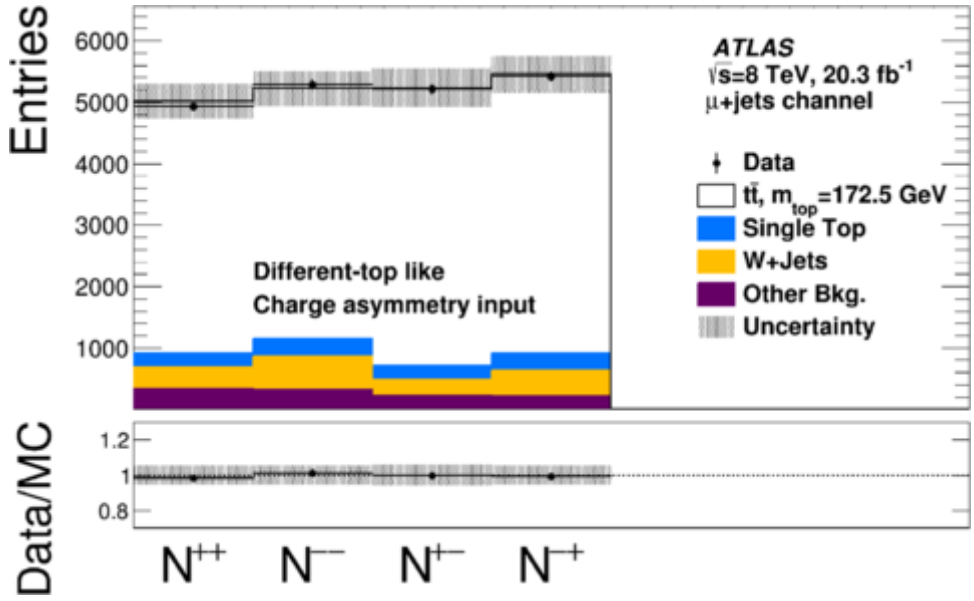

Figure 94.: Different-top like charge pairings distribution in the muon-channel (the electron channel is similar). The hashed area represents all the experimental systematic uncertainties as well as the b-hadron production and hadron-to-muon branching ratio uncertainties. The lower panel of the distributions show the ratio of the data divided by the simulation [16].

	Data (10^{-2})	MC (10^{-2})	Existing limits (2σ) (10^{-2})	SM prediction (10^{-2})
A^{ss}	-0.7 ± 0.8	0.05 ± 0.23	-	$< 10^{-2}$
A^{os}	0.4 ± 0.5	-0.03 ± 0.13	-	$< 10^{-2}$
A^{b}_{mix}	-2.5 ± 2.8	0.2 ± 0.7	< 0.1	$< 10^{-3}$
$A^{b\ell}_{\text{dir}}$	0.5 ± 0.5	-0.03 ± 0.14	< 1.2	$< 10^{-5}$
$A^{c\ell}_{\text{dir}}$	1.0 ± 1.0	-0.06 ± 0.25	< 6.0	$< 10^{-9}$
A^{bc}_{dir}	-1.0 ± 1.1	0.07 ± 0.29	-	$< 10^{-7}$

Table 23.: Comparison of measurements of charge asymmetries and constraints on CP asymmetries, with MC simulation, existing experimental limits [42, 44] and SM predictions [39, 43, 45]. The latter two columns represent upper limits on the absolute values $|A|$. For A^{b}_{mix} the last two columns are determined using the prescription from Ref. [39], with inputs from the HFAG world average of b-hadrons properties [42] and either the world average [42] or the SM predictions [43] for a^{d}_{sl} and a^{s}_{sl} respectively.

uncertainty will be smaller than the systematic uncertainties hence the aim is to reduce this systematic uncertainty in Run-2 analysis.

Part III.

Run-2 analysis

7

EVENT SELECTION

In this Chapter, the Run-2 analysis event selection will be described and only the Run-2 objects definition will be considered in the following. References to the Run-1 event selection will be given in this Chapter, if relevant.

7.1 DATA AND SIMULATION SAMPLES

The charge asymmetry analysis, the subject of this thesis, is performed using the 2015 and 2016 data samples collected by the ATLAS experiment in pp collisions at a centre of mass energy of $\sqrt{s} = 13$ TeV , with 25 ns bunch spacing, corresponding to an integrated luminosity of 36.1 ± 1.2 fb^{-1}.
Data are used only if recorded during stable beam conditions and with all relevant ATLAS detector subsystems operational, as required by the so called ATLAS Good Run List.
The expected signal and background distributions are simulated using Monte Carlo (MC) simulation samples. All simulated samples were processed through the same reconstruction algorithms and analysis chain as the data.

Details on the simulation samples used to model the $t\bar{t}$ signal and the backgrounds are listed below. Signal simulation samples:

- Nominal $t\bar{t}$: Powheg [97] generator interfaced with Pythia8 [98] to model the parton shower
- Additional radiation $t\bar{t}$ sample (see Section 9.2.4): Powheg generator interfaced withPythia8 to model the parton shower
- PDFs (see Section 9.2.7): the default PDF is NNPDF3.0 which is one of the component PDFs used in PDF4LHC15
- MC generator systematic on $t\bar{t}$: aMC@NLO [99] generator interfaced withPythia8 to model the parton shower
- Parton shower systematic on $t\bar{t}$: Powheg generator interfaced with Herwig7.1.3 [100] to model the parton shower

Background simulation samples:

- single top t-channel, s-channel and Wt-channel: Powheg generator interfaced withPythia6 [101] to model the parton shower
- W+jets: Sherpa2.2.1 [102] generator
- Z+jets: Sherpa2.2.1 generator
- Diboson WW, WZ, ZZ: Sherpa2.2.1 generator

All the samples were adopted following the recommendations of the ATLAS Top quark group. Most of them used the full ATLAS detector simulation [103] given by GEANT4 [104], however some systematic samples were generated with a faster simulation making use of parametrised showers in the ATLAS calorimeters (ATLFAST2 [105]).
All the $t\bar{t}$ samples used, have a `caveat`: two reweightings are applied on them. These reweightings are applied on:

1. the production fractions of B-hadrons and C-hadrons
2. the branching ratio (BR) of the decay of B-hadrons and C-hadrons to muons

These reweightings guarantee the uniformity of the treatment of those variables among the different generators employed for the MC samples. The production fractions and BRs are reweighted to the Particle Data Group values, the corresponding uncertainties are considered as systematics. More details on this procedure are given in the Systematic Chapter.
The physics objects used for event selection in this analysis are electrons, muons, jets and b-jets.

7.2 OBJECT SELECTION

Objects reconstructed with the ATLAS detector, as outlined in Chapter 5, are required to undergo the selections described in the following sections to enter the analysis presented in this thesis.

7.2.1 *Electrons*

Electron candidates [106, 107] are reconstructed from energy deposits (clusters) in the electromagnetic calorimeter associated to reconstructed tracks in the Inner Detector. Candidates are required to be within the range $|\eta_{\text{cluster}}| < 2.47$ and candidates in the calorimetry transition region $1.37 < |\eta_{\text{cluster}}| < 1.52$ are excluded.

Electrons must pass the Tight likelihood identification criterion (`TightLH`, see Section 5.2) and further selections on the transverse and longitudinal impact parameters:

1. $|z_0 \sin\theta| < 0.5$ mm
2. $|\frac{d_0}{\sigma(d_0)}| < 5$

where d_0 is the distance of closest approach of the track to the primary vertex in the x-y plane and $\sigma(d_0)$ is its uncertainty, and z_0 is the equivalent shift along the z-axis.
Electrons must have $p_T > 27$ GeV for both 2015 and 2016 data sets; moreover a veto on additional leptons in the event is applied.

To further reduce the background from non-prompt electrons, photon conversions and hadrons decays, electron candidates are also required to be isolated. Both tracking and calorimeter information are used for the isolation requirement. Two sets of cuts are applied on ID and calorimeter-based parameters, respectively:

- p_T dependent cuts are applied to the scalar sum of the transverse momenta of other tracks from the primary vertex within a cone around the electron track (the so called *Pt-Cone*),
- E_{T} dependent cuts are applied to the scalar sum of the transverse energies, measured in the calorimeter cells within a cone, called *Et-Cone*, excluding the energy associated to the particle itself.

The analysis described in this thesis exploits an efficiency targeted operating point (called *gradient* isolation working point): the *Pt-Cone* and *Et-Cone* parameters described above are used in order to obtain a given isolation efficiency ε. The target efficiency used in the *gradient* isolation working point is $\epsilon = 0.1143\ p_T\ [\mathrm{GeV}] + 92.14\%$ (until the plateau is at 100% efficiency) for both the calorimeter-based and track-based cuts [108].
Typical ε values, obtained combining ID and calorimeter based efficiencies, are 90% at p_T=25 GeV and 99% efficiency at p_T=60 GeV [110], but these efficiencies are quoted based on examination of events without jets (and are thus slightly smaller for events in this analysis topology).
Moreover a procedure, known as overlap removal, is employed: if a reconstructed electron is close to another reconstructed object (typically jets), within a cone of $\Delta R < 0.2$, the jets are removed. Both electrons and jets are reconstructed using the energy deposits in the ATLAS calorimeter system, so the overlap removal prevents double counting of energy clusters. In addition if there are surviving jets within a cone of $\Delta R < 0.4$ of electrons, the electrons are discarded in order to suppress semileptonic $b \to e$ decays.

7.2.2 *Muons*

Muon candidates are reconstructed from track segments in the Muon Spectrometer and matched with tracks found in the Inner Detector. The final muon candidates are refitted using the complete track information from both detector systems, and they are required to satisfy $p_T > 4$ GeV and $|\eta| < 2.5$.
The absolute value of a muon's d_0 significance must be less than 3, and the value of $|z_0 \sin\theta|$ must be less than 0.5 mm.
This analysis exploits two different muon objects: prompt muons (or "isolated muons" or "hard muons") coming from the W-boson leptonic decay and muons originating from the b-hadron semileptonic decay (called "soft muons" or SMT-muons in the following).
Different additional requirements are then applied to select and distinguish prompt muons and soft muons.
Prompt muons are required to:

1. have $p_T > 27$ GeV
2. satisfy the *Medium* quality requirements [111]
3. be isolated according to the *gradient* isolation working point (see Section 7.2.1)
4. be separated by $\Delta R > 0.4$ from the nearest selected jet. However, if this jet has less than three associated tracks, the muon is kept and the jet is removed to avoid an inefficiency for high-energy muons undergoing significant energy loss in the calorimeter.

Muons with $p_T > 4$ GeV not passing the above selection can be selected as soft muons.

Soft Muons

Soft muons are required to:

1. pass the *Tight* quality requirements [111]
2. be closer than 0.4 in ΔR within a selected jet
3. have $|d_0| < 3$ mm
4. have $|z_0 sin\theta| < 3$ mm

In case more than one muon passing these criteria is found for a given jet, the soft muon with the highest p_T is chosen. The closest jet to a soft muon is defined as a "SMT-tagged" jet in the following. Moreover, for soft muons no overlap removal with jets is applied. More details on the soft muon tagging used in Run-2

analysis are in Chapter 5 and in reference [112], where there is also a dedicated study to muon performances inside jets showing that the muon reconstruction and identification efficiencies are compatible for isolated/prompt and non isolated/non prompt muons.

7.2.3 *Jets*

Candidate jets are reconstructed using the three-dimensional topological energy clusters [113] deposited in the calorimeters. Jets reconstruction is performed using the anti-k$_T$ jet algorithm [114] with a radius parameter of 0.4.
Reconstructed jets are required to have $p_T > 25$ GeV and $|\eta| < 2.5$. Quality criteria (also called *jet cleaning procedure*) are required to identify jets arising from non-collision sources or detector noise and any event containing at least one such jet is removed. This procedure causes a negligible loss of efficiency [115].
In order to avoid selecting jets from secondary pp-interactions, an additional requirement is imposed on the Jet Vertex Tagger (JVT)[1] [116]. Jets with $p_T < 60$ GeV and in the central ($|\eta| < 2.4$) region of the detector must have JVT> 0.59 to reduce the effects of pile-up minimum bias interactions. This requirement is applied on both data and simulation samples.

b-tagging

An algorithm based on multivariate techniques is used to identify jets originating from the hadronisation of a b quark (b-tagged jets). This algorithm combines information from the impact parameter of displaced vertex tracks and topological properties of secondary and tertiary decay vertices reconstructed within the jet.
In this analysis, the b-tagging is performed placing a selection requirement on the weight of the MV2c10 tagger, which is trained on simulated $t\bar{t}$ events in order to discriminate b-jets from light-jets (90%) and c-jets (10%) backgrounds.
The ATLAS Flavour Tagging Group supports several MV2c10 working points at 85, 77, 70, and 60% b-jet efficiency (see Table 17 and Figure 68 for insights). This analysis approach is to use the recommended working point with 77% efficiency for b-tagged jets with $p_T > 20$ GeV and $|\eta| < 2.5$ in $t\bar{t}$ events.
Additional b-tagging is performed using the semi-leptonic muon tagging (SMT), as defined in Section 5.4.1.
In the b-tagging, several improvements with respect to Run-1 can be noticed: for example the additional impact parameter and track information provided by the IBL, and an improved multivariate training (MV2 versus MV1) used to make the selec-

1 Due to increase in collsion energy in the ATLAS Run-2, a new method called the Jet Vertex Tagger has been developed to replace the JVF method. JVT identifies and suppresses pile-up jets and it is fully described in [116]

tion, for further details on the Multi Variate techniques adopted in ATLAS refer to Section 5.4.1.Going from Run-1 to Run-2 measurement, there were improvements also in the SMT definition, as outlined in the next Section.

Run-1 and Run-2 SMT comparison

For the charge asymmetry measurement performed in Run-2, the SMT algorithm definition changed and a Tight-based algorithm (see Section 5.3 for Tight muon definition) was implemented, as described in Section 5.4.1.
In Run-2, the baseline selection employed for soft muons is the following:

- $p_{\mathrm{T}}^{\mu} > 4\,\mathrm{GeV}$
- $|\eta| < 2.5$
- $|d_0| < 3\,\mathrm{mm}$
- $|z_0 \sin\theta| < 3\,\mathrm{mm}$
- Combined Medium muons

On top of this baseline selection, several options were considered in order to improve the rejection of fake soft muons: the first tested option was tested a cut on MI, in analogy with the Run-1 SMT, another option is the usage of the Tight working point for muons. Among the cuts applied to select Tight muons, one is similar to the aforementioned MI and it is defined as:

$$\mathrm{MI}_{\mathrm{CB}} = \frac{p_{\mathrm{T}}^{\mathrm{ID}} - p_{\mathrm{T}}^{\mathrm{ME}}}{p_{\mathrm{T}}^{\mathrm{CB}}} \tag{60}$$

where CB stands for Combined muons.
Figures 95 and 96 show a comparison of the efficiency of the MI and of the Tight requirement for muons originated by heavy-flavour hadrons, as estimated on the $t\bar{t}$ Montecarlo sample. A Tight-based SMT shows a slightly higher efficiency and is chosen as soft muon tagging in this analysis. For completeness, the results for the mistag rate for a MI-based (Run-1) and Tight-based (Run-2) SMT algorithm are reported in Table 24. The mistag rate for the Tight-based SMT algorithm was measured on a W+jets MC simulation sample. Both taggers show similar performances. Considering that the Tight working point for muons is fully supported by the ATLAS performance group, the Tight-based SMT was chosen as baseline option.

The SF for the SMT Mistag rate measured in Run-2, in the inclusive jet p_T region is $SF = 1.096 \pm 0.140$ quoting both statistical and systematic uncertainty.

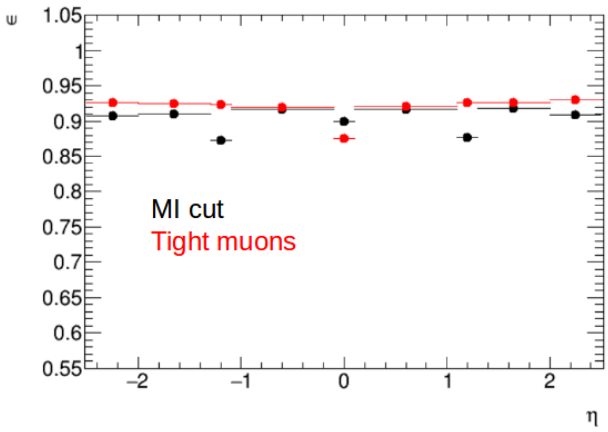

Figure 95.: Fraction of combined muons originated by heavy-flavour hadrons passing a $MI < 0.1$ cut (black) or the tight requirement (red) as a function of η of the muon.

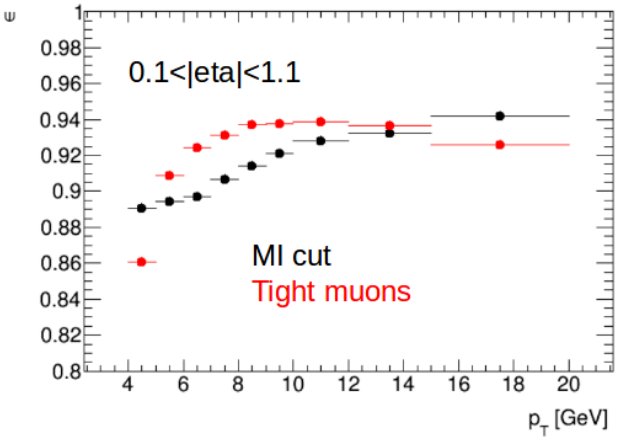

Figure 96.: Fraction of combined muons originated by heavy-flavour hadrons passing a $MI < 0.1$ cut (black) or the tight requirement (red) as a function of p_{T} of the muon.

jet p_T [GeV]	Mistag rate MI-based SMT [10^{-3}]	Mistag rate tight-based SMT [10^{-3}]
25-35	1.01 ± 0.087	1.10 ± 0.09
35-45	1.78 ± 0.19	1.84 ± 0.20
45-55	2.56 ± 0.32	2.79 ± 0.33
55-80	2.55 ± 0.26	2.38 ± 0.24
80-110	3.38 ± 0.36	3.05 ± 0.34
110-140	5.00 ± 0.60	4.79 ± 0.59
140-180	5.65 ± 0.56	5.50 ± 0.53
180-220	6.72 ± 0.73	5.44 ± 0.91
220-280	8.84 ± 0.97	8.37 ± 0.92
280-360	13.5 ± 1.42	11.2 ± 1.27
360-460	15.9 ± 2.03	12.5 ± 1.92
460-500	10.5 ± 4.52	9.58 ± 4.18
500-1000	24.4 ± 2.25	19.6 ± 1.93

Table 24.: Mistag rate for a MI-based and Tight-based SMT algorithm.

7.2.4 *Missing Transverse Energy and W Transverse Mass*

Semileptonic $t\bar{t}$ events are characterised by the presence of missing energy in the plane transverse to the beam axis, due to neutrinos. The missing transverse energy in the event, E_T^{miss}, is defined as the magnitude of the negative vector sum p_T of all selected and calibrated physics objects in the event.
Another related parameter is the W transverse mass defined by the formula 61:

$$m_T(W) = \sqrt{2p_{\mathrm{T}}^{\ell} E_T^{miss}(1 - \cos\Delta\phi)} \tag{61}$$

where p_{T}^{ℓ} (E_{T}^{miss}) is the transverse momentum (energy) of the muon or the electron (neutrino) and $\Delta\phi$ is the azimuthal angle separation between the lepton and the direction of the missing transverse energy.
The following requirement, called triangular cut, is applied to select events containing neutrinos:

- $E_T^{miss} > 30\,\mathrm{GeV}$ and $E_T^{miss} + m_T(W) > 60\,\mathrm{GeV}$

7.3 TRIGGER SELECTION

The event selection used in this analysis is seeded by the lowest un-prescaled single electron and single muon triggers.
For the 2015 data set, this analysis exploits three electron high-level triggers with different p_T thresholds (24, 60 and 120 GeV) with electron identification qualities set to medium, medium, and loose respectively. For the trigger with the lowest p_T threshold, there is also an isolation requirement from hadronic activity in the calorimeter, and η-dependent trigger thresholds are applied.
About muons, two triggers with p_T thresholds set to 20 GeV and 50 GeV have been used. For the lowest muon trigger a loose isolation cut is also required.
The trigger menu used in the 2016 data analysis shows several changes, implemented to take into account the increase of the LHC instantaneous luminosity. This translates in higher p_T threshold requirements for electrons and muons. So, the electron p_T thresholds were set to 26, 60 and 140 GeV, respectively. The lowest p_T threshold electron trigger applies also a track isolation requirement of $\frac{p_T^{cone20}}{E_T} > 0.1$[2] in order to reduce the effects of multijet backgrounds.
The muon p_T thresholds were set to 26 and 50 GeV thresholds. Tighter identification and isolation requirements are also required both for electrons and muons. For the muon trigger with the lowest p_T threshold there is a further isolation requirement: $\frac{p_T^{varcone30}}{p_T} < 0.07$[3].
Single electron (muon) triggers are combined with a logical `OR` to identify electron (muon) signals.

7.4 EVENT SELECTION

The event selection aims at selecting a sample enriched in $t\bar{t}$ events and it is seeded by the lowest un-prescaled single electron or single-muon trigger chains. Different trigger chains are used for data collected in 2015 and 2016, as summarised in Section 7.3.

In addition, events are required to have at least one reconstructed vertex: there must be at least two tracks with $p_T > 0.4$ GeV and they have to be consistent with the beam-collision region in the $x - y$ plane. If cases with multiple vertices are reconstructed, the primary vertex is taken as the vertex with the largest sum of the

2 The track isolation p_T^{cone} is computed by summing the p_T of all Inner Detector tracks within a cone of $dR = 0.X(0.2, 0.3, 0.4)$ centered around the lepton track.

3 If there are boosted signatures or very busy environments, in which other objects can end up very close to the lepton direction, a variable-cone size track isolation, called $p_T^{varcone}$, can be used. For this variable, the cone size gets smaller for larger transverse momentum of the lepton.

squared transverse momenta of its associated tracks.

The event pre-selection can be summarised as follows:

- the event has to pass the lowest un-prescaled single-electron or single-muon trigger selection
- there must be exactly one electron or *prompt* muon with $p_T > 27$ GeV, matched to the trigger
- no additional electrons or *prompt* muons with $p_T > 25$ GeV
- at least four jets.

In addition to this preselection criteria, other additional requirements are applied:

- $E_T^{miss} > 30\,\text{GeV}$ and $E_T^{miss} + m_T(W) > 60\,\text{GeV}$ (triangular cut)
- one jet tagged by both the SMT-tagged jet and the MV2c10 algorithms. If more than one SMT-tagged jet is present in the event, only the one with the highest-p_T muon is considered.

All these requirements identify the analysis signal selection.

7.5 SIGNAL COMPOSITION AND $t\bar{t}$ BACKGROUND

Soft muons in $t\bar{t}$ events can originate from various sources.
Truth information about the soft muon decay chains are stored in Montecarlo simulations. It is possible to identify the origin of the soft muon as coming from a b-quark produced in a $t \to Wb$ decay if the B-hadron and the b-quark are spatially matched within $\Delta R < 0.1$. These events will be classified as signal soft muons.
It might happen that a muon is produced by a B-hadron not coming from the top decay chain (e.g. coming from a b-quark produced by a ISR/FSR gluon splitting), or from a c-hadron associated with a c-quark not coming from the $t \to b$ decay chain (either from gluon splitting, or e.g. from the $W \to cs$ decay for the hadronically decaying W in top pair events). These soft muons will be referred to as SMT-background.
Moreover, there are reconstructed muons with no associated truth information: these are typically called SMT-fakes. They are muons coming from the decay of light hadrons, such as pions or kaons, or from detector background.
This translates into three $t\bar{t}$ events categories, classified according to the soft muon origin: $t\bar{t}$ SMT-signal, $t\bar{t}$ SMT-background and $t\bar{t}$ SMT-fakes.

The following list accounts for all these possibilities and shows the fraction of events falling in each category, as measured on $t\bar{t}$ simulated events relative to the baseline selection described above:

- $t\bar{t}$ SMT-signal (about 77% of the events):
  - $t \to b$, $b \to B$, $B \to \mu$: 44.8%
  - $t \to b$, $b \to B$, $B \to c$, $c \to \mu$: 29.4%
  - $t \to b$, $b \to B$, $B \to \tau$, $\tau \to \mu$: 2.1%
  - $t \to b$, $b \to B$, $B \to c$, $c \to \tau$, $\tau \to \mu$: 0.7%
- $t\bar{t}$ SMT-bkg (about 15.5% of the events), where b, c, and τ not coming from $t \to b$ decay chain come from gluon splitting:
  - b not coming from $t \to b$ decay chain, $b \to \mu$: 1.1%
  - c not coming from $t \to b$ decay chain, $c \to \mu$: 11.1%
  - τ not coming from $t \to b$ decay chain, $\tau \to \mu$: 0.6%
  - $W \to \mu$ (dilepton $t\bar{t}$ events): 2.9%
- $t\bar{t}$ SMT-fakes: 7.5%

For this measurement only $t\bar{t}$ SMT-signal events are proper signal, containing full lepton charges information.

7.6 EVENT YIELDS IN THE OPTIMISED SELECTION

The event selection outlined in Section 7.4 is optimised in order to maximise the signal purity in the final data sample and to reduce the uncertainties on the final results. This analysis is not expected to be limited by its statistical uncertainty, but by its systematic uncertainties. This means that E_T^{miss} and $m_T(W)$ cuts can be safely applied to enhance the signal purity without concerns on statistics limitations (as it was the case for the Run-1 analysis).
The optimal selection aims at maximising the signal significance, defined as $S/\sqrt{S+B}$, and minimising the background fraction, defined as $B/(S+B)$. S and B denote the number of signal and background events respectively after a selection is performed.
In order to reduce the SMT-background events, a combinations of the SMT tagger with the MV2c10 tagger is considered. A reconstructed jet is identified as a b-originated jet if it is tagged by both the SMT tagger and the MV2c10 tagger: this defines the b-tag double selection, used in the optimised selection.
Tables 25 and 26 show the yields breakdown in the signal and background regions

in the lepton, electron and muon+jets channels and if the event is tagged with the SMT method only (labelled as SMT-tag) or if the SMT information is combined with the MV2c10 tagger (b-tag double). Table 27 shows that the SMT information combined with the MV2c10 tagger maximises the signal significance while reducing the background, so this will be considered as the optimised event selection in the analysis.

≥ 4 jets, $E_T^{miss} > 30$ GeV, $E_T^{miss} + m_T(W) > 60$ GeV, b-tag double									
	ℓ+jets			e+jets			μ+jets		
$t\bar{t}$ (SMT-signal)	315 000	$\pm$	562	162 000	$\pm$	402	154 000	$\pm$	392
$t\bar{t}$ (SMT-background)	22 700	$\pm$	151	11 700	$\pm$	108	11 000	$\pm$	105
$t\bar{t}$ (SMT-fakes)	15 300	$\pm$	124	7940	$\pm$	89	7320	$\pm$	86
Single top	20 400	$\pm$	143	10 500	$\pm$	154	9890	$\pm$	150
W+jets	25 900	$\pm$	161	12 900	$\pm$	114	13 000	$\pm$	113
Z+jets	7280	$\pm$	85	4140	$\pm$	64	3140	$\pm$	56
Diboson	120	$\pm$	11	66	$\pm$	8	54	$\pm$	7
Multi-jet	8480	$\pm$	92	4560	$\pm$	68	3920	$\pm$	63
Total	415 000	$\pm$	644	213 000	$\pm$	462	202 000	$\pm$	449
$\sum$ Backgrounds	100 000	$\pm$	316	51 900	$\pm$	228	48 300	$\pm$	220

Table 25.: Event yields after the b-tag double selection. The first column shows the overall yields, while the split in the electron and muon channels is shown in the second and third columns. The reported uncertainties on the predictions from the different processes only include the statistical uncertainties (from the limited number of simulated events, or, in the case of the multi-jet background, from the Matrix Method).

7.7 FIDUCIAL VOLUME

Since an Unfolding procedure (outlined in Section 10.2) is needed to extract the charge asymmetry measured by this analysis, it is useful to define a fiducial volume as close as possible to the nominal event selection.
The fiducial selection requirements are listed below:

1. only one prompt electron OR muon, with a veto on second hard lepton (no additional electron or prompt muon with $p_{\mathrm{T}} > 15\,\mathrm{GeV}$)
2. hard lepton $p_{\mathrm{T}} > 27\,\mathrm{GeV}$
3. lepton $|\eta| < 2.5$

≥ 4 jets, $E_T^{miss} > 30$ GeV, $E_T^{miss} + m_T(W) > 60$ GeV, SMT-tag									
	ℓ+jets			e+jets			μ+jets		
$t\bar{t}$ (SMT-signal)	385 000	$\pm$	620	197 000	$\pm$	444	187 000	$\pm$	433
$t\bar{t}$ (SMT-background)	62 900	$\pm$	251	32 600	$\pm$	180	30 300	$\pm$	174
$t\bar{t}$ (SMT-fakes)	35 600	$\pm$	189	18 600	$\pm$	136	17 000	$\pm$	130
Single top	28 200	$\pm$	168	14 600	$\pm$	180	13 600	$\pm$	175
W+jets	76 100	$\pm$	276	37 800	$\pm$	194	38 300	$\pm$	196
Z+jets	36 700	$\pm$	192	9200	$\pm$	96	27 500	$\pm$	166
Diboson	838	$\pm$	29	383	$\pm$	20	465	$\pm$	21
Multi-jet	15 600	$\pm$	125	8590	$\pm$	93	6960	$\pm$	83
Total	641 000	$\pm$	801	319 000	$\pm$	565	322 000	$\pm$	567
$\sum$ Backgrounds	256 000	$\pm$	506	122 000	$\pm$	349	134 000	$\pm$	366

Table 26.: Event yields after the SMT-tag selection. The first column shows the overall yields, while the split in the electron and muon channels is shown in the second and third columns. The reported uncertainties on the predictions from the different processes only include the statistical uncertainties (from the limited number of simulated events, or, in the case of the multi-jet background, from the Matrix Method).

b-tag double			
	ℓ+jets	e+jets	μ+jets
$S/\sqrt{S+B}$	489	350	342
$B/(S+B)$	0.240	0.240	0.240
SMT-tag			
	ℓ+jets	e+jets	μ+jets
$S/\sqrt{S+B}$	481	330	350
$B/(S+B)$	0.400	0.420	0.380

Table 27.: Signal significance and background in the two b-tagging options considered.

4. at least 4 reconstructed jets, using the anti-kt algorithm with a cone radius of $\Delta R = 0.4$
5. jet $p_{\mathrm{T}} > 25\,\mathrm{GeV}$
6. jet $|\eta| < 2.5$
7. at least one b-jet with a semileptonic $b \to \mu$ decay
8. $E_T^{miss} > 30\,\mathrm{GeV}$ and $E_T^{miss} + m_T(W) > 60\,\mathrm{GeV}$

7.8 BACKGROUND ESTIMATION

Although a large $t\bar{t}$ pair production is expected at the LHC (given a centre of mass energy of 13 TeV and an integrated luminosity of $36.1\,\mathrm{fb}^{-1}$, $\sim$ 30 millions of $t\bar{t}$ events are expected), it is crucial to distinguish signal from background events.
The signal final state signature is defined by two charged leptons, missing transverse energy and four jets, out of which at least one has to be b-tagged, and this physics signature can be shared by several other physics processes arising from pp collisions can fake the signal.
After event selection, the main background processes arise from the production of single top quarks, as well as W- or Z-boson production in association with jets. A small contribution comes from diboson (WW, WZ, ZZ) production. Events not containing real prompt leptons also contribute to the selected sample via the misidentification of a jet or a photon as an electron or the presence of non-prompt electrons or muons passing the prompt isolated lepton selection (multijet contribution).
The crucial feature for this charge asymmetry measurement is to understand if the final state lepton charges are produced symmetrically or asymmetrically in the background processes. For example in multijet, Z+jets and diboson backgrounds leptons are produced charge symmetrically, and the charges of the hard charged-lepton (from the W-boson decay) and the soft-muon are uncorrelated. The contribution of these backgrounds should be flat in the the charge asymmetries (CA) distributions. Other backgrounds, such as W+jets and single-top, produce leptons in the final state whose charges are correlated. These charge asymmetric production will contribute with non-flat distributions to the charge asymmetries and must be estimated carefully.
Figure 97 shows several examples of Feynman diagrams for each background channel, with short labels to identify production charge (a)symmetries and lepton charge correlations in each case.

Most of the backgrounds are well-modelled by Montecarlo simulations, but the W+jets and multijet backgrounds need a data driven estimation and they will be discussed separately.

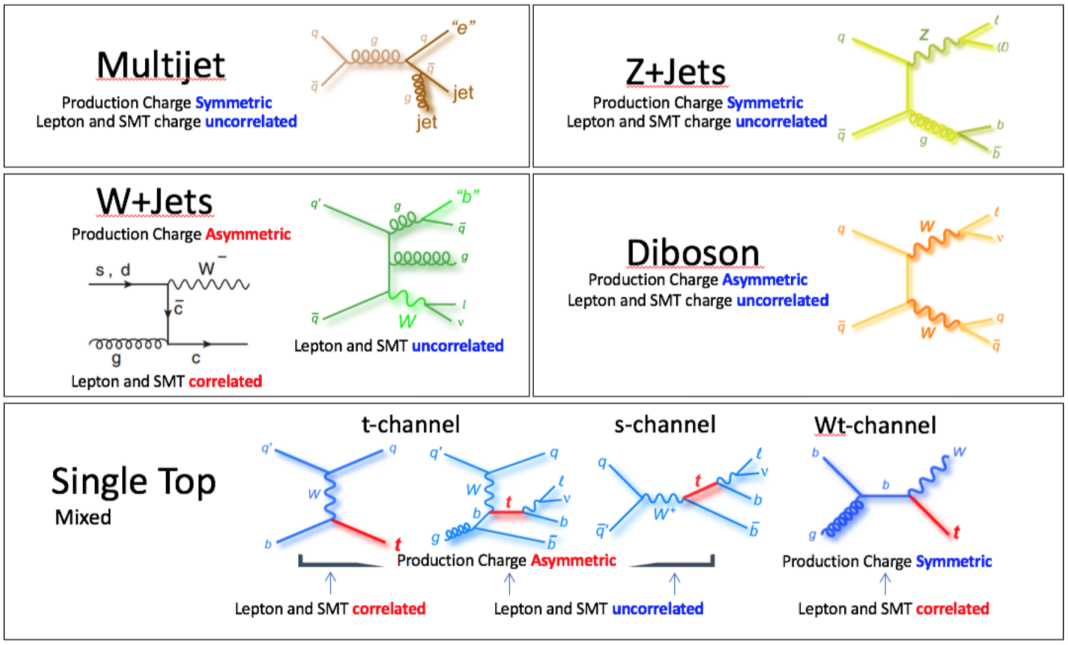

Figure 97.: Examples of Feynman diagrams for each of the primary backgrounds to the $t\bar{t}$ lepton+jets signal events. Labels indicate the production charge (a)symmetries and correlations between the charges of the charged final state leptons from the W-boson decay and the SMT.

7.8.1 *Diboson Background*

Diboson events (WW, WZ, ZZ), where one of the bosons decays leptonically and the other one decays hadronically, may satisfy the event selection as they contain real leptons, missing transverse momentum, and jets with either one real heavy flavour b-tagged jet or a mistagged light-flavour jet. WW and ZZ diboson events are produced charge symmetrically, however WZ events are produced charge asymmetrically because the W^+-boson production has a larger cross section compared to the W^--boson production due to the valence quark content of the colliding protons (uud).

7.8.2 *Single-top Background*

Single-top events can satisfy the event selection requirements because they contain a real charged-lepton and missing momentum, if the W-boson decays leptonically, and a real b-jets from the top-quark decay. Other jets can be detected in coincidence with single-top decays and thus provide the signal signature. At the LHC, t-channel ($\sim$ 72% of the overall single-top cross section) and s-channel ($\sim$ 4%) sin-

gle top events are produced asymmetrically, with more top quark events produced than anti-top quark events, while the Wt channel ($\sim 24\%$) single top events are produced symmetrically. In the first single-top diagram of Figure 97 they two leptons will be correlated in charge, if the charged lepton and the SMT muon both originate from the decay products of the top quark. In the second and third diagram, the lepton and soft muon charges are uncorrelated and the b-jet could be tagged. In the Wt diagram the charges are correlated again, assuming both leptons originate from the decay products of the top quark.

7.8.3 *Z+jets Background*

Z+jets events can result in leptons (charged or neutral) coincident with heavy or light flavour jets resulting from gluon splitting, for example. If the Z-boson decays into two charged leptons ($Z \to e^+e^-$ or $Z \to \mu^+\mu^-$) and one of the leptons fails to be reconstructed (due to detector inefficiencies or fall outside of the selection acceptance) it may fake the missing transverse momentum in the event. In cases when the Z decays via two un-charged leptons ($Z \to \nu\bar{\nu}$), one of the additional jets may fake the signature of a real electron in the calorimeters. Finally, $Z \to \tau^+\tau^-$ events may fake the signal signature because they may result in a real lepton and neutrino, if one of the τs undergoes a leptonic decay, and jets if the other τ decays hadronically. In Z+jets events the SMT muon and the charged prompt lepton are uncorrelated.

7.8.4 *Multijet Background*

Multijet events have a huge cross section and contain numerous jets which may satisfy the imposed b-tagging requirements. Also the SMT tagging requirements can be passed by one of the jets. If a jet is misidentified as a lepton or if a heavy flavour jet really contains a lepton, due to a semileptonic decay, it may satisfy the lepton selection requirements. Missing momentum could be present in multijet events due to misconstruction. Even if the misconstruction probability is small, the multijet background is significative because its production cross section is very large.
The isolated charged lepton and SMT charges are uncorrelated in multijet backgrounds.
To estimate the multijet backgrounds data driven methods are utilised because our knowledge of QCD processes is not good enough to predict multijet final states.
The analysis presented in this thesis is based on $t\bar{t}$ semi-leptonic events and the evaluation of the background due to the mis-identification of the prompt lepton is

of primary importance.
Also this background estimation, as the W+jets one, is performed using a data-driven method called Matrix Method [118] because the Montecarlo simulations do not reproduce data in a good way.
The multijet background consists of two components: events where a jet or a photon is misidentified as a lepton (referred to as fake lepton) or events containing non-prompt leptons. The multijet background estimation starts selecting a data sample enhanced in fake and non-prompt leptons, obtained removing the lepton isolation requirements and, for electrons, loosening the identification criteria. Then, the efficiency for these 'loose' leptons to satisfy the nominal selection ('tight') criteria is measured in data, separately for real prompt leptons and for fake or non-prompt leptons.
Z-boson events where the Z-boson decays leptonically in muon or electron pairs are utilised to measure the real prompt lepton efficiency, while the efficiency for fake and non-prompt leptons is measured in a data sample with low missing transverse momentum and low values of the reconstructed leptonic W-boson transverse mass.
The number of fake or non-prompt leptons satisfying the tight criteria can be calculated by inverting the matrix defined by the system of equations 62.

$$\begin{aligned} N^{l} &= N_{r}^{l} + N_{f}^{l} \\ N^{t} &= \varepsilon_{r} N_{r}^{l} + \varepsilon_{f} N_{f}^{l} \end{aligned} \tag{62}$$

where N^{l} (N^{t}) is the number of events observed in data passing the loose (tight) lepton selection, N_{r}^{l} (N_{f}^{l}) is the number of events with a real prompt (fake or non-prompt) lepton in the loose lepton sample, and finally ε_{r} (ε_{f}) is the efficiency for these events to pass the tight lepton selection.

The efficiencies $\varepsilon_{f} N_{f}^{l}$ can be extracted from the equations above and consequently a weight can be assigned to each event selected in the loose lepton data sample. Thanks to this procedure it is possible to provide a prediction for both the yields and the kinematic distribution shapes for the fake and non-prompt lepton background.
The obtained efficiencies ε_{r} and ε_{f} are parameterised as a function of the following event and object variables:

- lepton transverse momentum, p_{T}^{lep}
- lepton pseudorapidity, η^{lep}
- leading jet transverse momentum, $p_{T}^{j_0}$
- number of b-tagged jets

- azimuthal separation, $\Delta\phi(\ell, E_{\mathrm{T}}^{\mathrm{miss}})$
- minimum distance $\min_{j\in\mathrm{Jets}} \Delta R(\ell, j)$

The parameterisations are split according to the channel (e+jets and μ+jets) and by year (2015 and 2016) and for the real and fake efficiency.

7.8.5 *W+jets Background*

Also to estimate the W+jets background a data-driven method is utilised, as described in the next section. This is one of the most prevalent background of this analysis because of its large production cross-section and because of the presence of real charged-leptons, b-jets and missing momentum in the final state. In particular, in the Wc production mode there is correlation between the prompt charged lepton and the soft muon (coming from $c \to \mu$), due to the correlation of the initial charges of the W-boson and c-quark. In the other cases the charges are uncorrelated.

7.9 DATA-DRIVEN DETERMINATION OF THE W+JETS BACKGROUND

7.9.1 *W+jets normalisation*

Data-driven methods are adopted to estimate the W+jets background because MC simulations are not reliable: in MC simulations there is significant uncertainty on the overall normalisation of the W+jets background and on the quark-flavour composition of the jets.
The W+jets background estimation consists mainly of two components: the W+jets absolute normalisation and the flavour fractions evaluation ($W + cc$, $W + bb$, $W + c$ and $W + lf$).
In pp collisions the W+jets production is charge-asymmetric meaning that there is a non-unitary ratio of positive to negative W-bosons. This is a consequence of the parton PDFs composition and the valence quark anti-quark content of the protons (uud), generating a larger production cross-section for positively charged W bosons, compared to negatively charged W bosons, as expressed in formula 63.

$$r = \frac{\sigma\left(pp \to W^{+}\right)}{\sigma\left(pp \to W^{-}\right)} = \frac{N_{W^{+}}^{MC}}{N_{W^{-}}^{MC}} > 1 \tag{63}$$

$N_{W^\pm}^{MC}$ are the number of positive/negative W-boson events in MC simulations.
r is a well known and theoretically understood quantity [117], that can be safely estimated in MC simulations (r_{MC}).
The other $t\bar{t}$ backgrounds produce symmetrically positive and negative leptons, with the exception of single-Top production via $s-$ or $t-$channel. In the data-driven determination of the W+jets background, the single-Top contribution, estimated from MC simulations, is subtracted from the data yields.
The ratio r can be related to the yields from the data samples containing a positive and a negative high-p_T lepton, D^+ and D^- respectively, through formula 64.

$$N_{W^+} + N_{W^-} = \frac{\left(N_{W^+}^{MC} + N_{W^-}^{MC}\right)}{\left(N_{W^+}^{MC} - N_{W^-}^{MC}\right)} \left(D^+ - D^-\right) = \left(\frac{r_{MC}+1}{r_{MC}-1}\right) \left(D^+ - D^-\right) \quad (64)$$

A normalisation scale factor for the W+jets process can therefore be measured as:

$$SF_{CA} = \frac{(\frac{r_{MC}+1}{r_{MC}-1})(D^+ - D^-)}{N_{W^+}^{MC} + N_{W^-}^{MC}} \quad (65)$$

This step is performed without any b-tagging requirement.

7.9.2 *W+jets flavour composition*

Another method is required to estimate the flavour fractions present in the jets from the W+jets background.
The flavour composition of the W+jets background can be broken down into four sub-categories: $W + cc$, $W + bb$, $W + c$ and $W + lf$ (where lf is the acronymous for light flavour), and they are fixed with data driven techniques to accurately predict the number of W+jets events which will satisfy the tagging requirements used within the analysis.
A set of scaling factors, K_i ($i = c, c\bar{c}, b\bar{b}, lf$), are derived and they are used to alter the relative flavour fractions in MC simulations in order to provide a data-driven W+jets estimation. The system has three constraints:

1. the sum of the flavour fractions at pre-tag level that must sum to one
2. the total number of positive charged data events, tagged by the SMT tagger
3. the total number of negatively charged data events, tagged by the SMT tagger

However, four scaling factors are required to fully describe the system. To be able to solve the system another assumption is necessary: $K_{bb} = K_{cc}$; this consequently

leads to the final scale factors for $W + bb$ and $W + cc$ also being set equal to one another.
A further step is required in order to determine the total number of positively and negatively charged data events: all non W+jets MC and multijet contributions are subtracted from the tagged data yields, as described in Equation 66.

$$D_{W^{\pm}} = N^{\pm}_{\mathrm{D}ata} - N^{\pm}_{\mathrm{MC}} - N^{\pm}_{\mathrm{M}ultijet} \tag{66}$$

The resulting system of three equations and three unknowns is described by the linear equation system in matrix 67, where SF_{CA} is the scale factor for the charge asymmetry, described in equation 65, and $N^{i}_{MC,W^{\pm}}$ are the tagged yields for the W+jets MC for each flavour i.

$$\begin{bmatrix} SF_{CA} \cdot \left(N^{bb}_{MC,W^-} + N^{cc}_{MC,W^-}\right) & SF_{CA} \cdot N^{c}_{MC,W^-} & SF_{CA} \cdot N^{lf}_{MC,W^-} \\ (f_{bb} + f_{cc}) & f_c & f_{LF} \\ SF_{CA} \cdot \left(N^{bb}_{MC,W^+} + N^{cc}_{MC,W^+}\right) & SF_{CA} \cdot N^{c}_{MC,W^+} & SF_{CA} \cdot N^{lf}_{MC,W^+} \end{bmatrix} \cdot \begin{bmatrix} K_{bb,cc} \\ K_c \\ K_{LF} \end{bmatrix} = \begin{bmatrix} D_{W^-} \\ 1.0 \\ D_{W^+} \end{bmatrix} \tag{67}$$

This linear equation system is solved via matrix inversion and using an iterative approach.
The complete procedure used to evaluate the W+jets background is the following:

1. the W+jets normalisation is estimated in data at pre-tag level with the charge asymmetry method, which results in a scale factor SF_{CA}, as in equation 65;

2. the SF_{CA} is applied to the W+jets MC simulations, and the flavour composition is measured in data for the tagged sample (i.e. events with at least one jet tagged by MV2c10). Corrections factors K_i are calculated for the flavour fractions of W+jets;

3. the K_i factors are applied at pre-tag level, since they modify the SF_{CA} measurement, and points 2 and 3 are iterated until both SF_{CA} and the K_i factors are stable.

The combination of the data-driven methods listed above provides the total estimation for the W+jets background.
The W+jets background evaluation is obtained in a region (1-lepton and 2-jet exclusive bin) with high-statistics with the aim of reducing the uncertainties. The K_i factors calculated in the two jets bin are used also in other multiplicity bins, in particular for the analysis region of 1-lepton and 4-jets inclusive region. The W+jets normalisation is instead evaluated in each jet multiplicity bin.
Table 28 shows the W+jets data driven method results in the 1-lepton and 2-jet

exclusive bin region. The data-driven estimate is recalculated for every systematic variation affecting the analysis.

	SF_{CA}^{2jets}	K_{bbcc}	K_c	K_{lf}
Nominal	1.132	0.988	1.110	0.974
Syst	[%]	[%]	[%]	[%]
Data Stat	±0.4	±2.7	±2.1	±0.3
MC Stat	±3.0	±17.9	±13.2	±1.9
luminosity	±2.5	±0.7	±1.8	±0.6
pileup	±1.8	±6.0	±7.2	±1.3
jvt	±0.3	±0.0	±0.1	±0.0
muon trigger	±1.3	±0.5	±1.1	±0.4
muon ID	±0.9	±0.3	±0.8	±0.3
muon isolation	±0.3	±0.1	±0.2	±0.1
muon TTVA	±0.1	±0.0	±0.1	±0.0
b-tagging SF (b TAG)	±0.6	±3.9	±2.8	±1.3
b-tagging SF (c TAG)	±0.8	±2.0	±3.7	±1.3
b-tagging SF (light TAG)	±2.1	±11.5	±9.8	±4.1
b-tagging extrapolation	±0.0	±0.1	±0.3	±0.1
muon scale	±0.2	±1.3	±1.1	±0.2
MET soft term	±0.5	±5.9	±3.8	±0.5
JER	±7.8	±23.4	±6.0	±1.1
JES	±12.1	±14.7	±9.5	±3.3
$t\bar{t}$ xsec	±0.8	±0.5	±3.8	±1.0
Z+jets xsec	±1.5	±0.5	±6.5	±1.8
singleTop xsec	±0.1	±1.8	±0.0	±0.2
diboson xsec	±0.0	±0.0	±0.2	±0.0
multijet norm	±3.7	±1.4	±16.3	±4.4
$t\bar{t}$ modelling	±0.7	±1.0	±3.3	±0.8
singleTop modelling	±0.2	±4.0	±1.5	±0.3
$t\bar{t}$+singleTop radiation	±0.4	±1.5	±1.7	±0.5
W+jets PDF	±4.5	±13.7	±11.2	±3.9
Total Syst	±16.5	±39.2	±31.0	±8.9

Table 28.: Results for the charge asymmetry SF and for the flavour fractions K factors; the impact of systematic uncertainties (see Chapter 9) is shown. The systematic uncertainties have been symmetrised here. All these quantities are calculated for events with exactly two jets. The percentages are calculated as $100 \cdot \frac{modified-nominal}{nominal}$.

As discussed above, the procedure to correct W+jets is to take the K_i factors from the 2 jets bin, and the SF_{CA} factor from the relative jet multiplicity bin. The final result to be used for the normalisation of the $W + bb$ and $W + cc$ components in the signal region is $0.903 \pm 24.4\%$, for the $W + c$ component the result is $1.014 \pm 44.7\%$, and finally for the $W + lf$ component the result is $0.890 \pm 31.1\%$.

7.10 CONTROL PLOTS

This section is dedicated to control plots where data is compared to the sum of the predicted signal and backgrounds, for different distributions relevant for this measurement and after the event selection described in the previous sections. In the data/MC agreement there does not appear to be any discrepancy. The distributions are shown in the lepton+jets (where lepton means electron or muon) channels. In all plots, the statistical and systematic uncertainties (see Chapter 9) are shown.

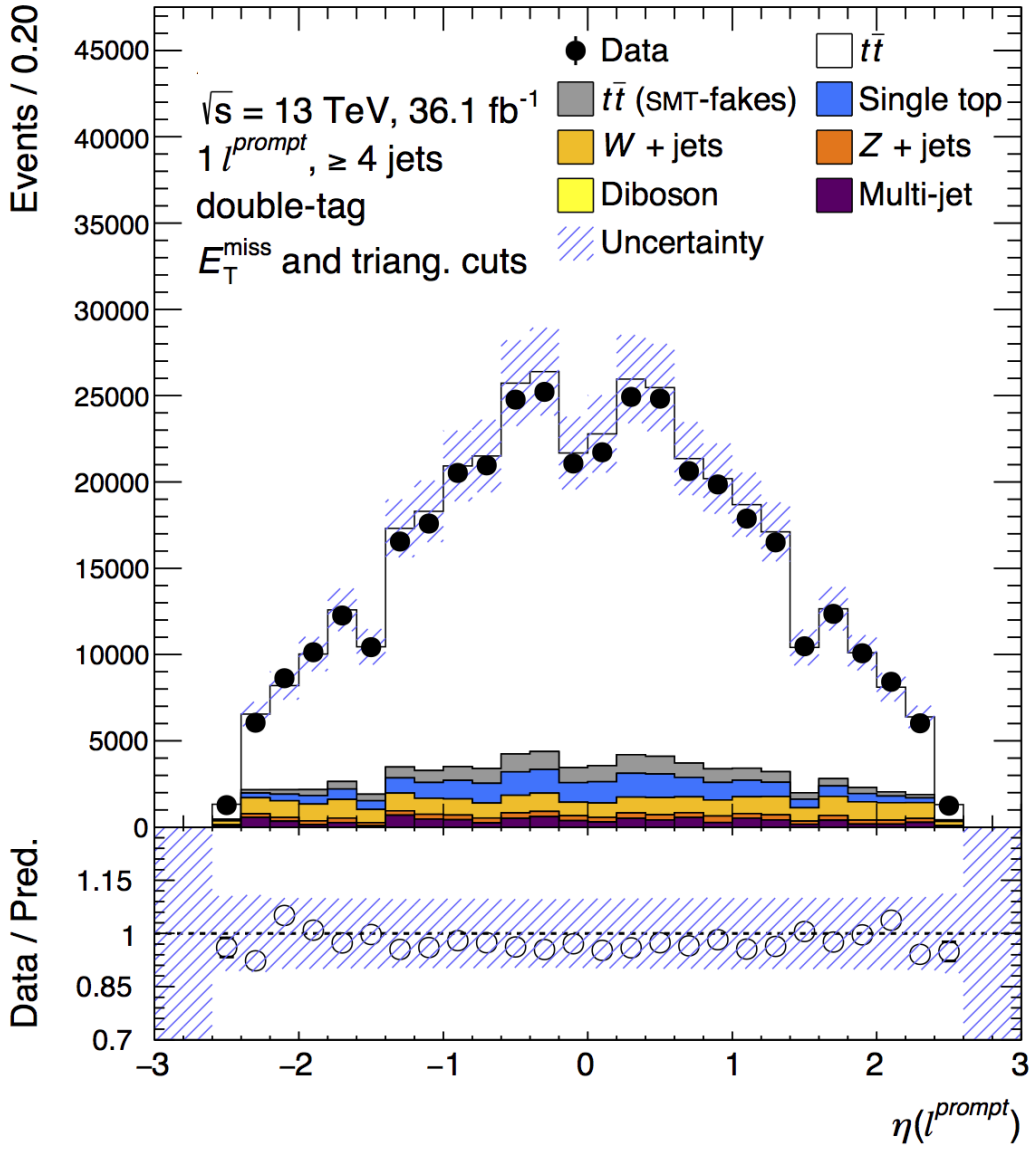

Figure 98.: The isolated lepton η lepton+jets channel.

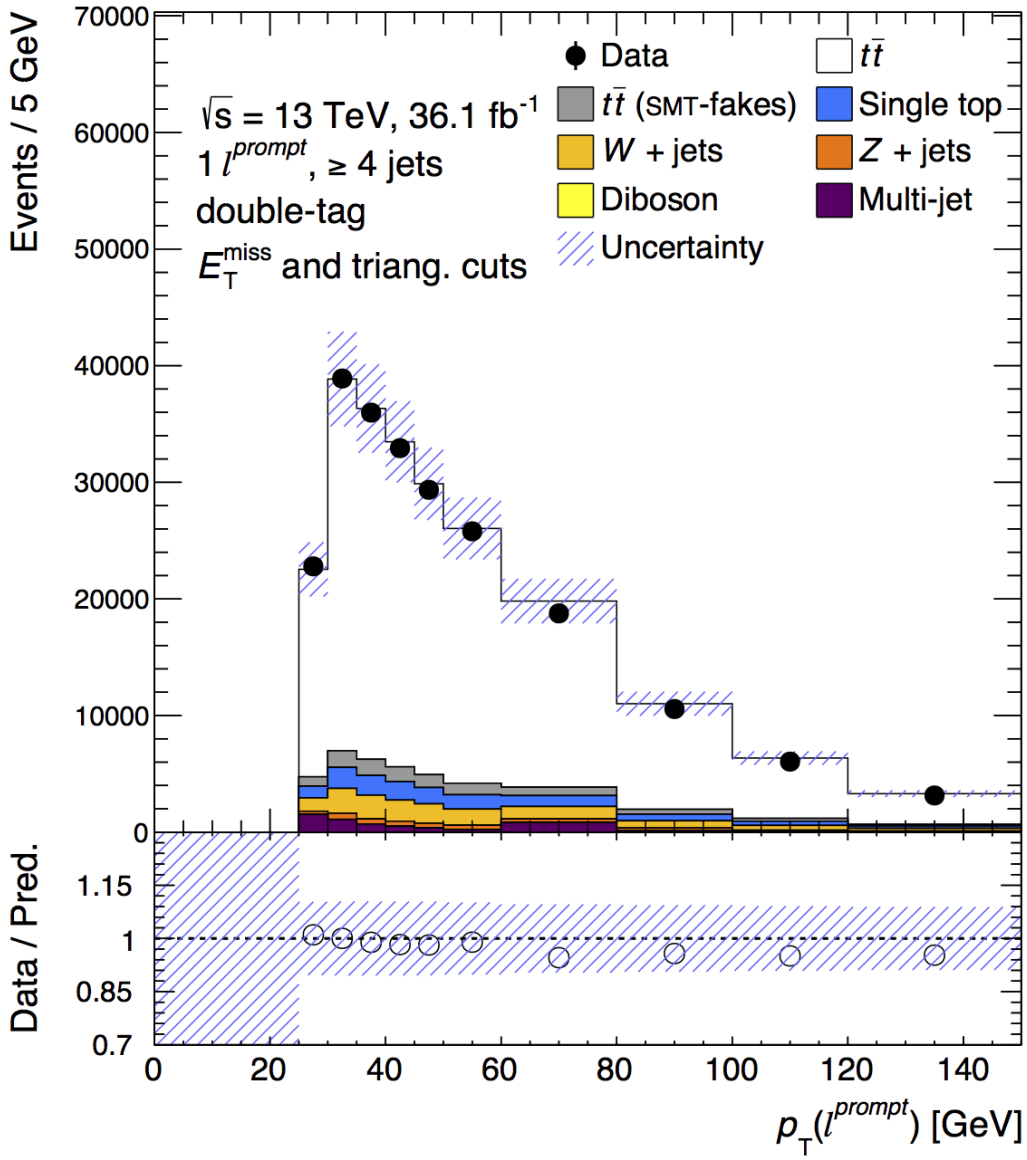

Figure 99.: The isolated lepton p_T, lepton+jets channel.

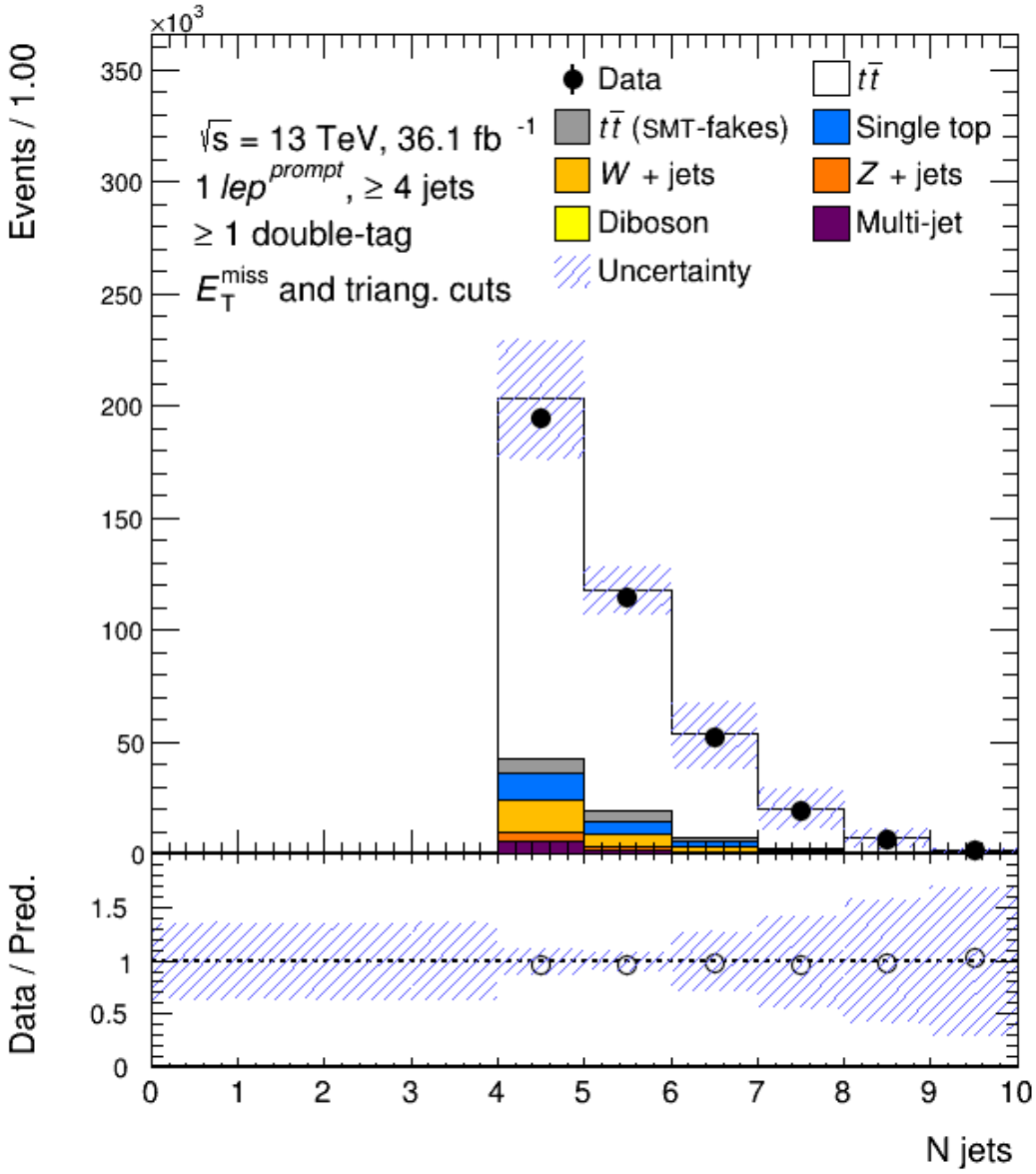

Figure 100.: Number of jets in the *b*-tag double selection, lepton+jets channel.

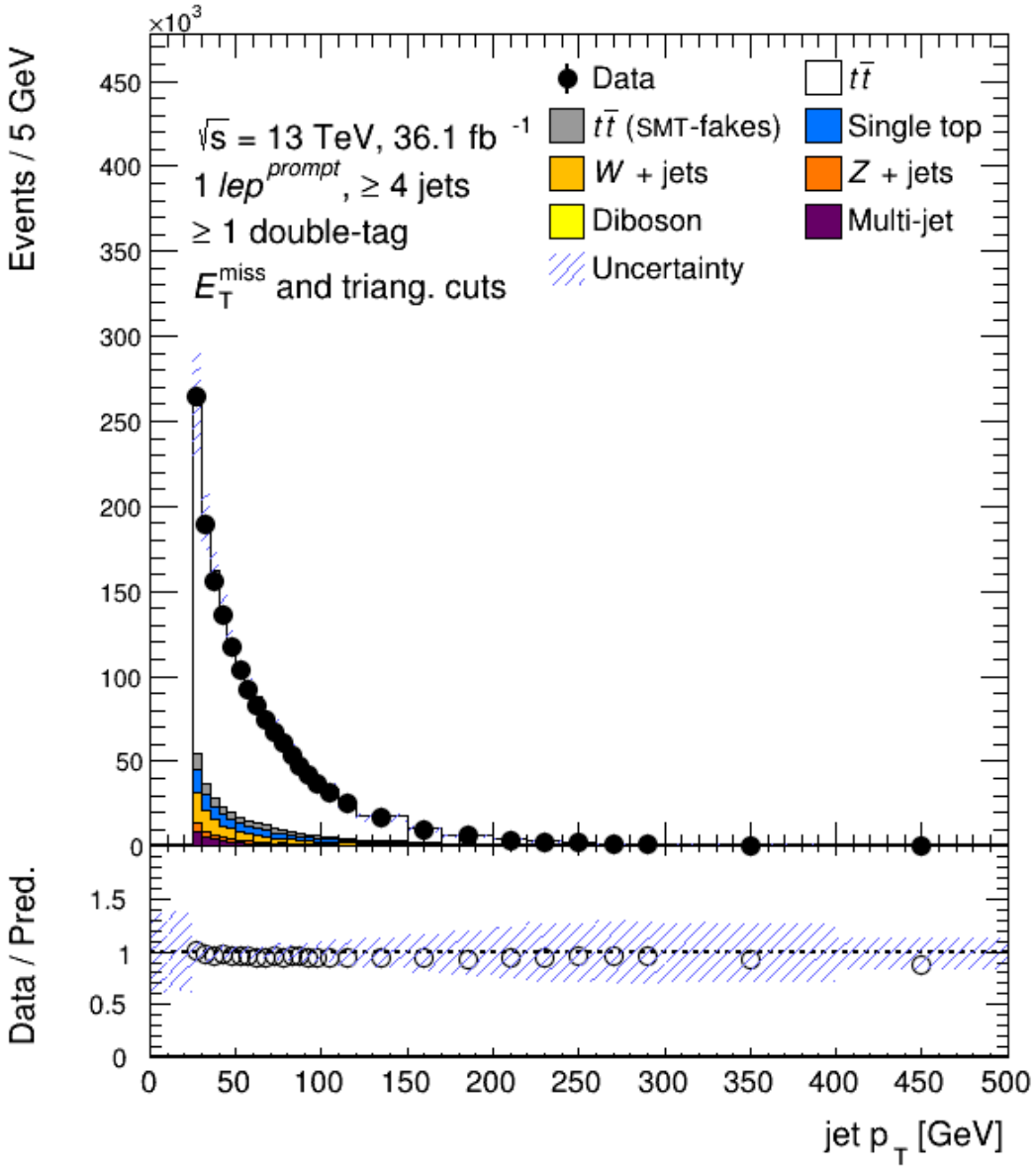

Figure 101.: Jet p_T, lepton+jets channel.

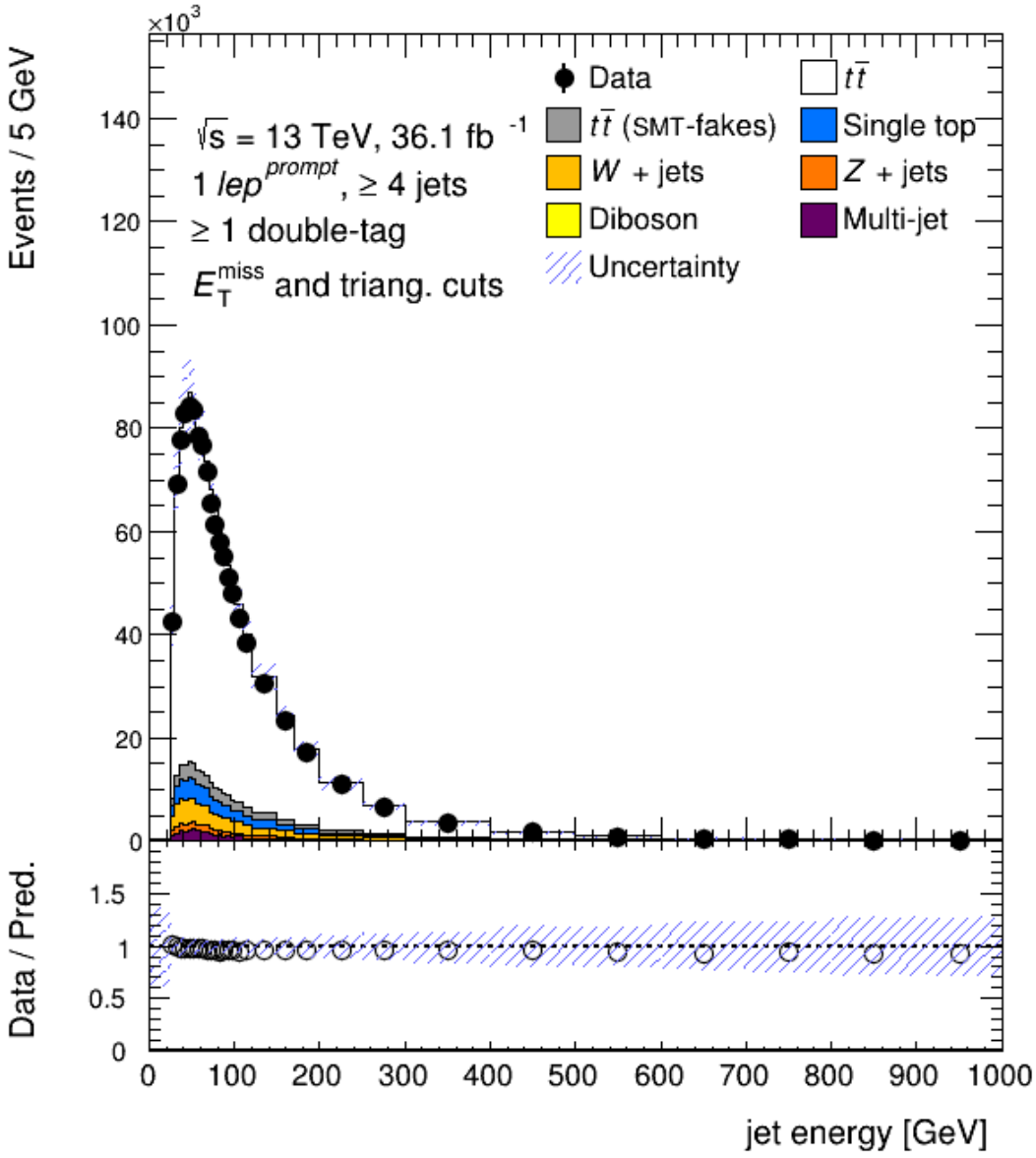

Figure 102.: Jet energy, lepton+jets channel.

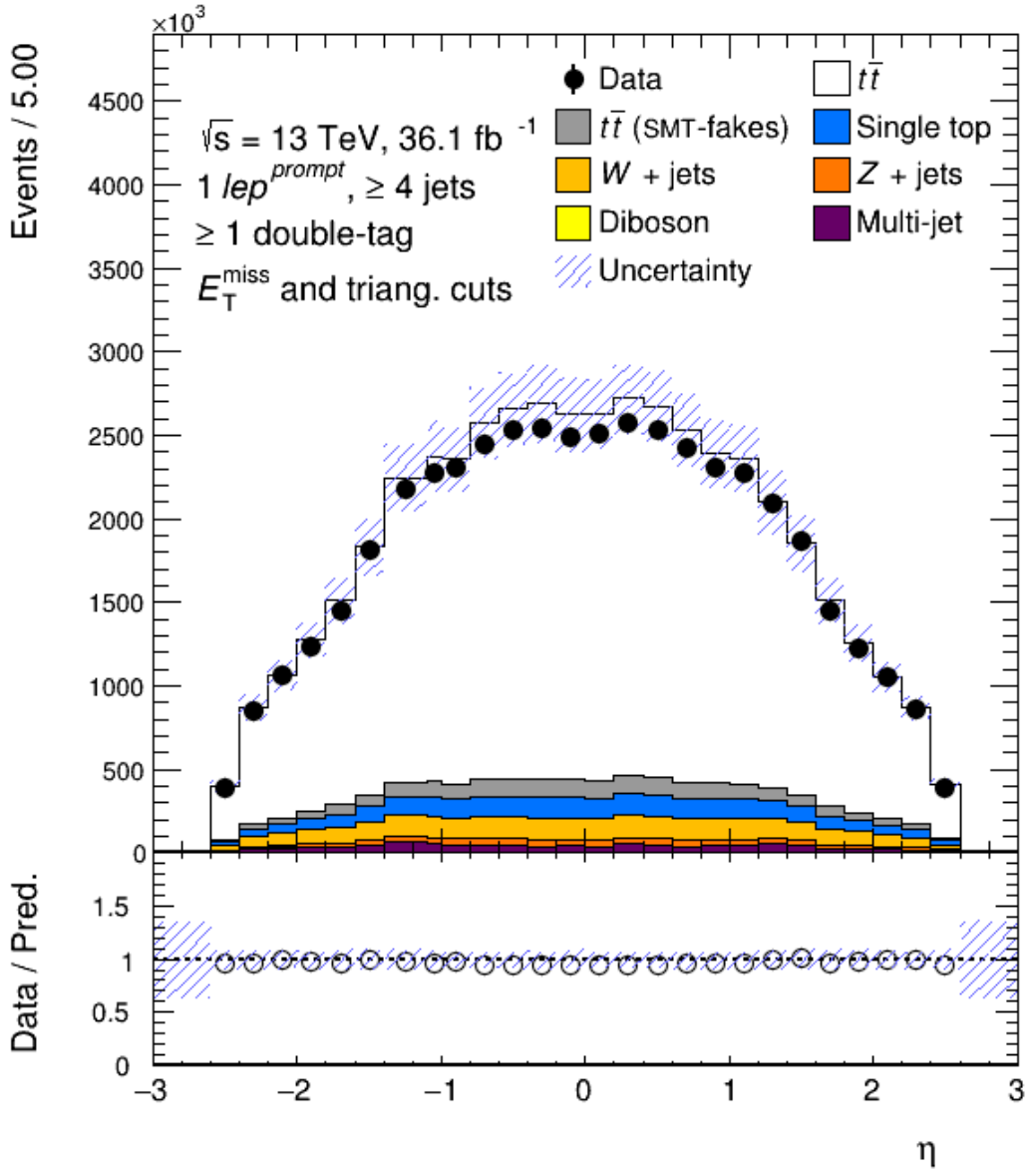

Figure 103.: Jet η, lepton+jets channel.

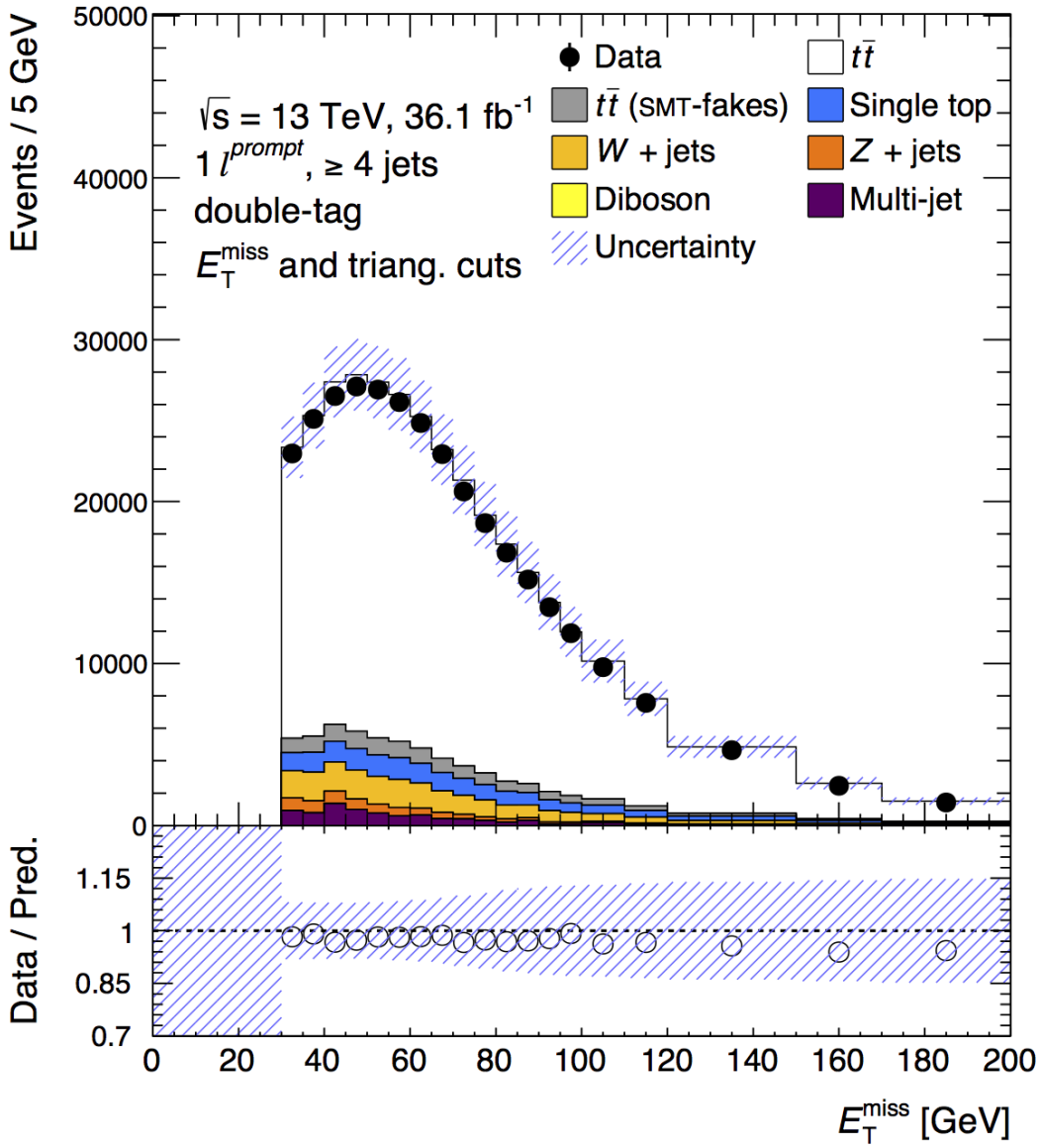

Figure 104.: Missing transverse energy, lepton+jets channel.

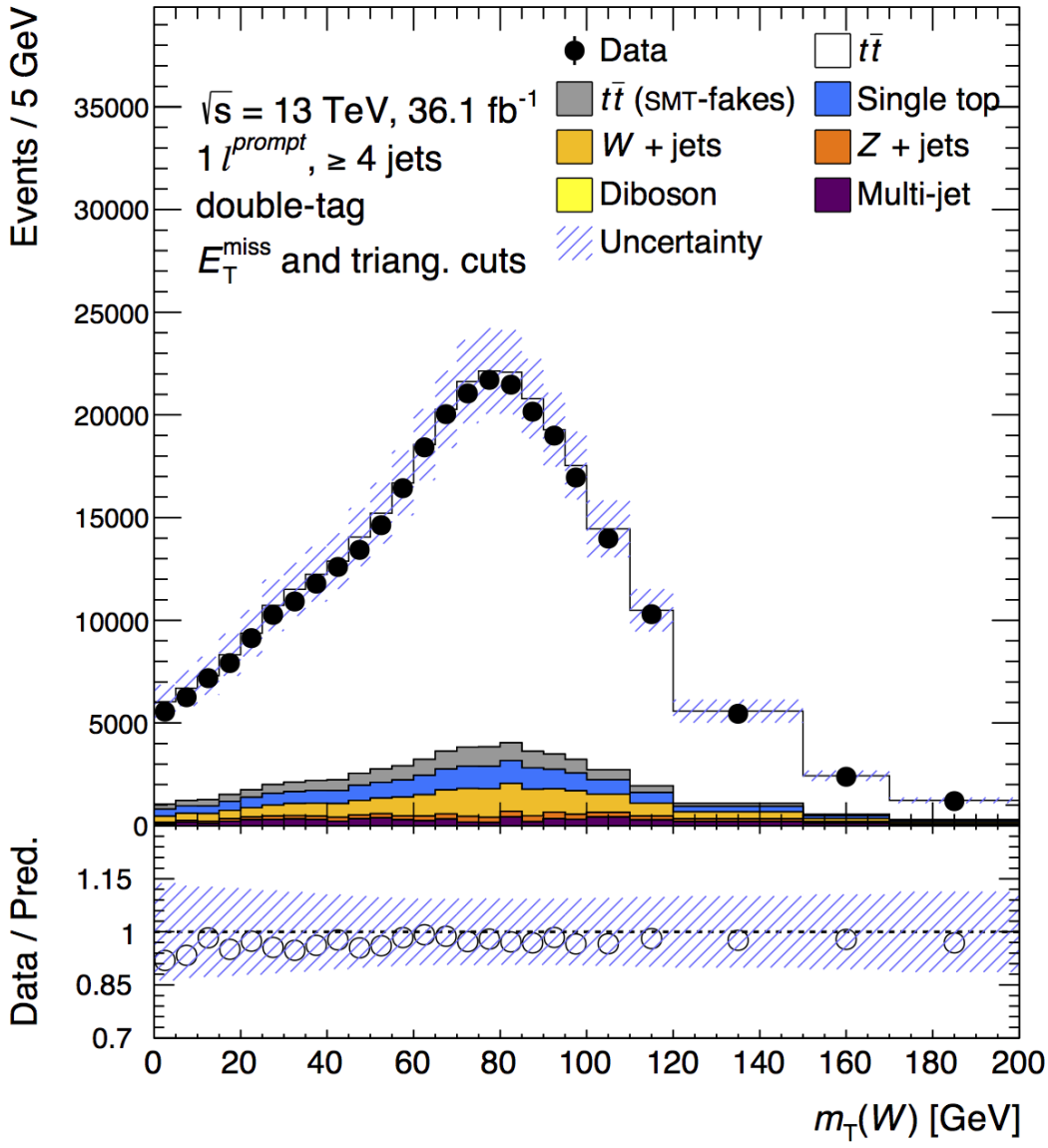

Figure 105.: The transverse mass of the isolated lepton - neutrino pair $m_T(W)$, lepton+jets channel.

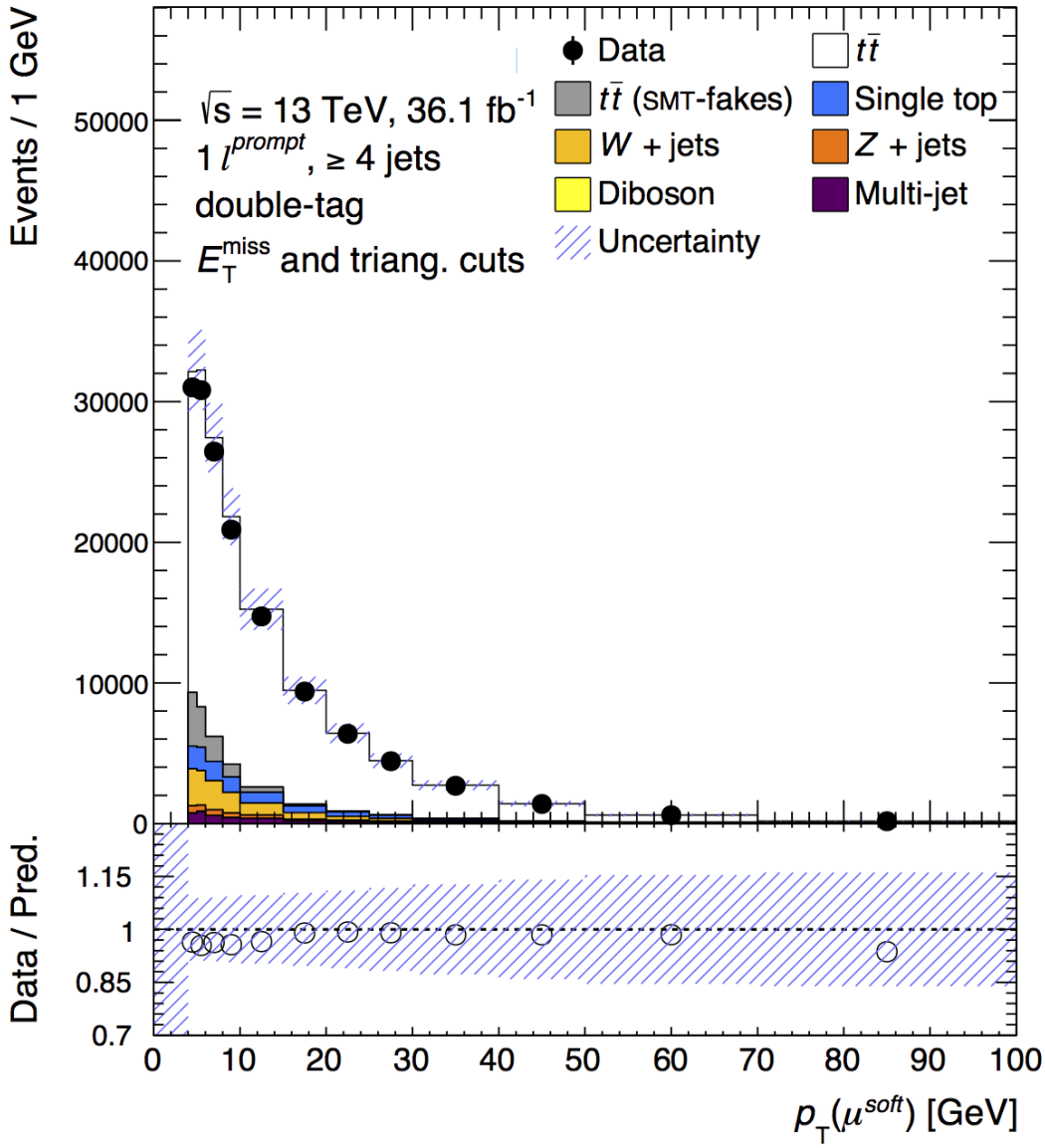

Figure 106.: The soft muon p_T, lepton+jets channel.

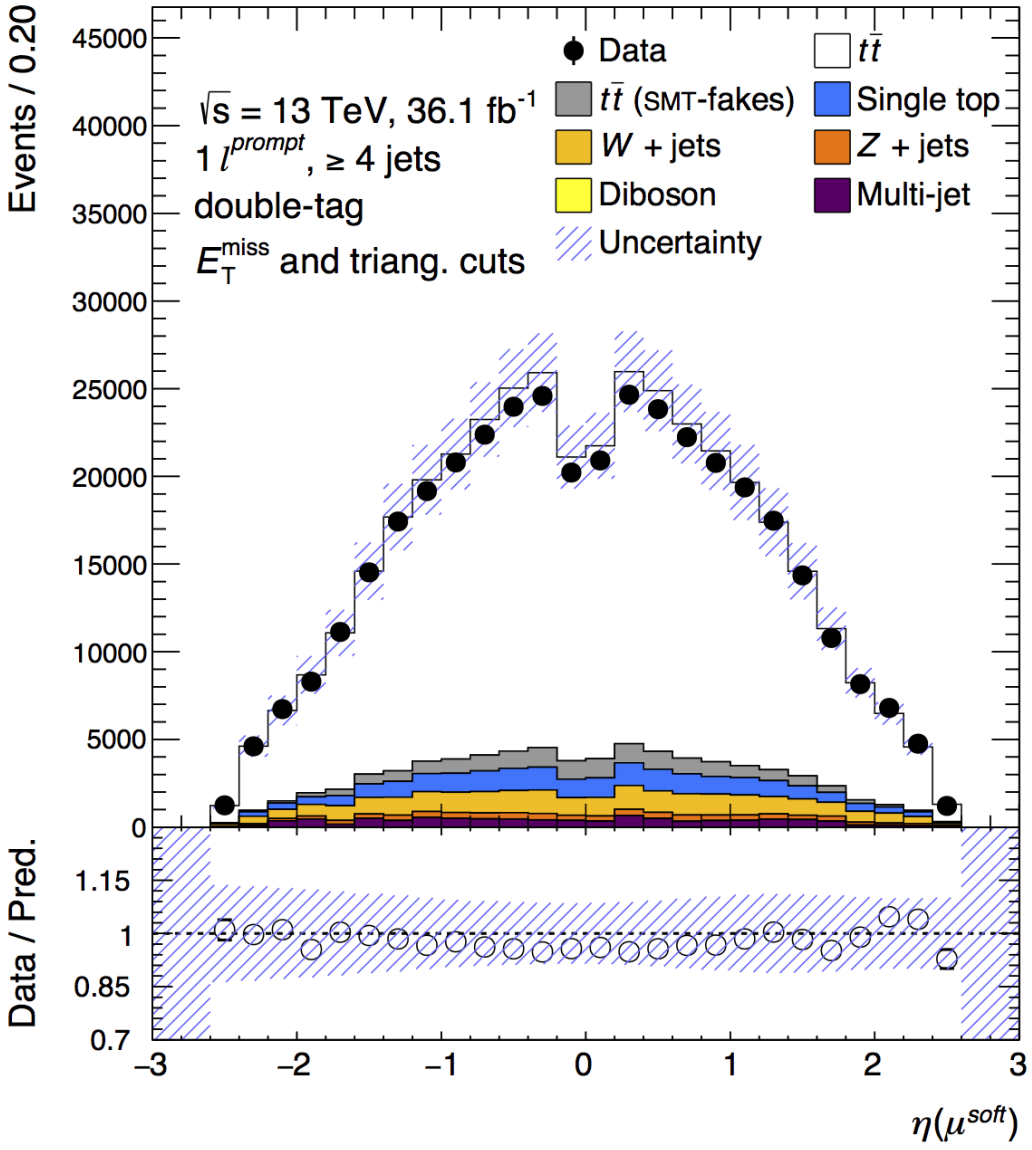

Figure 107.: The soft muon η, lepton+jets channel.

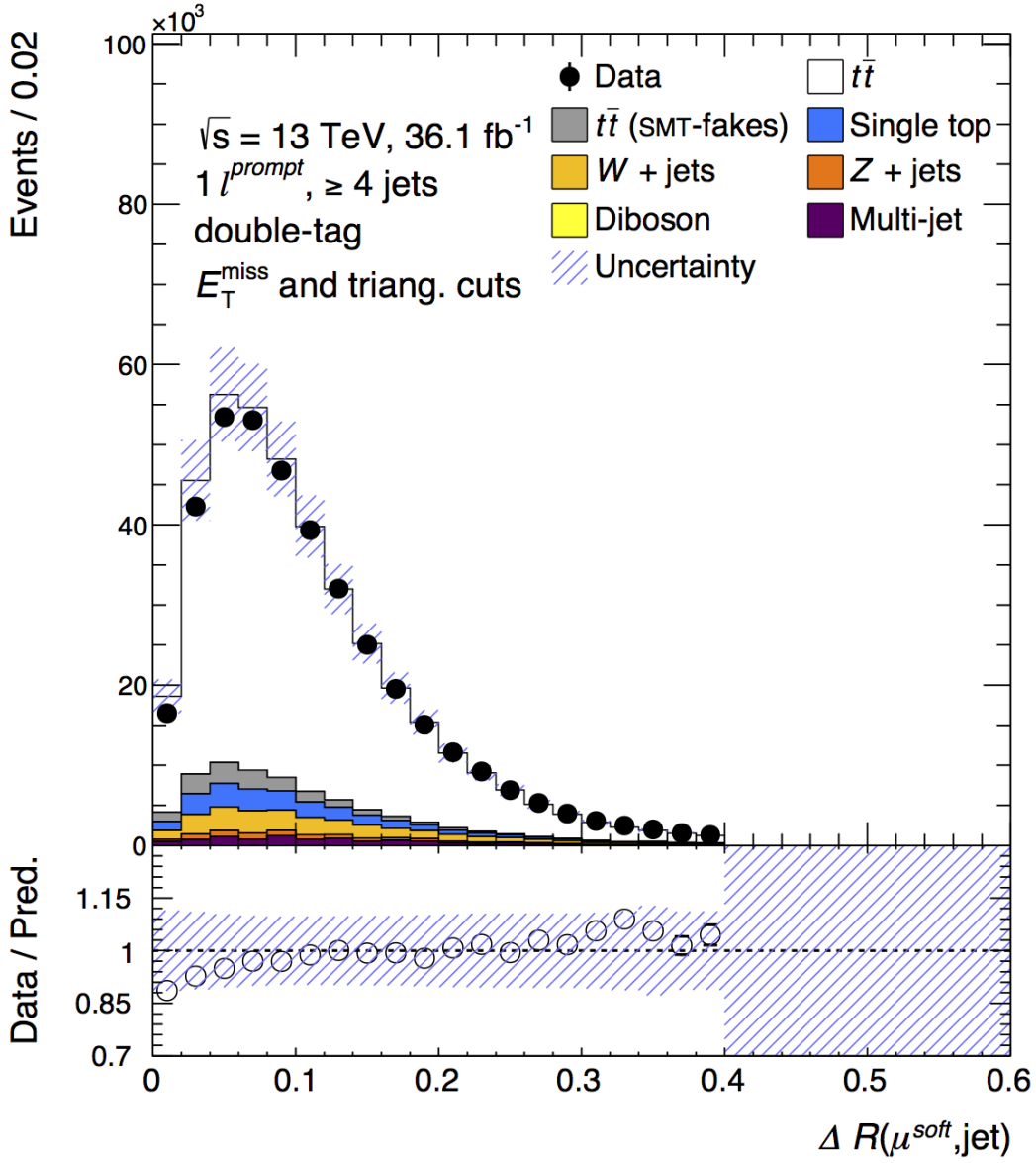

Figure 108.: Angular distance between the soft muon and the jet, lepton+jets channel.

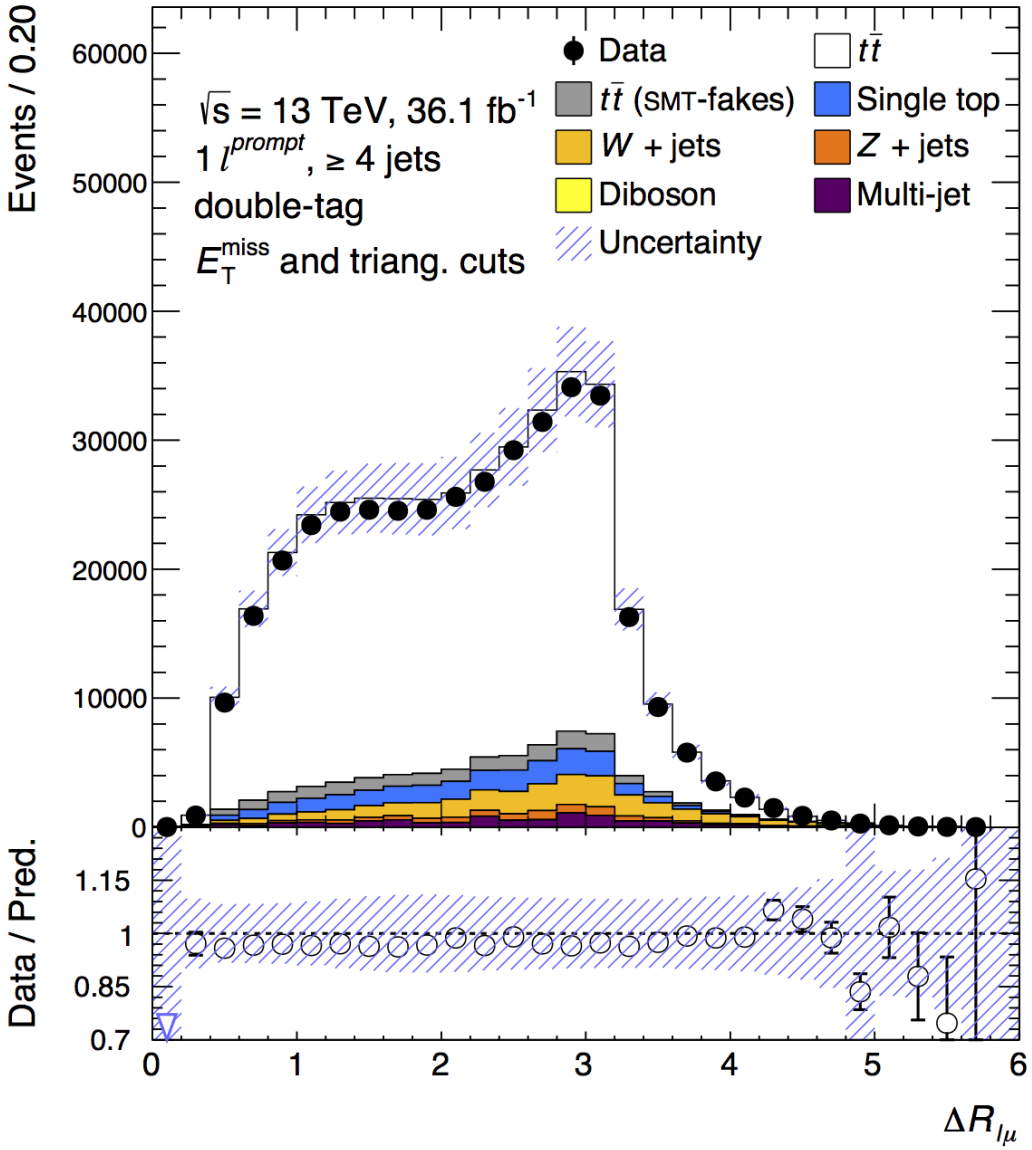

Figure 109.: Angular distance between the soft muon and the prompt lepton, lepton+jets channel.

8

KINEMATIC LIKELIHOOD FITTER

To accurately reconstruct $t\bar{t}$ events and find the correct charge-pairings of soft muons and charged hard lepton from the W- boson decay, it is important to separate events into two categories. In $t\bar{t}$ events, if both the leptons originate from the decay products of an individual top quark (they are on the same side of the decay) they are classified as same top (ST) events; if the two leptons come from the decay products of two different top quarks they are classified as different top (DT). In order to determine the ST/DT separation, a kinematic fitting is employed. The default settings and the optimal configuration of the kinematic fitting is described below. The best purity achieved is of the order of 90%*, with an increase of* $\sim$ 10% *with respect to Run-*1 *performances. This is a crucial task for the CA asymmetry analysis because a better performing fitter corresponds to a better accuracy in the systematic uncertainties which affect the analysis.*

8.1 KINEMATIC LIKELIHOOD FITTER

The KLFitter [96] is a kinematic likelihood based fitter which fully reconstructs the $t\bar{t}$ system shown in figure 110, for the $t\bar{t}$ semi-leptonic decay.

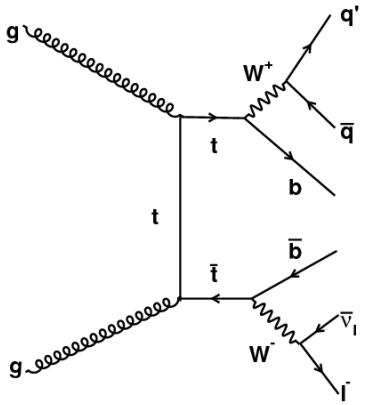

Figure 110.: Leading order Feynman diagram for semi-leptonic $t\bar{t}$ process.

Since top quarks decay to a W boson and a bottom quark in nearly 100% of all cases ($\left|V_{tb}^{\mathrm{CKM}}\right| = 1.021 \pm 0.032$ [1]), top pair events are characterised by two b-jets and the W boson decay products in the final state. The signature of $t\bar{t}$ lepton+jets events used here is defined by exactly one prompt lepton (electron or muon) and four jets, out of which two have to satisfy the b-tagging conditions. Naively one can expect that the original light quarks, coming from the hadronically decay of the W boson, and the b quarks will result in four particle-level jets, however additional radiation and pile-up effects can lead to more than four jets, while the acceptance can reduce the number of reconstructed jets. Moreover also the hadronic decays of τ leptons can fake a jet in the event selection.
The KLFitter manages all the possible permutations of the identified jets and leptons and picks the most probable configuration according to the $t\bar{t}$ event topology. The goal of the fitter is to find the correct matchings between measured objects and those in the model and to fit the measured properties of the reconstructed objects and simultaneously correct the event kinematic to improve the agreement with the expected true values. Within the framework of this analysis, the aim is to obtain the most likely pairings between reconstructed objects and the final state model particles (shown in Figure 110) for the $t\bar{t}$ decay, while fitted parameters are not exploited.
In principle, four reconstructed jets in four positions opens the possibility for 24 possible permutations, according to the formula 68 which describes the number of possible permutations if the total number of jets in the event is n.

$$P_{n,k} = \frac{n!}{(n-k)!} \tag{68}$$

$P_{n,k}$ is the number of arrangements of a k-element subset of an n-set. k corresponds to the number of partons in the final state and, for example, it is equal to 4 in $t\bar{t}$ events shown in Figure 110. However, as none of the functions within the likelihood are sensitive to an interchange of positions between the two hadronic W-bosons jets, the reconstruction is simplified to 12 permutations (in general, the reconstruction is simplified to $\frac{P_{n,k}}{2}$).

8.1.1 *Kinematic Likelihood approach*

The KLFitter makes use of the Bayesian Analysis Toolkit (BAT) [119] and the ROOT [120] class TMinuit [121] in order to find the global minimum of the negative log likelihood $-\ln L$, when testing each of the four reconstructed jets as placed in

each of the possible positions within the event topology and it returns refitted values for the 4-vectors parameters of each object (p_T, η, φ, E). This means that among all the possible assignments of jets and leptons the chosen configuration for each event is the one with the largest value of the likelihood function.
The global maximum (if it exists) of a likelihood function provides the maximum likelihood estimate (MLE) for multiple parameters. In statistics, an MLE is known to be a consistent estimator which satisfies the requirements to be unbiased and efficient in the limit of infinite events. However, with finite N events there is a known bias proportional to $1/N$.
From a practical point of view, if the likelihood function has multiple constituents, it is more convenient calculating the maximum of the corresponding log-likelihood function because this technique provides the advantage of turning the product of each probability density function (pdf) into a sum of pdfs. The parameter values which maximise L will also maximise $\ln L$. Moreover, minimising the negative of the log-likelihood function is equivalent to maximising the positive log-likelihood and this choice is largely due to a historical convention.
In the context of this analysis, it is possible to build a likelihood function using the measured jet and lepton properties and several constraints from theory and from detector resolution.

8.1.2 *Constraints*

The signature of $t\bar{t}$ semileptonic decays consists of four measured jets (two b-jets from top-quark decays, and two light-jets from a W-boson decay), a charged hard lepton and missing momentum due to a neutrino.
The first constraint is on the invariant mass of two light jets m_{jj}: they are required to follow a Breit-Wigner (BW) distribution around the W-boson mass $M_W = 80.4\,\text{GeV}$ of width $\Gamma_W = 2.1\,\text{GeV}$. Also, the hard lepton and the neutrino coming from the leptonically decaying W have to satisfy a similar requirement, as shown below. Moreover it is possible to introduce further constraints by reconstructing the invariant masses of the top quarks on either side of the decay, via m_{jjj} and $m_{\ell\nu j}$, and requiring these to be within a BW of the top-quark mass $M_t = 172.5\,\text{GeV}$ with a width of $\Gamma_t = 1.5\,\text{GeV}$. The BW distribution, shown in formula 69, provides information on how much a measured value of a mass M_x peaks around an expected central mass M_0 and width Γ.

$$BW\left(M_x|M_0\right) = \frac{2}{\pi}\frac{\Gamma M_0^2}{\left(M_x^2 - M_0^2\right)^2 + M_0^2\Gamma^2} \tag{69}$$

Neutrino transverse momentum can be estimated from the missing transverse energy (MET) in the event because neutrinos are very unlikely to interact and be detected directly within the detector volume. The x and y components of the neutrino momentum are identified with the transverse components of the missing energy ($E_{\mathrm{T}}^{\mathrm{miss}}$), as shown in equation 70 and 71, where φ_{MET} is the azimuthal angle.

$$E_x^{\mathrm{miss}} = E_{\mathrm{T}}^{\mathrm{miss}} \cdot \cos\left(\varphi_{\mathrm{MET}}\right) \tag{70}$$

$$E_y^{\mathrm{miss}} = E_{\mathrm{T}}^{\mathrm{miss}} \cdot \sin\left(\varphi_{\mathrm{MET}}\right) \tag{71}$$

A constraint on the W-boson mass provides the indirect measurement of the neutrino momentum along the z direction via formula 72.

$$M_W^2 = \left(P_\nu + P_\ell\right)^2 \tag{72}$$

where P_ν and P_ℓ are the four-momenta of the neutrino and of the charged lepton, respectively. If two solutions exist, the one which gives the maximum likelihood is chosen, while if no solution exists, the longitudinal momentum p_ν^z is considered as an additional free parameter in the fit.

8.1.3 *Transfer Functions*

Transfer functions (TFs) map the response of calibrated reconstructed objects onto that of the true associated particles. The detector response is simulated by smearing the particle energies with assumed resolution functions.
Transfer functions relate the input and the output of a given system and they are defined as the conditional probability of reconstructing a jet with energy $\tilde{E}_i$ given that there was a quark with energy E_i in the truth final state.
Transfer functions are derived for all the objects involved in $t\bar{t}$ events: electrons, muons, light (u, d, s, c) jets, b-tagged jets and $E_{\mathrm{T}}^{\mathrm{miss}}$. These are derived from $t\bar{t}$ MC simulations. TFs are parametrised depending on the object type, energy, transverse momentum, η-region and ϕ-region and are motivated by detector geometry: indeed the detector performances are not uniform in the whole ATLAS apparatus.
The pairing of the reconstructed objects to the underlying partons is performed requiring:

- a matching in $\Delta R\left(\mathrm{quark}, \mathrm{jet}\right) \leq 0.3$ between the parton and the reconstructed jet
- a matching in $\Delta R\left(\mathrm{truth}, \mathrm{reco}\right) \leq 0.1$ for leptons

If the matching was not unique the event is discarded. Transfer functions for the energy are parametrised by double-Gaussian functions, as shown in the formula 73.

$$W(E_{\text{truth}}, E_{\text{reco}}) = \frac{1}{\sqrt{2\pi}(p_2 + p_3 p_5)} (e^{-\frac{(\Delta E - p_1)^2}{2p_2^2}} + p_3 e^{-\frac{(\Delta E - p_4)^2}{2p_5^2}}) \tag{73}$$

where $[p_1, p_2, p_3, p_4, p_5]$ are parameters depending on the true energy and $\Delta E = \frac{E_{\text{truth}} - E_{\text{reco}}}{E_{\text{truth}}}$ is not symmetric because the true energy of a particle is generally higher than the one measured by the detector. The TFs are therefore asymmetric. In this parametrisation the energy is expressed in GeV.
The transfer functions used in this analysis are extracted from ATLAS Run-2 data at a centre-of-mass energy of 13 TeV.

8.1.4 *Likelihood Function*

In $t\bar{t}$ lepton+jets events, the KLFitter tests all the possible permutations of the identified jets and leptons and selects the most probable configuration according to the event topology.
For each possible permutation, a likelihood is calculated with parameters set by the following parameters:

- four quark energy resolution functions $\left(W(\tilde{E}_i|E_i)\right)$
- one lepton energy resolution function $\left(W(\tilde{E}_l|E_l)\right)$
- neutrino p_T resolution function $\left(W(E_x^{miss}|p_x^\nu) \cdot W(E_y^{miss}|p_y^\nu)\right)$
- Breit-Wigner functions which provide constraints on the W boson mass (*i.e.* $BW(m_{l\nu}|M_W)$) and optionally on a set of floating values for the Top pole mass

Hence the likelihood is the product all of the above constraints and transfer functions (TFs) and the following represents the likelihood as prescribed in the nominal usage of the KLFitter:

$$\begin{aligned} L = \left(\prod_{i=1}^{4} W(\tilde{E}_i|E_i)\right) \cdot W(\tilde{E}_l|E_l) \cdot W(E_x^{miss}|p_x^\nu) \cdot W(E_y^{miss}|p_y^\nu) \cdot \\ BW(m_{jj}|M_W) \cdot BW(m_{l\nu}|M_W) \cdot BW(m_{jjj}|M_t) \cdot BW(m_{l\nu j}|M_t) \end{aligned} \tag{74}$$

KLFitter does not take into account any b-tagging information, by default. But to improve measurements b-tagging efficiencies can be used, as discussed in Section 8.2.2.

The lepton information is used in the invariant mass constraints, however it is assumed that there is no uncertainty on the measured direction of the lepton and hence this angular information does not float during the fit. Also the angles of the reconstructed particle jets are assumed to be measured with negligible uncertainty.

8.1.5 *Likelihood extended*

The top quark decays via electroweak interactions, whose $V - A$ structure provides predictions on the angular distribution of the charged lepton.
In the KLFitter package there is the option to use an extended likelihood fit where helicity corrections in the decays of the W-bosons are implemented. These corrections are described by the formula 75.

$$\frac{1}{\Gamma_W}\frac{d\Gamma_W}{d\cos\theta^*_{\ell b_{lep}}} = \frac{3}{4}F_0\left(1-\cos\theta^*_{\ell b_{lep}}\right)^2 + \frac{3}{8}F_L\left(1-\cos\theta^*_{\ell b_{lep}}\right)^2 + \frac{3}{8}F_R\left(1-\cos\theta^*_{\ell b_{lep}}\right)^2 \tag{75a}$$

$$\frac{1}{\Gamma_W}\frac{d\Gamma_W}{d\cos\theta^*_{q b_{had}}} = \frac{3}{4}F_0\left(1-\cos\theta^{*2}_{q b_{had}}\right) + \frac{3}{8}\left(F_L+F_R\right)\left(1-\cos\theta^{*2}_{q b_{had}}\right) \tag{75b}$$

where $F_{0,L,R}$ are the measured fractions of longitudinal, left-, and right-handed W-boson helicity, as detailed in [122].

8.1.6 *Fitting Parameters*

There are 8 parameters which are used in the fitting procedure and they account for the transfer functions of the measured objects and the kinematical constraints on W-boson and Top quark decay vertices. These are listed below:

- energies of the four quarks E^i_{jet} (4 parameters);
- energy of the charged lepton E_ℓ, electron or muon (1 parameter);
- momentum components of the neutrino (3 parameters).

Each parameter can vary in the kinematic fit within a fixed range. The ranges of the jet energies, lepton energy and the neutrino momentum components are set individually around the measured values:

- $E^i_{jet} \in \left[\tilde{E}^i_{jet} - 3\sigma, \tilde{E}^i_{jet} + 3\sigma\right]$
- $E^i_{\ell} \in \left[\tilde{E}^i_{\ell} - 3\sigma, \tilde{E}^i_{\ell} + 3\sigma\right]$

- $p^{\nu}_{x,y} \in \left[\tilde{p}^{\nu}_{x,y} - 3\sigma, \tilde{p}^{\nu}_{x,y} + 3\sigma\right]$
- $p^{\nu}_{z} \in [-1000., 1000.]$ GeV

8.2 NOMINAL SETUP AND KLFITTER OPTIMISATION

The default setup of the KLFitter [96] is outlined below. This setup is designed to give a good basis from which to build a likelihood, providing good identification of event topologies.

- b-tagging: MV2c10 set at 77% working point
- Number of b-tagged jets: ≥ 1 b-tagged jet
- kVetoNoFit: no b-tagged jets allowed in light-flavour positions
- Fixed top mass: 172.5 GeV
- Jet selection: only the four jets with the highest p_T are selected per event
- Likelihood: basic likelihood in Equation 74 and the permutation which returns the maximum likelihood is taken as the best option

Several configurations were tested in order to maximise the power of the algorithm to discriminate between hard lepton-SMT muon pairs coming from the same or a different top.

In order to measure and maximise the performance of the KLFitter the purity of its decisions was studied, the purity is described by the formula 76 for the same top (ST) case but relevant for the different top (DT) case also

$$\rho_{\mathrm{KL}} = \frac{\mathrm{N}^{\mathrm{ST}}_{\mathrm{truth}} \text{ and } \mathrm{N}^{\mathrm{ST}}_{\mathrm{KLF}}}{\mathrm{N}^{\mathrm{ST}}_{\mathrm{KLF}}} = \mathrm{P}\left(\mathrm{T}_{\mathrm{ST}} | \mathrm{KLF}_{\mathrm{ST}}\right) \tag{76}$$

where, $\mathrm{N}^{\mathrm{ST}}_{\mathrm{truth}}$ is the number of true ST events, $\mathrm{N}^{\mathrm{ST}}_{\mathrm{KLF}}$ is the number of events identified by KLF as ST and $\mathrm{P}\left(\mathrm{T}_{\mathrm{ST}} | \mathrm{KLF}_{\mathrm{ST}}\right)$ is the probability of an event being a truth ST event given a ST KLFitter decision.

The signal selection was chosen to minimise the the b-tagging systematics, *i.e.* the systematic uncertainties on the MV2c10 tagger efficiency and mis-tag rate (especially from c-jets). The nominal selection, referred to as 'double-tag' relies on the presence of at least one jet b-tagged by both the MV2c10 and SMT algorithms, and the soft muon associated with this jet is used to build the charge asymmetries. The studies presented here are performed using the double-tag selection.

The left columns in Table 29 (labeled as Without SLC) shows the KLFitter purity performances in the lepton, electron and muon channels using the nominal configuration and the b-tag double option.

8.2.1 *Semi-leptonic corrections*

The KLFitter performance increases significantly if semi-leptonic corrections (SLC) are applied. As the jets in consideration are b-jets decaying semileptonically, part of the original jet energy and transverse momentum will be removed by the soft muon and its associated neutrino. The effect of these decays is corrected by finding muons within $\Delta R\left(\mu^{\text{soft}}, \text{jet}\right) < 0.5$ of the b-tagged jets and adding the energy of these muons to that of the jet (while taking into account the muon energy loss in the calorimeter) and derive the corresponding four vector and transverse momentum.
This correction was implemented in the KLFitter tools for these studies and it is applied as follows:

1. Identify reconstructed soft muons within the radius of the jet cone ($\Delta R\left(\mu^{\text{soft}}, \text{jet}\right) < 0.5$)
2. Subtract, from the reconstructed jet, the energy lost by the muon due to ionisation in the detector E_{μ}^{Loss}
3. Reconstruct the corrected jet four-momentum as:

$$\begin{bmatrix} p_{\text{T}} \\ \eta \\ \phi \\ E \end{bmatrix}_{jet} \rightarrow \begin{bmatrix} p_{\text{T}}^{\text{SLC}} = f(E^{\text{SLC}}, \eta) \\ \eta \\ \phi \\ E^{\text{SLC}} = E + E_{\mu} - E_{\mu}^{Loss} \end{bmatrix}_{jet}$$

4. No neutrino correction is applied

Table 29 shows the improvement of the KLFitter purity performances when applying semi-leptonic corrections.

The advantage of semi-leptonic corrections may be seen by comparing the histograms in Figures 111, 112, 113, 114. The improvement in the KLFitter performance is produced by providing the fitter with reconstructed b-jets closer in properties to the b-quarks present at parton level in the $t\bar{t}$ decay.
In order to obtain the correct jet-parton pairings in the event topology, the KLFitter TFs are required to alter the reconstructed jet p_{T} by a lesser amount during the fit when applying semi-leptonic corrections. This feature results in a higher likelihood for the correct jet permutations.

	Without SLC		With SLC	
Channel	Same Top	Different Top	Same Top	Different Top
Statistical	±0.1	±0.1	±0.1	±0.1
lepton+ jets	72.0	72.1	75.1	76.7
electron+ jets	72.3	72.7	75.5	77.4
muon+ jets	71.7	71.5	74.8	75.9

Table 29.: Purity of the KLFitter selection in the lepton, electron and muon channels using the *b*-tag double option, without and with semileptonic corrections applied and four leading jets. Results are expressed in percentage.

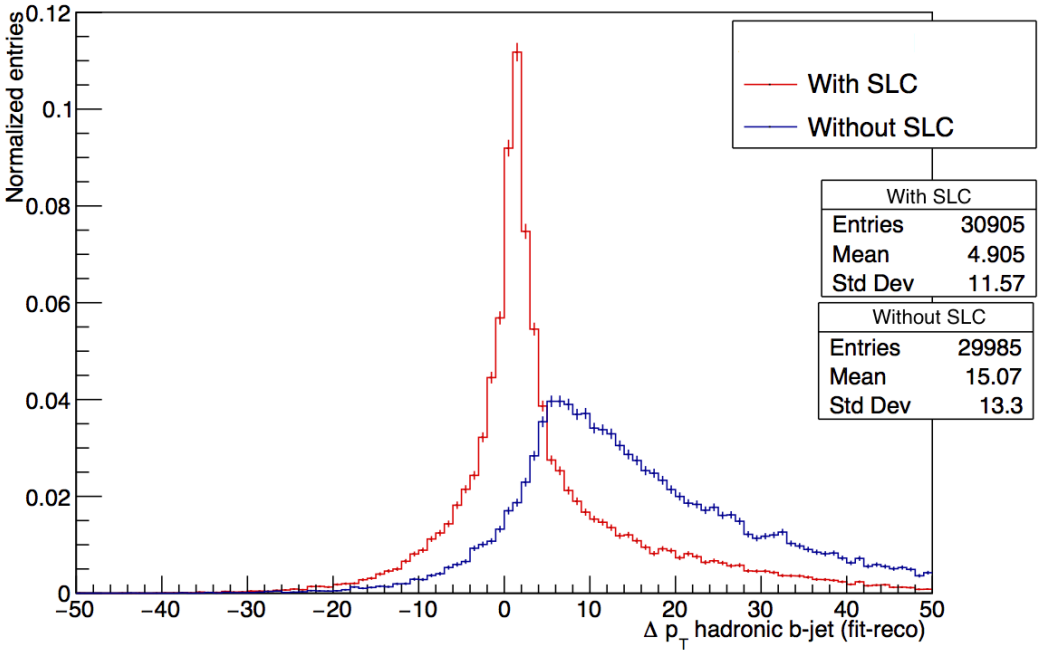

Figure 111.: *electron*+jets channel, the hadronic side of $t\bar{t}$ decay is shown. Difference between reconstructed *b*-jet p_T (with and without SLC correction) and fitted jet pT returned by the KLFitter. The shift of the mean towards zero in the SLC corrections indicates a less strenuous fit performed, and leads to a higher permutation likelihood. The *muon*+jets distribution is similar.

8.2.2 *b-tagging*

Better KLF performances are achieved if we give priority to the *b*-tagged jets when adding particles to the KLFitter. When the KLFitter was implemented, a constraint was set: among the permuted jets there must be at least one double *b*-tagged

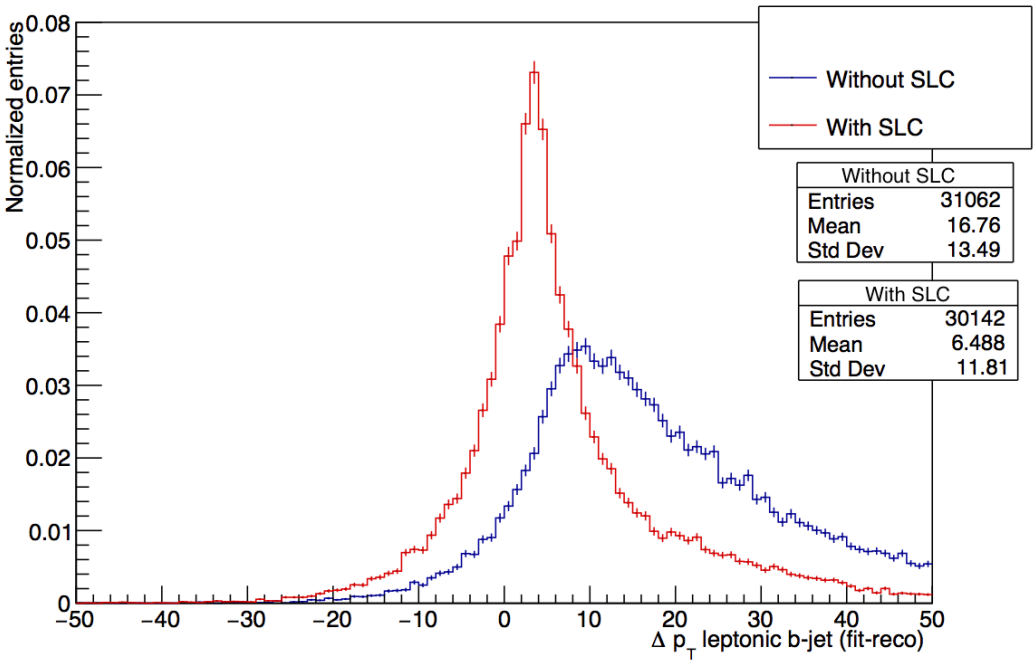

Figure 112.: *electron*+jets channel, the leptonic side of $t\bar{t}$ decay is shown. Difference between reconstructed b-jet p_{T} (with and without SLC correction) and fitted jet p_T returned by the KLFitter. The shift of the mean towards zero in the SLC corrections indicates a less strenuous fit performed, and leads to a higher permutation likelihood. The muon+jets distribution is similar.

jet. There are cases where the KLFitter identifies as the best permutation a combination of four jets and the SMT-tagged jet is not among them. In the context of the analysis presented here it is essential to include the SMT jet in the best permutation. For this reason, permutations where the SMT jet is excluded are removed from the KLFitter selection. Moreover, events where there are one or two b-jets but the fitter discards one of them are also removed. These further constraints force the KLFitter to include the soft muon originating jet in the selected best permutation.

The CPV analysis exploits the SMT-tagged jets to construct the charge and CP violation asymmetries so it is reasonable to prioritise the SMT-tagged jets when feeding the fitter. The following procedure was implemented:

- Require maximum 2 b-tagged jets, if there are more than 2 b-tagged jets in the event the ones with the lowest p_{T} are considered light jets by the KLFitter. The detailed prescription follows:
  1. Add the SMT+MV2c10 tagged jets first, up to 2 total jets
  2. Add the SMT or MV2c10 tagged jets, up to 2 total jets

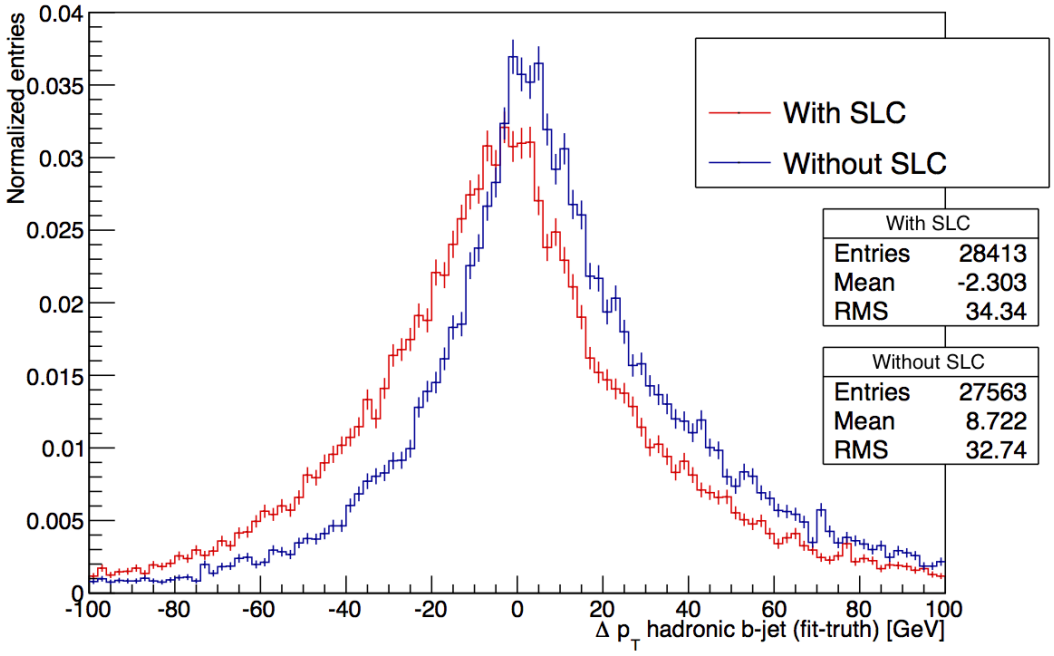

Figure 113.: *electron*+jets channel, the hadronic side of $t\bar{t}$ decay is shown. Difference between MC truth b-jet p_{T} (with and without SLC correction) and fitted jet p_T returned by the KLFitter. The shift of the mean towards zero in the SLC corrections indicates a less strenuous fit performed, and leads to a higher permutation likelihood. The muon+jets distribution is similar.

3. Add remaining light or tagged jets in order of high to low p_{T}

- A tightened kVetoNoFit selection: permutations where the SMT jet is excluded or where there are one or two b-jets in the event but the fitter discards one of them are removed. In this mode b-jets are fully trusted.

8.2.3 *Jet multiplicity*

The event selection of this analysis requires at least 4 jets to pass quality and momentum cuts. The KLFitter default configuration allows the fitter to permute only 4 jets, but there are events where the inclusion of the 5th or 6th reconstructed jet can be beneficial. For example ISR/FSR jets from alternative sources can be measured with a higher p_{T} than the primary jets and in these events the fitter could fail in reconstructing the correct event topology because it is permuting the wrong objects. On the other hand, the inclusion of more jets increases the number of permutations per event for which a likelihood has to be calculated, leading to

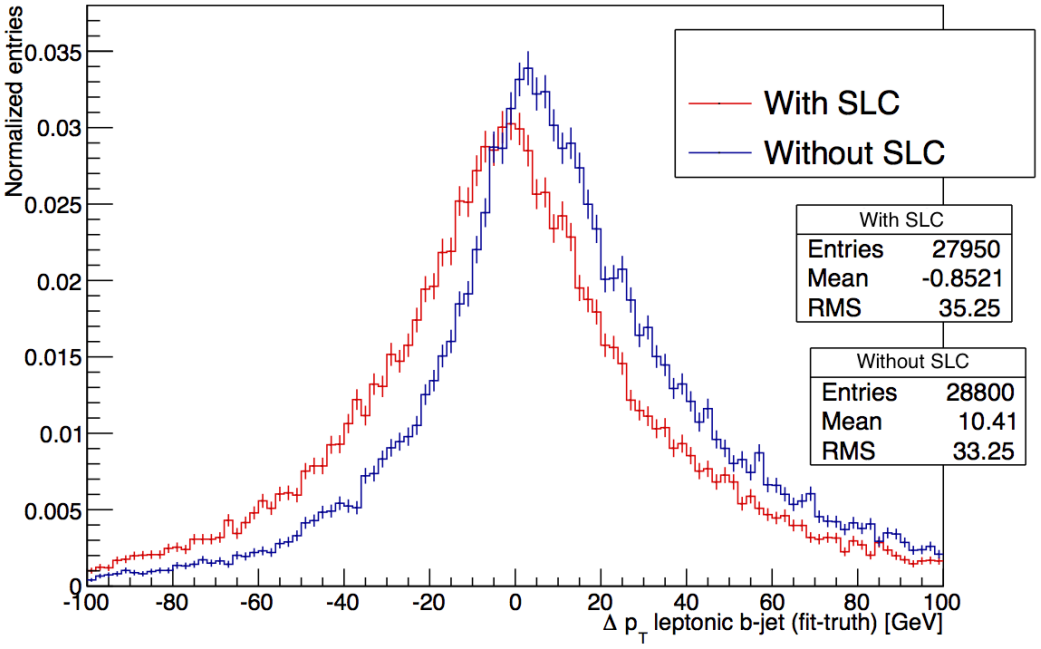

Figure 114.: *electron*+jets channel, the leptonic side of $t\bar{t}$ decay is shown. Difference between MC b-jet p_{T} (with and without SLC correction) and fitted jet p_T returned by the KLFitter. The shift of the mean towards zero in the SLC corrections indicates a less strenuous fit performed, and leads to a higher permutation likelihood. The muon+jets distribution is similar.

an increase in the processing time and computer time required. To test the fitter performance, up to 6 jets (with SLC applied) were added to the KLFitter.
Table 30 shows that there is an improvement in the fitter performances in the 5 leading jets configuration.

8.2.4 *Top mass treatment*

In the nominal likelihood calculation there is a constraint on the Top mass, set to 172.5 GeV for each side of the $t\bar{t}$ decay. This configuration sets a strong limit on how far the fitter can modify or smear the jet and lepton energies and angular distributions within their resolutions.
It is interesting to study the option of permitting free Top mass. Table 31 shows a drop in the KLF performance in the free Top mass setting versus the nominal configuration which is, for this reason, preferred from now on.

Jet multiplicity		Same Top	Different Top
Statistical		±0.1	±0.1
lepton +	4	75.1	76.7
	5	76.3	77.3
	6	73.4	74.1
electron +	4	75.5	77.4
	5	76.4	77.9
	6	73.7	74.6
μ +	4	74.8	75.9
	5	76.1	76.8
	6	73.1	73.5

Table 30.: Purity of the KLFitter selection in the lepton, electron and muon channels using the *b*-tag double option, in three different configurations: 4, 5, and 6 leading jets. Results are expressed in percentage.

Top mass treatement		Same Top	Different Top
Statistical Uncertainty		±0.1	±0.1
lepton+jets	Free	66.3	66.7
	172.5 GeV	76.3	77.3
electron+jets	Free	66.2	67.0
	172.5 GeV	76.4	77.9
muon+jets	Free	66.4	66.5
	172.5 GeV	76.1	76.8

Table 31.: Purity of the KLFitter selection in the lepton, electron and muon channels using the *b*-tag double option, as a function of the Top mass treatment. Results are expressed in percentage.

8.2.5 *Final configuration*

Finally, the setup which maximises the purity for this analysis is described below:

- *b*-tag double selection
- semi-leptonic corrections (SLC) applied if a soft muon is found inside a jet
- *b*-jet tagging method used to feed the KLF: maximum 2 *b*-tagged jets are required, if there are more than 2 *b*-tagged jets, the ones with the lightest p_T are considered light jets by the KLFitter.

- Fixed top mass (172.5 GeV)
- Permute the 5 hardest jets (b-jet priority)
- kVetoNoFit (No tagged jets in light-flavour positions); moreover permutations where the SMT jet is excluded or where there are one or two b-jets in the events but the fitter discards one of them are removed
- $>= 1$ jet tagged by MV2c10

The performance of the KLFitter in this configuration is described in Table 32.

Moreover, it is possible to achieve ever better performances (as in Table 32) if the angular corrections outlined in 8.1.5 are applied because they take into account the V-A angular structure of $t\bar{t}$ decays and this further constraint helps in fully reconstructing the event.

	Without AC		With AC	
Channel	Same Top	Different Top	Same Top	Different Top
Statistical	± 0.1	± 0.1	± 0.1	± 0.1
lepton+ jets	76.3	77.3	77.2	78.1
electron+ jets	76.4	77.9	77.3	78.4
muon+ jets	76.1	76.8	77.1	77.8

Table 32.: Purity of the KLFitter selection in the lepton, electron and muon channels using the b-tag double option, without and with angular corrections applied and five leading jets. Results are expressed in percentage.

Using this configuration, the performance of the KLFitter is presented in Tables 33, 34, 35 in the four charge asymmetry bins, only for $t\bar{t}$ signal events. The magnitude of the MC statistical uncertainty on all the performance tables in this section is on the order of 0.001 (0.1%).

	Same Top				Different Top			
	N^{++}_{Reco}	N^{--}_{Reco}	N^{+-}_{Reco}	N^{-+}_{Reco}	N^{++}_{Reco}	N^{--}_{Reco}	N^{+-}_{Reco}	N^{-+}_{Reco}
N^{++}_{Truth}	77.4	0	0	22.5	77.4	0	0	22.5
N^{--}_{Truth}	0	77.9	22.0	0	0	77.9	22.1	0
N^{+-}_{Truth}	0	24.0	76.0	0	0	20.7	79.2	0
N^{-+}_{Truth}	23.8	0	0	76.2	21.3	0	0	78.6

Table 33.: Purity of the KLFitter in $t\bar{t}$ events for same and different-top like events. Statistical error: ± 0.1, *electron*+jets channel. Results are expressed in percentage.

	Same Top				Different Top			
	N^{++}_{Reco}	N^{--}_{Reco}	N^{+-}_{Reco}	N^{-+}_{Reco}	N^{++}_{Reco}	N^{--}_{Reco}	N^{+-}_{Reco}	N^{-+}_{Reco}
N^{++}_{Truth}	76.0	0	0	23.9	76.5	0	0	23.4
N^{--}_{Truth}	0	75.4	24.5	0	0	76.2	23.8	0
N^{+-}_{Truth}	0	24.5	75.5	0	0	23.0	76.9	0
N^{-+}_{Truth}	24.7	0	0	75.3	23.0	0	0	77.4

Table 34.: Purity of the KLFitter in $t\bar{t}$ events for same and different-top like events. Statistical error: ± 0.1, *muon*+jets channel. Results are expressed in percentage.

	Same Top				Different Top			
	N^{++}_{Reco}	N^{--}_{Reco}	N^{+-}_{Reco}	N^{-+}_{Reco}	N^{++}_{Reco}	N^{--}_{Reco}	N^{+-}_{Reco}	N^{-+}_{Reco}
N^{++}_{Truth}	77.3	0	0	22.6	77.4	0	0	22.6
N^{--}_{Truth}	0	77.6	22.3	0	0	77.7	22.3	0
N^{+-}_{Truth}	0	24.0	75.9	0	0	21.4	78.9	0
N^{-+}_{Truth}	23.9	0	0	76.1	21.4	0	0	78.5

Table 35.: Purity of the KLFitter in $t\bar{t}$ events for same and different-top like events. Statistical error: ± 0.1, *muon*+jets and *electron*+jets channels combined. Results are expressed in percentage.

An example of KLFitter likelihood output in the optimised configuration is shown in Figure 115. Figures 116 and 117 show the p_T distributions of the b-jets reconstructed by the KLFitter in the leptonic side of the $t\bar{t}$ decay or in the hadronic side of the $t\bar{t}$ decay, respectively.

A study of angular separation between hard and soft lepton is presented in the next Section in order to check an alternative method able to discriminate same- and different-top events and compare its purity to the KLFitter ones. Moreover, the possibility of improving the KLFitter purity exploiting the combination of the KLFitter decision and the angular information is investigated in the next Section.

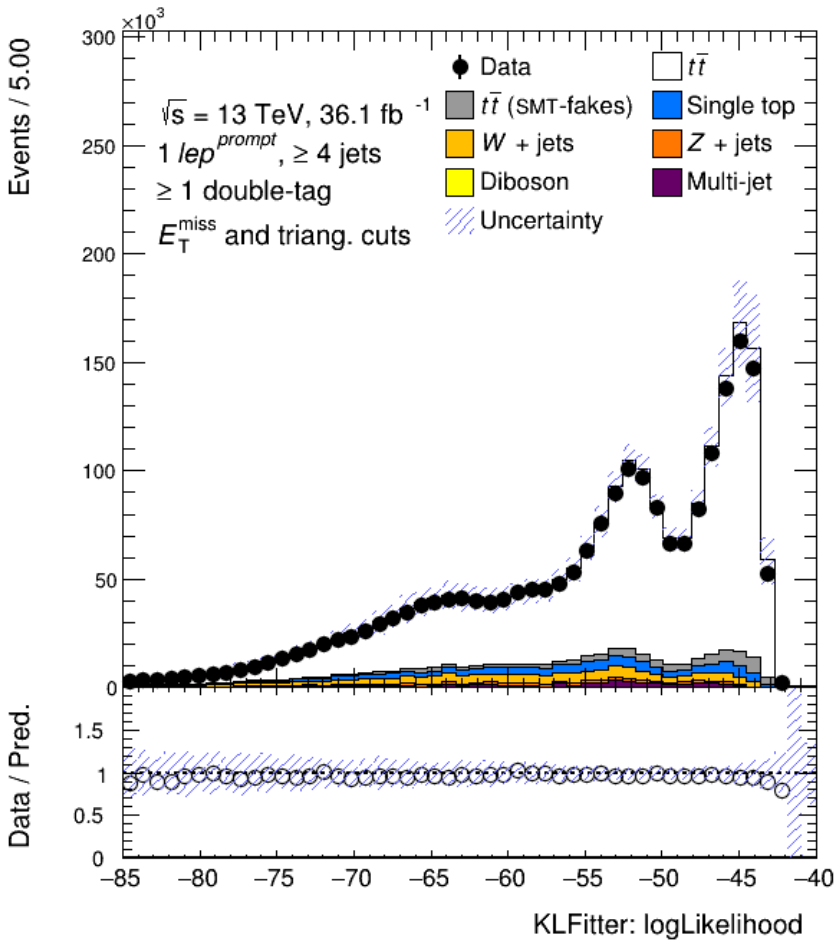

Figure 115.: KLFitter likelihood in the lepton+jets channel. Statistical and systematic uncertainties are quoted.

8.3 STUDY OF ANGULAR SEPARATION BETWEEN HARD AND SOFT LEPTON

To discriminate same and different top like events we investigated also a suitable cut on the angular separation between the hard lepton and the soft muon. Several studies were performed on the $\Delta R(\ell, \mu)$ variable, defined below.

$$\Delta R\,(\ell, \mu) = \sqrt{\Delta\eta^2_{(\ell\mu)} + \Delta\phi^2_{(\ell\mu)}} \tag{77}$$

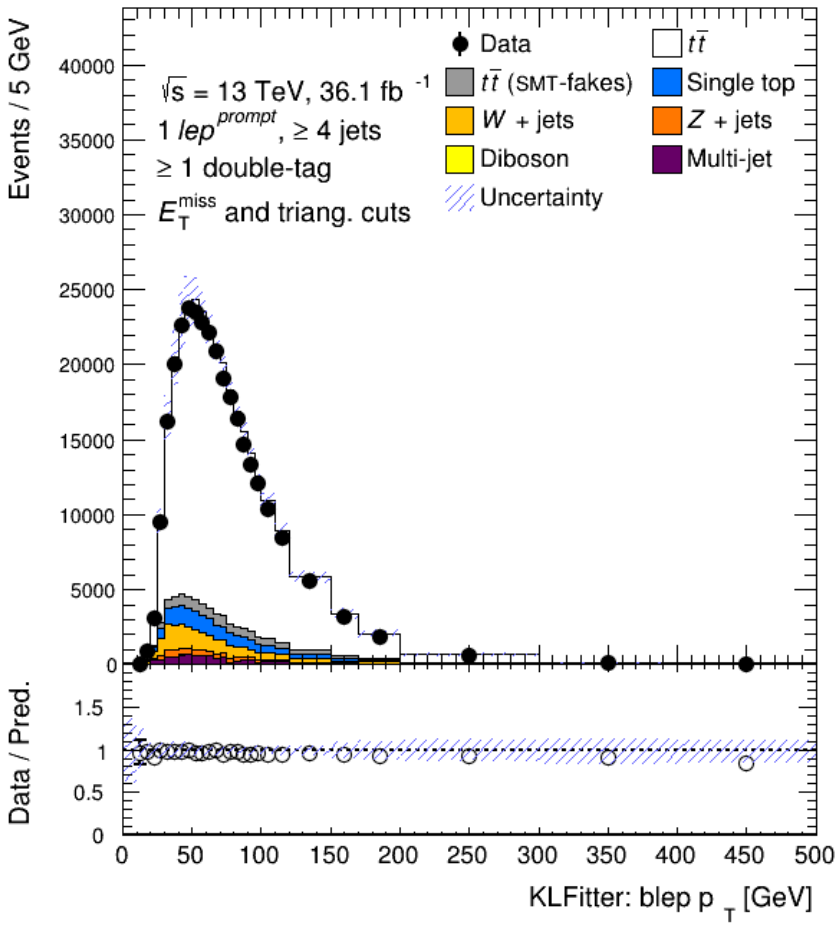

Figure 116.: p_T distribution of the b-jet reconstructed by the KLFitter in the leptonic side of the $t\bar{t}$ decay, in the lepton+jets channel. Statistical and systematic uncertainties are quoted.

Figure 118 shows the angular separation between the hard lepton from the W boson decay and the soft muon in $t\bar{t}$ events, classified as same top or different top events by the truth information. According to the shapes of the same and different top like distributions in Figure 118, a cut at $\Delta R(\ell, \mu) = 2.$ was tested: if the angular separation between the hard lepton and the soft muon is less than 2 the event is classified as same top, vice versa the event is classified as different top.

Table 36 shows the $\Delta R(\ell, \mu)$ method performance: the purity gets worst by a few % with respect to the KLF based selection and the angular separation between the hard lepton and the soft muon is not a suitable method to improve, by itself, the purity in distinguishing between same- and different-top like events.

Nevertheless, the $\Delta R(\ell, \mu)$ variable conveys useful information about the event topology so it could be beneficial to gather information from both the KLFitter

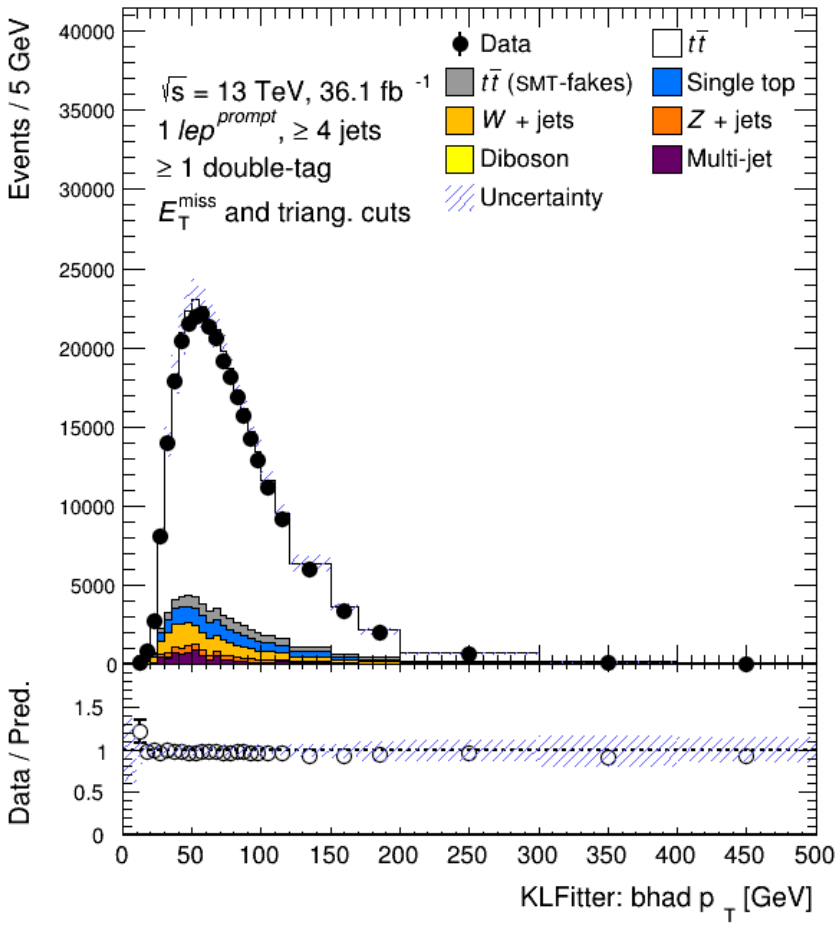

Figure 117.: p_T distribution of the b-jet reconstructed by the KLFitter in the hadronic side of the $t\bar{t}$ decay, in the lepton+jets channel. Statistical and systematic uncertainties are quoted.

Channel	Same Top	Different Top
Statistical	± 0.1	± 0.1
$lepton + jets$	72.4	70.2
$electron + jets$	72.4	71.0
$\mu + jets$	72.3	69.5

Table 36.: Purity of the $\Delta R(\ell, \mu)$ selection in the lepton, electron and muon channels using the b-tag double option. Results are expressed in percentage.

response and the $\Delta R(\ell, \mu)$ method.
The combination of the KLFitter and the angular information provides a sizeable increase in the purity performance. From the inspection of the $\Delta R(\ell, \mu)$ distribution

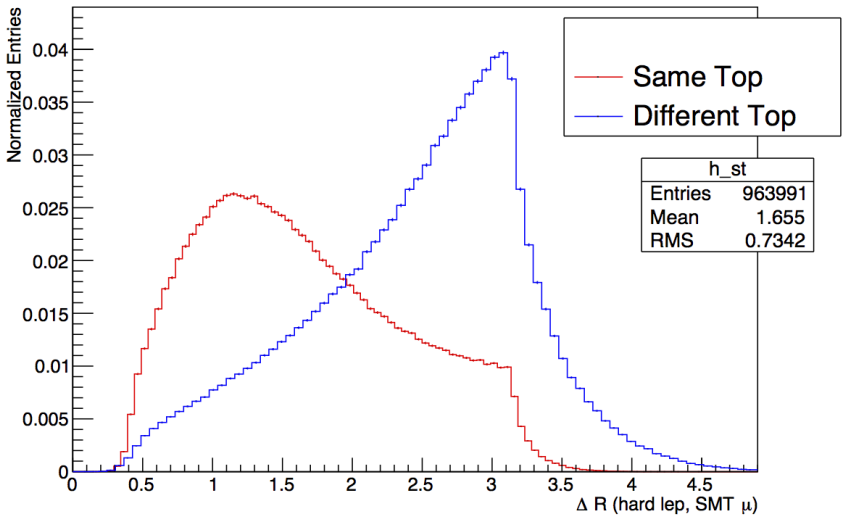

Figure 118.: Angular separation between the hard lepton and the soft muon in $t\bar{t}$ events, classified as same top (red) or different top (blue) events by the truth information.

in cases when the KLFitter classifies the events as same top (see Figure 119) or different top (see Figure 120), as a function of the truth information, it is possible to find a $\Delta R(\ell,\mu)_{\text{cut}}$ point that optimises the discrimination of same top and different top events.

The optimised configuration is obtained when applying a $\Delta R(\ell,\mu)$ cut on top of the KLF decision ($\Delta R(\ell,\mu)$&KLF):

- the event is classified as same top if the KLFitter says the event is same top and $\Delta R(\ell,\mu) < 1.7$
- the event is classified as different top if the KLFitter says the event is different top and $\Delta R(\ell,\mu) \in (2.5, 3.5)$
- other combinations are rejected because they do not lead to a sizeable improvement in the purity results

Table 37 highlights the sizeable purity improvement achieved by the KLFitter&$\Delta R(\ell,\mu)$ selection in discriminating same top from different top like events. The KLFitter&$\Delta R(\ell,\mu)$ selection guaranties a correct same-top/different-top decision in almost 90% of the cases. On the other hand, this tighter selection reduces the size of the sample leading to an increased statistical uncertainty on the measurement.

There is a clear difference in performance between SS and OS bins, which will discussed in the next Section. There is also a difference in performance between ST and DT type events, similar to that observed in [96] and it is not deemed to be an

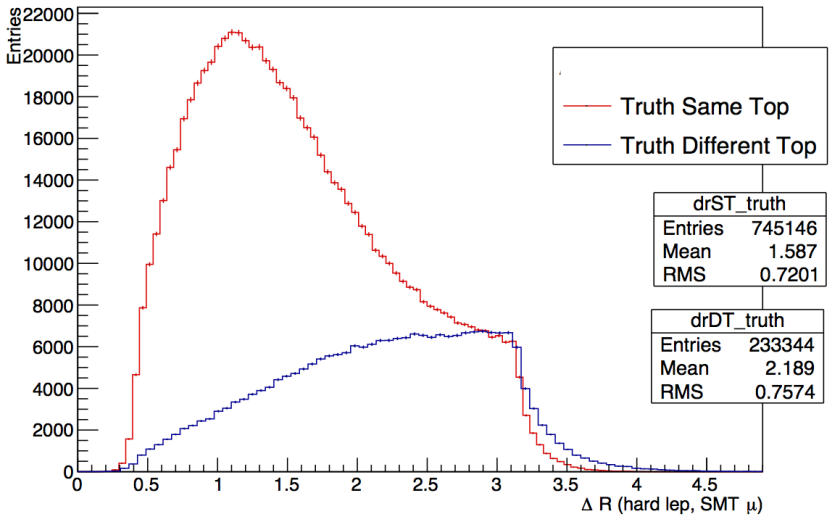

Figure 119.: Angular separation between the hard lepton and the soft muon in $t\bar{t}$ events, classified as same top (red) or different top (blue) events by the truth information, in cases when the KLFitter classifies the event as same top.

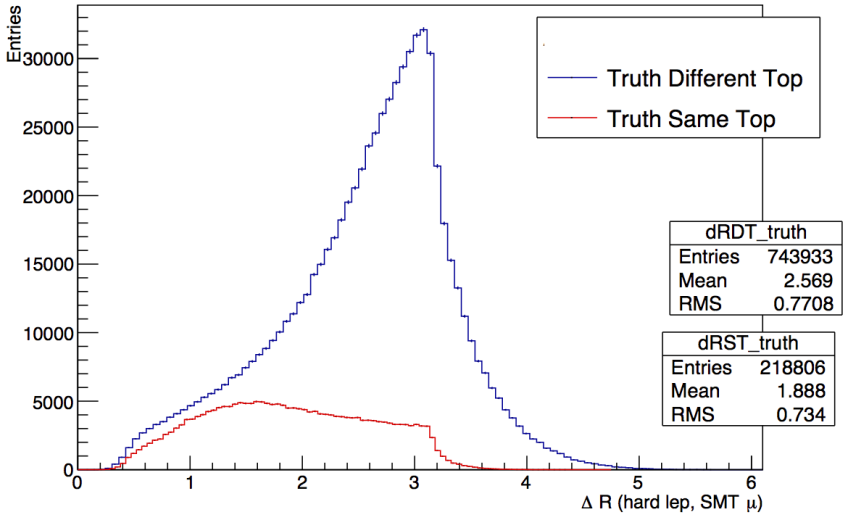

Figure 120.: Angular separation between the hard lepton and the soft muon in $t\bar{t}$ events, classified as same top (red) or different top (blue) events by the truth information, in cases when the KLFitter classifies the event as different top.

issue.

This behaviour could be related to the neutrinos alignment in the event (there is one neutrino coming from the leptonic W decay and one associated with the soft

	KLF&$\Delta R(\ell,\mu)$				KLF			
	N^{++}_{Reco}	N^{--}_{Reco}	N^{+-}_{Reco}	N^{-+}_{Reco}	N^{++}_{Reco}	N^{--}_{Reco}	N^{+-}_{Reco}	N^{-+}_{Reco}
N^{++}_{Truth}	88.1	0	0	11.8	77.2	0	0	22.8
N^{--}_{Truth}	0	88.1	11.8	0	0	77.6	22.3	0
N^{+-}_{Truth}	0	12.2	87.8	0	0	23.7	76.3	0
N^{-+}_{Truth}	12.4	0	0	87.5	23.8	0	0	76.2

Table 37.: Purity of the KLF&$\Delta R(\ell,\mu)$ selection in the lepton+jets channel using the b-tag double option. Same top and different top channels are combined. Statistical error: ± 0.1

muon). Considering the event topology, the missing momentum from the semi-leptonic decay (the neutrino associated with the soft muon) will tend to be more aligned with the MET in the ST events and less aligned with the MET in the DT events. The measurement of the MET angular information will be worse in DT events, as the difference in angle is greater. The $x - y$ MET components provided to the fitter will vary by a larger degree from the truth in the DT case than the ST case, leading to a worse reconstruction.

8.4 APPLICATION OF KLFITTER DECISION

It is important to investigate the event composition, in terms of signal and backgrounds, and check if any mistake in the KLFitter classification implies an asymmetry in the measurement. The Montecarlo (MC) provides the information required to track the full history of every soft muon contained in the truth record for each event. Each soft muon can be either a signal soft muon or a background soft muon. Signal soft muons belong to the decay chains:

1. $t \to \ell\nu b \to \ell\mu X$ ($t\bar{t}$ eq. 1 in the legend of Figures 121, 122, 123, and 124)
2. $t \to \ell\nu\,(b \to c) \to \ell\mu X$ ($t\bar{t}$ eq. 2 in the legend of Figures 121, 122, 123, and 124)
3. $t \to \ell\nu\,(b \to \tau) \to \ell\mu X$ ($t\bar{t}$ eq. 3 in the legend of Figures 121, 122, 123, and 124)
4. $t \to \ell\nu\,(b \to c \to \tau) \to \ell\mu X$ ($t\bar{t}$ eq. 4 in the legend of Figures 121, 122, 123, and 124)

where, in case of $\bar{t}$, one has to consider the charge conjugate of the particles listed above. The KLFitter performances for signal events are shown in Tables 33, 34 and 35.
As shown in Figures 121, 122 for the electron channel and 123, 124 for the muon channel, the signal $t\bar{t}$ process is dominated by direct $b \to \mu$ decays which will

populate the opposite-sign (OS) bins in same top events and the same-sign (SS) bins in different top events.

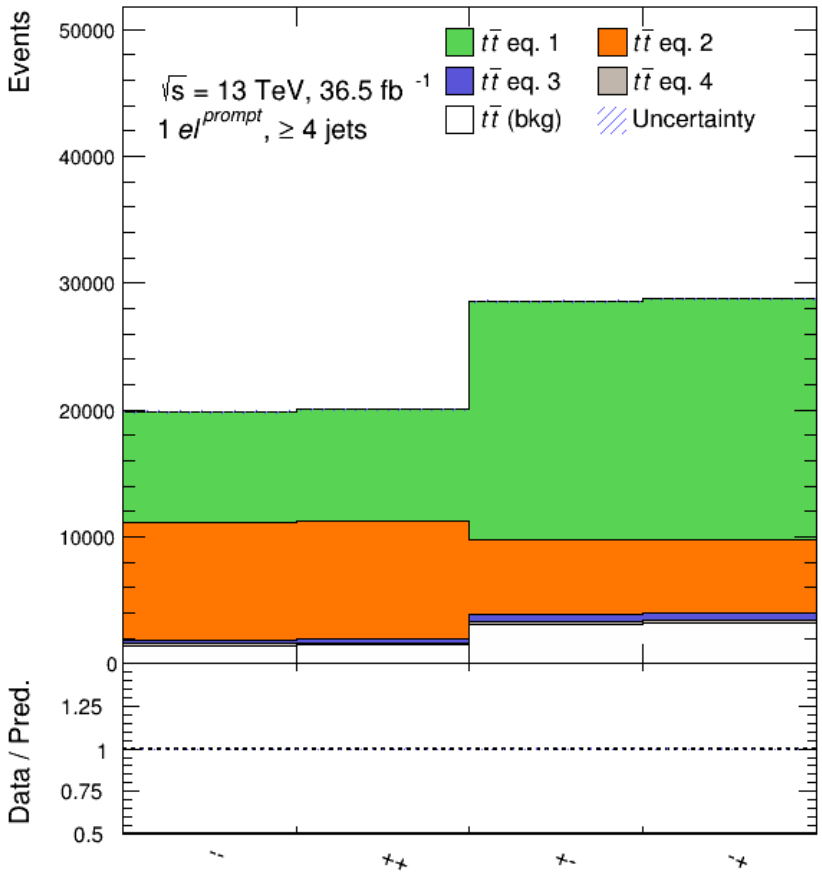

Figure 121.: Same top like events in the e+jets channel. The $--$, $++$, $+-$ and $-+$ labels on the x-axis refer to the number of events where the charges of the hard lepton and soft muon are $--$, $++$, $+-$ and $-+$, respectively.

On the other hand, background soft muons originate from dilepton events, b quarks not coming from top quarks (such as pileup events ($g \to b\bar{b} \to \mu X$)) or additional radiation events ($g(q) \to b\bar{b} \to \mu X$), $c \to \mu$ events or $t\bar{t}$ events where the hadronic decaying W boson goes to a c quark ($t \to Wb \to csb \to b\mu X$). Moreover there are soft muons which have a τ or light flavour origin, such as $\pi^{\pm} \to \mu^{\pm}\nu$ or $K^{\pm} \to \mu^{\pm}\nu$.
Tables 38 and 39 show the yields of the background composition for the nominal $t\bar{t}$ MC, split in same top (ST) and different top (DT) like events according to the KLFitter classification, in the *muon*+jets channel. Tables 40 and 41 are the corresponding yields in the electron+jets channel. For these tables the KLFitter decision

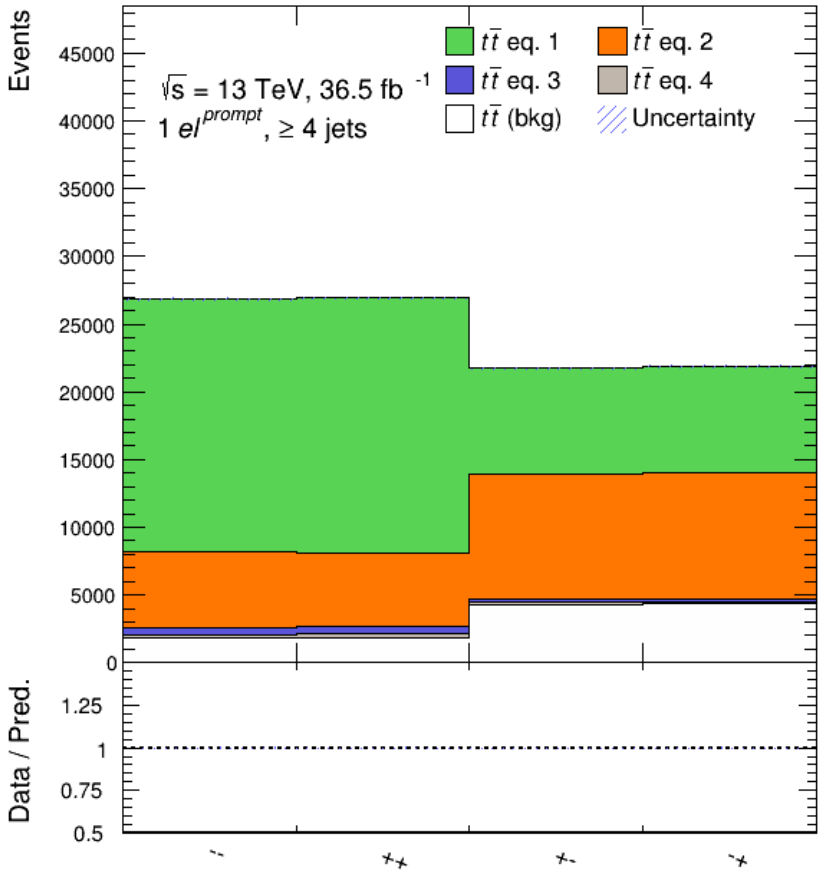

Figure 122.: Different top like in the e+jets channel. The $--$, $++$, $+-$ and $-+$ labels on the x-axis refer to the number of events where the charges of the hard lepton and soft muon are $--$, $++$, $+-$ and $-+$, respectively.

has been made using the optimised configuration as described in Section 8.2.5 and the yields are separated by reconstructed charge-pair bin.

The background distribution is symmetric in its pileup and additional radiation components ($b \to \mu$, $b \to c \to \mu$) between same sign and opposite sign and also between ST and DT, within the errors.

For the light flavour background distribution, it is observed to be slightly asymmetric between same sign and opposite sign in both muon and electron+jets channels. However the largest bin deviation is of the order of 10^{-3} of the total $t\bar{t}$ events and it is considered to have a negligible effect on charge and CP asymmetries.

The $c \to \mu$ background is asymmetric, in favour of opposite sign events, in all channels. If the soft muon originates from a W-boson hadronic decay, it will be on the other side of the $t\bar{t}$ decay with respect to the leptonically decaying W. In this

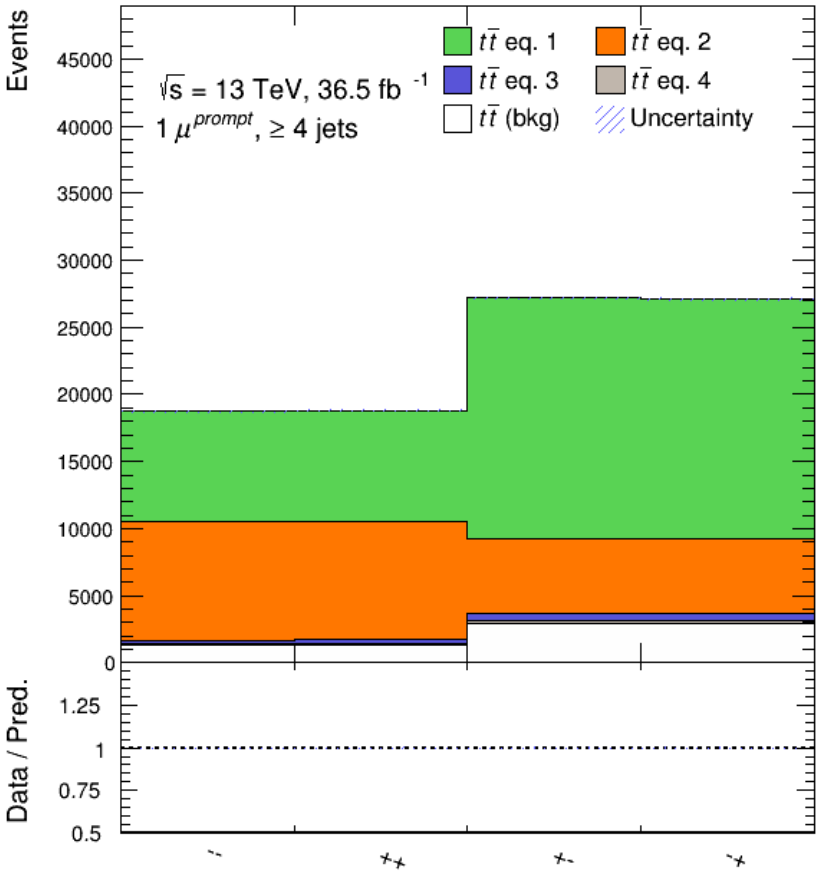

Figure 123.: Same top like in the *muon*+jets channel. The $--$, $++$, $+-$ and $-+$ labels on the x-axis refer to the number of events where the charges of the hard lepton and soft muon are $--$, $++$, $+-$ and $-+$, respectively.

case, the charge pairing between the hard lepton and the soft muon is expected to be of opposite sign (OS). If the KLFitter correctly identifies this type of event as DT, it will populate the opposite sign bins. If the KLFitter mistakenly classifies the event as ST, it will populate the ST OS bins, as shown in Table 38 and 40. The dilepton background is completely asymmetric because the tagged muon is not a real SMT muon but is the second charged hard lepton from a W-boson in the event. By definition these two leptons have opposite charges and should be reconstructed as a DT-type event. When the KLFitter mistakenly classifies this type of event as ST, then it will enter the ST OS bins.
These effects are important to be taken into account when evaluating charge asymmetries because these KLF mistakes can spoil the measurement.

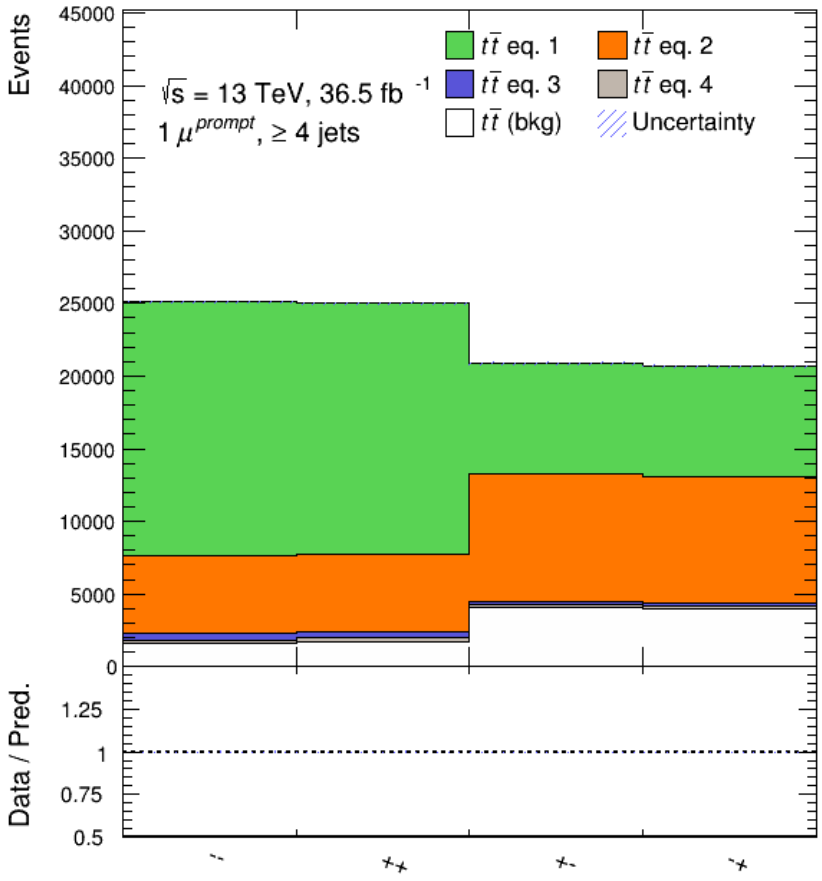

Figure 124.: Different top like events in the *muon*+jets channel. The $--$, $++$, $+-$ and $-+$ labels on the x-axis refer to the number of events where the charges of the hard lepton and soft muon are $--$, $++$, $+-$ and $-+$, respectively.

8.5 CONCLUSIONS ON KLFITTER STUDIES

The KLFitter configuration has been customised to meet the purity requirements necessary for the charge asymmetry analysis. The optimal KLFitter configuration (*i.e.* the configuration which provides the highest purity) has been described in Section 8.2.5. Other alternative methods have been evaluated to discriminate same- or different-top events. These methods are based on the angular matching between the soft muon and the hard lepton by itself or in conjunction with the KLFitter algorithm. The first scenario does not guarantee the same purity as the KLFitter method, while the $\Delta R(\ell, \mu)$ applied on top of the KLF decision increases the statistical error. For these reasons the KLFitter configuration described in Section 8.2.5 is

muon+jets Same Top				
	N_{Reco}^{++}	N_{Reco}^{--}	N_{Reco}^{+-}	N_{Reco}^{-+}
Total $t\bar{t}$	18840 ± 82	18969 ± 83	27408 ± 102	27260 ± 101
Total $t\bar{t}$ backgrounds	1422 ± 24	1458 ± 24	3126 ± 36	3102 ± 35
$b \to \mu$	222 ± 9	228 ± 9	229 ± 9	224 ± 9
$c \to \mu$	196 ± 9	186 ± 9	1199 ± 24	1165 ± 23
$b \to c \to \mu$	109 ± 6	111 ± 6	113 ± 6	115 ± 6
$\tau \to \mu$	9 ± 1	10 ± 2	92 ± 6	107 ± 6
Dilepton	0 ± 0	0 ± 0	480 ± 14	453 ± 12
Light $\to \mu$	886 ± 19	923 ± 20	1005 ± 20	1038 ± 20

Table 38.: Breakdown of $t\bar{t}$ background composition of *muon*+jets same-top like events, rounded to the nearest integer. The MC statistical uncertainty is quoted.

muon+jets Different Top				
	N_{Reco}^{++}	N_{Reco}^{--}	N_{Reco}^{+-}	N_{Reco}^{-+}
Total $t\bar{t}$	25155 ± 96	25118 ± 96	20825 ± 86	20747 ± 87
Total $t\bar{t}$ backgrounds	1670 ± 25	1805 ± 27	4062 ± 41	4063 ± 42
$b \to \mu$	240 ± 9	259 ± 10	253 ± 10	253 ± 10
$c \to \mu$	236 ± 10	248 ± 10	1970 ± 30	1948 ± 30
$b \to c \to \mu$	129 ± 6	131 ± 6	132 ± 6	125 ± 6
$\tau \to \mu$	13 ± 1	12 ± 2	87 ± 6	110 ± 6
Dilepton	0 ± 0	0 ± 0	612 ± 15	598 ± 15
Light $\to \mu$	1049 ± 19	1154 ± 21	991 ± 20	1028 ± 22

Table 39.: Breakdown of $t\bar{t}$ background composition of *muon*+jets different-top like events, rounded to the nearest integer. The MC statistical uncertainty is quoted.

used to produce a response matrix required for the unfolding of the measurement and described in detail in Chapter 10.

e+jets Same Top				
	N^{++}_{Reco}	N^{--}_{Reco}	N^{+-}_{Reco}	N^{-+}_{Reco}
Total $t\bar{t}$	19970 ± 85	20108 ± 86	28698 ± 105	28775 ± 105
Total $t\bar{t}$ backgrounds	1558 ± 25	1622 ± 26	3286 ± 37	3365 ± 38
$b \to \mu$	263 ± 10	271 ± 10	246 ± 10	253 ± 10
$c \to \mu$	213 ± 9	221 ± 10	1215 ± 23	1223 ± 24
$b \to c \to \mu$	114 ± 6	123 ± 6	119 ± 6	126 ± 6
$\tau \to \mu$	10 ± 1	17 ± 2	101 ± 6	109 ± 6
Dilepton	2 ± 1	3 ± 1	521 ± 14	492 ± 14
Light $\to \mu$	1173 ± 22	1236 ± 20	1066 ± 21	1155 ± 22

Table 40.: Breakdown of $t\bar{t}$ background composition of e+jets same-top like events, rounded to the nearest integer. The MC statistical uncertainty is quoted.

e+jets Different Top				
	N^{++}_{Reco}	N^{--}_{Reco}	N^{+-}_{Reco}	N^{-+}_{Reco}
Total $t\bar{t}$	26976 ± 101	27057 ± 101	21827 ± 89	22070 ± 89
Total $t\bar{t}$ backgrounds	1670 ± 25	1805 ± 27	4062 ± 41	4063 ± 42
$b \to \mu$	272 ± 9	281 ± 10	269 ± 10	270 ± 10
$c \to \mu$	271 ± 10	296 ± 10	2070 ± 31	2049 ± 30
$b \to c \to \mu$	134 ± 6	136 ± 6	139 ± 6	140 ± 6
$\tau \to \mu$	13 ± 1	16 ± 2	115 ± 7	125 ± 7
Dilepton	7 ± 2	3 ± 1	657 ± 15	674 ± 16
Light $\to \mu$	1174 ± 23	1235 ± 22	1065 ± 21	1154 ± 22

Table 41.: Breakdown of $t\bar{t}$ background composition of e+jets different-top like events, rounded to the nearest integer. The MC statistical uncertainty is quoted.

9 SYSTEMATIC UNCERTAINTIES

Several sources of systematic uncertainties are included in the analysis. Systematic uncertainties are categorised in experimental and modelling uncertainties.
The impact of each systematic uncertainty on the final measurement is summarised in Chapter 10 for the method used to measure the charge asymmetries (labelled as CA in the following).

9.1 EXPERIMENTAL UNCERTAINTIES

Experimental systematic uncertainties affect the measurement of the properties of physics objects, like leptons, jets and missing transverse energy, used in the analysis described in this thesis.
All the reconstructed objects, such as the hard lepton, the four jets and the SMT muon as well as the b-tagging procedure are considered in the systematic uncertainties evaluation.
One of the advantages of the CA formulation outlined in Chapter 2 is related to the systematic uncertainties evaluation: many systematic uncertainties are mitigated due to the ratios of events cancelling out these effects to the first order. Since in pp collisions W^+ and W^- are produced asymmetrically, this ratio formulation is also crucial to remove the dependency of the analysis on the different number of reconstructed prompt leptons from W-bosons.

9.1.1 *Luminosity*

The uncertainty on the combined $2015 + 2016$ integrated luminosity is 2.1%. It is derived, following a methodology similar to that detailed in Ref. [123], from a preliminary calibration of the luminosity scale using x-y beam-separation scans performed in August 2015 and May 2016 (Van Der Meer scans). The uncertainties for the 2015 and 2016 data sets are partially correlated and are considered as fully correlated between the 2015 and the 2016 data-sets in this analysis.
The uncertainty on the luminosity affects the measurement of the $t\bar{t}$ cross-section $\sigma_{t\bar{t}}$, because luminosity and cross sections are related through formula 78, where

N_{Data} is the number of data events, N_{Bkg} is the number of background events, and $\epsilon_{\text{selection}}$ is the efficiency of the event selection.

$$\sigma_{t\bar{t}} = \frac{N_{\text{Data}} - N_{\text{Bkg}}}{\int \mathcal{L}dt \times \epsilon_{\text{selection}} \times BR} \tag{78}$$

However the up and down luminosity variations lead to an overall shift of the event yields and it is negligible when measuring CA, as they are expressed as ratios (see Chapter 2).

9.1.2 *Beam Energy*

The top pair production cross section is also affected by the uncertainty on the LHC beam energy . The uncertainty on the measurement of the beam energy at the LHC for the 13 TeV data set is 1.5% [124]. However, a shift in the overall event yield does not affect the measured CA.

9.1.3 *Pileup and JVT*

Pileup levels in MC simulations are re-weighted to match the conditions in data, and a corresponding uncertainty is considered [125] using pileup up and down variations. The same principle applies also to the JVT uncertainty: up and down variations are considered to evaluate the JVT related uncertainty [126].

9.1.4 *Reconstructed objects*

Leptons

Uncertainties associated with leptons arise from the trigger, reconstruction, identification, and isolation, as well as the lepton momentum scale and resolution. The reconstruction, identification and isolation efficiencies of electrons and muons, as well as the efficiency of the trigger used to record the events, differ slightly between data and simulation, which is compensated for by dedicated scale factor (SFs), according to the charge of the lepton. Details about electron and muon reconstruction and identification efficiency in ATLAS are given in Chapter 5.

Efficiency SFs are derived using $Z \to \ell^+\ell^-$ ($\ell = e, \mu$) data and simulated samples, and are applied to the simulation to correct for differences. The effect of these uncertainties is propagated as corrections to the event weight. All the leptons SFs are binned in p_T and η ranges. For the high-p_T leptons the total uncertainty on efficiency SFs is estimated to be less than 0.5% for muons across the entire p_T spec-

trum and for electrons with $p_T > 30\,\text{GeV}$, while it exceeds 1% for low p_T electrons [81] [127].

Additional sources of uncertainty originate from the corrections applied to adjust the lepton momentum scale and resolution in the simulation to match those in data. These are measured using reconstructed distributions of the $Z \to \ell^+\ell^-$ and $J/\psi \to \ell^+\ell^-$ masses, as well as the measured E/p in $W \to e\nu$ events, where E and p are the electron energy and momentum, as measured by the calorimeter and the tracker respectively [128]. To evaluate the effect of momentum scale uncertainties, the event selection is re-done with the lepton momentum varied by $\pm 1\sigma$. Concerning the momentum resolution uncertainties, the event selection is re-done with the lepton momentum smeared.
The soft muon specific uncertainties are measured with dedicated techniques. The official reconstruction SFs for muons with Tight WP, provided by the ATLAS Muon Combined Performance (MCP) group, is found to be valid also for muons inside jets, produced by a heavy-flavour hadron decay. Several studies have been performed together with the MCP ATLAS group to verify that the official reconstruction SFs for Tight muons inside jets are the same as the ones for isolated muons.

The reconstruction SF is derived from a data/MC simulations comparison in two distinct energy regimes: for $J/\psi \to \mu^+\mu^-$ events with $p_T < 15\,\text{GeV}$, and from $Z \to \mu^+\mu^-$ events with $p_T > 15\,\text{GeV}$. The uncertainties on the SFs used on soft muon reconstruction for $p_T > 15\,\text{GeV}$ are taken as fully correlated with those of the high-p_T muons used in the W-lepton selection, since they are consistently measured on $Z \to \mu^+\mu^-$ events (the only difference being the quality working point, which is Medium for the W-muons and Tight for the soft muons). In the $p_T < 15\,\text{GeV}$ region, the uncertainty on the SFs for soft muon reconstruction ranges from the 2.5% level for very low p_T ($4 - 5\,\text{GeV}$) to about 1%, and is taken as fully uncorrelated with that in the $p_T > 15\,\text{GeV}$ region.

As the backgrounds to $Z \to \ell^+\ell^-$ and $J/\psi \to \ell^+\ell^-$ (such as $W \to \mu\nu$ events) are not charge-symmetric, this leads to small differences between positively and negatively charged lepton scale factors, especially in the electron case. These differences are small but still relevant for a precision measurement, such as the one presented in this thesis, which aims at a sensitivity of the order of 10^{-4}.

Lepton Charge Misidentification

Charge misidentification occurs if an isolated prompt lepton is reconstructed with a wrong charge assignment.
Since the muon mass is about 200 times bigger than the electron mass, muons undergo a low bremsstrahlung probability and hence their charge misidentification probability is considered negligible in ATLAS.

On the other hand, electrons are more likely to release energy through bremsstrahlung and the emitted photon can subsequently convert into electron-positron pairs; together with the mis-association of one of the conversion tracks with the cluster of the original electron, this might lead to the electron charge misidentification.
Moreover, high E_{T} electrons have increasingly straight tracks in the detector and the charge misidentification can be caused by a failure to correctly determine the curvature of the track associated to the electron, using the rigidity equation in the Inner Detector. Since muons positive/negative curvature, and hence their charge, is measured independently by two sub-detectors in ATLAS (the Inner Detector and the Muon Spectrometer) the probability of charge misidentification for muons is negligible.
The charge misidentification is estimated both in data and simulation using $Z \rightarrow e^{+}e^{-}$ tag-and-probe methods (see reference [129]). The charge misidentification probability is directly proportional to the amount of traversed material, meaning that the misidentification probabilities are quite low in the detector central region but increases up to almost 3% for very high values of pseudorapidity.
Figures 125 and 126 show the electron charge misidentification probability as a function of E_{T} and $|\eta|$, alongside with their SFs. The uncertainty associated with the charge misidentification is evaluated varying up and down the number of positively (negatively) misidentified electrons in the signal region.

Jets Energy Scale

Uncertainties associated with jets arise from many sources, among them the most relevant for this analysis are the jet energy scale (JES) and resolution (JER).
There are a number of effects that can spoil the accuracy of the jet energy measurement, for example the pile-up modelling, additional radiation and detector response. Other sources of JES uncertainty depend on the jet clustering of the anti-k_T algorithm, the jet flavour composition (the quarks and gluons composition of the jet), the gluon in jets energy scale (referred to as jet flavour response uncertainty). Moreover, η-calibration and mis-modelling due to the *punch-through* of high-p_{T} single hadrons have to be taken into account. All these mis-modelling effects lead to differences between MC simulations and data. Simulations are corrected using SFs for each source of JES systematic uncertainty. The JES systematic contribution to this analysis is evaluated by repeating the CA measurement varying the SFs up and down by their uncertainties.

A mis-modelling in the jet energy could affect the fiducial volume where the CA is measured.

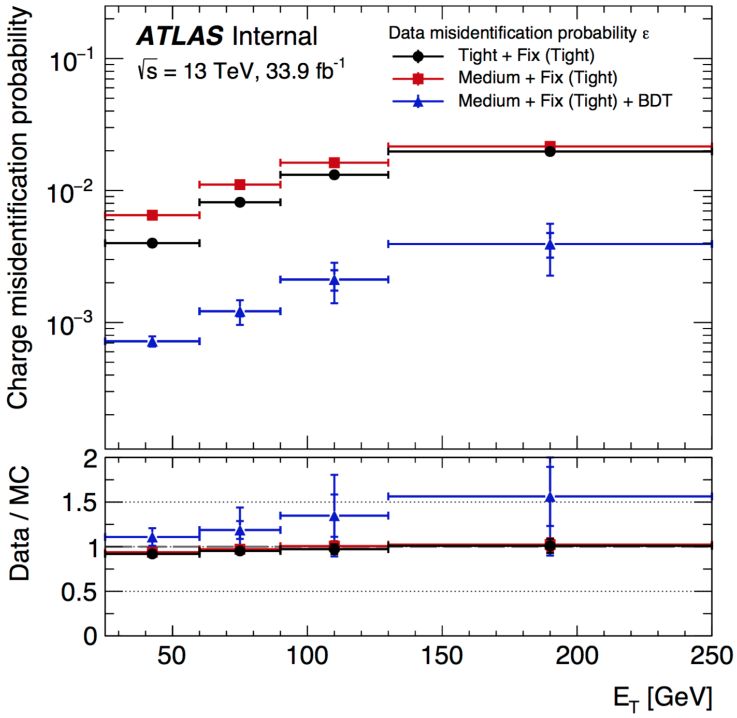

Figure 125.: Charge-misidentification rates in 2016 data and simulated $Z \to e^+e^-$ events as a function of E_{T} ([129]). This plot shows the impact of applying the BDT requirement to suppress charge misidentification (red squares vs. blue triangles). Medium identification with BDT vs. Tight identification without BDT is also explored (black circles vs. blue triangles). The Fix (Tight) isolation requirement is applied in all cases.

The JES and its uncertainty were derived by combining information from test-beam data, LHC collision data and simulation [130]. Figure 127 shows that the JES uncertainty is about 5.5% for jets with $p_T = 25\,\mathrm{GeV}$ and quickly decreasing with increasing jet p_T. It represents one of the leading sources of uncertainty associated with reconstructed objects, affecting the relative normalisations of signal and the $t\bar{t}$ backgrounds in the different bins of number of jets.
Figure 128 shows the JES uncertainty as a function of η for jet of $p_T = 60\,\mathrm{GeV}$: this uncertainty ranges from 3% to 4%.

Jets Energy Resolution

The jet energy resolution (JER) uncertainty was measured in Run-1 data and simulation as a function of jet p_T and rapidity using di-jet events. Data and MC

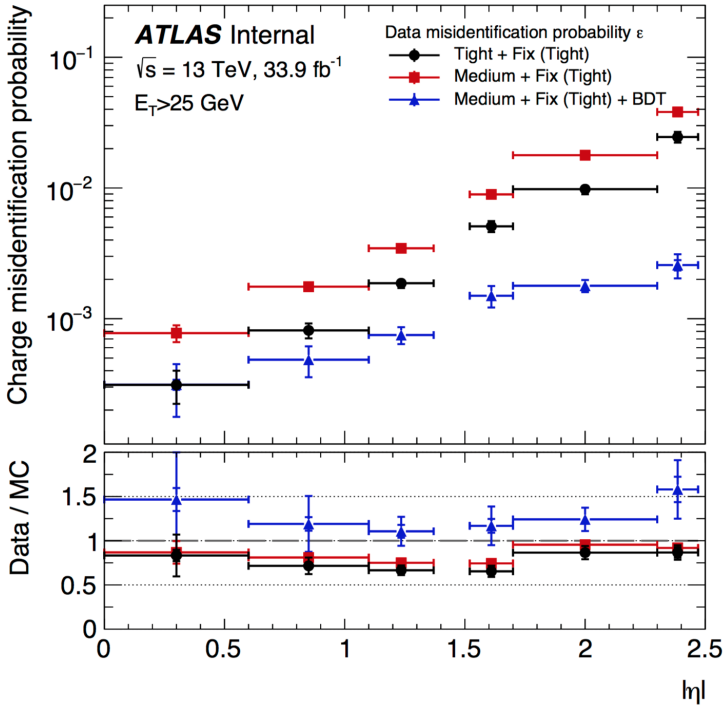

Figure 126.: Charge-misidentification rates in 2016 data and simulated $Z \to e^+e^-$ events as a function of $|\eta|$ ([129]). This plot shows the impact of applying the BDT requirement to suppress charge misidentification (red squares vs. blue triangles). Medium identification with BDT vs. Tight identification without BDT is also explored (black circles vs. blue triangles). The Fix (Tight) isolation requirement is applied in all cases.

were found to agree within 10% [131]. Additional uncertainties have been assessed in the extrapolation from Run-1 to Run-2 conditions [130]. The combined (Run-1 and Run-2) uncertainty is propagated by smearing the jet p_T in the simulation [132].

Missing Transverse Energy

The E_T^{miss} reconstruction is affected by uncertainties associated with leptons and jet energy scales and resolutions, which are propagated to E_T^{miss} and thus are included under the corresponding per-object uncertainty category.

Additional small uncertainties associated with the modelling of the underlying event, in particular its impact on the p_T scale and resolution of unclustered energy, are taken into account [133].

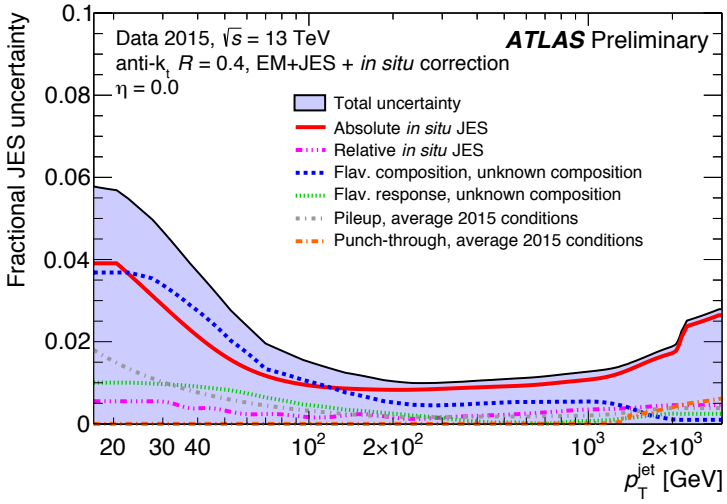

Figure 127.: JES uncertainties, estimated for the 2015 data taking period as a function of jet p_T for jets of $\eta = 0$. ([130]).

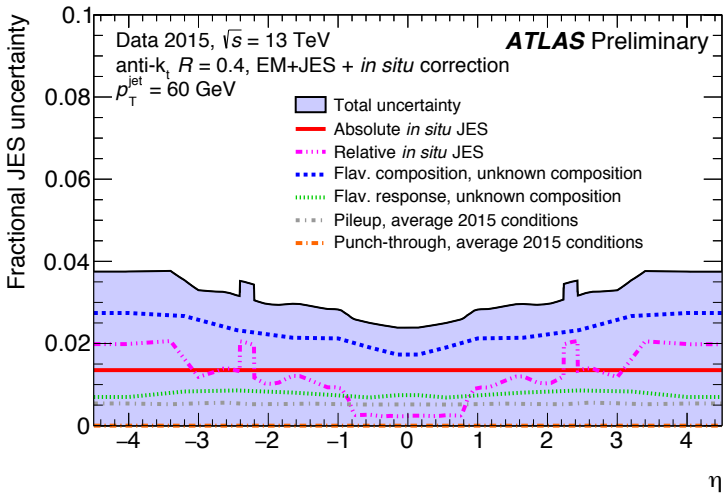

Figure 128.: JES uncertainties, estimated for the 2015 data taking period as a function of jet η for jets of $p_T = 60\,\text{GeV}$. ([130]).

Flavour tagging

Displaced Vertex Based Techniques

B-tagging efficiencies in simulated samples are corrected to match efficiencies in data. Correction scale factors (SFs) are derived for jets originating from b, c and light quarks separately in dedicated calibration analyses. For jets originating from b- and c-quarks SFs are derived as a function of p_T whereas the light-jet efficiency is scaled by p_T- and η-dependent factors. Tagging efficiencies exhibit a dependence

on the hadron p_T over jet p_T ratio as well as the minimal space angle between the jet in question and the neighbouring jets. These dependencies are determined by the parton shower and hadronisation model used in the simulation. To account for these effects, MC-to-MC correction factors are introduced, that correct the data-to-MC SFs for the difference in the tagging efficiency of the parton shower and hadronisation model used in the calibration analysis to that of the sample in question. Calibration SFs are provided for fixed (cumulative) WPs, i.e. efficiencies above and below a given WP are calibrated.

Uncertainties on the data-to-MC SFs are estimated by varying each source of uncertainty up and down by one standard deviation. These uncertainties are fed into an eigen-variation (EV) model with a reduction scheme such that only substantial EVs are treated separately while all small variations are combined into a single variation. For cumulative working points, a total of 6, 3 and 16 independent EVs are considered for b-, c- and light-jets respectively. These systematic uncertainties are taken as uncorrelated between b-jets, c-jets, and light-jets. Furthermore, the efficiency of tagging the hadronic decays of τ-leptons in simulations is treated in the same way as the efficiency of tagging c-jets, with an additional uncertainty accounting for the fact that the correction factors derived for c-jets are also used for hadronic decays of τ-leptons [89].

SMT technique

The Tight-based SMT algorithm adopted in the Run-2 CAs measurement requires a Tight muon inside a jet, with an angular matching $\Delta R(\mu, \text{jet}) < 0.5$. The efficiency of this SMT algorithm in tagging heavy flavour originating jets is shown in Section 7.2.3.
The soft muon component relative to the light hadron decays and to detector background needs a specific SF. Chapter 6 outlines part of these SFs dedicated studies in the Run-1 measurement. An analogous procedure was performed also for the Run-2 analysis, using the W+jets data-driven technique outlined in Section 7.9. The systematic uncertainty on CAs is derived varying these SFs up and down and calculating the CAs in the two cases.

Background

The data-driven multijet background is affected by statistical uncertainties and additional uncertainties, deriving from the techniques used in its estimation. Uncertainties on the CA measurement are obtained by varying up and down each background cross section by its total uncertainty.
Shape uncertainties are not considered because they do not affect the CA measurement since they are based on simple event counting.

9.2 SIGNAL MODELING

The event selection described in Section 7 leaves the selected sample dominated by $t\bar{t}$ events. Uncertainties affecting $t\bar{t}$, and in particular the ones which modify the kinematics of the lepton from the W-boson decay and the kinematics of the B-hadron giving rise to the soft muon, but also the fraction of events from different soft-muon flavour component (from B-hadrons, C-hadrons, light jets and W-boson), are labelled as signal modelling uncertainties. The $t\bar{t}$ inclusive cross-section uncertainty does not affect the measurement at all, since CAs are measured using a ratio formula 2 .

9.2.1 *B-hadron and C-hadron production fractions*

The B-hadron production fractions in simulation differ from the world average measurements. Dedicated SFs are derived and systematic uncertainties are evaluated to account for this effect, which is crucial to the measurement. B hadron production fractions and $b \to \mu$ branching ratios are re-weighted to the PDG values and an associated systematic uncertainty is introduced.
The production fractions for weakly decaying B-hadrons are documented in the PDG [1], and shown in Table 42. This table was produced by the Heavy Flavor Averaging Group (HFAG) [134] using data obtained from the DELPHI [135], CDF [136, 137, 138, 139] and LHCb [24, 140, 141] experiments. The PDG additionally provides the correlations between the different B-hadrons, which are given by Equations 79, 80 and 81.

$$cor(B_s^0, b-baryon) = -0.254 \tag{79}$$

$$cor(B_s^0, B^{\pm} = B^0) = -0.143 \tag{80}$$

$$cor(b-baryon, B^{\pm} = B^0) = -0.921 \tag{81}$$

Taking into account these correlations, the maximal variations are shown in Table 43.

The production fractions, and scale factors, for weakly decaying B-hadrons observed in Powheg+Pythia8 MC are shown in Table 44, and for Powheg+Herwig7 in Table 45. Scale factors will be applied to each b-hadron present in a MC event, with the overall event weight given by the product of all b-hadrons in the event. The

Hadron	PDG ID	Production fraction
B^0	511	0.404 ± 0.006
B^+	521	0.404 ± 0.006
B_s^0	531	0.103 ± 0.005
b-baryon		0.088 ± 0.001

Table 42.: The production fractions for weakly decaying b-hadrons at high energy.

uncertainties come entirely from the PDG values and are propagated throughout the analysis.

Hadron	PDG	$B^{\pm,0}$ up	$B^{\pm,0}$ down	B_s^0 up	B_s^0 down	b-baryon up	b-baryon down
B^0	0.404±0.006	0.410	0.398	0.403	0.405	0.398	0.410
B^+	0.404±0.006	0.410	0.398	0.403	0.405	0.398	0.410
B_s^0	0.103±0.005	0.102	0.108	0.108	0.098	0.102	0.104
b-baryon	0.088±0.012	0.077	0.099	0.085	0.091	0.100	0.076

Table 43.: The production fractions for b-hadrons at high energy shown with systematic variations that are determined by the correlations

A re-weight of the c-hadron production fractions has been applied as well, given that the contribution of soft-muons coming from c-hadrons that do not come from B-hadrons decays is not negligible in the final selection. Similarly to what is done for B-hadrons, PDG values are used to constrain c-hadron production fractions. In Table 46 the average of the c-hadron production fractions measurements is reported [1]. Table 47 and Table 48 show the SF to be applied to the $t\bar{t}$ samples hadronised with Pythia8 and Herwig7 respectively.

Hadron	PDG	MC	Nominal SF
B^0	0.404±0.006	0.429	0.932
B^+	0.404±0.006	0.429	0.932
B_s^0	0.103±0.005	0.095	1.084
b-baryon	0.088±0.012	0.047	1.872

Table 44.: The production fractions for b-hadrons observed in Powheg+Pythia8 MC.

Hadron	PDG	MC	Nominal SF
B^0	0.404±0.006	0.388	1.041
B^+	0.404±0.006	0.387	1.044
B_s^0	0.103±0.005	0.077	1.377
b-baryon	0.088±0.011	0.147	0.599

Table 45.: The production fractions for b-hadrons observed in Powheg+Herwig7 MC.

Hadron	Production fraction
D^0	0.564 ± 0.001
D^+	0.226 ± 0.008
D_s^0	0.080 ± 0.005
c-baryon	0.109 ± 0.009

Table 46.: The production fractions for weakly decaying c-hadrons at high energy.

Hadron	PDG	MC	Nominal SF
D^0	0.564±0.015	0.553	1.020
D^+	0.226±0.008	0.290	0.779
D_s^0	0.080±0.005	0.093	0.860
c-baryon	0.109±0.009	0.038	2.868

Table 47.: The production fractions for c-hadrons observed in Powheg+Pythia8 MC.

Hadron	PDG	MC	Nominal SF
D^0	0.564±0.015	0.582	0.969
D^+	0.226±0.008	0.258	0.876
D_s^0	0.080±0.005	0.084	0.952
c-baryon	0.109±0.009	0.059	1.847

Table 48.: The production fractions for c-hadrons observed in Powheg+Herwig7 MC.

		PYTHIA8		HERWIG7	
Hadron	PDG	MC Observed	SF	MC Observed	SF
$b \to \mu$	0.1095± 0.0027	0.106	1.032	0.104	1.048
$b \to \tau$	0.0042 ± 0.0004	0.0064	0.656	0.0063	0.667
$b \to c \to \mu$	0.0802 ± 0.0019	0.085	0.943	0.079	1.014
$b \to c\bar{c} \to \mu$	0.0161 ±0.003	0.018	0.882	0.023	0.684
$c \to \mu$	0.082 ± 0.005	0.088	0.932	0.082	0.999

Table 49.: Hadron to μ branching ratios and scale factors for Powheg+Pythia8 and Powheg+Herwig7.

9.2.2 *Hadrons to μ branching ratios*

The B- and c-hadron to μ branching ratios in MC simulations are different to those given by the PDG. Since they strongly depend on the B-hadron production fractions it is fundamental to have in both samples the same B^0, B^+, B_s^0, baryon admixture. This is achieved by applying the production fraction Scale Factors computed in Section 9.2.1 first and then by computing the BRs Scale Factors. The uncertainties come entirely from the PDG values and are propagated throughout the analysis. Table 49 shows the hadron to μ branching ratios and scale factors for Powheg+Pythia8 and Powheg+Herwig7, if compared to PDG [1] values.

9.2.3 *Asymmetry in Single Top Production*

In pp collisions at the LHC, single top quarks are produced asymmetrically in the t-channel and in the s-channel, with more top quark events produced than anti-top quark events, while the Wt-channel single top events are produced symmetrically. Figure 129 shows the single top production modes.
These asymmetries occur because proton valence quarks produce more W^+-bosons than W^--bosons in pp collisions, resulting in more $W^+ \to tb$ vertices than their charge conjugate.
Table 50 shows the theoretical production cross sections for single top in pp collisions at $\sqrt{s} = 13\,\text{TeV}$ at the LHC.

Since an asymmetry in the single top production can affect the CA measurement, a dedicated uncertainty is evaluated by varying the theoretical cross-sections for the t-channel and s-channel within their uncertainties, but preserving the overall number of events. Shifting up and down the production cross sections for tops and anti-tops, four systematic variations are considered in the t- and s-channels,

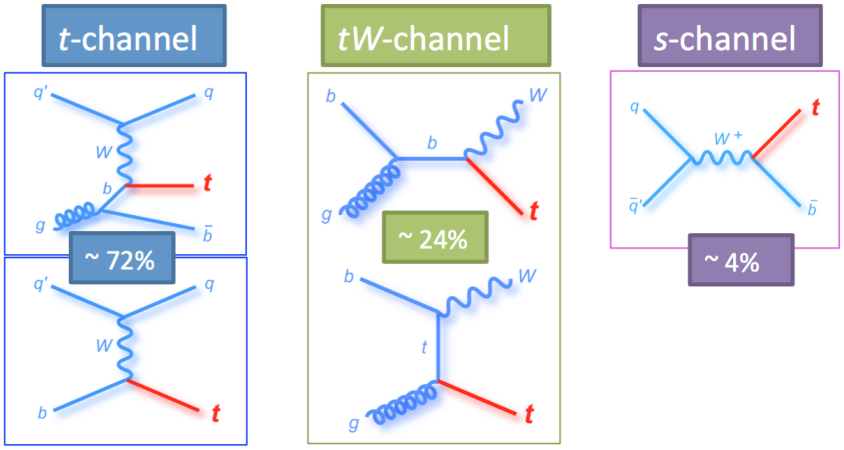

Figure 129.: Sketch of single top production modes[32].

Process	Total cross section pb	Top cross section pb (%)	AntiTop cross section pb (%)
t channel	$216.99^{+9.04}_{-7.71}$	136.02 (62.68)	80.95 (37.31)
s channel	$10.32^{+0.40}_{-0.36}$	6.35 (61.53)	3.97 (38.47)
Wt channel	71.7 ± 3.85	35.85 (50.00)	35.85 (50.00)

Table 50.: Theoretical production cross sections for single top in pp collisions at $\sqrt{s} = 13\,\text{TeV}$ at the LHC. The number in parentheses refer to the expected relative amount of t and $\bar{t}$ for each single top channel, according to predictions.

as detailed in Tables 51 and 52, and then summed in quadrature to give the final uncertainty. CAs are calculated in each case.

9.2.4 *Initial State Radiation Uncertainties*

An uncertainty on the modelling of initial state radiation is estimated with variations of scales in the MC simulation nominal $t\bar{t}$ sample.
CAs are evaluated in samples with additional jets coming from an increased initial

Systematic	Total XS (pb)	Top XS (pb)	AntiTop XS (pb)	Top (%)	AntiTop (%)	Top SF	AntiTop SF
Nominal	216.99	136.02	80.95	62.68	37.31	1.00	1.00
Top ↑	226.30	145.06	80.95	64.18	35.81	1.02	0.95
Top ↓	209.28	128.31	80.95	61.31	38.68	0.98	1.04
Antitop ↑	226.03	136.02	89.99	60.18	39.81	0.96	1.06
Antitop ↓	209.28	136.02	73.24	64.99	35.00	1.04	0.94

Table 51.: Systematic variations on the single-top t-channel production asymmetry,with relative t and $\bar{t}$ cross sections determined in MC simulations.

Systematic	Total XS (pb)	Top XS (pb)	AntiTop XS (pb)	Top (%)	AntiTop (%)	Top SF	AntiTop SF
Nominal	10.32	6.35	3.97	61.53	38.47	1.00	1.00
Top ↑	10.72	6.75	3.97	62.97	37.03	1.02	0.96
Top ↓	9.96	5.99	3.97	60.14	39.85	0.98	1.04
Antitop ↑	10.72	6.35	4.37	59.23	40.76	0.96	1.06
Antitop ↓	9.96	6.35	3.61	63.75	36.24	1.04	0.94

Table 52.: Systematic variations on the single-top t-channel production asymmetry,with relative t and $\bar{t}$ cross-sections determined in MC simulations.

state radiation in pp collisions. Similarly, a sample with decreased radiation is exploited to evaluate the down uncertainty on CAs.
These two additional radiation samples are obtained by varying the value of the coupling α_S^{ISR} in simulations.
The presence of additional radiation jets significantly affects the KLFitter performances, which degrade if an additional radiation jet is mistakenly considered in the $t\bar{t}$ event reconstruction. The additional radiation uncertainty is the dominant systematic uncertainty on the CA measurement.
Since the Additional Radiation systematic are expected to be the dominant systematic uncertainty in Run-2 CAs, a dedicated study was performed on that.
Table 53 shows the impact of the systematic uncertainty coming from the additional radiation on the CAs evaluation on a $t\bar{t}$ MC simulation sample, after the KLFitter decision (the same- different-top discrimination is already performed) and before any unfolding procedure. Also the MC statistical uncertainty is quoted in the table: it is the statistical uncertainty on the systematic uncertainty itself and represents the statistical power of the additional radiation sample used in the studies performed in this thesis. This means that the evaluation of the systematic uncertainty on the additional radiation is limited by the MC statistical uncertainty.
No improvement is observed in the additional radiation systematic if the ΔR cut is performed on top of the KLFitter decision to discriminate same- different-top events, as shown in Table 54. Moreover, if the ΔR cut is applied on top of the KLFitter decision, there is an increase of the statistical error. For this reason the KLFitter decision was finally chosen to discriminate same- different-top events and evaluate CAs.

Figures 130 and 131 show the charge asymmetry input bins (N^{++}, N^{--}, N^{+-}, N^{-+}) for the nominal $t\bar{t}$ signal sample together with the two additional radiation samples (radiation high and radiation low) used. These plots confirm that the nominal and the varied samples agree within the statistical uncertainty.

$(\times 10^{-2})$	A^{SS}		A^{OS}	
Source	Shift up	Shift down	Shift up	Shift down
Statistical	$+0.17$	-0.17	$+0.15$	-0.15
$t\bar{t}$ Radiation	$+0.24$	-0.25	$+0.17$	-0.19
MC Stat	$+0.67$	-0.67	$+0.38$	-0.38

Table 53.: Modelling systematics at $36.1\,\text{fb}^{-1}$, b-tag double selection and KLFitter is used. The MC statistical uncertainty is the statistical uncertainty on the systematic uncertainty itself and represents the statistical power of the additional radiation sample used in the studies performed in this thesis.

$(\times 10^{-2})$	A^{SS}		A^{OS}	
Source	Shift up	Shift down	Shift up	Shift down
Statistical	$+0.24$	-0.24	$+0.20$	-0.20
$t\bar{t}$ Radiation	$+0.60$	-0.63	$+0.19$	-0.19
MC Stat	$+0.67$	-0.67	$+0.42$	-0.42

Table 54.: Modelling systematics at $36.1\,\text{fb}^{-1}$, b-tag double selection and ΔR cut on top of KLFitter decision is used. The MC statistical uncertainty is the statistical uncertainty on the systematic uncertainty itself and represents the statistical power of the additional radiation sample used in the studies performed in this thesis.

Moreover, Figures from 132 to 138 show that there are no anomalies observed in the kinematic variables of interest in the nominal or in the systematic variation samples. Figures are shown for the N^{--} and N^{-+} channels, the distributions for the N^{++} and N^{+-} channels are analogous. Figures 139 show that also in the KLFitter output variables, such as the jet index of the b-jet coupled with the hadronically decaying W-boson, there are no observed anomalies. In all these figures the ratio panel shows the percentage variation between the nominal and the systematic variation samples.
A further check (see Figures from 140 to 142) was performed to prove that there are no discrepancies in the charge asymmetry inputs if studied in the nominal or in the variated samples, in the different $t \to Wb \to X\mu$ decay chains.
Given that no significative variation was observed in the kinematic variables between the nominal $t\bar{t}$ and the additional radiation samples, there is no reason to believe that there are mis-modellings and no further cut is applied. The additional radiation systematic will be the dominant systematic in Chapter 10 and it will be quoted together with its MC statistical uncertainty because every attempt to reduce the additional radiation systematic (*i.e.* the ΔR cut on top of the KLFitter decision) is not significative if compared to its statistical uncertainty.

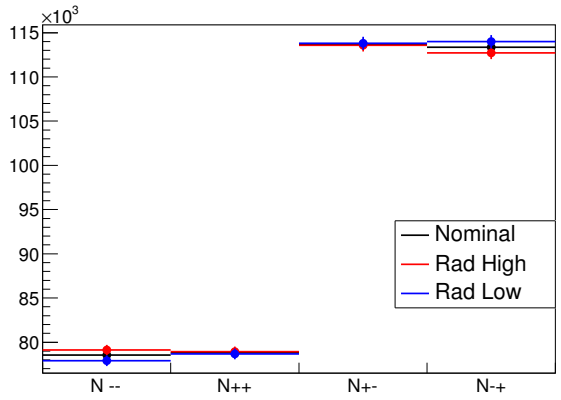

Figure 130.: Charge asymmetry inputs in the lepton+jets channel, shown for the nominal $t\bar{t}$ channel and the additional radiation samples.

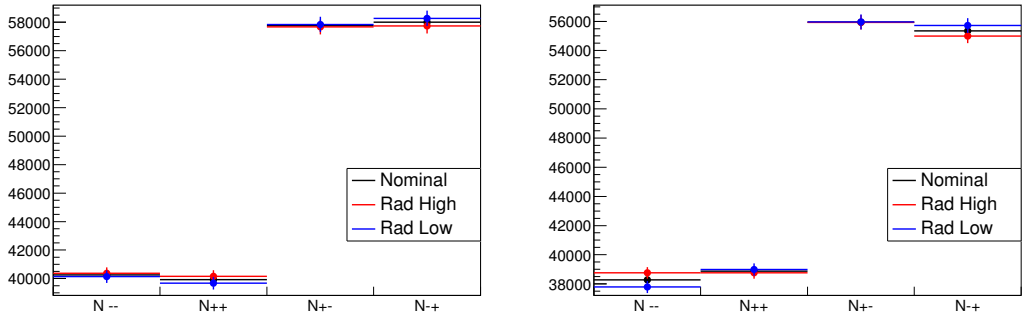

Figure 131.: Charge asymmetry inputs in the electron+jets (letf) and muon+jets (right) channel, shown for the nominal $t\bar{t}$ channel and the additional systematic variations.

9.2.5 *Next to Leading Order (NLO) Generator Uncertainties*

Uncertainties due to the choice of the event generator are estimated by comparing a sample generated with our nominal MC sample Powheg+Pythia8 with a sample generated with MG5_aMC@NLO+Pythia8.
This uncertainty results in a different migration matrix when unfolding the CAs values.

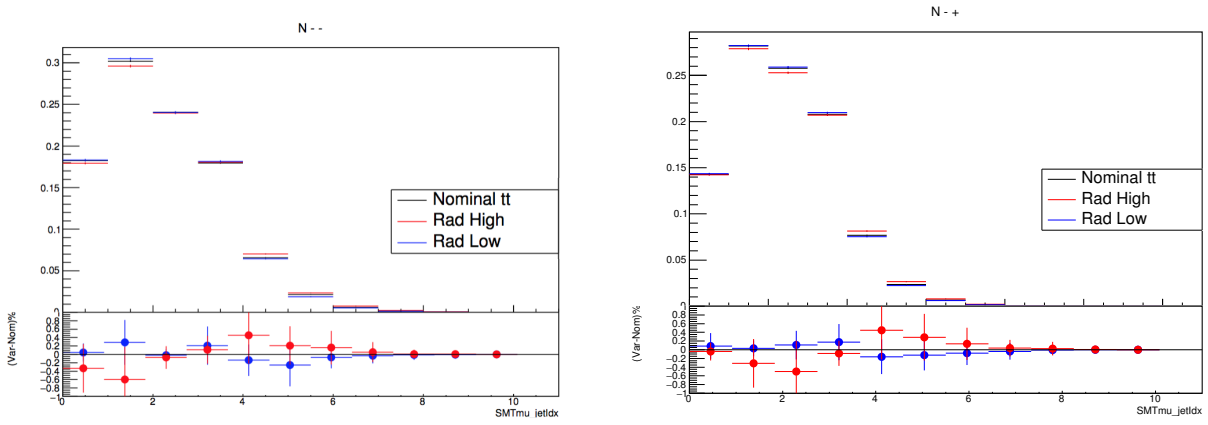

Figure 132.: Index of the jet tagged by the SMT algorithm in the N^{--} (left) and N^{-+} (right) signal channel.

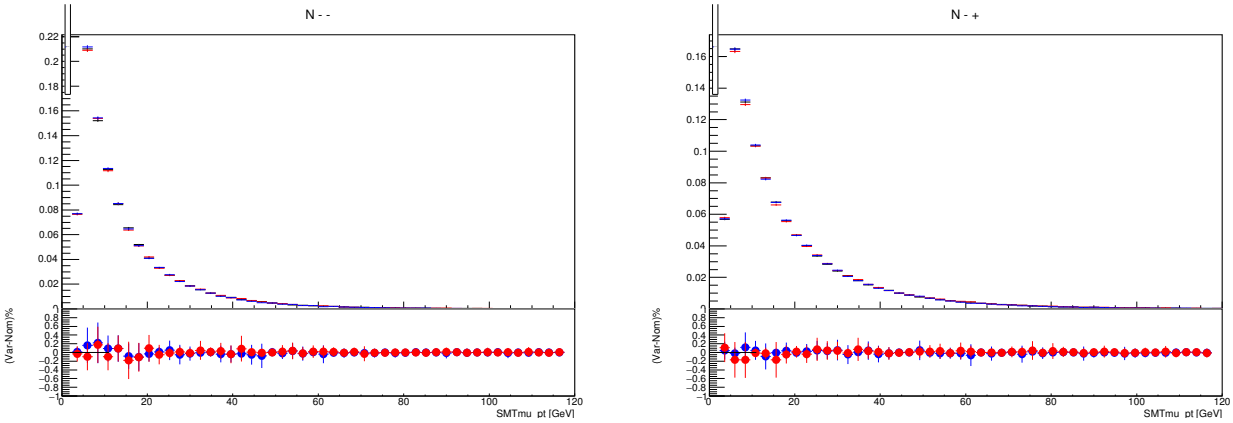

Figure 133.: Soft muon $p_T$in the N^{--} (left) and N^{-+} (right) signal channel.

9.2.6 *Parton Shower and Hadronisation Uncertainties*

Another source of uncertainties for the measurement presented in this thesis comes from the modelling of final state radiation, from the b-quark.
Two different MC simulation samples (Powheg, interfaced with Pythia8 and Herwig7 separately) are used to describe the parton shower and hadronisation in different ways, leading to different CA results.

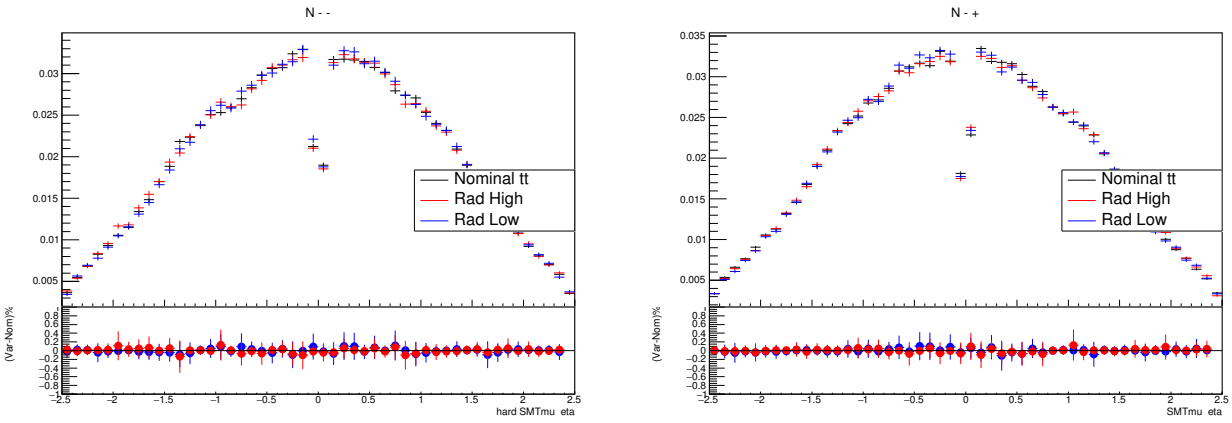

Figure 134.: Soft muon η in the N^{--} (left) and N^{-+} (right) signal channel.

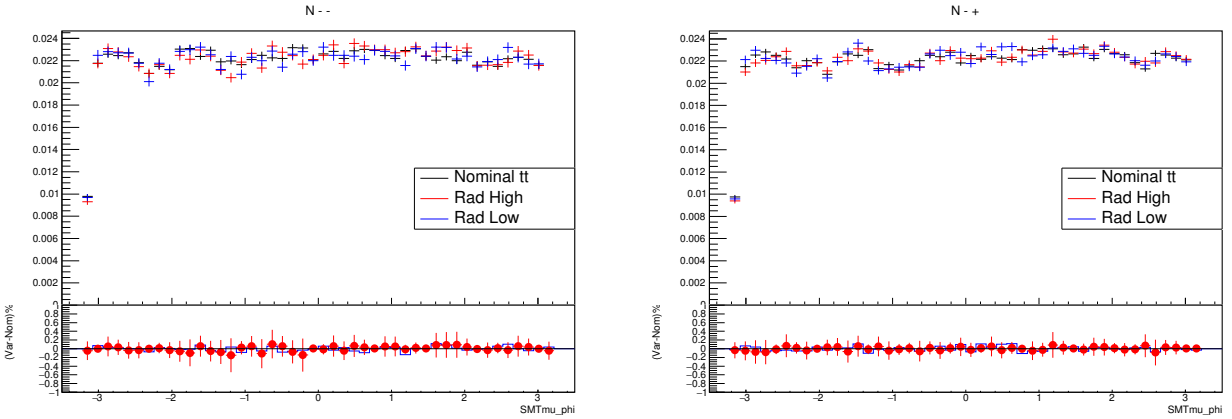

Figure 135.: Soft muon ϕ in the N^{--} (left) and N^{-+} (right) signal channel.

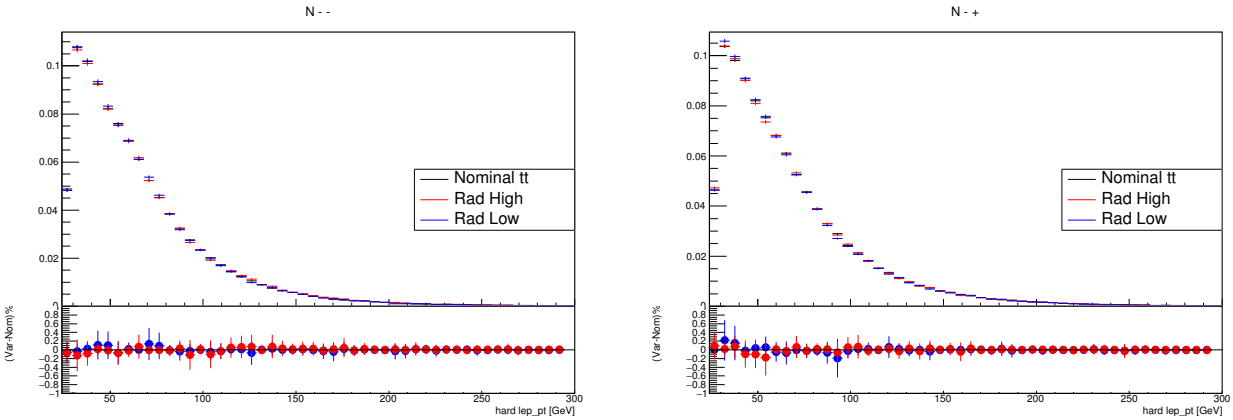

Figure 136.: Hard lepton p_T in the N^{--} (left) and N^{-+} (right) signal channel.

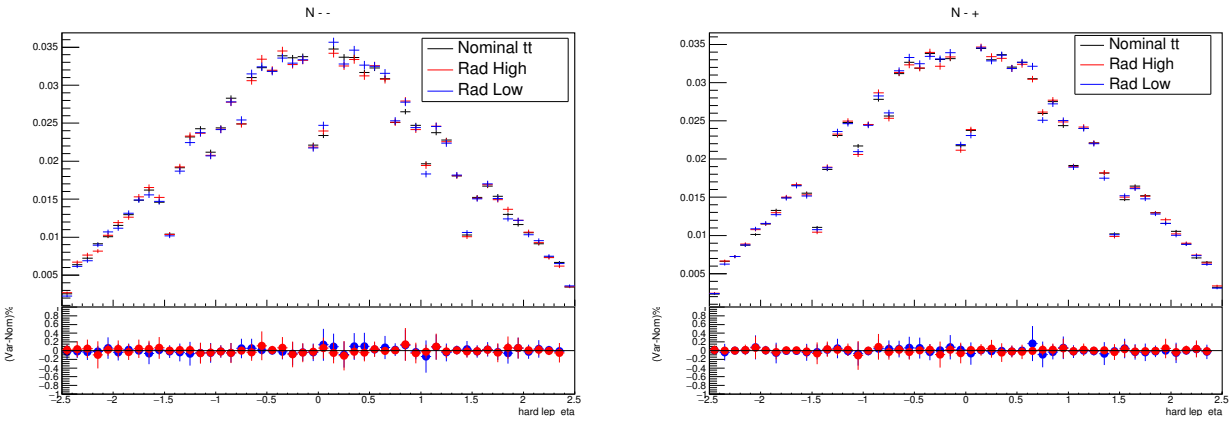

Figure 137.: Hard lepton η in the N^{--} (left) N^{-+} (right) signal channel.

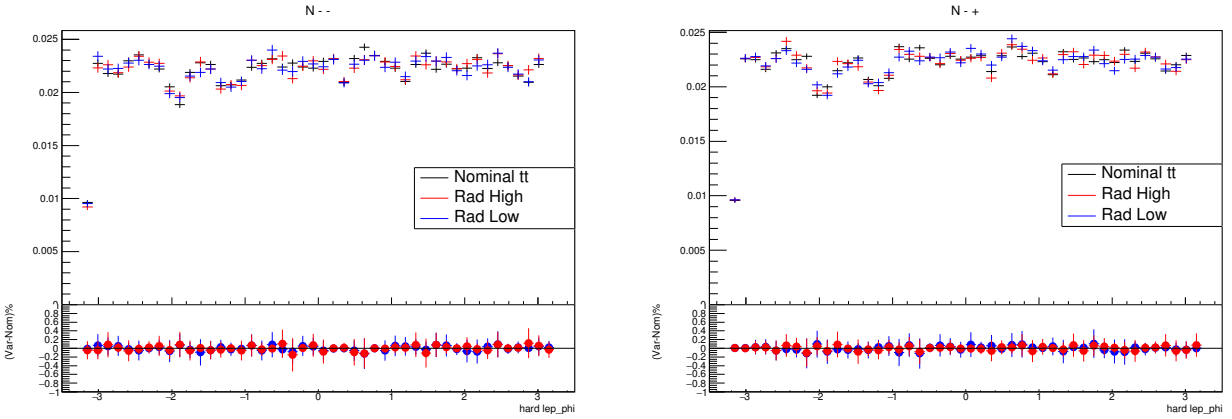

Figure 138.: Hard lepton ϕ in the N^{--} (left) N^{-+} (right) signal channel.

9.2.7 *Parton Distribution Function uncertainties*

As described in Section 1.2, the parton distribution function (PDF) describes the fraction of energy carried by each parton inside of the protons used in the LHC collisions. Different PDF sets are considered. The default PDF is NNPDF3.0 which is one of the component PDFs used in PDF4LHC15. As such, the systematic uncertainty due to PDFs has been evaluated using the PDF4LHC15 error set applied to the nominal $t\bar{t}$ MC. PDF uncertainties are now provided using the internal reweighting mechanism inside Powheg. The PDF weights used are 30 and the error set in Powheg is the one defined by the ordered weights numbers 112-141 as recommended by the Top Working Group [142]. For each of the 30 weights, CAs are extracted and the total systematic uncertainty due to this effect is the sum in quadrature of the single variations.

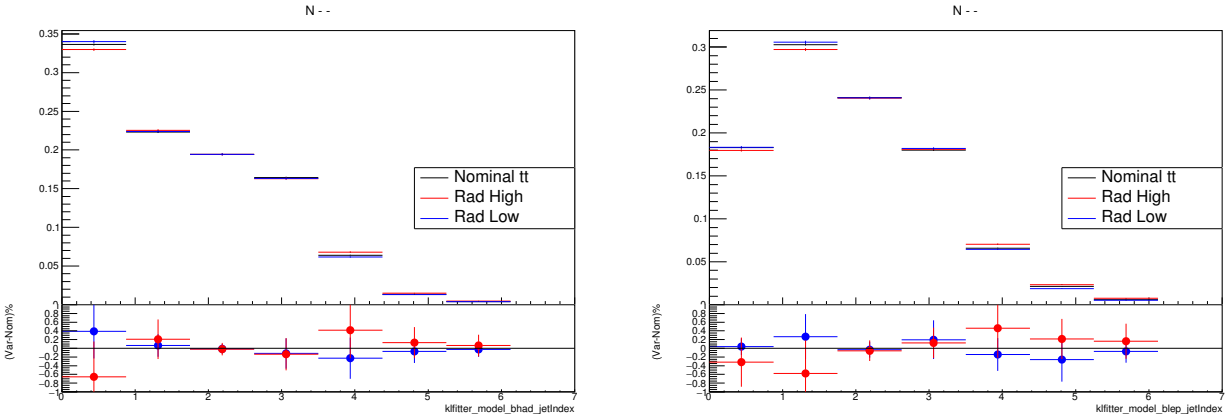

Figure 139.: Index of the b-jet coupled with the leptonically decaying W-boson by the KLFitter in the N^{--} (left) and N^{+-} (right) channel.

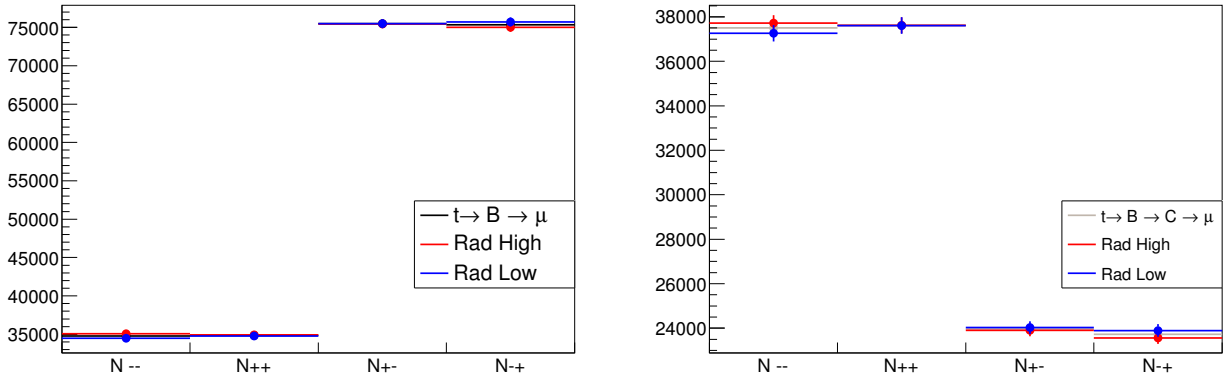

Figure 140.: Charge asymmetry inputs in the $t \to b \to \mu$ (left) and $t \to b \to c \to \mu$ (right) decay channel.

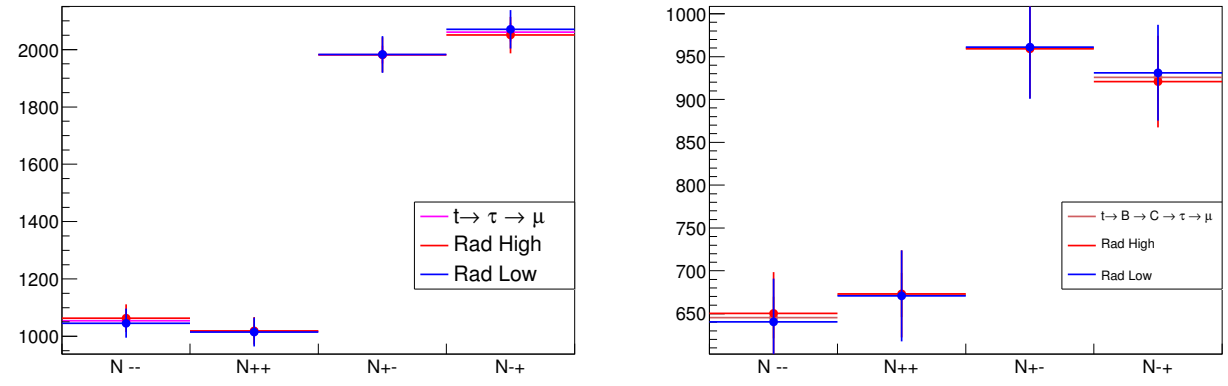

Figure 141.: Charge asymmetry inputs in the $t \to b \to \tau \to \mu$ (left) and $t \to b \to c \to \tau \to \mu$ (right) decay channel.

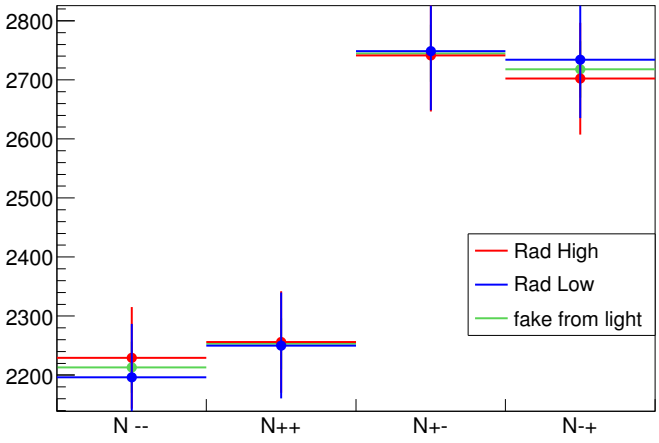

Figure 142.: Charge asymmetry inputs in the fake channel.

10

CHARGE ASYMMETRIES RESULTS

The results of the charge asymmetries measurement are presented in this Chapter, using the definitions and optimisation of the analysis provided in the previous Chapters.

10.1 MEASUREMENT OF CHARGE ASYMMETRIES BEFORE UNFOLDING

The measurement of the charge asymmetries (CA) is performed as described in Section 2.1, using Equations 82.

$$A^{ss} = \frac{P\left(b \to \ell^{+}\right) - P\left(\bar{b} \to \ell^{-}\right)}{P\left(b \to \ell^{+}\right) + P\left(\bar{b} \to \ell^{-}\right)} \qquad A^{os} = \frac{P\left(b \to \ell^{-}\right) - P\left(\bar{b} \to \ell^{+}\right)}{P\left(b \to \ell^{-}\right) + P\left(\bar{b} \to \ell^{+}\right)} \tag{82a}$$

$$A^{ss} = \frac{\left(\frac{N^{++}}{N^{+}} - \frac{N^{--}}{N^{-}}\right)}{\left(\frac{N^{++}}{N^{+}} + \frac{N^{--}}{N^{-}}\right)} \qquad A^{os} = \frac{\left(\frac{N^{+-}}{N^{+}} - \frac{N^{-+}}{N^{-}}\right)}{\left(\frac{N^{+-}}{N^{+}} + \frac{N^{-+}}{N^{-}}\right)} \tag{82b}$$

Equations 83 show CAs as calculated with the nominal MC $t\bar{t}$ simulation sample, using the same procedure as applied to the data.

$$A^{ss} = 0.0005 \pm 0.0017\,(\text{stat.}) \tag{83a}$$

$$A^{os} = -0.0002 \pm 0.0015\,(\text{stat.}) \tag{83b}$$

Table 55 shows a breakdown of all the systematic uncertainties affecting the CAs, before any unfolding procedure is applied. The systematic uncertainty is dominated by the modelling uncertainties and, in particular, by the additional radiation systematics coming from initial state radiation.

The raw charge asymmetries in Table 55 are found to be compatible with zero, and in good agreement with the Standard Model expectations.
Figures 143, 144, 145 show the charge asymmetry inputs in the lepton+jets channel (where the lepton can be an electron or a muon). In Figure 143 all the CAs inputs

$(\times 10^{-2})$	$A_{\mathrm{RAW}}^{\mathrm{SS}}$	$A_{\mathrm{RAW}}^{\mathrm{OS}}$
	0.05	-0.02
Source		
Statistical	± 0.17	± 0.15
Sources of experimental uncertainties		
Lepton charge misidentification	± 0.0005	± 0.0002
Lepton Energy Resolution	± 0.005	± 0.005
Lepton Trigger, Reco ID SF	± 0.002	± 0.002
MET uncertainties	± 0.015	± 0.015
Jet energy scale	± 0.03	± 0.02
Jet energy resolution	± 0.00	± 0.00
JVT	± 0.001	± 0.001
Pileup	± 0.008	± 0.008
SMT Uncert	± 0.001	± 0.001
W+Jets Estimate		
W+jets k_{light}	± 0.001	± 0.018
W+jets $k_{bb/cc}$	± 0.025	± 0.003
W+jets k_c	± 0.004	± 0.013
SMT fake norm.	± 0.001	± 0.001
Fakes norm. (e+jets)	± 0.017	± 0.012
Fakes norm. (μ+jets)	± 0.016	± 0.012
b-tag	± 0.01	± 0.001
c-tag	± 0.003	± 0.003
$light$-tag	± 0.02	± 0.01
Sources of modelling uncertainties		
B Hadron production		
$t\bar{t}$ b-prod.frac.(B)	± 0.002	± 0.002
$t\bar{t}$ b-prod.frac.(B_s)	± 0.001	± 0.001
$t\bar{t}$ b-prod.frac.(baryons)	± 0.001	± 0.001
Total B Hadron production	± 0.0025	± 0.0025
SMT Branching ratio	± 0.003	± 0.003
Additional Radiation	$\pm 0.24\,(\pm 0.67)$	$\pm 0.18\,(\pm 0.38)$
MC Generator	± 0.047	± 0.032
Parton Shower	$\pm 0.15\,(\pm 0.42)$	$\pm 0.11\,(\pm 0.35)$
Parton Distribution Function	± 0.067	± 0.050
Single Top production	± 0.003	± 0.002
Total experimental uncertainties	± 0.05	± 0.04
Total modelling uncertainties	± 0.29	± 0.22
Total systematic uncertainty	± 0.29	± 0.22
Total uncertainty	± 0.34	± 0.28

Table 55.: Systematic uncertainties at 36.1 fb^{-1} for the raw charge asymmetries, b-tag double selection. The MC statistical uncertainty is shown in brackets for the additional radiation systematic.

are considered, and for different-top like events the sign of the W-boson lepton has been reversed in order to consistently represent the charge of the b-quark at production in both the same- and different-top scenarios. Figures 144, 145 show the CA inputs for same-top like and different-top like events respectively.

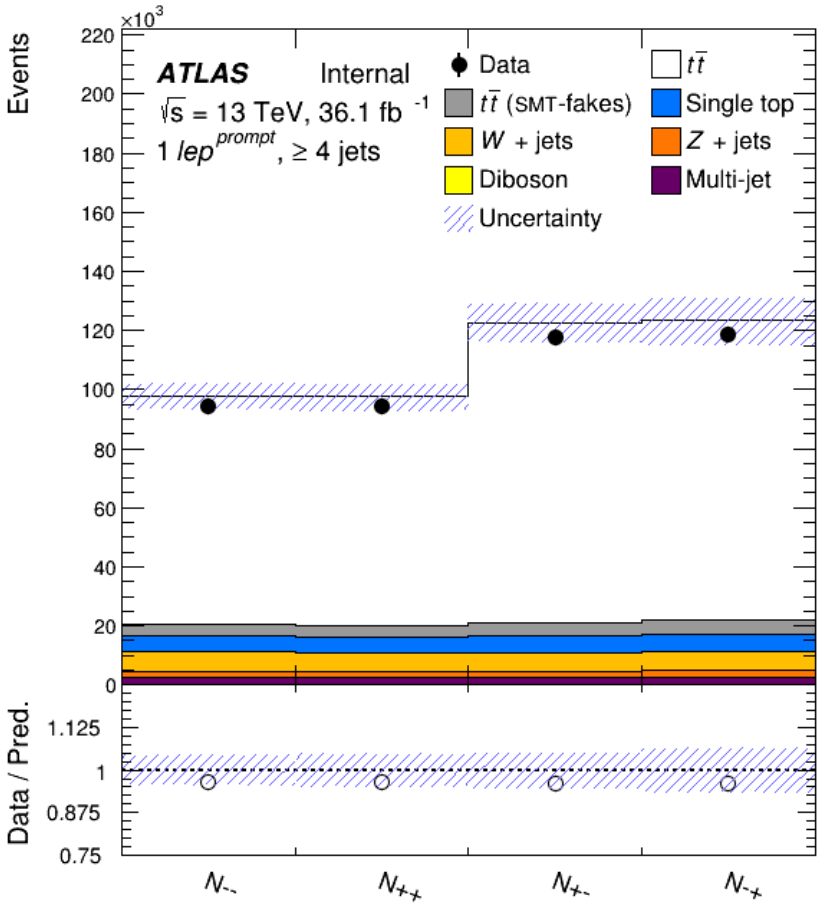

Figure 143.: Charge asymmetry inputs in the lepton+jets channel. All inputs are considered, including the different-top like events: for these events the sign of the W-boson lepton has been reversed in order to consistently represent the charge of the b-quark at production in both the same- and different-top scenarios.

Table 56 shows the yields of SMT muons from $t\bar{t}$ signal and from all the backgrounds, as outlined also in Section 7.6. In Table 56 the statistical and systematic uncertainties are quoted, while in Section 7.6 only the statistical uncertainty was shown. Moreover, the $t\bar{t}$ signal in Table 56 is comprehensive also of the $t\bar{t}$ (SMT-bkg) outlined in Section 7.6. Data and expectations are in good agreement, well in the errors.

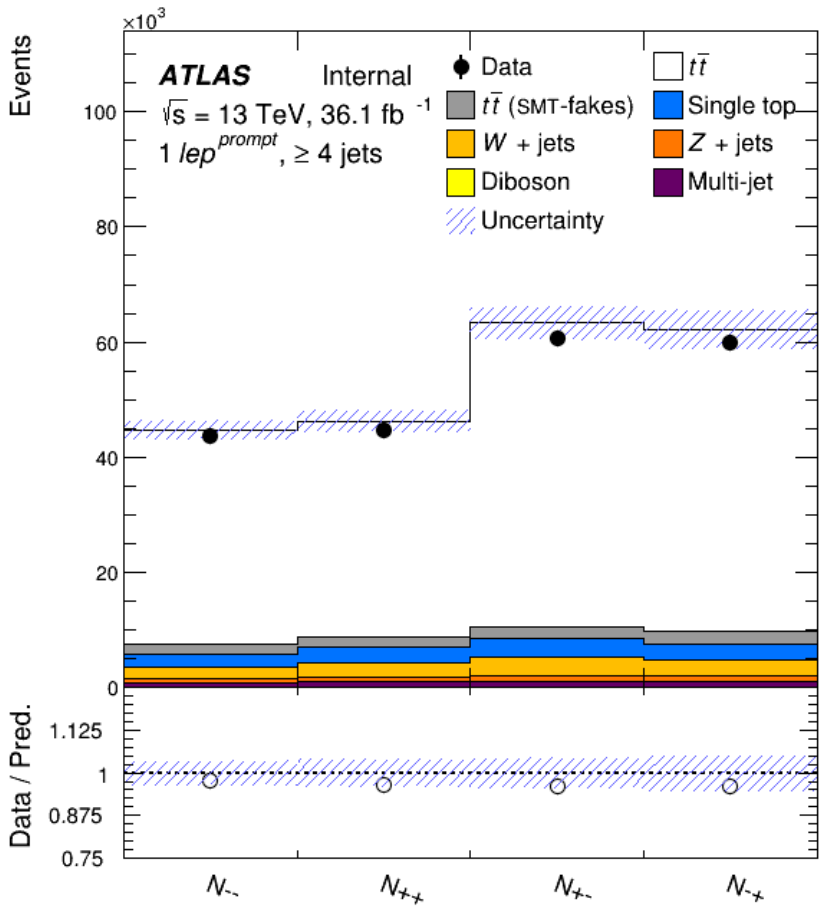

Figure 144.: Charge asymmetry inputs in the lepton+jets channel for same-top like events.

10.2 UNFOLDING

High energy physics measurements are subject to distortions, due to detector effects such as a limited acceptance and a limited resolution of the observed quantities.
Since the observed CAs have to be compared with theoretical predictions, it is needed to account for these detector effects and a dedicated procedure called unfolding is applied.
Assume that a certain quantity x and its distribution $f(x)$ are measured in an ideal detector (infinite acceptance and resolution), their relation with the experimental quantity y and its distribution $f(y)$ which are the results from a real detector is given by the folding integral in Equation 84:

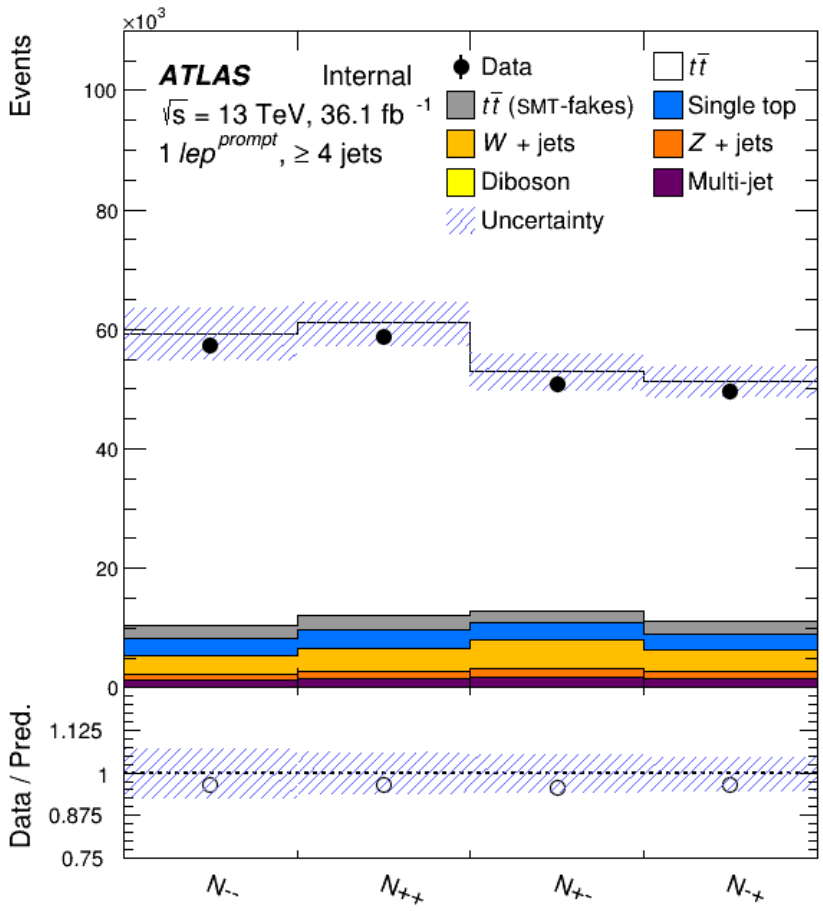

Figure 145.: Charge asymmetry inputs in the lepton+jets channel for different-top like events.

$$f(y) = \int A(x,y)\, f(x)\, dx + b(y) \tag{84}$$

where the distribution $b(y)$ represents the background contribution to the measured distribution $f(y)$, $A(x,y)$ is a resolution function which represents the smearing effects on the measurements.
The unfolding problem is the inverse problem and consists in the calculation of the inverse of the resolution function $A(x,y)$. To get a numerical solution for Equation 84, discrete quantities x and y can be used and the distributions $f(x)$ and $f(y)$ can be represented by histograms. This means that Equation 84 can be translated into Equation 85.

	ℓ+jets
$t\bar{t}$ (SMT-signal)	331 000 ± 19 800
$t\bar{t}$ (SMT-fakes)	15 300 ± 339
Single top	20 600 ± 2010
W+jets	23 500 ± 3230
Z+jets	6490 ± 1050
Diboson	122 ± 15.2
Fakes and non-prompt	8830 ± 3230
Total	405 000 ± 21 000
Data	389980

Table 56.: Yields of the analysis in the lepton+jets channel, considering all the charge asymmetry inputs, including the different-top like events, as in Figure 143.

$$y = Ax + b \tag{85}$$

where y (and b) are vectors with n elements, x is a vector with m elements and A is a $n \times m$ matrix. A is generally called response matrix and relates x and y using information on the acceptance and smearing of the reconstruction process. Some events generated at truth level in a bin j could be reconstructed in bin i where $i \neq j$ and this phenomenon is called migration in the response matrix.

10.2.1 *Unfolding Formulation for CAs*

Regarding the CAs, the complete unfolding formulation is shown in Equation 86.

$$N^i_{truth} = \frac{1}{\varepsilon^i} \sum_{j=1}^{4} \mathcal{M}^{-1}_{ij} f^j_{acc} \left(N^j_{data} - N^j_{bkg} \right) \tag{86}$$

where $i, j = N^{++}, N^{--}, N^{+-}, N^{-+}$, the index i runs over the particle-level (MC truth simulation sample) while the index j runs over the reconstruction-level. The particle-level is referred to the case where in the measurement are considered final state objects after decay, parton shower and hadronisation. The CA measurement was performed at particle-level, in the fiducial phase space defined in Section 7.7. The $\left(N^j_{data} - N^j_{bkg} \right)$ are the number of observed data events minus the estimated backgrounds. Since there is a limited detector acceptance, not all the events can be

used to measure a physical quantity and to account for that the acceptance term f^j_{acc} is introduced and it is parametrised in Equation 87, where N_{reco} is the number of events at reconstructed level and $N_{reco\wedge fid}$ is the number of events present at both reconstructed level and in the fiducial volume.

$$f^j_{acc} = \left(\frac{N_{reco\wedge fid}}{N_{reco}}\right) \tag{87}$$

This is a bin by bin correction term applied to correct for SMT muons which are present at reconstructed level but not at the fiducial level (the fiducial volume for this analysis was defined in Section 7.7). The acceptance terms measured for the CAs analysis are: $f^{++}_{acc} = 0.724 \pm 0.003$, $f^{--}_{acc} = 0.726 \pm 0.003$, $f^{+-}_{acc} = 0.733 \pm 0.003$ and $f^{-+}_{acc} = 0.732 \pm 0.003$.
A finite resolution means that it is impossible to measure a physical quantity with an infinite accuracy and hence an efficiency term ε^i is necessary to perform a bin by bin correction and account for SMT muons which are present at truth level but not at reconstructed level. ε^i is defined in Equation 88, where N_{fid} is the number of events in the fiducial volume.

$$\varepsilon^i = \left(\frac{N_{reco\wedge fid}}{N_{fid}}\right) \tag{88}$$

The efficiency terms measured for the CAs analysis are: $\varepsilon^{++} = 0.335 \pm 0.002$, $\varepsilon^{--} = 0.327 \pm 0.002$, $\varepsilon^{+-} = 0.302 \pm 0.001$ and $\varepsilon^{-+} = 0.302 \pm 0.001$.
Finally, $\mathcal{M}^{-1}_{ij}$ is a discrete 4×4 matrix which corrects for migrations between the four CAs bins which are mainly caused by mistakes in the same-top different-top classification performed by the KLFitter or they are due to charge mis-identification of the triggered leptons (these latter effects are very small and of the order of 10^{-4}). The migration matrix is evaluated only for events at reconstructed level which have an SMT muon coming from the $t\bar{t}$ decay chains (as in Section 7.5) and which are matched with truth level events. The migration matrix in the $t\bar{t}$ nominal case is given in Table 57. The unfolding method applied in the analysis described in this thesis is the Iterative Bayesian method [143] described below.

10.2.2 *Iterative Bayesian Unfolding*

The bayesian unfolding is an iterative procedure, useful to invert the migration matrix.
This approach exploits a prior probability p_i for finding a given true event in a

	N^{++}_{Reco}	N^{--}_{Reco}	N^{+-}_{Reco}	N^{-+}_{Reco}
N^{++}_{Truth}	76.2	1.0	1.0	21.8
N^{--}_{Truth}	0.4	77.8	21.2	0.5
N^{+-}_{Truth}	0.5	22.7	76.1	0.6
N^{-+}_{Truth}	21.7	1.0	1.0	76.2

Table 57.: Migration matrix for the CAs bins in the $t\bar{t}$ nominal configuration, results are expressed in percentage. Statistical error: ± 0.1.

given reconstructed bin and uses the Bayes theorem [144] to update estimators for the true bin contents as defined in Equation 89.

$$\hat{\mu}_i = \frac{1}{\varepsilon^i} \sum_{j=1}^{N} P\left(\text{true value in bin } i | \text{found in bin } j\right) n_j = \frac{1}{\varepsilon^i} \sum_{j=1}^{N} \left(\frac{\mathcal{M}_{ij} p_i}{\sum_{k=1}^{N} \mathcal{M}_{ik} p_k} \right) n_j \quad (89)$$

$\hat{\mu}_i$ is the estimator for the number of events in truth bin i, n_j is the number of events in reconstructed bin j, and finally $\varepsilon^i = P\left(\text{true value in bin } i | \text{found in bin } j\right) = \sum_{j=1}^{N} \mathcal{M}_{ij}$ is the probability to observed an event. This method is applied iteratively 4 times for the CAs measurement, when a balance between the variance on the estimated μ_i and the bias is achieved.

10.3 CLOSURE TEST AND BIAS

A closure test was performed to check the correct functioning of the unfolding procedure. All the unfolding ingredients such as the acceptance and efficiency factors and the response matrix are all built using MC simulations $t\bar{t}$ events and the same MC simulation events at reconstruction-level are used as the pseudo-data to unfold. Following this procedure, the unfolded output should reproduce exactly the MC simulations at the fiducial truth-level: this test was performed in the CAs analysis and the system fully closed.
The bias on the unfolding procedure was evaluated and Table 58 shows that it is negligible. The bias is defined as the difference between the unfolded CAs (CA_{UF}) and their true fiducial values (CA_{Fid}). The test was performed injecting fictitious asymmetries in the fiducial CAs equal to $\sim 1\%$, $\sim 3\%$ and $\sim 6\%$.

A^{ss}		
Injected Asymmetry	Bias	Percentage Bias
0.0660	0.0020	3%
0.0330	0.0010	4%
0.0124	0.0008	6%
A^{os}		
Injected Asymmetry	Bias	Percentage Bias
−0.0320	0.0010	3%
−0.0158	0.0005	3%
0.061	0.0003	4%

Table 58.: Bias of the unfolding on the truth-level charge asymmetry A_{ss} and A_{os} (prior to efficiency factors).

10.4 MEASUREMENT OF CHARGE ASYMMETRIES AFTER THE UNFOLDING

Table 59 shows the full breakdown of the statistical and systematic uncertainties on CAs at 36.1 fb^{-1}, using the b-tag double selection, after unfolding.

The modelling uncertainties are the dominant uncertainties and the additional radiation uncertainty is the largest one. As shown in Section 9.2.4 the additional radiation uncertainty estimation is limited by its own statistical uncertainty. The diagonal values of the response matrices for the modelling uncertainties such as additional radiation, parton shower and MC generator are shown in Table 60 and compared with the nominal migration matrix. The differences between these matrices are taken into account when computing the systematic uncertainty on CAs after unfolding.

The results for the Run-2 charge asymmetry measurement in both the same sign and opposite sign channels are shown in Equation 90, results are found to be compatible with zero and in agreement with the standard model expectations.

$$A^{SS} = -0.0013 \pm 0.0021\,(\text{stat.})^{+0.0008}_{-0.0008}\,(\text{expt.}) \pm 0.0046\,(\text{model}) = -0.0013 \pm 0.0051\,(\text{Total}) \tag{90a}$$

$$A^{OS} = 0.0007 \pm 0.0014\,(\text{stat.})^{+0.0003}_{-0.0003}\,(\text{expt.}) \pm 0.0024\,(\text{model}) = 0.0007 \pm 0.0028\,(\text{Total}) \tag{90b}$$

$(\times 10^{-2})$	A^{SS}	A^{OS}
	-0.13	0.07
Source		
Statistical Uncertainty	± 0.21	± 0.14
Sources of experimental uncertainties		
Lepton Charge MisID	± 0.0005	± 0.0002
Lepton Energy Resolution	± 0.011	± 0.005
Lepton Trigger, Reco ID SF	± 0.0026	± 0.0012
MUON Uncertainties	± 0.017	± 0.007
MET uncertainties	± 0.02	± 0.009
Jet energy scale	± 0.07	± 0.034
Jet energy resolution	± 0.017	± 0.008
JVT	± 0.00007	± 0.00003
Pileup	± 0.01	± 0.006
SMT Uncert	± 0.025	± 0.012
SMT-fakes Estimate	± 0.005	± 0.001
W+Jets Estimate	± 0.009	± 0.004
Z+Jets Estimate	± 0.0006	± 0.0000
b-tag	± 0.009	± 0.00045
c-tag	± 0.0007	± 0.0003
light-tag	± 0.0004	± 0.0002
Total *b*-tag	± 0.0012	± 0.0006
Sources of modelling uncertainties		
B Hadron production		
$t\bar{t}$ *b*-prod.frac.(B)	± 0.005	± 0.002
$t\bar{t}$ *b*-prod.frac.(B_s)	± 0.009	± 0.004
$t\bar{t}$ *b*-prod.frac.(baryons)	± 0.007	± 0.003
Total B Hadron production	± 0.012	± 0.006
SMT Branching ratio		
$b \to \mu$	± 0.007	± 0.003
$b \to \tau \to \mu$	± 0.00001	± 0.00001
$b \to c \to Ws$	± 0.003	± 0.0001
$b \to c \to s$	± 0.005	± 0.002
Total SMT BR	± 0.009	± 0.004
Additional Radiation	$\pm 0.44\,(\pm 0.67)$	$\pm 0.23\,(\pm 0.38)$
MC Generator	± 0.07	± 0.03
Parton Shower	± 0.10	± 0.04
Parton Distribution Function	± 0.07	± 0.05
Single Top production	± 0.003	± 0.001
Total experimental uncertainties	± 0.08	± 0.03
Total modelling uncertainties	± 0.46	± 0.24
Total systematic uncertainty	± 0.46	± 0.24
Total uncertainty	± 0.50	± 0.27

Table 59.: Systematic uncertainties breakdown on CAs at 36.1 fb^{-1}, *b*-tag double selection, in units of 10^{-2}. The MC statistical uncertainty is shown in brackets for the additional radiation systematic

Sample	$++$	$--$	$+-$	$-+$
Nominal	76.2	77.8	76.1	76.2
Additional Radiation	77.1	78.2	77.3	77.3
Parton Shower	75.2	77.8	76.1	75.5
MC Generator	74.8	76.6	76.1	74.8

Table 60.: Elements on the diagonal of the migration matrix for the CAs bins for the nominal, the additional radiation, the parton shower and the MC generator simulation samples; results are expressed in percentage. Statistical error: ± 0.1.

The Run-2 results are also in agreement with the Run-1 results [16] in Equation 91 and the overall uncertainty on the Run-2 measurement is halved with respect to the Run-1 uncertainties.

$$A^{SS} = -0.0071 \pm 0.0061\,(\text{stat.})^{+0.0022}_{-0.0019}\,(\text{expt.}) \pm 0.0047\,(\text{model}) = -0.0071 \pm 0.0081\,(\text{Total}) \tag{91a}$$

$$A^{OS} = 0.0041 \pm 0.0035\,(\text{stat.})^{+0.0013}_{-0.0011}\,(\text{expt.}) \pm 0.0027\,(\text{model}) = 0.0041 \pm 0.0046\,(\text{Total}) \tag{91b}$$

These CA measurement results will be a benchmark for the $\mathcal{CP}$ violation asymmetries results which will be performed using b-hadrons from top quark decays in ATLAS Run-2. Since, the overall uncertainty on CAs is halved with respect to the Run-1 result, the measurement of the $\mathcal{CP}$ violation asymmetry will also benefit from a significantly decreased uncertainty with respect to Run-1 [16] and will be competitive with other collider experiment results.

11

CONCLUSIONS

A measurement of charge asymmetries in heavy flavour decays was performed using inclusive $t\bar{t}$ events, in the lepton+jets channel. This measurement was based on data collected by the ATLAS detector at the LHC during 2015 and 2016, in pp collisions at a centre of mass energy of 13 TeV with an integrated luminosity of 36.1 fb^{-1}.

Same-sign and opposite-sign asymmetries were measured, using the charges of the two leptons in the final state: one prompt lepton from the W-boson in the top-quark decay and a soft muon from the semi-leptonic decay of a b- or c-hadron.

The calibration of the momentum imbalance based Soft Muon Tagging algorithm used in the Run-1 measurement was also presented in this thesis. Soft muons were identified using the fractional difference in absolute momentum, the Momentum Imbalance (MI), between a muon track measured in the Inner Detector (ID) and Muon Spectrometer (MS) (extrapolated back to the primary vertex): the MI was shown to be a powerful variable to discriminate between true soft muons from heavy-flavour decays and fake leptons. Scale factors were derived for the mistag rate of the SMT with a precision of 20%.

The Run-2 event selection was outlined and optimised in order to maximise the signal and reject the backgrounds. Backgrounds were estimated using MC simulations for the Z+jets, diboson and single-top backgrounds, while data-driven methods were used to estimate the multijet and W+jets backgrounds. The configuration which maximises the signal purity was found to be the combination of the SMT and the MV2c10 taggers at a 77% working point. This b-tag double configuration reduces the contributions from fake SMT muons in $t\bar{t}$ events (*i.e.* soft muons coming from $c \to \mu$ decays and pile-up events).

The KLFitter set-up and optimisation was performed: this tool was used to reconstruct the $t\bar{t}$ system and assign the W-boson lepton and the soft muon to same- or different-top decay. The KLFitter correctly discriminates between same- and different-top events in 78% of the cases. Further studies were performed to investigate the possibility to add an angular matching cut on top of the KLFitter decision: this configuration improves the purity of the same- or different-top decision but does not reduce the additional radiation systematic uncertainty whilst increasing the statistical uncertainty on the charge asymmetry measurement.

Same-sign and opposite-sign charge asymmetries were measured after the unfolding procedure and the statistical and systematics uncertainty evaluation leads to a

total uncertainty on the measurement which significantly improves the sensitivity with respect to the same measurement performed in Run-1.

11.1 FUTURE PERSPECTIVES

The measurement is dominated by the modelling uncertainty, the additional radiation uncertainty in particular. Any further improvement in these regards is currently limited by the statistical uncertainty on the additional radiation systematic. However, increasing the jet p_T cut from 25 GeV to 30 GeV reduces the additional radiation systematic to 0.0019 on A^{ss} and 0.0010 on A^{os}, but at the same time the statistical uncertainty on the measurement goes up to 0.0035 on A^{ss} and 0.0020 on A^{os}. The caveat is that these variations are embedded in the statistical uncertainty on the additional radiation systematic, so they can be fluctuations. Larger MC samples are necessary to fix this issue and be able to perform further studies to improve the additional radiation systematic uncertainty.
The full Run-2 charge asymmetries measurement will be performed with an integrated luminosity of $140\,\text{fb}^{-1}$ and the statistical uncertainty is expected to be 0.0012 on A^{ss} and 0.0007 on on A^{os}. In these configuration, any further cut on the jet p_T could be performed without any concerns about the increase of the statistical uncertainty.
Finally, $\mathcal{CP}$ violation asymmetries will be extracted from CA measurements, following the procedure outlined in Section 2.1. Since the overall uncertainty on CAs is halved with respect to the Run-1 measurement, also the $\mathcal{CP}$ violation asymmetries measurement will have a reduced uncertainty and this will help in the comparison with the D0 result [36] and the other collider experiments outlined in Section 2.2.

A

SAMPLE LIST

A.1 L1CALO SAMPLE LIST

Tables here present the GRL, the list of samples used in trigger efficiency studies, and the enhanced minimum bias samples used for the study of trigger rates.

Good Run List
data16_13TeV.periodAllYear_DetStatus-v83pro20-15_DQDefects-00-02-04_PHYS_StandardGRL_All_Good_25ns.xml

Data samples used for trigger efficiency studies
data16_13TeV.00308047.physics_Main.merge.DAOD_L1CALO1.f741_m1677_c1010_m1652

Data samples used for trigger rate studies
data16_13TeV.00302956.physics_EnhancedBias.recon.ESD.r8445_r8540

A.2 RUN-2 CHARGE ASYMMETRY ANALYSIS SAMPLE LIST

A.2.1 *Simulation samples*

process	DSID	MC generator, parton shower, simulation	PDF
$t\bar{t}$ (PP8)	410501	Powheg+Pythia8, $hdamp = 1.5m_t$, FullSim (AFII for crosschecks)	NNPDF30 NLO
$t\bar{t}$ (PP8, Radiation Low)	410511	Powheg+Pythia8, A14v3cDo, $hdamp = 1.5m_t$, AFII	NNPDF30 NLO
$t\bar{t}$ (PP8, Radiation High)	410512	Powheg+Pythia8, A14v3cUp, $hdamp = 3m_t$, AFII	NNPDF30 NLO
$t\bar{t}$ (PPH7.1)	411168	Powheg+Herwig7.1.3, $hdamp = 1.5m_t$, AFII	NNPDF30 NLO
$t\bar{t}$ (aMC)	410225	aMC@NLO+Pythia8, AFII	NNPDF30 NLO
$t\bar{t}$ (PP8) dilepton	410503	Powheg+Pythia8, $hdamp = 1.5m_t$, FullSim (AFII for crosschecks)	NNPDF30 NLO
$t\bar{t}$ (PPH7.0) dilepton	410527	Powheg+Herwig7.0.4, AFII	NNPDF30 NLO
$t\bar{t}$ (aMC) dilepton	410226	aMC@NLO+Pythia8, AFII	NNPDF30 NLO
single top t-channel	410011-12	Powheg+Pythia6, FullSim	CT10
single top s-channel	410025-26	Powheg+Pythia6, FullSim	CT10
single top Wt channel	410013-14	Powheg+Pythia6, FullSim	CT10
W+jets	364156-364197	Sherpa 2.2.1, FullSim	NNPDF30 NLO
Z+jets	364100-364141 and 364204-364215	Sherpa 2.2.1, FullSim	NNPDF30 NLO
Diboson WW, WZ, ZZ	361063-361097	Sherpa, FullSim	CT10

A.2.2 *Data samples*

2015 Data samples
data15_13TeV.periodD.physics_Main.PhysCont.DAOD_TOPQ1.grp15_v01_p2950
data15_13TeV.periodE.physics_Main.PhysCont.DAOD_TOPQ1.grp15_v01_p2950
data15_13TeV.periodF.physics_Main.PhysCont.DAOD_TOPQ1.grp15_v01_p2950
data15_13TeV.periodG.physics_Main.PhysCont.DAOD_TOPQ1.grp15_v01_p2950
data15_13TeV.periodH.physics_Main.PhysCont.DAOD_TOPQ1.grp15_v01_p2950
data15_13TeV.periodJ.physics_Main.PhysCont.DAOD_TOPQ1.grp15_v01_p2950

2016 Data samples
data16_13TeV.periodA.physics_Main.PhysCont.DAOD_TOPQ1.grp16_v01_p2950
data16_13TeV.periodB.physics_Main.PhysCont.DAOD_TOPQ1.grp16_v01_p2950
data16_13TeV.periodC.physics_Main.PhysCont.DAOD_TOPQ1.grp16_v01_p2950
data16_13TeV.periodD.physics_Main.PhysCont.DAOD_TOPQ1.grp16_v01_p2950
data16_13TeV.periodE.physics_Main.PhysCont.DAOD_TOPQ1.grp16_v01_p2950
data16_13TeV.periodF.physics_Main.PhysCont.DAOD_TOPQ1.grp16_v01_p2950
data16_13TeV.periodG.physics_Main.PhysCont.DAOD_TOPQ1.grp16_v01_p2950
data16_13TeV.periodI.physics_Main.PhysCont.DAOD_TOPQ1.grp16_v01_p2950
data16_13TeV.periodK.physics_Main.PhysCont.DAOD_TOPQ1.grp16_v01_p2950
data16_13TeV.periodL.physics_Main.PhysCont.DAOD_TOPQ1.grp16_v01_p2950

BIBLIOGRAPHY

[1] The Review of Particle Physics (2018) M. Tanabashi et al. (Particle Data Group), Phys. Rev. D 98, 030001 (2018).

[2] Michael E. Peskin and Daniel V. Schroeder. An Introduction to quantum field theory. Levant Boks, 1995.

[3] I. J. R. Aitchinson and A. J. G. Hey. Gauge theories in particle physics: A pratica introduction. Vol. 2: Non-Abelian gauge theories: QCD and the electroweak theory. Taylor & Francis, 2004.

[4] Chen-Ning Yang and Robert L. Mills., Conservation of Isotopic Spin and Isotopic Gauge Invariance, Phys. Rev. 96 (1954).

[5] E. Fermi, Tentativo di una teoria dei raggi β, Il Nuovo Cimento (1924-1942) 11 (2008) 1.

[6] A. Salam and J. C. Ward, Weak and electromagnetic interactions, Il Nuovo Cimento (1955-1965) 11 (1959) 568.

[7] Super-Kamiokande collaboration, Y. Fukuda et al., Evidence for oscillation of atmospheric neutrinos, Phys. Rev. Lett. 81 (1998) 1562.

[8] SNO collaboration, Q. R. Ahmad et al., Direct Evidence for Neutrino Flavor Transformation from Neutral-Current Interactions in the Sudbury Neutrino Observatory, Phys. Rev. Lett. 89 (2002) 011301.

[9] B. Pontecorvo, Neutrino Experiments and the Problem of Conservation of Leptonic Charge, Zh. Eksp. Teor. Fiz., vol. 53, p. 1717, 1967.

[10] Z. Maki, M. Nakagawa, and S. Sakata, Remarks on the unified model of elementary particles, Prog. Theor. Phys., vol. 28, pp. 870-880, 1962.

[11] Nicola Cabibbo, Unitary Symmetry and Leptonic Decays, Phys. Rev. Lett. (1963).

[12] Makoto Kobayashi and Toshihide Maskawa, CP Violation in the Renormalizable Theory of Weak Interaction, Prog. Theor. Phys. (1973).

[13] P. W. Higgs, Broken symmetries and the masses of gauge bosons, Phys. Rev. Lett. 13 (1964) 508.

[14] F. Englert and R. Brout, Broken symmetry and the mass of gauge vector mesons, Phys. Rev. Lett. 13 (1964) 321.

[15] J. H. Christenson, J. W. Cronin, V. L. Fitch, and R. Turlay, Evidence for the 2π decay of the K^0 meson, Phys. Rev. Lett. 13 (1964) 138.

[16] The ATLAS Collaboration, Measurements of charge and CP asymmetries in b-hadron decays using top-quark events collected by the ATLAS detector in pp collisions at $\sqrt{s} = 8$ TeV, JHEP 02 (2017) 071.

[17] CKM Fitter, preliminary results, as of Summer 2018, http://ckmfitter.in2p3.fr/www/results/ plots_summer18/ckm_res_summer18.html

[18] List of publications, http://inspirehep.net/searchp=collaboration:%27PAMELA%27.

[19] List of publications, http://inspirehep.net/searchp=collaboration:%27AMS%27.

[20] WMAP, C. L. Bennett et al., First year Wilkinson Microwave Anisotropy Probe (WMAP) observations: Preliminary maps and basic results, Astrophys. J. Suppl. 148 (2003) 1.

[21] A. D. Sakharov, Violation of CP Invariance, C Asymmetry, and Baryon Asymmetry of the Universe, Pisma Zh. Eksp. Teor. Fiz. 5 (1967) 32, Usp. Fiz. Nauk161,61(1991)

[22] BaBar Collaboration, B. Aubert et al., Observation of CP violation in the B^0 meson system, Phys. Rev. Lett. 87 (2001) 091801.

[23] Belle Collaboration, K. Abe et al., Observation of large CP violation in the neutral B meson system, Phys. Rev. Lett. 87 (2001) 091802.

[24] LHCb Collaboration, R. Aaij et al., First observation of CP violation in the decays of B_s^0 mesons, Phys. Rev. Lett. 110 (22) (2013) 221601.

[25] NA31 Collaboration, J. Burkhardt et al., First Evidence for Direct CP Violation, Phys. Lett. B206 (1988) 169-176.

[26] NA48 Collaboration, V. Fanti et al., A New measurement of direct CP violation in two pion decays of the neutral kaon, Phys. Lett. B465 (1999) 335-348.

[27] KTeV Collaboration, A. Alavi-Harati et al., Observation of direct CP violation in $K_{S,L} \to \pi\pi$ decays, Phys. Rev. Lett. 83 (1999) 22-27.

[28] The CDF collaboration, Observation of Top Quark Production in pp Collisions with the Collider Detector at Fermilab, Phys. Rev. Lett. 74 (1995) 2626.

[29] The D0 collaboration, Observation of the Top Quark, Phys. Rev. Lett. 74 (1995) 2632.

[30] Top Working Group summary plots,
https://twiki.cern.ch/twiki/bin/view/LHCPhysics/LHCTopWGSummaryPlots

[31] The ATLAS Collaboration, Observation of Higgs boson production in association with a top quark pair at the LHC with the ATLAS detector, Physics Letters B Volume 784.

[32] Top figures,
https://www-do.fnal.gov/Run2Physics/top/
top_public_web_pages/top_feynman_diagrams.html

[33] LHCb Collaboration, R. Aaij et al., Measurement of the semileptonic CP asymmetry in $B^0 - \bar{B}^0$ mixing, Phys. Rev. Lett. 114 (2015) 041601.

[34] LHCb Collaboration, R. Aaij et al., Measurement of the CP asymmetry in $B_s^0 - \bar{B}_s^0$ mixing, Phys. Rev. Lett. 117 (6) (2016) 061803.

[35] BaBar Collaboration, J. P. Lees et al., Study of CP Asymmetry in $B^0 - \bar{B}^0$ Mixing with Inclusive Dilepton Events, Phys. Rev. Lett. 114 (8) (2015) 081801.

[36] D0 Collaboration, V. M. Abazov et al., Study of CP-violating charge asymmetries of single muons and like-sign dimuons in $p\bar{p}$ collisions, Phys. Rev. D89 (1) (2014) 012002.

[37] The ATLAS Collaboration, Measurement of the charge asymmetry in top-quark pair production in the lepton-plus-jets final state in pp collision data at $\sqrt{s} = 8$ TeV with the ATLAS detector, Eur. Phys. J. C76 (2) (2016) 87.

[38] J.H.Kuhnand, G.Rodrigo, Charge asymmetries of top quarks at hadron colliders revisited, JHEP 01 (2012) 063

[39] O. Gedalia, G. Isidori, F. Maltoni, G. Perez, M. Selvaggi and Y. Soreq, Top B Physics at the LHC, Phys. Rev. Lett. 110 232002 2013.

[40] CMS Collaboration, Measurement of the $\mathcal{CP}$-violating weak phase ϕ_s and the decay width difference $\Delta\Gamma_s$ using the $B_s^0 \to J/\psi\,\phi(1020)$ decay channel in pp collisions at $\sqrt{s} = 8$ TeV, Physics Letters B Volume 757, 10 June 2016, Pages 97-120

[41] The ATLAS Collaboration, Measurement of the $\mathcal{CP}$-violating phase ϕ_s and the B^0 meson decay width difference with $B_s^0 \to J/\psi\,\phi(1020)$ decays in ATLAS, JHEP08 (2016) 147

[42] Heavy Flavor Averaging Group (HFAG) collaboration, Y. Amhis et al., Averages of b-hadron, c-hadron and τ-lepton properties as of summer 2014.

[43] M. Artuso, G. Borissov and A. Lenz, CP violation in the B_s^0 system, Rev. Mod. Phys. 88 (2016) 045002.

[44] D. Genon, On the origin of the D0 like-sign dimuon charge asymmetry, Phys. Rev. D. 87 074020.

[45] S. Bar-Shalom, G. Eilam, M. Gronau, J. L. Rosner, Second order direct CP asymmetry in $B_s \to X\ell\nu$, Phys. Lett. B 694 (2011) 374-379.

[46] Sebastien Descotes-Genon and Jernej F. Kamenik, A possible explanation of the D0 like-sign dimuon charge asymmetry, Phys. Review D 87, 074036 (2013).

[47] O. S. Bruning, P. Collier, P. Lebrun, S. Myers, R. Ostojic, J. Poole, and P. Proudlock, LHC Design Report Vol.1: The LHC Main Ring, 2004.

[48] https://home.cern/resources/faqs/facts-and-figures-about-lhc

[49] https://home.cern/science/accelerators/large-hadron-collider

[50] https://project-hl-lhc-industry.web.cern.ch/content/project-schedule

[51] https://twiki.cern.ch/twiki/bin/view/AtlasPublic/LuminosityPublicResults

[52] The ATLAS Collaboration, The ATLAS Experiment at the CERN Large Hadron Collider, 2008 Jinst 3 s08003.

[53] ALICE Collaboration, ALICE physics performance: Technical Design Report, CERN- LHCC-2005-030 (2005).

[54] CMS Collaboration, CMS Physics: Technical Design Report Volume 1: Detector Performance and Software, CERN-LHCC-2006-001 (2006).

[55] LHCb Collaboration, The LHCb Detector at the LHC, JINST 3 (2008) S08005.

[56] The ATLAS Collaboration, ATLAS Insertable B-Layer Technical Design Report, 437 CERN- LHCC-2010-013. ATLAS-TDR-19, 2010.

[57] The ATLAS Collaboration, The ATLAS superconducting magnet system at the Large Hadron Collider, Physica C: Superconductivity, Volume 468, Issues 15-20, 15 September 2008.

[58] The ATLAS collaboration, The ATLAS Inner Detector commissioning and calibration. In: Eur. Phys. J. C70 (2010). DOI:10.1140 /epjc/s10052-010-1366-7.

[59] The ATLAS collaboration, The upgraded Pixel detector and the commissioning of the Inner Detector tracking of the ATLAS experiment for Run-2 at the Large Hadron Collider. In: PoS EPS-HEP2015 (2015). eprint: 1608.07850.

[60] The ATLAS collaboration, Operation and performance of the ATLAS semiconductor tracker. In: JINST 9 (2014). DOI: 10.1088/1748- 0221/9/08/P08009.

[61] The ATLAS collaboration, ATLAS Transition Radiation Tracker (TRT): Straw Tube Gaseous Detectors at High Rates. Tech. rep. CERN, 2013. URL: https://cds.cern.ch/record/1537991.

[62] The ATLAS Collaboration, ATLAS liquid-argon calorimeter: Technical Design Report. Technical Design Report ATLAS. CERN, Geneva, 1996.

[63] The ATLAS Collaboration, ATLAS tile calorimeter: Technical Design Report. Technical Design Report ATLAS. CERN, Geneva, 1996.

[64] The ATLAS Collaboration, ATLAS muon spectrometer: Technical Design Report. CERN, Geneva, 1997.

[65] Nitesh Soni, ATLAS Forward Detectors and Physics, arXiv:1006.5426v1.

[66] The ATLAS collaboration, ATLAS Letter of Interest Phase 1 upgrade, https://cds.cern.ch/record/1402470/files/LHCC-I-020.pdf

[67] Nakahama, Y. and others, The ATLAS Trigger System: Ready for Run-2, J. Phys. 1-6, 2015.

[68] The ATLAS Collaboration, Performance of the ATLAS Trigger System in 2015, ATL-COM-DAQ-2016-034.

[69] The ATLAS Collaboration, The ATLAS Level-1 Calorimeter Trigger, 2008 JINST 3 P03001.

[70] The ATLAS Collaboration, Performance of primary vertex reconstruction in proton-proton collisions at $\sqrt{s} = 7$ TeV in the ATLAS experiment, Tech. Rep. ATLAS-CONF-2010-069, CERN, Geneva, Jul 2010

[71] ID tracking performances, https://twiki.cern.ch/twiki/bin/view/ AtlasPublic/InDetTrackingPerformanceApprovedPlotsRun_2

[72] T.Cornelissen, M.Elsing, S.Fleischmann, W.Liebig, E.Moyse, andA.Salzburger, Concepts, Design and Implementation of the ATLAS New Tracking (NEWT), Tech. Rep. ATL-SOFT- PUB-2007-007. ATL-COM-SOFT-2007-002, CERN, Geneva, Mar 2007

[73] R. E. Kalman, A new approach to linear filtering and prediction problems, Transactions of the ASME-Journal of Basic Engineering, vol. 82, no. Series D, pp. 35-45, 1960

[74] The ATLAS Collaboration, Performance of the ATLAS Inner Detector Track and Vertex Reconstruction in the High Pile-Up LHC Environment, ATLAS-CONF-2012-042 (2012)

[75] The ATLAS Collaboration, Topological cell clustering in the ATLAS calorimeters and its performance in LHC Run-1,arXiv:1603.02934, 2016

[76] T. G. Cornelissen, M. Elsing, I. Gavrilenko, J. F. Laporte, W. Liebig, M. Limper, K. Nikolopoulos, A. Poppleton, and A. Salzburger, The global 2 track fitter in ATLAS, J. Phys. Conf. Ser., vol. 119, p. 032013, 2008

[77] The ATLAS Collaboration, Improved electron reconstruction in ATLAS using the Gaussian Sum Filter-based model for bremsstrahlung, Tech. Rep. ATLAS-CONF-2012-047, CERN, Geneva, May 2012

[78] The ATLAS Collaboration, Electron efficiency measurements with the ATLAS detector using the 2012 LHC proton-proton collision data, Eur. Phys. J. C 77 (2017) 195, arXiv:1612.01456

[79] The ATLAS Collaboration, Electron efficiency measurements in 2015 data, ATLAS-CONF-2016-024, arXiv:1902.04655

[80] J. Illingworth and J. Kittler, A survey of the Hough transform, Computer Vision, Graphics, and Image Processing 44 (1988) 87-116

[81] The ATLAS Collaboration, Muon reconstruction performance of the ATLAS detector in proton-proton collision data at $\sqrt{s} = 13$ TeV, The European Physical Journal C, vol. 76, no. 5, pp. 1-30, 2016

[82] The ATLAS Collaboration, Measurement of the muon reconstruction performance of the ATLAS detector using 2011 and 2012 LHC proton-proton collision data, Eur. Phys. J., vol. C74, no. 11, p. 3130, 2014

[83] The ATLAS Collaboration, Jet energy measurement and its systematic uncertainty in proton-proton collisions at $\sqrt{s} = 13$ TeV with the ATLAS detector, Eur. Phys. J. C 75 (2015) 17

[84] M. Cacciari, G. P. Salam, and G. Soyez, The anti-kt jet clustering algorithm, Journal of High Energy Physics, vol. 2008, no. 04, p. 063, 2008

[85] The ATLAS Collaboration, Calibration of the performance of b-tagging for c and light- flavour jets in the 2012 ATLAS data, Tech. Rep. ATLAS-CONF-2014-046, CERN, Geneva, Jul 2014

[86] The ATLAS Collaboration, Performance of b-jet Identifcation in the ATLAS Experiment, JINST 11 (2016) 04008

[87] The ATLAS Collaboration, Expected Performance of the ATLAS Experiment-Detector,Trigger and Physics, arXiv:0901.0512

[88] A. Hoecker et al., Toolkit for Multivariate Data Analysis with ROOT, arXiv:physics/0703039

[89] The ATLAS Collaboration, Optimisation of the ATLAS b-tagging performance for the 2016 LHC Run, ATL- PHYS-PUB-2016-012

[90] The ATLAS Collaboration, Expected performance of the ATLAS b-tagging algorithms in Run-2, ATL-PHYS- PUB-2015-022

[91] The ATLAS Collaboration, Calibration of the Momentum Imbalance based Soft Muon Tagger Algorithm, ATL-COM-PHYS-2014-723

[92] The ATLAS Collaboration, ATL-PHYS-PUB-2015-027, Performance of missing transverse momentum reconstruction with the ATLAS detector in the first proton-proton collisions at $\sqrt{s} = 13$ TeV

[93] How to clean jets, Available via atlas
twiki: view/atlasprotected/howtocleanjets, November, 2011.

[94] The ATLAS Collaboration, Tagging and suppression of pileup jets, ATL-PHYS-PUB-2014-001.

[95] MCP Guidelines for Analyses of 2012 Data, Available via atlas twiki: view/atlasprotected/mcpanalysisguidelinesdata2012, May, 2014.

[96] J. Erdmann et al., A likelihood-based reconstruction algorithm for top-quark pairs and the KLFitter framework, Nucl. Instrum. Meth. A 748 (2014) 18.

[97] P.Nason, A New method for combining NLO QCD with shower Monte Carlo algorithms, JHEP 11 (2004) 040. arXiv:hep-ph/0409146.

[98] T. Sjostrand, et al., A Brief Introduction to PYTHIA 8.1, Comput. Phys. Commun. 178 (2008) 852-867. arXiv:0710.3820.

[99] S.Frixione,B.R.Webber, Matching NLO QCD computations and parton shower simulations, JHEP 06 (2002) 029. arXiv:hep-ph/0204244.

[100] M. Bahr, et al., Herwig++ physics and manual, Eur. Phys. J. C 58 (2008) 639-707, arXiv:0803.0883.

[101] T. Sjostrand, et al., PYTHIA 6.4 Physics and Manual, JHEP 05 (2006) 026. arXiv:hep- ph/0603175.

[102] Sherpa Manual Version 2.2.1, https://sherpa.hepforge.org/doc/SHERPA-MC-2.2.1.html

[103] The ATLAS Collaboration, The ATLAS Simulation Infrastructure, Eur. Phys. J. C 70 (2010) 823, arXiv: 1005.4568.

[104] GEANT4 Collaboration, S. Agostinelli et al., GEANT4: A Simulation toolkit, Nucl. Instrum. Meth. A 506 (2003) 250.

[105] The ATLAS Collaboration, The simulation principle and performance of the ATLAS fast calorimeter simulation FastCaloSim, ATL-PHYS-PUB-2010-013, 2010.

[106] The ATLAS Collaboration, Electron performance measurements with the ATLAS detector using the 2010 LHC proton-proton collision data, Eur. Phys. J. C 72 (2012) 1909, arXiv: 1110.3174.

[107] The ATLAS Collaboration, Electron identification measurements in ATLAS using $\sqrt{s} = 13$ TeV data with 50 ns bunch-spacing, ATLAS-PHYS-PUB-2015-041 (2015).

[108] Lepton isolation recommendations, https: //twiki.cern.ch/twiki/bin/viewauth/AtlasProtected/IsolationSelectionTool

[109] Lepton isolation recommendations, https://twiki.cern.ch/twiki/bin/viewauth/AtlasProtected/IsolationSelectionTool

[110] The ATLAS Collaboration, Electron efficiency measurements with the ATLAS detector using the 2015 LHC proton-proton collision data, ATLAS-CONF-2016-024.

[111] The ATLAS Collaboration, Muon Combined Performance in Run 2 (25 ns runs), ATL-COM-MUON-2015-093.

[112] The ATLAS Collaboration, Calibration of the Soft Muon Tagger in Run-2 data, ATL-COM-PHYS-2017-1110.

[113] W. Lampl and others, Calorimeter Clustering Algorithms: Description and Performance, ATL-LARG-PUB-2008-002.

[114] Cacciari, M and Salam, G and Soyez, G, The anti-k_t jet clustering algorithm,JHEP(04)63 2018.

[115] The ATLAS Collaboration, Selection of jets produced in 13 TeV proton-proton collisions with the ATLAS detector, ATLAS-CONF-2015-029.

[116] The ATLAS Collaboration, Performance of pile-up mitigation techniques for jets in pp collisions at $\sqrt{s} = 8$ TeV using the ATLAS detector, arXiv, CERN-PH-EP-2015-206.

[117] C.-H.Kom,etal.,Charge asymmetry in W+jets production at the LHC, Eur.Phys.J.C69 (2010) 67-73. arXiv:1004.3404, doi:10.1140/epjc/s10052-010-1353-z.

[118] The ATLAS Collaboration, Estimation of non-prompt and fake lepton backgrounds in final states with top quarks produced in proton-proton collisions at $\sqrt{s} = 8$ TeV with the ATLAS Detector, ATLAS-CONF-2014-058, 2014.

[119] A. Caldwell, D. Kollar, K. Kroninger, Comput. Phys. Commun. 180 (2009) 2197

[120] R. Brun, et al., ROOT: An object oriented data analysis framework, Nucl. Instrum. Meth. A389 (1997) 81-86

[121] F. James, et al., Minuit: A System for Function Minimization and Analysis of the Parameter Errors and Correlations, Comput. Phys. Commun. 10 (1975) 343-367

[122] A. Czarnecki, et al., Helicity fractions of W bosons from top quark decays at NNLO in QCD, Phys. Rev. D81 (2010) 111503. arXiv:1005.2625, doi:10.1103/PhysRevD.81.111503.

[123] M. Aaboud et al., Luminosity determination in pp collisions at $\sqrt{s} = 8$ TeV using the ATLAS detector at the LHC, Eur. Phys. J. C76 (2016) 653

[124] J. Wenninger, Machine Protection and Operation for LHC, in: Proceedings, 2014 Joint International Accelerator School: Beam Loss and Accelerator Protection: New- port Beach, CA, USA, November 5-14, 2014, 2016, pp. 377-401. arXiv:1608.03113

[125] The ATLAS Collaboration, Simulation of top-quark production for the ATLAS experiment at $\sqrt{s} = 13$ TeV, ATL-PHYS-PUB-2016-004, 2016, url: https://cds.cern.ch/record/2120417

[126] JVT Recommendations, https://twiki.cern.ch/twiki/bin/view/ AtlasProtected/JVTCalibration

[127] The ATLAS Collaboration, Electron and photon reconstruction and performance in ATLAS using a dynamical, topological cell clustering-based approach, ATL-PHYS-PUB-2017-022

[128] The ATLAS Collaboration, Electron efficiency measurements with the ATLAS detector using the 2015 LHC proton-proton collision data, ATLAS-CONF-2016-024 (2016)

[129] The ATLAS Collaboration, Electron reconstruction and identification in the ATLAS experiment using the 2015 and 2016 LHC proton-proton collision data at $\sqrt{s} = 13$ TeV

[130] The ATLAS Collaboration, Jet Calibration and Systematic Uncertainties for Jets Reconstructed in the ATLAS Detector $\sqrt{s} = 13$ TeV, ATL-PHYS-PUB-2015-015 (2015)

[131] The ATLAS Collaboration, Jet energy measurement and its systematic uncertainty in proton-proton collisions at $\sqrt{s} = 7$ TeV with the ATLAS detector, Eur. Phys. J. C 75 (2015) 17

[132] JER Recommendations, https: //twiki.cern.ch/twiki/bin/view/ AtlasProtected/JetResolution2015Prerecom, Accessed: 2018-03-06

[133] ETMiss Recommendations, https://twiki.cern.ch/twiki/bin/viewauth/ AtlasProtected/EtmissRecommendationsRel20p7, Accessed: 2018-03-06

[134] Heavy Flavour Averaging Group (HFAG) Collaboration, (2014), arXiv:1412.7515

[135] DELPHI Collaboration, Phys. Lett. B 576 (2003) 29, arXiv: 0311005

[136] CDF Collaboration, Phys. Rev. D 77 (2008) 072003, arXiv: 0801.4375

[137] CDF Collaboration, Phys. Rev. Lett. 84 (2000) 1663, arXiv: 9909011

[138] CDF Collaboration, Phys. Rev. D 60 (1999) 092005

[139] CDF Collaboration, Phys. Rev. D 79 (2009) 032001, arXiv: 0810.3213

[140] LHCb Collaboration, Phys. Rev. Lett. 107 (2011) 211801, arXiv: 1106.4435

[141] LHCb Collaboration, JHEP 04 (2013) 001, arXiv: 1301.5286

[142] Top MC PDF Recommendations, https: //twiki.cern.ch/twiki/bin/view/ AtlasProtected/TopMCPDFReccommendations

[143] G. D'Agostini, Nucl. Instrum. Meth. A 362, 487 (1995)

[144] G. Cowan, Statistical data analysis, 1998